ISSN 1811-1165 (Print)
ISSN 2413-2179 (Online)

KARAGANDA BUKETOV UNIVERSITY

EURASIAN PHYSICAL TECHNICAL JOURNAL

VOLUME 22, NO. 4(54), 2025

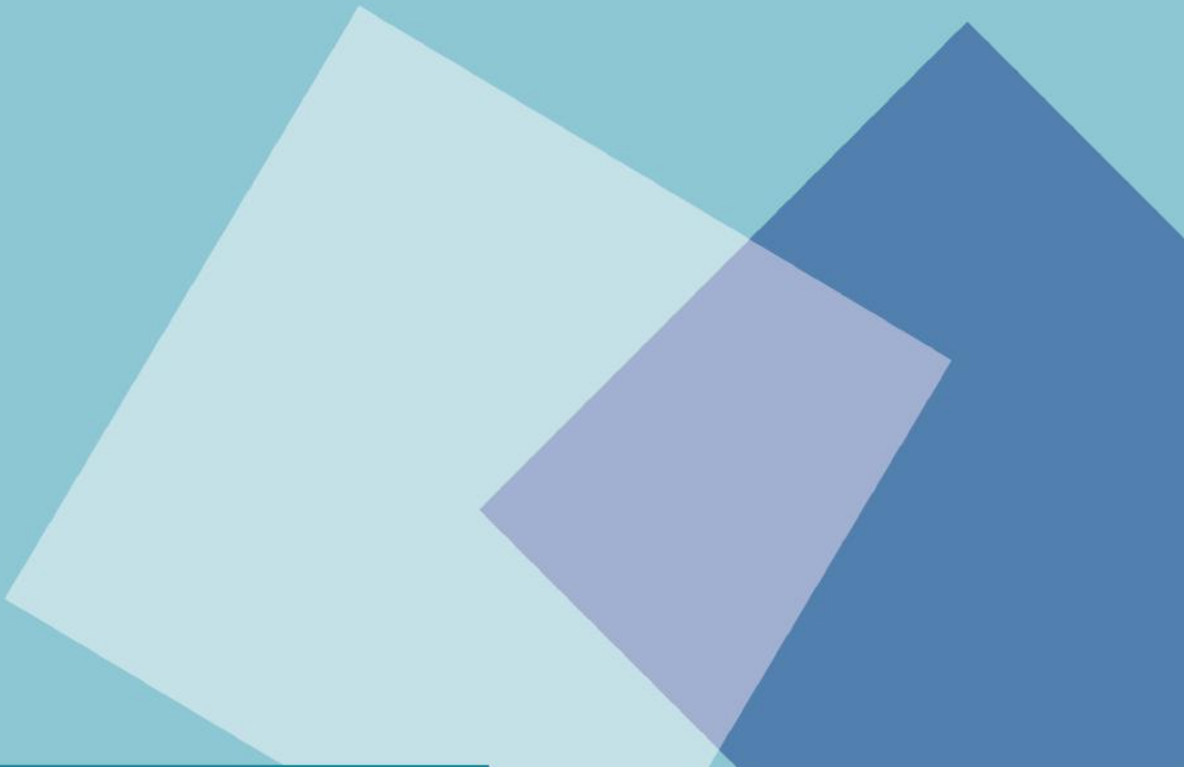

phtj.buketov.edu.kz

EURASIAN PHYSICAL TECHNICAL JOURNAL

p - ISSN 1811-1165
e - ISSN 2413-2179

Volume 22, No. 4(54), 2025
1st issue – June, 2004

Journal Founder:

NON-PROFIT LIMITED COMPANY «KARAGANDA NATIONAL RESEARCH UNIVERSITY NAMED AFTER ACADEMICIAN YE.A. BUKETOV»

https://phtj.buketov.edu.kz

www.facebook.com/groups/1103109540750967

Registration Certificate No.4382-Zh,
November 7, 2003.

Re-registration Certificate No. KZ32VPY00135738,
November 28, 2025 issued by the Information
Committee of the Ministry of Culture and Information
of the Republic of Kazakhstan

Contact information:

Editorial board of EAPhTJ
(Build. 2, room 216)
Karaganda Buketov University
Universitetskaya Str.28, Karaganda,
Kazakhstan, 100024
Subscription index: 75240

Tel: +7(7212) 77-04-03
Fax: +7(7212) 35-63-98
E-mail: ephtj@mail.ru,
ephtj2021@gmail.com

Signed to print 29.12.2025
Format 60x84 1/8. Offset paper.
Volume 18.88 p.sh. Circulation 300 copies.
Order No. 190.

Printed in the Publishing House of
Karaganda National Research University named
after academician Ye.A. Buketov

Tel. +7 (7212) 35-63-16.
E-mail: printed@karnu-buketov.edu.kz

EDITOR-IN-CHIEF

Sakipova S.E., Buketov Karaganda National Research University, Karaganda, Kazakhstan

ISSUE EDITOR

Kozlovskiy A.L., L.N. Gumilyov Eurasian National University, Astana, Kazakhstan

EDITORIAL BOARD

Aringazin A.K., L.N. Gumilyov Eurasian National University, Astana, Kazakhstan

Dzhumanov S., Institute of Nuclear Physics, Uzbekistan Academy of Sciences, Tashkent, Uzbekistan

Hançerlioğullari A., Kastamonu Üniversitesi, Kastamonu, Turkey

Ibrayev N.Kh., Institute of Molecular Nanophotonics, Buketov Karaganda National Research University, Karaganda, Kazakhstan

Jakovics A., Institute of Numerical Modelling, University of Latvia, Riga, Latvia

Kucherenko M.G., Director of the Laser and Information Biophysics Centre, Orenburg State University, Orenburg, Russia

Kuritnyk I.P., Department of Electronics and Automation, High school in Oswiecim, Poland

Kushpil S., Heavy Ion Group, Nuclear Physics Institute of the Czech Academy of Science, Řež near Prague, Czech Republic

Miau J.J., Department of Aeronautics and Astronautics, National Cheng Kung University, Tainan, Taiwan

Miroshnichenko A.S., Department of Physics and Astronomy, University of North Carolina at Greensboro, North Carolina, USA

Saulebekov A.O., Kazakhstan Branch of Lomonosov Moscow State University, Astana, Kazakhstan

Senyut V.T., Joint Institute of Mechanical Engineering of National Academy of Sciences of Belarus, Minsk, Belarus

Shrager E.R., National Research Tomsk State University, Tomsk, Russia

Stoev M., South-West University «Neofit Rilski», Blagoevgrad, Bulgaria

Suprun T., Institute of Engineering Thermophysics of NASU, Kyiv, Ukraine

Trubitsyn A.A., Ryazan State Radio Engineering University, Ryazan, Russia

Zeinidenov A.K., Buketov Karaganda National Research University, Karaganda, Kazakhstan

Zhanabaev Z.Zh., Al-Farabi Kazakh National State University, Almaty, Kazakhstan

TECHNICAL EDITOR

Kambarova Zh.T., Buketov Karaganda National Research University, Karaganda, Kazakhstan

© Buketov Karaganda National Research University, 2025

Eurasian Physical Technical Journal, 2025, Vol. 22, No. 4(54)

CONTENTS

MATERIALS SCIENCE

ENERGY

ENGINEERING

PHYSICS AND ASTRONOMY

Dear authors and readers!
Dear colleagues!

Please accept my most sincere congratulations on the upcoming New Year!
I wish you, your family, and loved one's good health, creative success, happiness, and prosperity!

It has become a good tradition to take stock of our joint work in the final days of the year.

The Certificate of re-registration of the periodical print and electronic publication No. KZ32VPY00135738 was received from the Information Committee of the Ministry of Culture and Information of the Republic of Kazakhstan in connection with the assignment of our publisher status to Karaganda National Research University named after academician Ye.A. Buketov (November 28, 2025).

Over the past year, the journal has successfully covered the results of scientific and applied research in technical physics.

The Eurasian Physical Technical Journal continues to be indexed in the SCOPUS database across all four categories, https://www.scopus.com/sourceid/21100920795. Now CiteScore equals 1.4

In 2025, according to the Scimago Journal & Country Rank (SJR) analytical platform, the h-index was **8**. In 2025, some of the journal's digital metrics in the Scopus database showed positive dynamics, particularly in the number of citations and the number of articles authored by women.

Attention to our journal is growing, and the geography of our authors is expanding. In 2025, more than 60 articles were published by authors from Kazakhstan, Azerbaijan, Uzbekistan, Ukraine, Russia, Nigeria, Indonesia, Iraq, Latvia, Romania, and China.

Last year articles devoted to research using modern computer technologies and neural networks generated the greatest interest. The review team has expanded; their high professionalism and objectivity ensure the quality of the published articles.

The last issue presents 14 articles with new research results on the most pressing problems in technical physics. The well-known Kazakh scientist A.L. Kozlovskiy (ih - 41) participated in the preparation of this issue. In the future, we plan to continue the practice of inviting issue editors.

I would like to express my appreciation and gratitude to the authors, editorial board members and each reviewer for their active participation in the journal's work. Your assistance in expanding the journal's portfolio, selecting the most interesting papers, and disseminating information about our journal is invaluable.

We hope the presented articles will not only be interesting but also useful in preparing new publications for researchers, teachers, graduate students, and postgraduates.

We would be grateful for any citations of articles published in the journal.
And we look forward to seeing you among our readers and authors in the future.

With respect and hope for fruitful collaboration,
Editor-in-Chief, Professor Sakipova S.E.
December, 2025

EURASIAN PHYSICAL TECHNICAL JOURNAL

2025, Volume 22, No. 4 (54)

https://doi.org/10.31489/2025N4/5-23

Received: 06/09/2025 Revised: 14/11/2025 Accepted: 20/12/2025

Research Article

UDC 539.199, 544.723.2

CONFORMATIONAL STRUCTURE OF BINARY POLYPEPTIDE COMPLEXES ON THE SURFACE OF A CHARGED GOLD NANOPARTICLE WITH CHANGING PH

Kruchinin N.Yu.*, Kucherenko M.G.

Center of Laser and Informational Biophysics, Orenburg State University, Orenburg, Russia
Corresponding author: kruchinin_56@mail.ru

Abstract. *Using molecular dynamics simulation, pH-sensitive conformations of binary complexes of homogeneous polypeptides located on the surface of a charged spherical gold nanoparticle were studied. A mathematical model of conformations has been developed taking into account interactions in a complex of two homogeneous polymers on the surface of a charged spherical nanoobject. When two polypeptides were adsorbed on a nanoparticle, the structure of the macromolecular corona depended significantly on the polypeptide combinations in the binary complex. Two identical homogeneous polypeptides shifted away from each other along the neutral surface when their pH deviated from the isoelectric point, while on the surface of a similarly charged nanoparticle, the macrochain corona became strongly loosened. On the charged nanoparticle, the polymer shell of the two polypeptides of opposite polarities delaminated, and the shell itself swelled significantly. When one of the polypeptides in this binary complex reached the isoelectric point, the second charged polypeptide unfolded and disengaged from the first macrochain, shifting away from the surface of the similarly charged nanoparticle.*

Keywords: polypeptide complex, molecular dynamics simulation, conformational transformations, charged nanoobject.

1. Introduction

Currently, shell nanosystems have found wide application in drug delivery [1], as elements in various sensors, such as sensors based on surface-enhanced Raman scattering (SERS) [2], surface plasmon resonance (SPR) [3] and Förster resonance energy transfer (FRET) [4]. Of great interest in biochemistry and biomedicine is the creation of such sensors, nanoprobes and nanocontainers whose characteristics are sensitive to changes in the pH of the medium [5-14]. Thus, in the works [5-9], polymer brushes and layers on various surfaces sensitive to changes in the pH are presented. It has been shown that the density of polymer brushes can be significantly varied [5-8]. This allows for the release of small dye molecules [5] or chromophores [6], the creation of pH-sensitive supramolecular switches [7], and the controlled adsorption of gold nanoparticles bound to the ends of macrochains in a polymer brush [8].

It is known that the intracellular pH in normal cells is in the range of 7.0–7.2 lower than the extracellular pH, which is in the range of 7.3–7.4. Cancer cells have a higher intracellular pH of 7.12–7.65 and lower extracellular pH of 6.2–6.9 compared to normal cells [10–11]. This allows using pH-sensitive conformational changes in macrochains for cancer diagnostics and therapy. A pH-sensitive nanoprobe was presented in [9], in which the conformational structure of the ligand shell around the quantum dot was reconstructed when the pH level changed from physiological to more acidic, corresponding to a cancer tumor [9]. Photothermal therapy uses gold nanoparticles with a polymer shell, which remain stable in healthy tissue and aggregate when entering a tumor due to changes in pH [12]. Studies [13-14] have examined nanocarriers that are sensitive to changes in pH, such as a gold nanoparticle with a peptide shell containing an anticancer drug. A gold nanoparticle with a polypeptide corona sensitive to pH changes can be used as such a nanosystem. The conformations of polyelectrolyte polypeptides change significantly on the charged surface of the adsorbent [15-21]. By simultaneously varying the charge of the nanoparticle and the degree of polyelectrolyticity of the polypeptide (by changing the pH), it is possible to control the conformational changes of the adsorbed polypeptide.

A more complex picture of conformational rearrangements with changes in pH will arise when several polypeptides are located on the surface of a charged spherical metal nanoparticle. When the pH level changes, two identical polypeptides will be charged with the same sign and magnitude of charge, which will lead to the repulsion of the polypeptides from each other. If the polypeptides in a binary complex consist of amino acid residues of different types, their charge will change differently depending on the values of the isoelectric points characteristic of each polypeptide. Therefore, on the surface of a charged nanoparticle, the conformations of two different polypeptides will change differently depending on the pH level. Such pH-sensitive conformational changes in binary complexes can be used to create small molecule nanocarriers (fluorescent dye molecules or drugs) contained in the structure of the polypeptide fringe and released during its rearrangement when the pH level changes. In addition, such pH-dependent conformations of pairs of macromolecules adsorbed on a charged nanoparticle can be used in SERS, SPR, FRET sensors and nanoprobes.

Thus, the aim of this work is to study the pH-dependent conformations of binary complexes of homogeneous polypeptides on the surface of a charged spherical gold nanoparticle.

2. Mathematical model of macrochain conformations taking into account interactions in a complex of two homogeneous polypeptides on the surface of a charged nanosphere with a change in the hydrogen index of the solvent

In the case where the links of two homogeneous polypeptides at a certain value of the hydrogen index of the solvent acquire charges of opposite sign, a spatial structure with intertwined, oppositely charged macrochains of polyelectrolytes can form on the surface of the charged nanosphere.

2.1 Single adsorbed polyelectrolyte polypeptide chain on the surface of a charged spherical nanoparticle

The description of the equilibrium structure of an adsorbed macrochain with links of length a at an absolute temperature T can be made on the basis of a conformational function $\psi(\mathbf{r})$ satisfying the nonlinear integro-differential equation of Grosberg-Khokhlov-Edwards [22-23]

$$\frac{a^2kT}{6}\nabla^2\psi(\mathbf{r}) = [V(\mathbf{r}) + V_{self}(\mathbf{r}) - \varepsilon]\psi(\mathbf{r}), \tag{1}$$

The self-consistent field potential $V_{self}(\mathbf{r})$ takes into account the volume interactions between the polymer links. The potential $V(\mathbf{r})$ characterizes the external field in which the polymer chain is located, and which in the case under consideration is created by the adsorbent nanoparticle, electrically neutral or charged.

The spatial distribution of the local density $n(\mathbf{r})$ of chain links is determined by the square of the conformational function $\psi(\mathbf{r})$ corresponding to the minimum eigenvalue ε_0: $n(\mathbf{r}) = \psi^2_{\min}(\mathbf{r})$. In the case of an electrically neutral spherical surface or a nanosphere, the field potential $V(\mathbf{r}) = V_{9-3}(r)$ is the van der Waals interaction potential $V_{9-3}(r)$ of the chain link with the nanoparticle. The exponents 3 and 9 of the power dependences of the potential $V_{9-3}(r)$ on the radius r are typical precisely for the spherical shape of a nanobody. The expression for the potential energy $V(r)$ of interaction of an atom with a nanosphere of radius R can be formed from paired atom-atom potentials of the form $\upsilon(r) = D\left[(r_0/r)^{12} - 2(r_0/r)^6\right]$, and is represented by a triple integral

$$V(r)=2\pi\int_0^{\pi}\int_0^{R} n_0\, \upsilon(\rho)\, r'^2 dr' \sin\theta d\theta,$$

where $\rho^2 = r'^2 + r^2 - 2rr'\cos\theta$. Here D and r_0 are the parameters of the 6–12 Lennard-Jones potential, n_0 is the concentration of nanosphere atoms. The potential energy of interaction of a chain link with an uncharged spherical nanoparticle of radius R, in the case of the initial pair potential of 6–12 Lennard-Jones for intermolecular interaction between the atoms of the link and the nanoparticle, is written as ($r > R$)

$$V_{9-3}(r)=\frac{\pi D n_0 r_0^6}{6r}\left(\frac{r_0^6}{60}\left[\frac{9R+r}{(R+r)^9}-\frac{9R-r}{(R-r)^9}\right]-\left[\frac{3R+r}{(R+r)^3}-\frac{3R-r}{(R-r)^3}\right]\right). \tag{2}$$

Here D and r_0 are the parameters of the 6-12 Lennard-Jones potential, n_0 is the concentration of metal atoms in the nanoparticle.

In the case of a charged nanoparticle with a spherically symmetrically distributed charge Q and a polyelectrolyte chain with a charge e of its link, the potential $V_{eQ}(r) = eQ/r$ of interaction of the macrochain monomer with the Coulomb field of the charged nanoparticle is added to the adsorption potential (2).

$$V_{9-3}^{eQ}(r) = V_{9-3}(r) + V_{eQ}(r) = V_{9-3}(r) + \frac{eQ}{r}. \tag{3}$$

2.2 Ideal Gaussian macromolecular chain without volume interaction of links

The equilibrium configurations of the macrochain in a model that does not take into account the volume interactions of the links ($V_{self}(\mathbf{r})$=0) are given by the conformational function $\psi_0(\mathbf{r})$, which determines the density of the monomeric subunits of the chain in this approximation as $n(\mathbf{r}) = \psi_0^2(\mathbf{r})$. The function $\psi_0(\mathbf{r})$ then satisfies the following differential equation [22]

$$\frac{a^2 kT}{6}\nabla^2\psi_0(\mathbf{r}) = [V(\mathbf{r}) - \varepsilon]\psi_0(\mathbf{r}). \tag{4}$$

In the case of a polyelectrolyte, it is possible to formulate the problem of determining the conformational structure of the fringe and obtain an exact analytical solution for the conformational function $\psi_0(\mathbf{r})$ satisfying equation (4) without appealing to perturbation theory as in earlier works [19-20]. Equation (4) is similar in certain features to the Schrödinger equation containing the Coulomb potential. In other words, a problem arises similar to the problem of a hydrogen-like atom with an additional potential (2), which, in order to obtain an analytical solution to the problem, is replaced by the model potential "wall – delta-functional well" $V_1(r) = V_\infty(R) - \alpha_0\delta(r - r_0)$ [24]. The total potential $V(r)$ in this case takes the form $V_1(r) = V_\infty(R) - \alpha_0\delta(r - r_0) + eQ/r$, where e is still the effective charge of the chain link, and Q is the charge of the sphere.

We define the following parameters: $q_0^2 = -\frac{6|\varepsilon_0|}{a^2 kT}$, $\kappa = \frac{3eQ}{a^2 kT q_0} = \frac{3eQ}{a\sqrt{6|\varepsilon_0|kT}}$. Instead of the radial function $\psi_0(\mathbf{r}) = F_0(r)$ satisfying equation (4), for a system with spherical symmetry we introduce the function *f(r)* by the relation $F_0(r) = \exp(-q_0 r) f(r)$, and the dimensionless radius $2q_0 r = \rho'$. By direct substitution into (4) we verify that the function $f(\rho')$ satisfies the degenerate hypergeometric equation

$$\rho' f'' + (\gamma - \rho') f' - \alpha f(\rho') = 0, \tag{5}$$

with γ=2 and $\alpha = 1 - \kappa$. Then the general solution of the boundary value problem for a spherical system with a macromolecular frame is a superposition of two degenerate hypergeometric functions of the first ${}_1F_1(\alpha,\gamma,\rho) \equiv M(\alpha,\gamma,\rho)$ and second $U(\alpha,\gamma,\rho)$ kind with arbitrary constants C_1 and C_2

$$f(\rho) = C_1 M(\alpha,2,\rho) + C_2 U(\alpha,2,\rho), \tag{6}$$

Degenerate hypergeometric functions of the first $M(\alpha,\gamma,\rho)$ and second $U(\alpha,\gamma,\rho)$ kind are defined by the expressions

$$M(\alpha,\gamma,\rho)=\frac{\Gamma(\gamma)2^{1-\gamma}e^{\rho/2}}{\Gamma(\gamma-\alpha)\Gamma(\alpha)}\int\limits_{-1}^{1} e^{-\rho t/2}(1-t)^{\alpha-1}(1+t)^{\gamma-\alpha-1}dt,\ \ \mathrm{Re}\gamma>\mathrm{Re}\alpha>0, \tag{7}$$

$$U(\alpha,\gamma,\rho)=\frac{1}{\Gamma(\alpha)}\int\limits_{0}^{\infty} e^{-\rho t}t^{\alpha-1}(1+t)^{\gamma-\alpha-1}dt\cdot \tag{8}$$

In radial ranges $2q_0R\le\rho\le 2q_0r_0$ and $2q_0r_0\le\rho$ for functions $f_{I,II}(\rho)$ we can write

$$\begin{cases} f_I(\rho)=C_1M(\alpha,2,\rho)+C_2U(\alpha,2,\rho), & q_0R\le\rho/2\le q_0r_0 \\ f_{II}(\rho)=C_3U(\alpha,2,\rho), & 2q_0r_0\le\rho \end{cases}. \tag{9}$$

$$U(\alpha,2,\rho)=\frac{1}{\Gamma(\alpha-1)}\left[\frac{1}{(\alpha-1)_1\rho}+\sum_{k=0}^{\infty}\frac{(\alpha)_k\rho^k}{k!(2)_k}\left(\ln\rho+\frac{\Gamma'(\alpha+k)}{\Gamma(\alpha+k)}-\frac{\Gamma'(2+k)}{\Gamma(2+k)}-\frac{\Gamma'(1+k)}{\Gamma(1+k)}\right)\right] \tag{10}$$

$$G(\alpha=1-\kappa,n=2,\rho)=\frac{(-1)^n}{(n-1)!\Gamma(\alpha-n+1)}\left\{\sum_{k=1}^{n-1}\frac{(-1)^{k-1}(k-1)!}{(\alpha-k)_k(n-k)_k}\rho^{-k}+\right.$$
$$\left.+\sum_{k=0}^{\infty}\frac{(\alpha)_k}{k!(n)_k}\rho^k\left[\ln\rho+\psi(\alpha+k)-\psi(n+k)-\psi(k+1)\right]\right\},\ (\alpha)_k=\frac{\Gamma(\alpha+k)}{\Gamma(\alpha)}, \tag{11}$$

$$\kappa=\frac{3e'Q}{a^2kTq_0}=\frac{3e'Q}{a\sqrt{6|\varepsilon_0|kT}}\,.$$

where Q is the charge of the nanoparticle, and the “energy” parameter $|\varepsilon_0|=\dfrac{q^2a^2kT}{6}$.

From the boundary conditions on the surface of the nanoparticle we obtain the following relationships between the constants C_1, C_2 and C_3:

$$C_2=-C_1\frac{M(\alpha,2,2q_0R)}{U(\alpha,2,2q_0R)},$$
$$C_3=C_1\left[\frac{M(\alpha,2,2q_0r_0)}{U(\alpha,2,2q_0r_0)}-\frac{M(\alpha,2,2q_0R)}{U(\alpha,2,2q_0R)}\right]. \tag{12}$$

Then the desired solutions of the Grosberg-Khokhlov equation take the form

$$\begin{cases} F_I(r)=C_1\left[M(\alpha,2,2q_0r)-\dfrac{M(\alpha,2,2q_0R)}{U(\alpha,2,2q_0R)}U(\alpha,2,2q_0r)\right]\exp\left(-q_0r\right), & R\le r\le r_0 \\ F_{II}(\rho)=C_1\left[\dfrac{M(\alpha,2,2q_0r_0)}{U(\alpha,2,2q_0r_0)}-\dfrac{M(\alpha,2,2q_0R)}{U(\alpha,2,2q_0R)}\right]U(\alpha,2,2q_0r)\exp\left(-q_0r\right), & r_0\le r \end{cases} \tag{13}$$

To determine the parameters q_l and ε_l it is necessary to solve the equation obtained for the jump in the radial derivative at the point r_0

$$F'_{II0}(r)\,|_{r=r_0+0}-F'_{I0}(r)\,|_{r=r_0-0}=-\frac{6\alpha_0}{a^2kT}F_{I0}(r_0) \tag{14}$$

Substituting (13) into (14) we obtain the general transcendental equation for the eigenvalues

$$\frac{3\alpha_0}{a^2\alpha kTq_0}-\left[\frac{U(\alpha+1,3,2q_0r_0)}{U(\alpha,2,2q_0r_0)}\right]=$$
$$=\left[\frac{M(\alpha+1,3,2q_0r_0)}{2U(\alpha,2,2q_0r_0)}+\frac{M(\alpha,2,2q_0R)}{U(\alpha,2,2q_0R)}\frac{U(\alpha+1,3,2q_0r_0)}{U(\alpha,2,2q_0r_0)}\right]\left[\frac{M(\alpha,2,2q_0r_0)}{U(\alpha,2,2q_0r_0)}-\frac{M(\alpha,2,2q_0R)}{U(\alpha,2,2q_0R)}\right]^{-1} \tag{15}$$

It should be noted that the degenerate hypergeometric functions (7) and (8) in a number of cases, with a certain relationship between the parameters α and γ, are expressed through the Bessel functions of the imaginary argument

$$I_\nu(\rho) = \frac{(\rho/2)^\nu}{\Gamma(\nu+1)} \exp(-\rho) M(\nu+1/2, 2\nu+1, 2\rho), \tag{16}$$

$$K_\nu(\rho) = \sqrt{\pi}(2\rho)^\nu \exp(-\rho) U(\nu+1/2, 2\nu+1, 2\rho). \tag{17}$$

Since γ=2 and $\alpha = 1-\kappa$, $\kappa = \frac{3e'Q}{a^2kTq_0} = \frac{3e'Q}{a\sqrt{6|\varepsilon_0|kT}}$, to obtain γ=2 it is necessary that γ=2=$(2\nu+1)$, whence it follows that $\nu = 1/2$. This means that $\alpha = 1$ and Q=0. Thus, in this case we obtain an electrically neutral nanoparticle, and the same, uncharged, macrochain. Formulas (13) go over to the previously obtained expressions with Bessel functions $I_{1/2}$, $K_{1/2}$.

In this case, for a spherically symmetric potential $V_1(r) = V_\infty(R) - \alpha_0\delta(r-r_0)$, the radial functions $\psi(\mathbf{r}) = F_0^{I,II}(r)$ are defined inside the spherical layer $R<r<r_0$ and in the region conjugate to it $r>r_0$ in the following form

$$\begin{cases} F_0^I(r) = A_0\left[\frac{I_{1/2}(q_0r)}{\sqrt{r}} - \frac{I_{1/2}(q_0R)}{K_{1/2}(q_0R)}\frac{K_{1/2}(q_0r)}{\sqrt{r}}\right], & R<r<r_0 \\ F_0^{II}(r) = A_0\left[\frac{I_{1/2}(q_0r_0)}{K_{1/2}(q_0r_0)} - \frac{I_{1/2}(q_0R)}{K_{1/2}(q_0R)}\right]\frac{K_{1/2}(q_0r)}{\sqrt{r}}, & r_0<r<\infty \end{cases}, \tag{18}$$

where $I_{1/2}(q_0r)$ and $K_{1/2}(q_0r)$ are modified Bessel functions of the first and second kind with half-integer index, and eigenvalues $q_0^2 = -\frac{6\varepsilon_0}{a^2kT}$, R is the radius of the nanoparticle. The transcendental equation (14) for the eigenvalue q_0 is transformed to the equation

$$\frac{a^2kT}{6\alpha r_0} = I_{1/2}(q_0r_0)K_{1/2}(q_0r_0) - K_{1/2}^2(q_0r_0)\frac{I_{1/2}(q_0R)}{K_{1/2}(q_0R)}, \tag{19}$$

which is related to (15), but allows us to define in a new way q_0, and with it the only discrete level of the spectrum ε_0. The conformational characteristics (18) of the chain in the case of an uncharged nanoparticle or an electrically neutral macromolecule are indifferent to changes in the charge states of the system components.

Thus, for the case of a polyelectrolyte fringe adsorbed by a charged nanosphere, neglecting volume interactions, we have an exact analytical solution to the problem presented by formulas (13) and (15). Note that, unlike the aligned polyampholyte links of a macrochain, for which there was always an attraction to the surface, regardless of the sign of the nanoparticle charge, in the case of a polyelectrolyte chain under consideration, there may be both an additional attraction (opposite signs of the charges of the link and the particle) against the background of the attractive potential responsible for the adsorption of the macromolecule, and a repulsion (identical signs of the charges), which hinders adsorption or even leads to desorption at a sufficiently high temperature of the system. This additional Coulomb attraction or repulsion of the links to the surface of the nanoparticle will ultimately determine the observed compression or loosening of the reinforced fringe of the adsorbate.

Quantitatively, this is reflected in the sign of the charge parameter $\alpha - 1 = \pm|\kappa|$. With the same signs of the charge of the links and the adsorbent, under the conditions of realized adsorption of the macrochain, swelling of the fringe will be observed, caused by the Coulomb repulsion from the surface of the links that have avoided attraction by the potential well. For the same reason, in the case of opposite charges, the macrochain fringe should experience Coulomb compression

$$\alpha = 1 \pm |\kappa|.$$

In order to develop an analytical model convenient for carrying out calculations, potential $V_{9-3}(r)$ (2) can be replaced by a simple model potential $V_{\alpha\delta}^\infty(r) = V_\infty(R) - \alpha_0\delta(r-r_0)$ “solid wall – delta-functional well”, in which the point r_0 of localization of the delta-functional well coincides with the radius r_m of the bottom of the potential well (2).

2.3 Accounting for volumetric interlink interactions of a polymer chain

The bulk interlink interactions of the polymer can be taken into account through the potential $V_{self}(\mathbf{r})$ of the self-consistent field using the Edwards method [23]

$$V_{self}(\mathbf{r}) = \mu^*\left(n(\mathbf{r})\right) = kT \cdot B \cdot n(\mathbf{r}), \tag{20}$$

where $\mu^*\left(n(\mathbf{r})\right)$ is the chemical potential of the chain links:

$$B(T) = \frac{2\pi}{3}\left(\frac{\beta'}{T}\right)^{1/4}\Gamma\left(3/4\right),$$

– the second virial coefficient [22], taking into account pairwise collisions of links and the effect of excluded volume due to the repulsive part of the 6–12 Lennard-Jones potential, and the constant

$$\beta' = \left[\beta \pm (Q \cdot e \cdot r_D^{11})\exp(-r/r_D)\,|_{r \to r_D}\right] \tag{21}$$

renormalized taking into account the additional charge on the links of the macrochain and the Debye screening with radius r_D. The gamma function Γ of ¾ takes the numerical value

$$\Gamma\left(3/4\right) = \sqrt{2\pi^2}\,/\,\Gamma(1/4), \quad \Gamma(1/4) = 2\sqrt{K(1/2)\sqrt{\pi}} \approx 3{,}626.$$

In the case of Coulomb interaction of polyelectrolyte units with each other, one can introduce the corresponding pair potential $\Phi_{qq}(r)$, and represent the renormalized constant β' in the form

$$\beta \to \beta' = \left[\left(D + \Phi_{qq}(r_0)\right) \cdot r_0^{12}\right]. \tag{22}$$

Then the model potential in the Grosberg-Khokhlov-Edwards equation (1) can be written as

$$V(r) + V_{self}(\mathbf{r}) = V_\infty(R) - \alpha_0\delta(r - r_0) + kT \cdot B \cdot n(\mathbf{r}).$$

Let us write equation (1) for the conformational function $\psi_1(\mathbf{r})$ of the first macrochain

$$\frac{a_1^2 kT}{6}\nabla^2\psi_1(r) = \left[V_{9-3}^{(1)}(r) + kTB_1 n_1(r) + e_1\varphi_2(r) + \frac{e_1 Q}{r} - \varepsilon_1\right]\psi_1(r). \tag{23}$$

Here, in (23), the electrostatic field potential $\varphi_2(r)$ is created by the charged chain 2 of the second polyelectrolyte and affects the formation of the secondary structure of chain 1 through its conformational function $\psi_1(\mathbf{r})$. It is also obvious that the potential $\varphi_2(r)$ satisfies the Poisson equation

$$\frac{1}{r^2}\frac{d}{dr}r^2\frac{d}{dr}\varphi_2(r) = -4\pi e_2\psi_2^2(r). \tag{24}$$

Equations similar to (23) and (24) can be written by considering the conformations of chain 2 in the field of the charged chain 1. Then, for the conformational functions $\psi_{1,2}(\mathbf{r})$ and potentials $\varphi_{1,2}(r)$, we obtain a closed system of nonlinear differential equations.

2.4 Formation of conformations of two interacting adsorbed polyelectrolyte chains on the surface of a charged nanosphere

Combining all the equations considered into a system, we obtain four interconnected ordinary differential equations

$$\begin{cases} \dfrac{a_1^2 kT}{6}\dfrac{1}{r^2}\dfrac{d}{dr}r^2\dfrac{d}{dr}\psi_1(r) = \left[V_{9-3}^{(1)}(r) + kT \cdot B_1\psi_1^2(r) + e_1\varphi_2(r) + \dfrac{e_1 Q}{r} - \varepsilon_1\right]\psi_1(r) \\ \dfrac{a_2^2 kT}{6}\dfrac{1}{r^2}\dfrac{d}{dr}r2\dfrac{d}{dr}\psi_2(r) = \left[V_{9-3}^{(2)}(r) + kT \cdot B_2\psi_2^2(r) + e_2\varphi_1(r) + \dfrac{e_2 Q}{r} - \varepsilon_2\right]\psi_2(r) \\ \dfrac{1}{r^2}\dfrac{d}{dr}r^2\dfrac{d}{dr}\varphi_1(r) = -4\pi e_1\psi_1^2(r) \\ \dfrac{1}{r^2}\dfrac{d}{dr}r^2\dfrac{d}{dr}\varphi_2(r) = -4\pi e_2\psi_2^2(r) \end{cases}. \tag{25}$$

The self-consistent system of equations (25) for conformational functions $\psi_{1,2}(\mathbf{r})$ and potentials $\varphi_{1,2}(r)$ is quite complex, and obtaining analytical expressions for functions $\psi_{1,2}(\mathbf{r})$ and $\varphi_{1,2}(r)$ is problematic. However, the general structure of the model based on system (25) is partially visible even without resorting to exact solutions of these equations. In addition, sufficient progress in solving the problem can be made by adopting the approximation of relatively weak electrolyte fields. Then, in the zero approximation, the potentials $\varphi_{1,2}(r)$ are not taken into account in the first two equations of system (25), and the conformational functions $\psi_{1,2}(\mathbf{r})$ in this approximation are found as $\psi_{1,2}(\mathbf{r}) \to \psi_{1,2}^{(0)}(\mathbf{r})$.

$$\begin{cases} \dfrac{a_1^2 kT}{6}\dfrac{1}{r^2}\dfrac{d}{dr}r^2\dfrac{d}{dr}\psi_1^{(0)}(r) = \left[V_{9-3}^{(1)}(r) + kT\cdot B_1\psi_1^{(0)2}(r) + \dfrac{e_1 Q}{r} - \varepsilon_1\right]\psi_1^{(0)}(r) \\ \dfrac{a_2^2 kT}{6}\dfrac{1}{r^2}\dfrac{d}{dr}r^2\dfrac{d}{dr}\psi_2^{(0)}(r) = \left[V_{9-3}^{(2)}(r) + kT\cdot B_2\psi_2^{(0)2}(r) + \dfrac{e_2 Q}{r} - \varepsilon_2\right]\psi_2^{(0)}(r) \\ \dfrac{1}{r^2}\dfrac{d}{dr}r^2\dfrac{d}{dr}\varphi_1^{(0)}(r) = -4\pi e_1\psi_1^{(0)2}(r) \\ \dfrac{1}{r^2}\dfrac{d}{dr}r^2\dfrac{d}{dr}\varphi_2^{(0)}(r) = -4\pi e_2\psi_2^{(0)2}(r) \end{cases}. \qquad (26)$$

In this case, the last two equations in (26) – the Poisson equations, become autonomous and can be solved by standard electrostatic methods for a given charge distribution density $e_{1,2}\left[\psi_{1,2}^{(0)}(r)\right]^2$ if the solutions $\psi_{1,2}^{(0)}(\mathbf{r})$ of the first two equations of system (26) are found beforehand. After this, the found potentials $\varphi_{1,2}^{(0)}(r)$ of the zero approximation are returned to system (25) to find the functions $\psi_{1,2}^{(1)}(\mathbf{r})$ and potentials $\varphi_{1,2}^{(1)}(r)$ of the first approximation. To achieve the required level of accuracy, this iterative procedure can be continued.

As in Section 2.2, to find in analytical form the radial distribution of links of a polymer chain adsorbed by a charged nanoparticle of radius *R*, the potential energy (2) of the interaction of an atom with a nanosphere should be replaced by a simple model potential $V_{\alpha\delta}^{\infty}(r) + \dfrac{e_{1,2}Q}{r} = V_{\infty}(R) - \alpha\delta(r - r_m) + \dfrac{e_{1,2}Q}{r}$ "solid wall – delta-functional well".

The solutions $\psi_{1,2}^{(0)}(r)$ of equations (26) without taking into account the effects of the self-consistent field are then written in the form (13), where the parameters $q_{1,2}^2 = -\dfrac{6\varepsilon_{1,2}}{a_{1,2}^2 kT}$ are the roots of two transcendental equations of type (15).

The only roots of these equations correspond to functions $\psi_{1,2}^{(0)}(r)$ whose squares give the desired expressions for the radial distributions $n_{1,2}^{(0)}(r) = \psi_{1,2}^{(0)2}(r)$ of the density of links of chains 1 and 2.

2.5 Calculation of field potentials and interaction energy of adsorbed polyelectrolyte chains

The Green's function of the two Laplace equations in (26) of the external Dirichlet problem (*r*>*R*) for a ball has the form

$$G(r,\theta,\phi;r_0,\theta_0,\phi_0) = \frac{1}{4\pi}\left(\frac{1}{r_{MM_0}} - \frac{R}{r_0\cdot r_{MM_1}}\right). \qquad (27)$$

The point M1 is the conjugate point of M0 relative to the surface of the sphere. Then the zeroth approximation potentials $\varphi_{1,2}^{(0)}(r)$ outside the sphere (*r*>*R*) can be written in quadratures

$$\varphi_{1,2}(r)=\int_0^{\pi}\sin\theta_0 d\theta_0\int_R^{\infty} e_{1,2}\psi_{1,2}^{(0)2}(r_0)G(r,\theta,\phi;r_0,\theta_0,\phi_0)2\pi r_0^2 dr_0\,. \tag{28}$$

The interaction energy of chains in some cases may be of independent interest and is determined by integrals

$$W[n_1(r),n_2(r)]=\int_R^{\infty} e_1 n_1(r)\varphi_2(r)4\pi r^2 dr=\int_R^{\infty} e_2 n_2(r)\varphi_1(r)4\pi r^2 dr\,. \tag{29}$$

3. Molecular dynamics simulation

Molecular dynamics (MD) simulations were performed for polypeptides on the surface of a gold nanoparticle with a radius of about 3 nm [25]. MD simulations were performed using the NAMD 2.14 software package [26]. A number of combinations of polypeptides, each 100 units long, were considered:

1) one macromolecule of histidine His amino acid residues,
2) two macromolecules of histidine amino acid residues – the **HH** polypeptide complex,
3) one polypeptide of histidine His units, and the other of glutamic acid Glu units – the **HG** polypeptide complex.

The following pH range was chosen: from 4 to 7.6. At pH≈4, all polyhistidine units have a positive charge, and at the isoelectric point for histidine $\mathrm{pI_{His}}\approx 7.6$, all units become uncharged $\mathrm{His^0}$. As the pH increases in this range, some amino acid residues change their charge and become neutral [27]. A number of macrochains with different charged units were considered:

1) polypeptide $\mathrm{His_{100}}$ (total charge of the macrochain +100*e*) - corresponds to a hydrogen index level of pH≈4;
2) polypeptide $\mathrm{(His_2His^0His)_{25}}$ (total charge +75*e*) - pH≈5.5;
3) polypeptide $\mathrm{(His^0His)_{50}}$ (total charge +50*e*) - pH≈6;
4) polypeptide $\mathrm{(His^0{}_2HisHis^0)_{25}}$ (total charge +25*e*) - pH≈6.5;
5) polypeptide $\mathrm{(His^0{}_5HisHis^0{}_4)_{10}}$ (total charge +10*e*) – pH≈7;
6) polypeptide $\mathrm{His^0{}_{100}}$ (uncharged macromolecule) at isoelectric point $\mathrm{pI_{His}}\approx 7.6$.

For polypeptides, the CHARMM36 force field was used [28–29]. The interaction with the gold nanoparticle was described by the Lennard-Jones potential [30]. Long-range electrostatic interactions were calculated using the particle–mesh Ewald (PME) method [31]. The entire system was contained in a cube with 25 nm edges containing TIP3P water molecules [32]. MD simulations were initially performed at a constant temperature of 600 K and at 300 K in the final portion of the trajectory. This allowed us to reach deeper minima in the macrochain's conformational energy, including over a shorter trajectory. To monitor the attainment of equilibrium conformations, we monitored the change in the root-mean-square distance (RMSD) between polypeptide atoms in different conformations. The simulation time reached 30 ns with a step size of 1 fs. Three different starting conformations were considered for each combination of macrochains.

Initially, the polymers were located near a neutral gold nanoparticle. In this case, a single polyhistidine or a pair of polyhistidines in the HH complex in the starting conformation were at the isoelectric point. As a result of the simulation, adsorption of a single polyhistidine (Fig. 1a) and two polyhistidines (Fig. 5a) on the surface of an uncharged gold nanoparticle was observed. The obtained equilibrium structures of polypeptides at the isoelectric point were subsequently used as starting points in modeling with a lower pH value.

The macrochains in the HG complex at the initial moment of time were at a hydrogen index value of pH≈5.5, that is, when most of the polyhistidine units were positively charged, and the polyglutamate units were negatively charged by approximately 90 percent - $\mathrm{(Glu_5Glu^0Glu_4)_{10}}$ (the parameters of which were set in the same way as in [33]). Therefore, a polymer complex of two oppositely charged macromolecules of polyhistidine and polyglutamate (Fig. 7a), intertwined with each other, was formed on the surface of the nanoparticle. Subsequently, during modeling for this nanosystem, the pH level increased, and the hydrogen index values were taken in the range from 6 to 8, in which all polyglutamate units were negatively charged. The following values of the surface charge density of the nanoparticle were considered: ±σ, ±2σ, ±5σ, ±10σ, ±20σ, where $\sigma\approx 0.2e/\mathrm{nm}^2$, $2\sigma\approx 0.4e/\mathrm{nm}^2$, $5\sigma\approx 1e/\mathrm{nm}^2$, $10\sigma\approx 2e/\mathrm{nm}^2$, $20\sigma\approx 4e/\mathrm{nm}^2$ (the partial charge of the atom on the surface is ±0.01*e*, ±0.02*e*, ±0.05*e*, ±0.1*e*, and ±0.2*e*, respectively [34]).

4. Results

4.1 Conformations of a single homogeneous polypeptide on a charged gold nanoparticle with changing pH

Molecular dynamics simulations of single polyhistidine at an isoelectric point of pI_{His}≈7.6 revealed polymer adsorption on the nanoparticle (Fig. 1a). As the pH value varied, the rigidity of the polyelectrolyte macrochain increased. At a low polyelectrolytic level, the adsorption pattern was similar to that observed at the isoelectric point. If the degree of polyelectrolyticity was high, then the macrochain initially compactly adsorbed on the surface of the nanoparticle began to unfold with the release of loops into the surrounding space (Fig. 1c). This type of adsorption is typical of highly charged polyelectrolytes [35]. Figure 2a shows that the strongest decrease in the density of polymer atoms is observed at the lowest pH≈4 value considered.

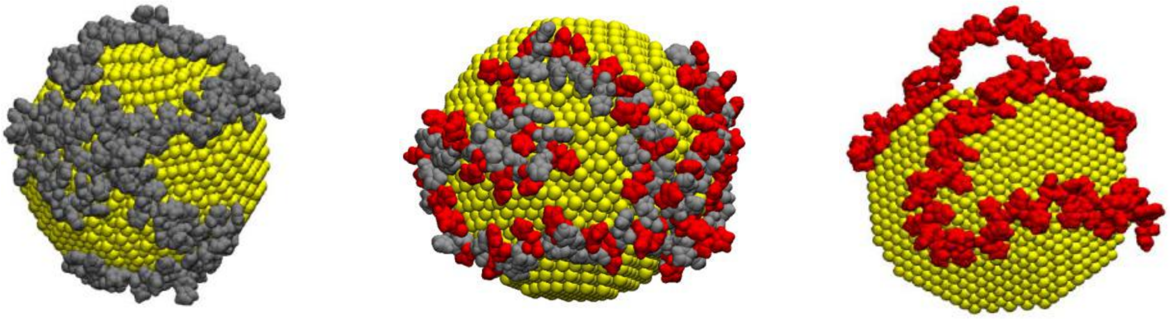

a b c

Fig. 1. Single polyhistidine on the surface of an uncharged gold nanoparticle after simulation at the isoelectric point pI_{His}≈7.6 (a), as well as at pH≈6 (b) and pH≈4 (c). Uncharged amino acid residues His0 are shown in gray, and positively charged His are shown in red.

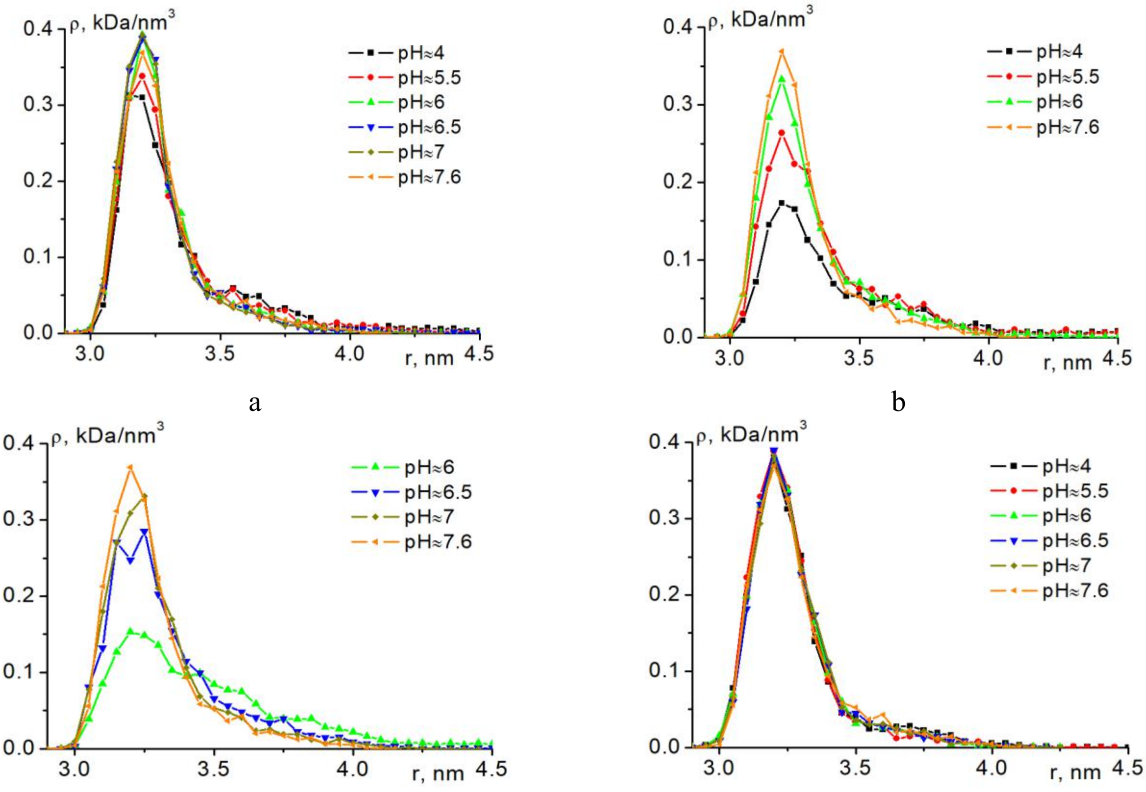

a b

c d

Fig. 2. Radial dependences of the average atomic density of a single polyhistidine on an uncharged gold nanoparticle (a), as well as on a charged gold nanoparticle with a surface density of +2σ (b), +5σ (c), and -5σ (d) at different pH levels.

If the nanoparticle was negatively charged, the positively charged polyhistidine units were attracted to the surface of the nanoparticle. This was most pronounced when the degree of polyelectrolyticity of the polypeptide was high. The swollen polyelectrolyte fringe at pH≈4 on an uncharged nanoparticle (Fig. 1c) was compressed on a negatively charged surface (Fig. 3a). When the nanoparticle was positively charged, the charged polyhistidine units were repelled from the like-charged surface. This led to the macromolecular corona first swelling, followed by polyelectrolyte desorption.

Figure 3b shows that at a surface charge density of +5σ and a pH of ≈6, desorption of a significant polymer fragment is observed. When the pH level was equal to pH≈4 and pH≈5.5, polyelectrolyte desorption occurred at a surface charge density of +5σ, while at pH≈6 the polypeptide desorbed at +10σ, and at pH≈6.5 – at +20σ. At pH≈7, macrochain desorption did not occur; however, the polyelectrolyte flake swelled significantly at +20σ compared to the neutral surface of the nanoparticle, when the polypeptide conformation was similar to the polypeptide conformation at the isoelectric point. Figures 2b and 2c show that, for the same nanoparticle charge, the density of polypeptide atoms near the nanoparticle surface varies significantly at different pH values. The lower the pH, the more severe the loosening of the macrochain fringe on the positively charged surface (Figures 2b and 2c). When the nanoparticle was negatively charged (Figure 2d), the radial atom density distribution curves were very close to each other due to the fact that the positively charged macrochain was adsorbed on the nanoparticle.

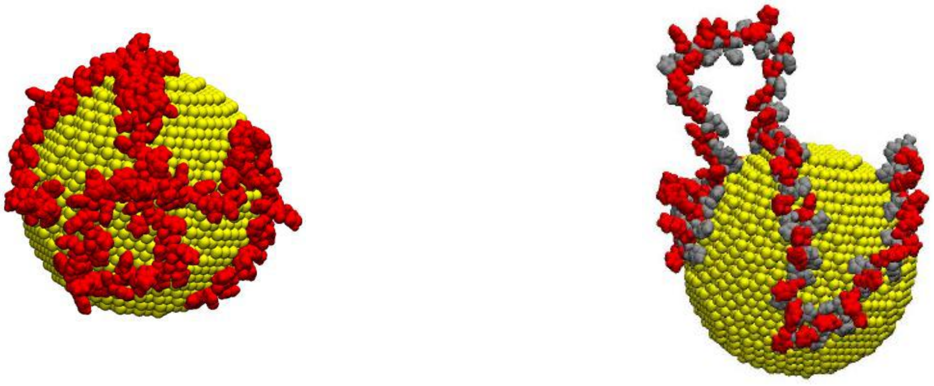

a b

Fig. 3. Single polyhistidine after simulation on the surface of a gold nanoparticle charged with a surface charge density of -5σ at pH≈4 (a), and at pH≈6 and +5σ (b). Uncharged amino acid residues His0 are shown in gray, and positively charged His are shown in red.

Figure 4 shows that for polypeptides with varying degrees of polyelectrolyticity, the conformational structure of the macromolecular corona around the nanosphere changes from dense to swollen over different ranges of surface charge density.

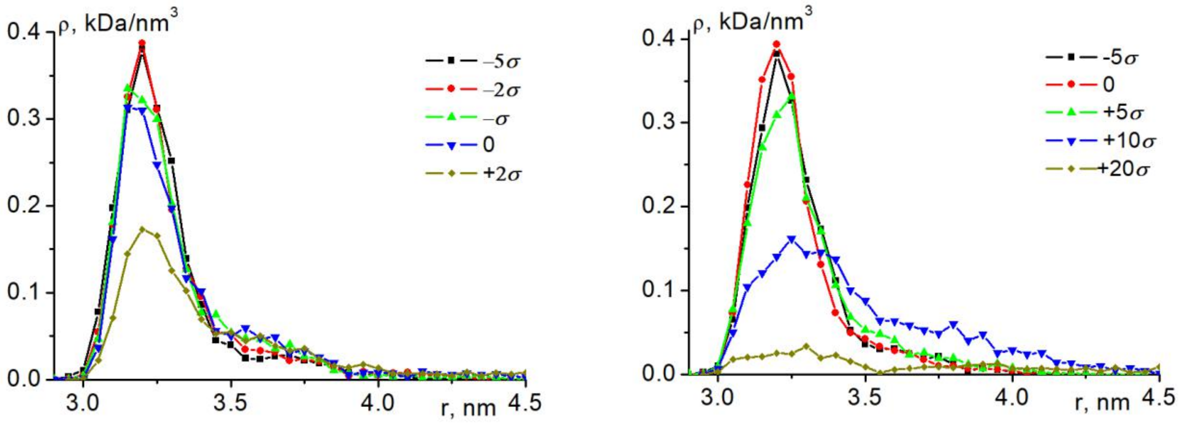

a b

Fig. 4. Radial dependences of the average atomic density of adsorbed single polyhistidine at different surface charge densities of gold nanoparticles at pH≈4 (a) and pH≈7 (b).

For a highly charged polymer molecule (Fig. 4a, pH ≈ 4), the polymer layer begins to swell at a surface charge density of -σ, i.e., with a charge opposite to that of the macrochain. For a polyelectrolyte with a low degree of polyelectrolyticity (Fig. 4b, pH≈7), swelling of the macrochain fringe begins to occur only at a surface charge density of the nanoparticle of +5σ, at which polyhistidine at pH≈4 has already desorbed.

4.2 Conformations of two identical polypeptides on a charged gold nanoparticle with changing pH

In the case of MD simulation, at the isoelectric point of two identical polypeptides on a spherical gold nanoparticle, both macrochains were adsorbed on its surface, partially intertwined with each other (Fig. 5a). As the pH level decreased, the macromolecules began to repel each other, as they became equally charged. With a small degree of polyelectrolyticity of polypeptides, the forces of electrostatic repulsion between the macrochains were insufficient to overcome the van der Waals forces and shift them from each other by a significant distance, therefore, the polypeptide fragments moved only slightly from each other. With a further decrease in the pH level and, accordingly, an increase in the degree of polyelectrolyticity, the polypeptides shift to different sides of the gold nanoparticle, repelling each other (Fig. 5b).

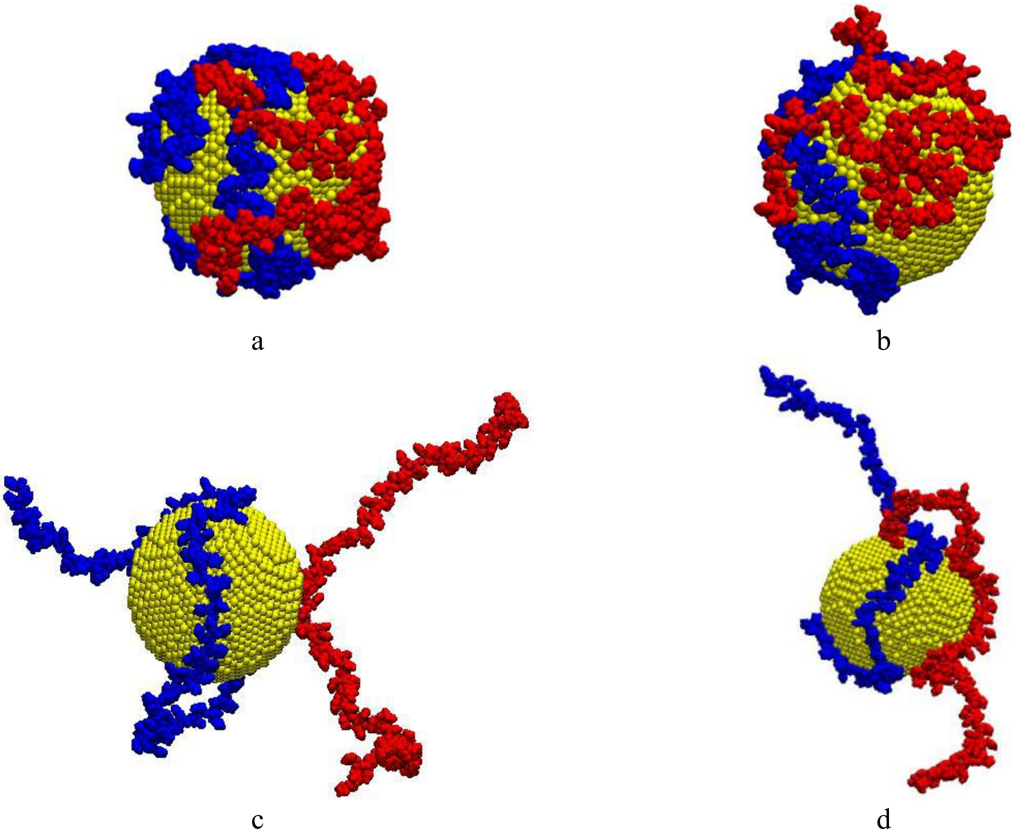

Fig. 5. Two macromolecules of histidine units (HH polypeptide complex) on the surface of a neutral gold nanoparticle after simulation: at the isoelectric point pI_{His}≈7.6 (a) and at pH≈4 (b), as well as on a nanoparticle charged with a surface density of -5σ at pH≈4 (c) and +5σ at pH≈6 (d). The first and second polypeptides are shown in red and blue, respectively.

Figure 6a shows that with decreasing pH and increasing the degree of polyelectrolyticity of the macrochains, there is a significant decrease in the concentration of units near the surface of the nanosphere. At pH≈4, the peak distribution for two macrochains decreased by approximately 30 percent compared to the peak of this distribution at the isoelectric point (Fig. 6a). This decrease is much greater than for a single polypeptide, where the peak distribution of polyelectrolyte atoms at pH≈4 decreased by approximately 13 percent compared to the peak distribution at the isoelectric point (Fig. 2a). This indicates a stronger swelling of the polymer layer with increasing polyelectrolyticity of two polyhistidines compared to a single macromolecule due to the electrostatic repulsion between similarly charged polypeptides.

Adsorption of positive polypeptide units in the HH binary complex occurred on the surface of a highly negatively charged nanoparticle (-5σ and below) at low pH. The loose polymer fringe on the neutral nanoparticle (Fig. 5b, pH≈4) contracted and tightly enveloped the oppositely charged nanoparticle (Fig. 5c, pH≈4). Figure 6b shows the combined distributions of two polyhistidine macromolecules on a charged nanoparticle with a surface density of -5σ. It can be seen that the distribution curves for the HH polypeptide complex with varying degrees of polyelectrolyte (pH≤7) are very close to those for their adsorption at the isoelectric point pI_{His}≈7.6.

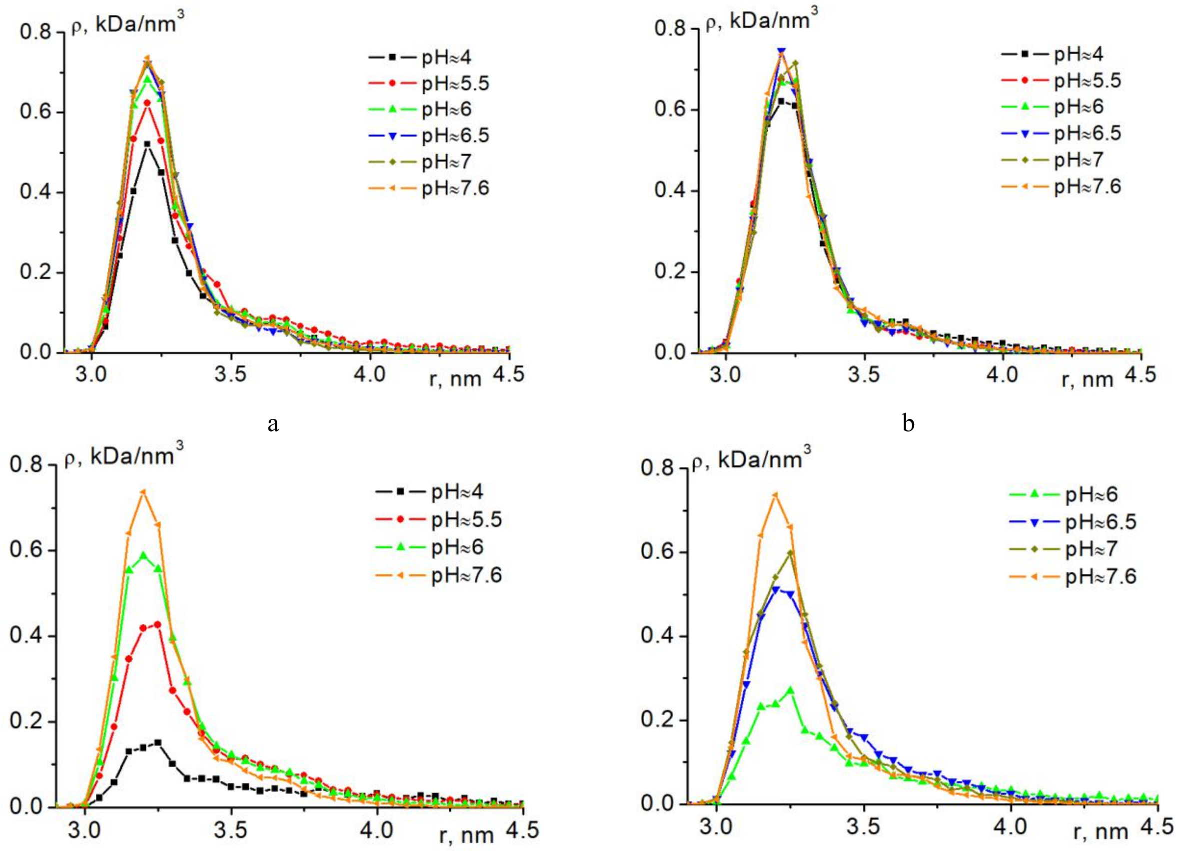

a

b

c

d

Fig. 6. Total radial dependences of the average density of atoms of two polyhistidine macromolecules on an uncharged (a) and charged gold nanoparticle with a surface density of -5σ (b), +2σ (c), and +5σ (d) at different pH levels.

As the nanoparticle charge increased, the polyelectrolyte fringe first swelled (Fig. 5d, +5σ at pH≈6), and then the macromolecules desorbed. The sparsity of the polyelectrolyte fringe of two polyhistidines around the gold nanoparticle at the same surface charge density depended significantly on the pH. Figures 6c and 6d show that at lower pH, the distributions for the HH polypeptide complex are significantly lower at the same charge, indicating significant swelling of the polyelectrolyte fringe. The lower the degree of polyelectrolyticity of the polypeptides in the HH complex, the higher the nanoparticle charge value at which desorption of macromolecules was observed: at pH≈4 and pH≈5.5 - at a surface charge density equal to +5σ, at pH≈6 - at +10σ, at pH≈6.5 - at +20σ, and at pH≈7 no desorption was observed, as in the case of single polyglutamate.

4.3 Conformations of a binary polyhistidine-polyglutamate complex on a charged gold nanoparticle with varying pH

At pH ≈ 5.5, polyhistidine and polyglutamate in the HG complex were oppositely charged and attracted to each other, intertwining (Fig. 7a). As pH increased, the charge of polyhistidine gradually decreased and became zero at the isoelectric point pI_{His}≈ 7.6, while the absolute charge of polyglutamate reached its maximum at pH≈6 and remained unchanged. The electrostatic attraction between the macrochains decreased with increasing pH, while the interunit repulsion in polyglutamate increased. Therefore, polyglutamate was released from its bond with polyhistidine and unfolded, releasing fragments into the space surrounding the nanoparticle (Fig. 7b). Meanwhile, polyhistidine remained folded on the surface of the gold nanoparticle.

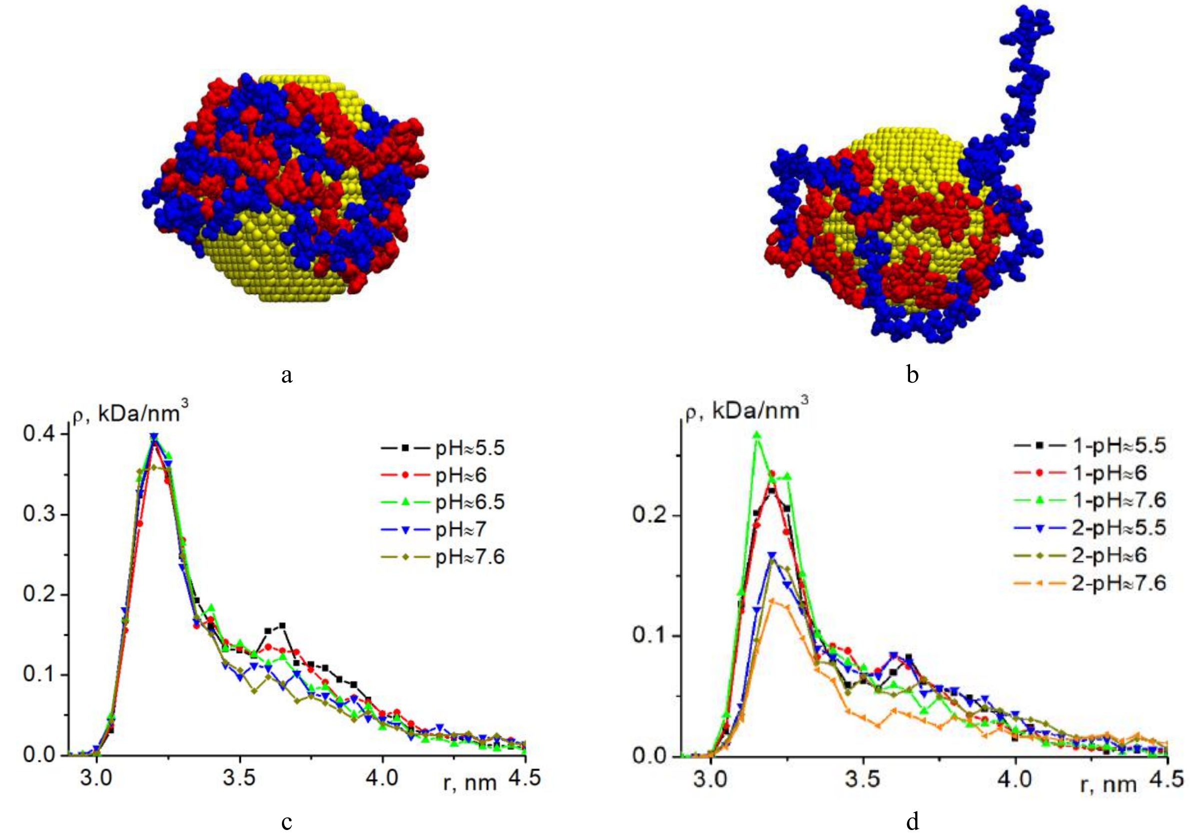

Fig. 7. Macromolecules of polyhistidine (red) and polyglutamate (blue) after simulation on the surface of an uncharged gold nanoparticle at pH≈5.5 (a) and pH≈7.6 (b). Total radial dependences of the average density of polypeptide atoms in the HG complex (c), as well as radial dependences of the average density of polyhistidine (d, curves 1) and polyglutamate (d, curves 2) atoms in the HG complex separately on the surface of an uncharged gold nanoparticle at different pH levels.

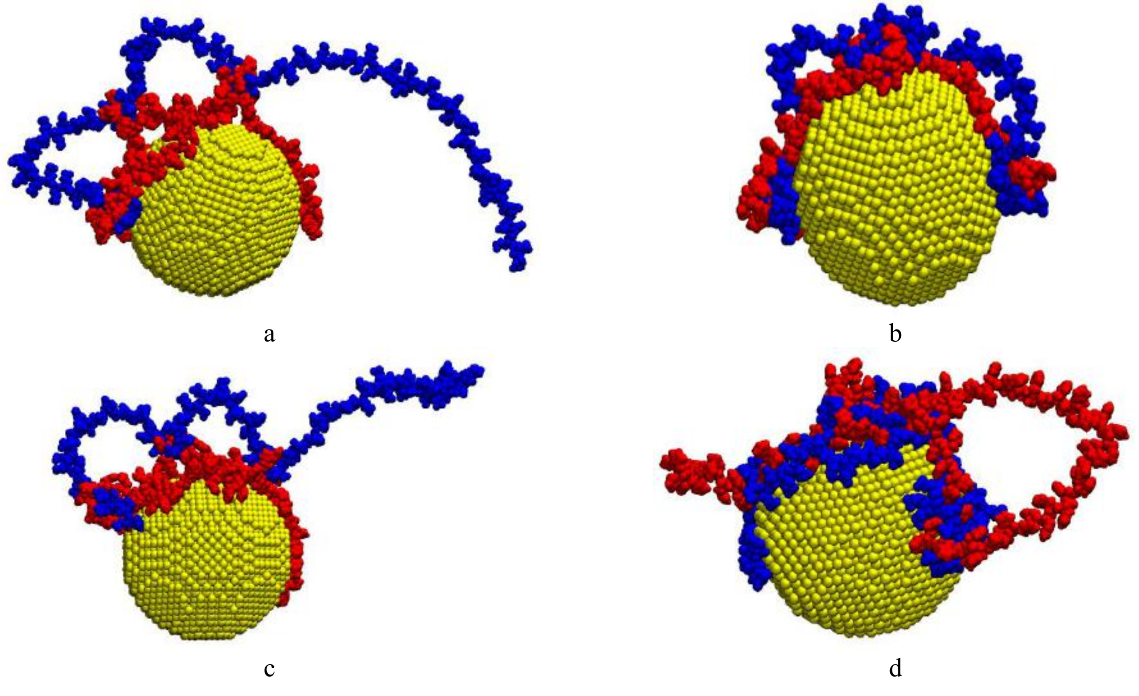

Fig. 8. Macromolecules of polyhistidine (red) and polyglutamate (blue) after simulation on the surface of a gold nanoparticle charged with a surface density of -5σ at pH≈7.6 (a) and pH≈6 (b), at -10σ and pH≈6 (c), at +10σ and pH≈5.5 (d).

Figure 7c shows the total distributions of polyhistidine and polyglutamate atoms in the HG complex at different pH levels on the surface of a neutral nanoparticle. It is clear that as the pH increases, the distribution curves become very close to each other, decreasing slightly at pH ≈ 7.6, when polyglutamate is maximally released from its bond with polyhistidine. A different picture is observed for the distributions of polyhistidine and polyglutamate atoms in the HG complex, constructed separately for each polypeptide (Fig. 7d). With increasing pH, the distributions for polyhistidine and polyglutamate behave differently: the curves for polyglutamate decrease, while the peak values of the distribution for polyhistidine increase (Fig. 7d).

The decrease in the concentration of polyglutamate atoms near the surface of the nanoobject is associated with the unfolding of the polymer with increasing pH (Fig. 7b). And the increase in the concentration of polyhistidine atoms near the surface is associated with the substitution of desorbed polyglutamate units (Fig. 7b). At pH≈7.6, polyhistidine was uncharged at the isoelectric point, so on the negatively charged surface of the nanoparticle, the negatively charged polyglutamate was repelled from the nanoparticle, and the polymer corona swelled. At a surface charge density of -5σ, polyglutamate was almost completely desorbed, retaining itself in the HG complex due to entanglement with polyhistidine and pulling its loops into the surrounding space (Fig. 8a). On a positively charged nanoparticle at pH≈7.6, the fringe swollen due to the unfolding of polyglutamate (Fig. 7b) was compressed due to the electrostatic attraction of the negatively charged polyglutamate to the surface. On a positively charged nanoparticle, a mirror image was observed when the pH level was reduced. The lower the pH level, the greater the degree of polyelectrolyticity of polyhistidine, and it was increasingly repelled from the surface of the nanoparticle (Fig. 8d). And polyglutamate, on the contrary, was increasingly attracted to the positively charged surface. A polymer fringe was formed, in which polyglutamate was concentrated at the surface, and polyhistidine was at the periphery. Thus, the structure and swelling character of the fringe from the HG polypeptide complex changed significantly with changes in both the surface charge and the pH level. Figure 9a shows the total distributions for the HG complex depending on the charge density on the nanoparticle surface at pH≈5.5.

It is evident that with an increase in the absolute value of the nanosphere charge, the total density of polypeptide atoms decreases. This is due to the swelling of the polypeptide fringe of two oppositely charged macrochains, since the macrochain charged like the nanoparticle shifts to the periphery. Therefore, the curves of the radial dependences of the average density of polyhistidine (Fig. 9b) and polyglutamate (Fig. 9c) atoms behave differently with a change in the nanoparticle charge at pH≈5.5. For polyhistidine (Fig. 9b), the atomic density at the surface of a negatively charged nanoparticle slightly increases compared to a neutral nanoparticle, while it decreases significantly on a positively charged surface. In this case, the density of polyglutamate atoms changes in a mirror image when the charge of the nanoparticle changes (Fig. 9c). And at pH≈7.6, when polyhistidine becomes neutral, the negatively charged polyglutamate macrochain is repelled from the surface (Fig. 8a), so the density of polyglutamate atoms at the surface of a negatively charged nanoparticle decreases significantly (Fig. 9d). Figure 10 shows the radial dependences of the average density of polyglutamate atoms at different pH levels at -5σ (Fig. 10a) and +5σ (Fig. 10b). It is evident (Fig. 10a) that with increasing pH, the number of polyglutamate atoms near the surface decreases significantly due to the release of polyglutamate from adhesion to neutralizing polyhistidine and the repulsion of polyglutamate from the surface. On a positively charged nanosphere (Fig. 10b), with increasing pH, the density of polyglutamate atoms increases slightly due to displacement toward the surface after release from polyhistidine.

4.4 Results of calculations based on the mathematical model

To compare the calculation results based on the analytical model with the MD simulation data, Fig. 11 a, b, c shows the graphs of the radial dependences of the conformational functions $\psi(r) \equiv F(r) = F_0^{I,II}(r)$ for different signs of the charge parameter $\alpha = 1 - \kappa,\ \kappa = \pm|\kappa|$. Curves 1 in all three Figures 11 a, b, c correspond to the same signs of the charges of the spherical nanoparticle and the polymer chain links: $qQ>0$, therefore the maxima of the curves $\psi(r) \equiv F(r) = F_0^{I,II}(r)$ at the points r_0 of the minimum potential are located below the maxima of curves 2, which are calculated for the case of qQ<0, i.e., with the appearance of additional attraction of the charged chain links to the nanoparticle surface. Curves 1 are characterized by a more gradual attenuation in the asymptotics, as should be the case of swelling of the polymer corona.

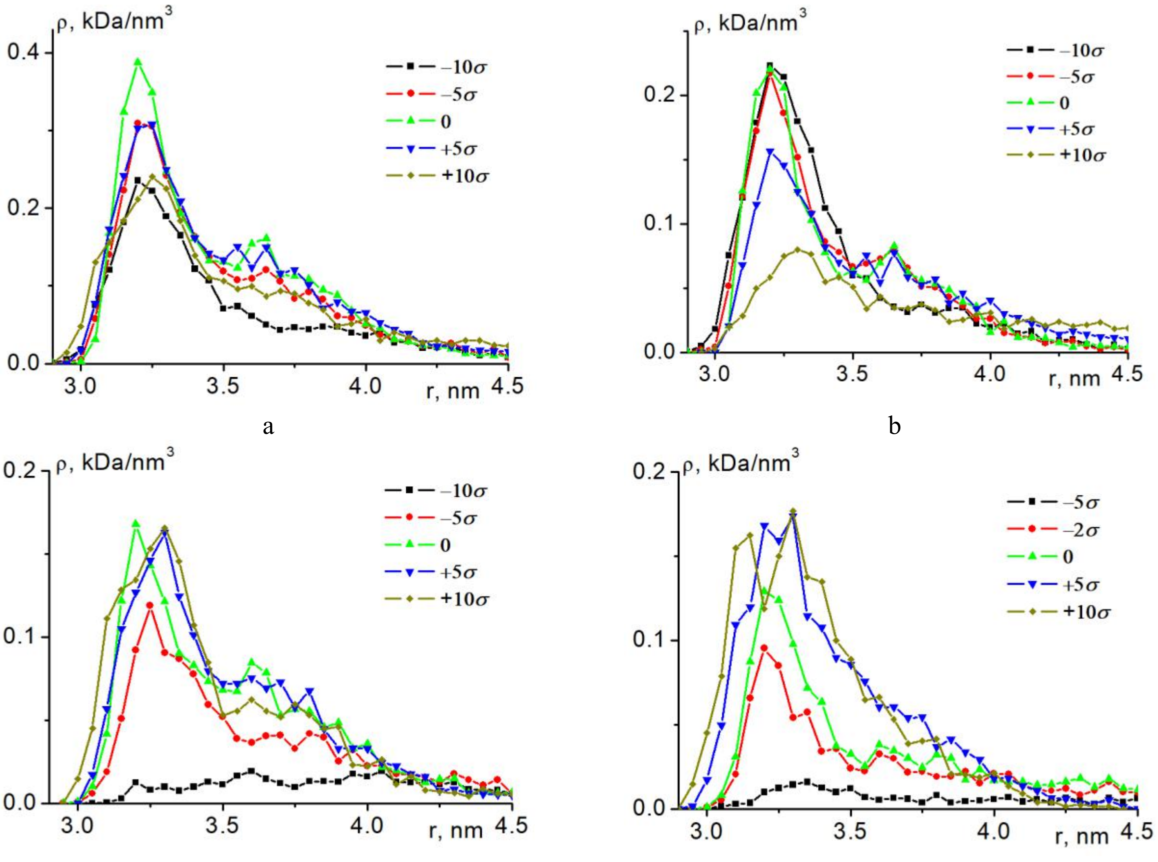

a b

c d

Fig. 9. Total radial dependences of the average density of polypeptide atoms in the HG complex (a), as well as radial dependences of the average density of polyhistidine (b) and polyglutamate (c) atoms in the HG complex separately at different surface charge densities of the gold nanoparticle at pH≈5.5, as well as radial dependences of the average density of polyglutamate atoms at pH≈7.6 (d).

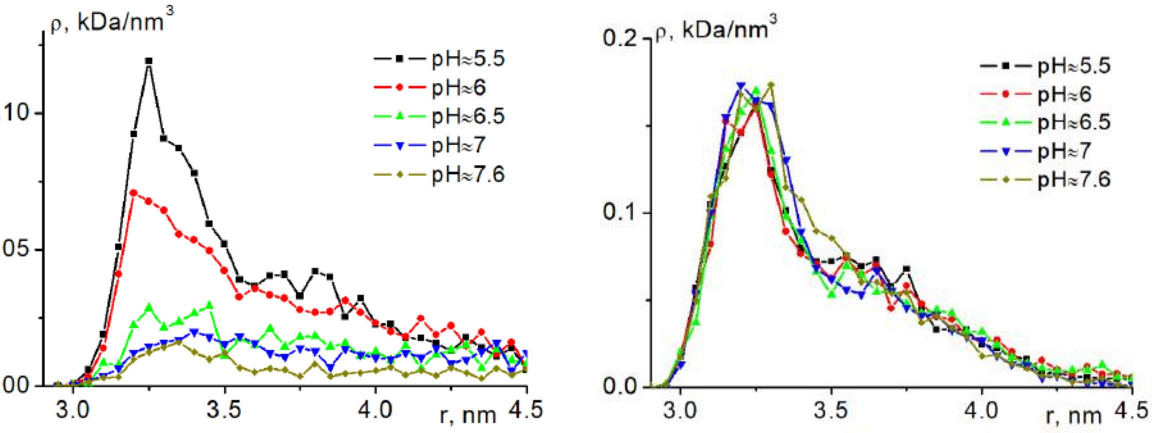

a b

Fig. 10. Radial dependences of the average density of polyglutamate atoms at different pH levels with a surface charge density of gold nanoparticles of -5σ (a) and +5σ (b).

For large values of the charge parameter modulus $|\kappa|=\dfrac{3|qQ|}{a^2kTq_0}$ – 0.9 for Fig. 11a versus 0.2 for Fig. 11b and 0.1 for Fig. 11c, curves 1 and 2 exhibit a larger amplitude of divergence of the function *F* with changes in the radial variable in Fig. 11a compared to Fig. 11b and Fig. 11c. That is, for uncharged nanoparticles or electrically neutral polymer chains, curves 1 and 2 coincide. To cover a wider range of values, the radial variable of the function *F* is expressed in dimensionless *rq* units.

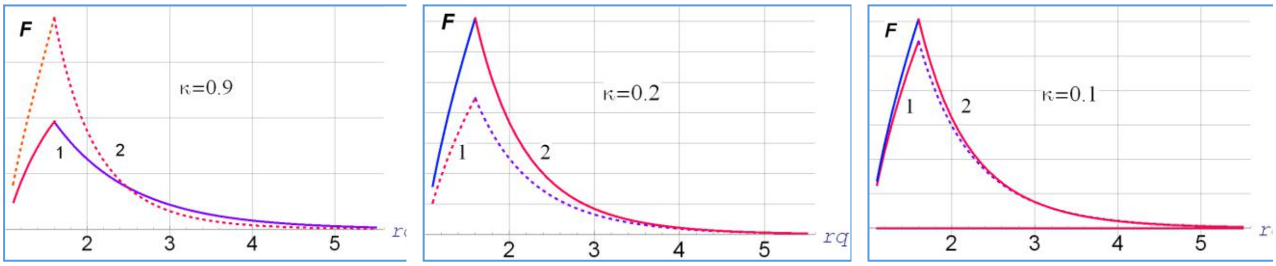

a b c

Fig. 11. Radial dependences of conformational functions for different signs of the charge parameter: 1– *qQ*>0, 2– *qQ*<0 and three values of its modulus: 0.9 (a), 0.2 (b) and 0.1 (c).

Thus, the theoretical model proposed in this paper qualitatively accurately conveys the observed features of the interaction of two polyelectrolyte chains with a charged nanoparticle, revealed by MD simulations with specific adsorbed polypeptides upon changes in the solution pH and the nanoparticle charge.

5. Conclusion

The conformations of homogeneous polypeptides adsorbed on the surface of a charged spherical gold nanoparticle are significantly restructured with changes in the pH level and charge of the nanoparticle, and in the case of adsorption of two polypeptides on a nanoparticle, the structure of the macromolecular fringe depends significantly on the combinations in which the polypeptides are found in the binary complex.

A single homogeneous polypeptide adsorbed on a neutral gold nanoparticle unfolds from a tangled ball structure when the pH level deviates from the isoelectric point, and the polymer fringe around the nanoparticle begins to swell. On an oppositely charged nanoparticle, the swollen polyelectrolyte fringe contracts, while on the surface of a similarly charged nanoparticle it swells (up to desorption) as the pH level deviates from the isoelectric point.

Two identical homogeneous polypeptides adsorbed on an uncharged gold nanoparticle begin to repel and shift from each other along the surface when the pH value deviates from the isoelectric point. Since the size of the nanoparticle is much smaller than the length of the macrochain, the desorption of polypeptide fragments in the binary complex begins at a lower degree of polyelectrolyticity of the macromolecules and the rarefaction of the peptide layer on the surface of the neutral nanoparticle was stronger than for a single macrochain at the same deviation of the pH level from the isoelectric point.

On the surface of a neutral gold nanoparticle, oppositely charged macrochains were tightly intertwined. On the charged nanoparticle, the macromolecule with the same charge as the nanoparticle shifted to the periphery, while the oppositely charged polyelectrolyte remained near the surface. This created two layers of different types of polypeptides within the polymer crown, which swelled significantly. Upon reaching the isoelectric point of one of the polypeptides, the charge of the second polypeptide became uncompensated. Therefore, the second charged polypeptide began to unfold and disengage from the first uncharged macromolecule. On the nanoparticle, which was oppositely charged relative to the second polypeptide, the macromolecular crown contracted. And if the nanoparticle was charged in the same way as the second polypeptide, then it shifted to the outer side of the polymer fringe and could desorb faster, the higher the absolute value of the nanoparticle charge was, and the pH level was closer to the isoelectric point of the first polypeptide.

To describe the conformations of adsorbed charged macrochains, a mathematical model based on a closed self-consistent system of equations for conformational functions $\psi_{1,2}(\mathbf{r})$ and electrostatic potentials $\varphi_{1,2}(r)$ is proposed. To take into account the volume interactions of chain links, self-consistent field potentials were introduced into the model using the Edwards method. Obtaining solutions to the closed system of differential equations is based on an iterative procedure. The proposed model qualitatively correctly conveys the observed features of the interaction of two polyelectrolyte chains, revealed as a result of MD simulation with specific adsorbed polypeptides with changes in pH and nanoparticle charge.

Thus, such changes in polypeptide conformations can be used to create pH-sensitive nanoprobes, nanocontainers, and elements of various biochemical sensors. If small functional molecules are introduced into the polypeptide edging, then when the pH level changes with a change in the conformations of the polypeptides, a shift of the introduced small molecules relative to the surface of the nanoparticle or their release from the polymer edging will occur. This nanosystem can be used as a pH-sensitive container for targeted delivery of drugs with their controlled release at the final destination. If molecules of organic dyes are included in the polymer edging, then the pH-sensitive change in the distance between them, as well as the change in the distance between the dyes and the plasmonic nanoparticle, can be used as a method for controlling the efficiency of the luminescent signal of this hybrid nanosystem, since the various channels of deactivation of the electronic excitation of photoactive molecules depend significantly on the spatial arrangement of the molecules relative to the plasmonic nanoparticle.

Conflict of interest statement

The authors declare that they have no conflict of interest in relation to this research, whether financial, personal, authorship or otherwise, that could affect the research and its results presented in this paper.

CRediT author statement

Kruchinin N.Yu.: Conceptualization, Methodology, Software, Investigation, Writing - Original Draft; **Kucherenko M.G.**: Conceptualization, Methodology, Investigation, Writing - Original Draft.
The final manuscript was read and approved by all authors.

Acknowledgements

This work was supported by the Ministry of Science and Higher Education of the Russian Federation within the framework of project no. FSGU-2023-0003

References

1 Kanp T., Dhuri A.M., Rode K., Aalhate M., Paul P., Nair R., Singh P.K. (2025) Exploring the potential of nanocarriers for cancer immunotherapy: insights into mechanism, nanocarriers, and regulatory perspectives. *ACS Appl. Bio Mater*., 8, 108–138. https://doi.org/10.1021/acsabm.4c01797

2 Mi S., Hu X., Yuan S., Yu H., Guo Y., Cheng Y., Yao W. (2024) Unveiling the correlation between protein, protein corona, and target signal loss in SERS detection. *Anal. Chem.,* 96, 19768–19777. https://doi.org/10.1021/acs.analchem.4c05084

3 Gao J., Yang W., Liu R., Feng, J., Li Y., Jiang M., Jiang, S. (2024) A reliable gold nanoparticle/Cu-TCPP 2D MOF/gold/D-shaped fiber sensor based on SPR and LSPR coupling for dopamine detection. *Applied Surface Science,* 655, 159523. https://doi.org/10.1016/j.apsusc.2024.159523

4 Liu M., Zhuang H., Zhang Y., Jia Y. (2024) A sandwich FRET biosensor for lysozyme detection based on peptide-functionalized gold nanoparticles and FAM-labeled aptamer. *Talanta,* 276, 126226. https://doi.org/10.1016/j.talanta.2024.126226

5 Kumar S., Dory Y.L., Lepage M., Zhao Y. (2011) Surface-grafted stimuli-responsive block copolymer brushes for the thermo-, photo- and pH-sensitive release of dye molecules. *Macromolecules,* 44, 7385–7393. https://doi.org/10.1021/ma2010102

6 Cui J., Nguyen T., Ceolín M., Berger R., Azzaroni O., del Campo A. (2012) Phototunable response in caged polymer brushes. *Macromolecules,* 45, 3213–3220. https://doi.org/10.1021/ma300274b

7 Jacquelín D.K., Perez M.A.,´Euti E.M., Arisnabarreta N., Cometto F.P., Paredes-Olivera, P., Patrito E.M. (2016) A pH-Sensitive supramolecular switch based on mixed carboxylic acid terminated self-assembled monolayers on Au(111). *Langmuir*, 32, 947–953. https://doi.org/10.1021/acs.langmuir.5b03807

8 Filip J., Popelka A., Bertok T., Holazova A., Osicka J., Kollar J., Ilcikova M., Tkac J., Kasak P. (2017) pH-Switchable Interaction of a carboxybetaine ester-based SAM with DNA and gold nanoparticles. *Langmuir,* 33, 6657–6666. https://doi.org/10.1021/acs.langmuir.7b00568

9 Debayle M., Marchandier T., Xu X., Lequeux N., Pons T. (2019) pH-Sensitive visible or shortwave infrared quantum dot nanoprobes using conformation-switchable copolymeric ligands. *ACS Appl. Mater. Interfaces,* 11, 25008–25016. https://doi.org/10.1021/acsami.9b06194

10 Shirmanova M.V., Druzhkova I.N., Lukina M.M., Matlashov M.E., Belousov, V.V., Snopova L.B., Prodanetz N.N., Dudenkova V.V., Lukyanov S.A., Zagaynova E.V. (2015) Intracellular pH imaging in cancer cells in vitro and tumors in vivo using the new genetically encoded sensor SypHer2. *Biochimica et Biophysica Acta (BBA) - General Subjects*, 1850, 1905-1911. https://doi.org/10.1016/j.bbagen.2015.05.001

11 Webb B., Chimenti M., Jacobson M.P., Barber D.L. (2011) Dysregulated pH: a perfect storm for cancer progression. *Nature Reviews Cancer,* 11, 671–677. https://doi.org/10.1038/nrc3110

12 Liu X., Chen Y., Li H., Huang N., Jin Q., Ren K., Ji J. (2013) Enhanced retention and cellular uptake of nanoparticles in tumors by controlling their aggregation behavior. *ACS Nano* 7, 6244–6257. https://doi.org/10.1021/nn402201w

13 Chen W., Lei Q., Luo G., Jia H., Hong S., Liu Y., Cheng Y., Zhang X. (2015) Rational Design of Multifunctional Gold Nanoparticles via Host−Guest Interaction for Cancer-Targeted Therapy. *ACS Appl. Mater. Interfaces,* 7, 17171–17180. https://doi.org/10.1021/acsami.5b04031

14 Yari-Ilkhchi A., Rafi A.A., Mahkam M. (2025) Design and development of pH-sensitive nanocarriers using molecularly imprinted polymers for the targeted delivery of sodium thiopental. *Nanoscale Advances,* 7, 2039-2046. https://doi.org/10.1039/d4na00926f

15 Kruchinin N.Yu., Kucherenko M.G. (2021) Rearrangements in the conformational structure of polyampholytic polypeptides on the surface of a uniformly charged and polarized nanowire: Molecular dynamics simulation. *Surfaces and Interfaces,* 27, 101517, https://doi.org/10.1016/j.surfin.2021.101517

16 Kruchinin N.Yu., Kucherenko M.G. (2022) Molecular dynamics simulation of the conformational structure of uniform polypeptides on the surface of a polarized metal prolate nanospheroid with varying pH. *Russian Journal of Physical Chemistry A*, 96, 624–632. https://doi.org/10.1134/S0036024422030141

17 Kruchinin N.Yu., Kucherenko M.G. (2022) Conformational Changes in Polyampholyte Macrochains on the Surface of an Oblate Metallic Nanospheroid in Alternating Electric Field. *High Energy Chemistry*, 56, 499-510. https://doi.org/10.1134/S0018143922060108

18 Kruchinin N.Yu. (2023) Rearrangement of the conformations of polyampholitic macromolecules on the surface of a charged spherical metal nanoparticle in an alternating electric field: molecular dynamic simulation. *Russian Journal of Physical Chemistry A,* 97, 2777–2785. https://doi.org/10.1134/S003602442312018X

19 Kruchinin N.Yu., Kucherenko M.G. (2024) Conformational structure of a complex of two oppositely charged polyelectrolytes on the surface of a charged spherical metal nanoparticle. *High Energy Chemistry,* 58, 615–623. https://doi.org/10.1134/S0018143924700590

20 Kucherenko M.G., Kruchinin N.Yu., Neyasov P.P. (2024) Conformational structure of polyampholytes and polyelectrolytes on the surface of a longitudinally polarized gold spherocylinder. *Eurasian Physical Technical Journal* 21 (3), 6-20. https://doi.org/10.31489/2024No3/6-20

21 Kruchinin N.Yu., Kucherenko M.G. (2025) Conformational changes of two oppositely charged polyelectrolytes, including those combined into a single block copolymer, on the surface of a charged or transversely polarized cylindrical metal nanowire. *Journal of Polymer Research,* 32,79. https://doi.org/10.1007/s10965-025-04305-3

22 Grosberg A.Y., Khokhlov A.R. (1994) Statistical Physics of Macromolecules. AIP Press, New York. 347.

23 Edvards S.F. (1965) The statistical mechanics of polymers with excluded volume. *Proc. Phys. Soc*., 85, 613-624. https://doi.org/10.1088/0370-1328/85/4/301

24 Kucherenko M.G., Rusinov A.P., Chmereva T.M., Ignat'ev A.A., Kislov D.A., Kruchinin N.Yu. (2009) Kinetics of photoreactions in a regular porous nanostructure with cylindrical cells filled with activator-containing macromolecules. *Optics and Spectroscopy* ,107, 480–485. https://doi.org/10.1134/S0030400X0909029X

25 Mhashal A.R., Roy S. (2014) Effect of Gold Nanoparticle on Structure and Fluidity of Lipid Membrane. *PLoS One* 9, e114152. https://doi.org/10.1371/journal.pone.0114152

26 Phillips J.C., Braun R., Wang W., Gumbart J., Tajkhorshid E., Villa E., Chipot C., Skeel R.D., Kale L., Schulten K. (2005) Scalable molecular dynamics with NAMD. *J. Comput. Chem.,* 26, 1781-1802. https://doi.org/10.1002/jcc.20289

27 Batys P., Morga M., Bonarek P., Sammalkorpi M. (2020) pH-Induced Changes in Polypeptide Conformation: Force-Field Comparison with Experimental Validation. *J. Phys. Chem. B,* 124, 2961-2972. https://doi.org/10.1021/acs.jpcb.0c01475

28 MacKerell Jr. A.D., Bashford D., Bellott, M., Dunbrack Jr. R.L., Evanseck J.D., Field M.J., Fischer S., Gao J., Guo H., Ha S., Joseph-McCarthy D., Kuchnir L., Kuczera K., Lau F.T.K., Mattos C., Michnick S., Ngo T., Nguyen D.T., Prodhom B., Reiher III W.E., Roux B., Schlenkrich M., Smith J.C., Stote R., Straub J., Watanabe M., Wiorkiewicz-Kuczera J., Yin D., Karplus M. (1998) All-Atom Empirical Potential for Molecular Modeling and Dynamics Studies of Proteins. *J. Phys. Chem. B,* 102, 3586-3616. https://doi.org/10.1021/jp973084f

29 Huang J., Rauscher S., Nawrocki G., Ran T, Feig M., de Groot B.L., Grubmüller H., MacKerell Jr. A.D. (2016) CHARMM36m: an improved force field for folded and intrinsically disordered proteins. *Nature Methods,* 14, 71-73. https://doi.org/10.1038/nmeth.4067

30 Heinz H., Vaia R.A., Farmer B.L., Naik R.R. (2008) Accurate simulation of surfaces and interfaces of face-centered cubic metals using 12−6 and 9−6 Lennard-Jones potentials. *J. Phys. Chem. C,* 112, 17281-17290. https://doi.org/10.1021/jp801931d

31 Darden T., York D., Pedersen L. (1993) Particle mesh Ewald: An N·log(N) method for Ewald sums in large systems. *J. Chem. Phys.* 98, 10089-10092. https://doi.org/10.1063/1.464397

32 Jorgensen W.L., Chandrasekhar J., Madura J.D., Impey R.W., Klein M.L. (1983) Comparison of simple potential functions for simulating liquid water. *J. Chem. Phys.*, 79, 926-935. https://doi.org/10.1063/1.445869

33 Radak B.K., Chipot C., Suh D., Jo S., Jiang W., Phillips J.C., Schulten K., Roux. B. (2017) Constant-pH Molecular Dynamics Simulations for Large Biomolecular Systems. *J. Chem. Theory Comput.*, 13, 5933-5944. https://doi.org/10.1021/acs.jctc.7b00875

34 Chen P., Zhang Z., Gu N., Ji M. (2018) Effect of the surface charge density of nanoparticles on their translocation across pulmonary surfactant monolayer: a molecular dynamics simulation. *Molecular Simulation*, 44, 85-93. https://doi.org/10.1080/08927022.2017.1342118

35 Harvey J.D., Baker H.A., Mercer E., Budhathoki-Uprety J., Heller D.A. (2017) Control of Carbon Nanotube Solvatochromic Response to Chemotherapeutic Agents. *ACS Appl. Mater. Interfaces*, 9, 37947–37953. https://doi.org/10.1021/acsami.7b12015

AUTHORS' INFORMATION

Kruchinin, Nikita Yurievich – Doctor of Physical and Mathematical Sciences, Associate Professor, Associate Professor of the Department of Radio physics and Electronics of the Orenburg State University, Orenburg, Russia; SCOPUS Author ID 35170029600; https://orcid.org/0000-0002-7960-3482; kruchinin_56@mail.ru

Kucherenko, Michael Gennadievich – Doctor of Physical and Mathematical Sciences, Professor, Director of the Center for Laser and Information Biophysics at Orenburg State University, Orenburg, Russia; SCOPUS Author ID 700358146; https://orcid.org/0000-0001-8821-2427; clibph@yandex.ru

EURASIAN PHYSICAL TECHNICAL JOURNAL

2025, Volume 22, No. 4 (54)

https://doi.org/10.31489/2025N4/24-30

Received: 16/02/2025 Revised: 14/11/2025 Accepted: 22/12/2025 Published online: 29/12/2025

Research Article

UDC 538.9; 621.727

INVESTIGATION OF OPTICAL AND ELECTRICAL PROPERTIES OF TITANIUM OXYNITRIDE FILMS

Makhabayeva A.T.[1], Chirkova L.V.[1], Guchenko S.A.[1], Tuleuov S.D.[1],
Makhanov K.M.[2], Shakirzyanov R.I.[2], Afanasyev D.A.[1]*

[1] Buketov Karaganda National Research University, Karaganda, Kazakhstan
[2] L.N. Gumilyov Eurasian National University, Astana, Kazakhstan
**Corresponding author*: a.d.afanasyev2@gmail.com

Abstract. In this work, titanium oxynitride films were obtained on the surface of glass and silicon substrates by magnetron sputtering in a mixture of argon-oxygen-nitrogen gases. The thickness of the obtained films, their deposition rate, and surface morphology were estimated depending on the type of substrate. The optical and electrical properties of films produced on the glass surface have been studied. A comparison of optical data with literature data showed the formation of amorphous films with a composition close to the stoichiometric composition of $TiO_{1.27}N_{0.49}$. The results showed that the obtained properties correspond to the literature data, which opens up new prospects for the use of the obtained titanium oxynitride films as an active element of memristors, and in other important areas of modern materials science.

Keywords: Titanium oxynitride, thin films, magnetron sputtering, absorption spectrum, electrical resistivity.

1. Introduction

Currently, memristors are one of the promising areas for creating an element base for use in neuromorphic applications and as elements of non-volatile memory [1-3]. The first experimental results on the manufacture of memristors were obtained on the basis of thin films of titanium dioxide TiO_2 [4]. Further, in the course of numerous research works, memristors based on various inorganic and organic materials were obtained. Fairly large number of inorganic materials with a memristive effect are known: oxide materials such as TiO_x, HfO_x, AlO_x, TaO_x, VO_x etc., oxides of rare earth metals: Y, Ce, Sm, Gd, Eu, Pr, Er, Dy, and Nd; perovskites: $SrTiO_3Ba_{0,7}Sr_{0,3}TiO_3$, $SrZrO_3$, $BiFeO_3$, as well as metal nitrides [5-8].

Titanium compounds such as titanium oxide and titanium nitride are materials on which a memristive effect is obtained or used as electrodes for memristors [4, 9, 10]. Memristors based on titanium oxynitride (TiO_xN_y) were also obtained in [11]. Titanium oxynitride occupies an intermediate state between titanium oxide and titanium nitride in its physico-chemical properties. It is possible to obtain materials similar in properties to titanium oxide or titanium nitride by changing the concentration of oxygen and nitrogen in TiO_xN_y films. Memristors based on titanium dioxide films with an admixture of copper were manufactured in [12]. Modification of films with copper leads to a significant improvement in the basic memristive characteristics compared with titanium dioxide-based storage devices. It is shown that the use of these films in the memristor structure makes it possible to increase the ratio of the state with high electrical resistance to the state with low electrical resistance by more than 10^2 times.

Recently, interest in titanium oxynitride films has been growing as a promising material for use in biomedical applications [13], for photocatalysis [14] and as plasmonic materials [15]. Various synthesis methods are used such as pulsed laser deposition [14], magnetron sputtering [16] ion beam deposited [17] low-pressure metal-organic CVD [18] etc. Despite numerous studies in this area, there are issues that, when considered, will allow us to optimize the technology for producing thin films of titanium oxynitride and better determine their physical and chemical properties.

In this paper, the optical and electrical properties of thin titanium oxynitride films obtained by magnetron sputtering are investigated. During the production of films, a mixture of oxygen and nitrogen gases was introduced into the volume of the working chamber simultaneously with argon in proportion to their concentration in the atmosphere. This suggests that titanium oxynitride films can be produced using the addition of a small volume of air.

2. Materials and experimental details

The magnetron sputtering method was used for obtaining titanium oxynitride films. It was used a modernized NNV-6.6-I1 installation [19]. The installation was equipped with a plasma source with a hot cathode "PINK" and a dual magnetron sputtering system with two planar magnetrons and targets. The targets with a diameter of 100 mm are made of titanium grade VT-01. Preliminary, prepared samples were placed in the installation chamber on a rotating substrate holder. Vit-3 vacuum meter was employed for pressure control in the chamber. The chamber was evacuated for an hour until a vacuum of 10^{-3} Pa was achieved. Then argon gas was pumped into the chamber and a pressure of 10 Pa was achieved using the gas leakage system. After switching on the "PINK" the samples were cleaned in argon plasma for 5 minutes. Then the argon pressure was reduced to 10^{-2} Pa, and the dual magnetron was switched on in pulse mode with a frequency of 30 kHz. The targets were "burned" for 2-5 minutes until stable parameters for current (1.17 A) and voltage (522 V) of discharge combustion were reached. This was indicated by the absence of microarcs on the target. Then, in addition to argon, a mixture of oxygen and nitrogen gases was introduced into the system using a needle-type manual leak in the proportion of 4 parts nitrogen (N_2) and 1-part oxygen (O_2).

The magnetron operated in the direct current mode. The gas feed rate increased until the discharge voltage began to grow. The gas flow rate was fixed and the rotary table with the substrates fixed on it was turned on. The substrate rotation speed was maintained constant. The thickness of the deposited layer on the substrate depended on the deposition time and the magnetron discharge power. The coatings were deposited for 15 minutes at a rotation speed of 2 revolutions per minute, with a discharge power of 0.6 kW. Air was let into the chamber and the deposited samples were removed when the deposition process was completed.

Cover glasses and silicon plates were used as substrates. The described method yielded 5 films on cover glasses and 2 films on silicon plates. The resulting films were golden in color, which is one of the proofs of the realization of the synthesis of titanium nitride TiN or titanium oxynitride films (TiO_xN_y). To determine the thickness of the obtained films, the substrates were weighed before the film was applied and with the resulting film on an electronic scale RADWAG AS 60/220.R2 [20]. The film thicknesses were estimated based on tabular values of TiO_xN_y material densities [21].

The dependence of the film density on its composition was constructed to estimate the density of titanium oxynitride films in Figure 1, Supplementary Material (SM). This graph contains extreme points in the form of titanium nitride (5.43 g/cm^3) [22] and amorphous titanium oxide films (3.0 g/cm^3) [23]. The density of titanium oxynitride films (4.25 g/cm^3) was taken as an intermediate value [24]. The film composition was established by comparing the absorption coefficient of the films (α) from the wavelength of light with the literature data.

Data on the substrates used, and the average values of the thicknesses of the films obtained and the deposition rates are shown in Table 1. Sample number 1 was submitted for surface properties studies using electron and probe microscopy methods, therefore optical and electrical studies were carried out with samples 2-4.

Table 1. Main characteristics of the obtained films and the process of their application.

Substrate material	Substrate area, cm^2	Film thickness, nm	Film spraying rate
Cover glass	3.28	91.9 ± 1.7 (P= 0.95)	6.13 nm/min
Silicon substrate	1,54	244.3	16.3 nm/min

The morphology of the films was studied using a NIST-NT atomic force microscope and a Hitachi 3030TM scanning electron microscope (SEM). The composition of the films was measured by EDX (Energy dispersion X-Ray spectroscopy) on a Hitachi 3030TM SEM. The optical properties of the films were studied using a Solar CM2203 spectrofluorometer. The electrical resistance of the films was measured using a two-probe method according to the method [25].

3. Results and discussion

The surface morphology of the obtained TiO_xN_y films is shown in Figure 1. The films obtained on silicon is fine-grained with a uniform grain distribution (Figures 1, a). The film on glass has large grains unevenly distributed over the surface in addition to small grains. Thus, the film obtained on the silicon surface has a less rough surface. The side view for the films is shown in Figure 2, SM. The results of the study of the morphology of the surface of the obtained films on SEM showed the absence of visible microdefects (Figure 3, SM).

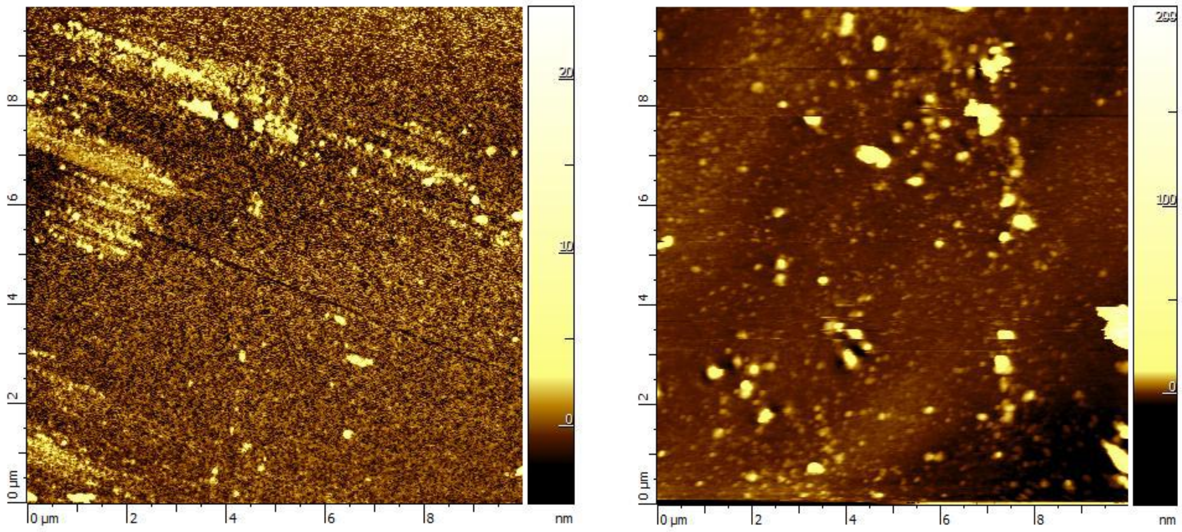

a) b)

Fig.1. AFM images of films with an area of 10 × 10 µm obtained on a silicon surface (a) and on a glass surface (b).

The results of film composition measurements by the EDX method on silicon substrates are presented in Figure 2. The spectrum contains small peaks corresponding to the characteristic radiation of the elements Ti, N, O, and the main peak belongs to silicon since the obtained films are thin.

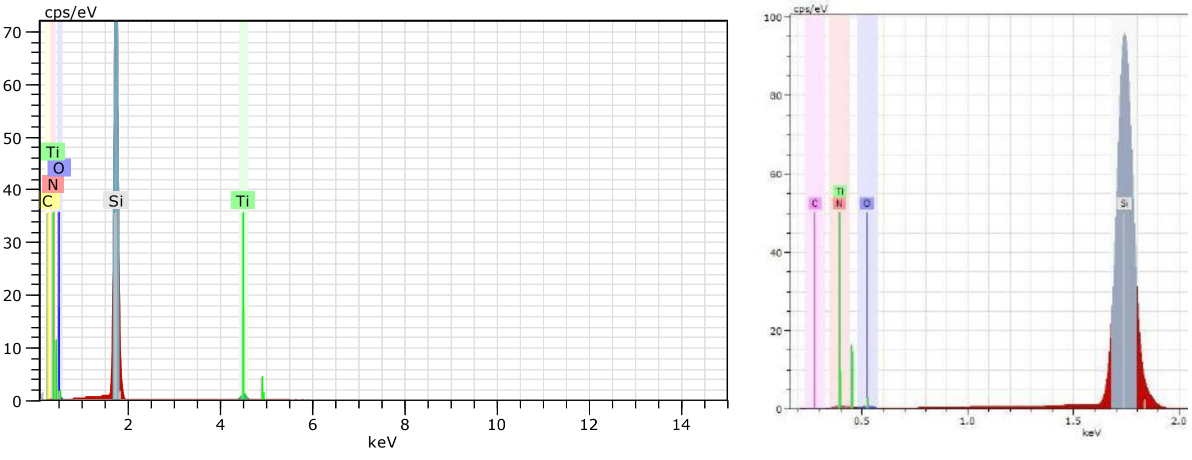

a) b)

Fig.2. EDX spectra of a film sample on a silicon surface:
a) full spectrum; b) enlarged fragment in the range up to 2 keV

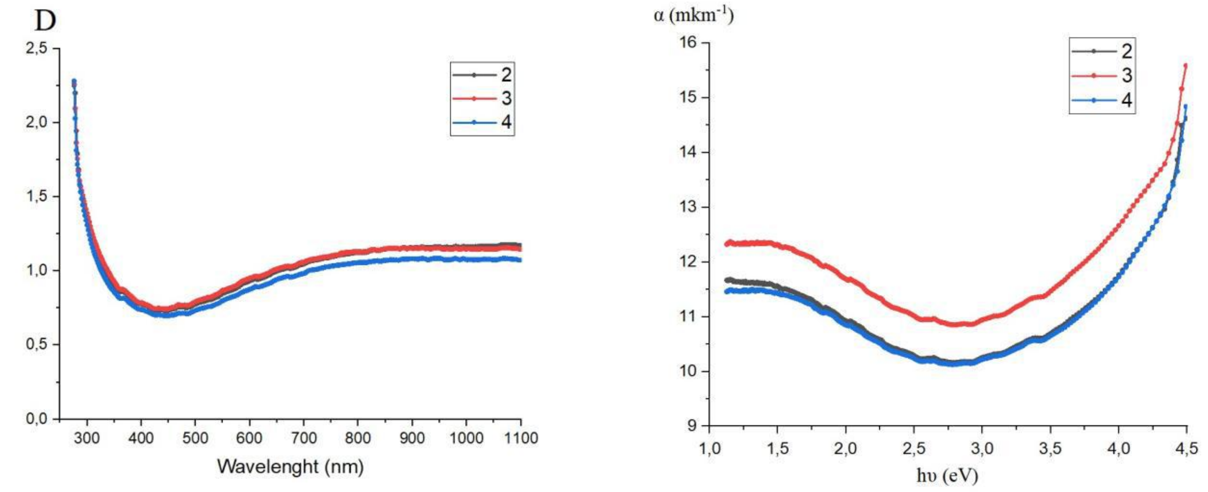

a) b)

Fig.3. The absorption spectrum of films (a) and the dependence of the absorption coefficient (α) on energy.

The EDX spectra confirmed the presence of titanium (peaks corresponding to energies of 0.4, 4.5 keV, etc.), nitrogen (0.3 keV), and oxygen (0.5 keV). The content of the elements by weight (wt.%) above 1% (measurement error). This allowed us to conclude that the Ti, N and O elements are present in the film.

The distribution map of the elements over the sample surface is shown in Figure 4, SM and the distribution maps of each element separately are shown in Figure 5, SM. The data obtained show that the distribution of all elements over the film surface is uniform. Figure 3, a, b shows the absorption spectra of several films on the surface of cover glasses. The spectral curves show an increase in optical density in the wavelength range from 450 nm to 1100 nm, Figure 3, a, which corresponds to energy values from 2.7 eV to ~ 1.1 eV. A comparison of the spectra obtained in the work (Figure 3, a, b) with the literature data [14, 15] shows that the studied films have an amorphous structure [14] and are similar in properties to samples with the stoichiometric composition $TiO_{1.27} N_{0.49}$ [15].

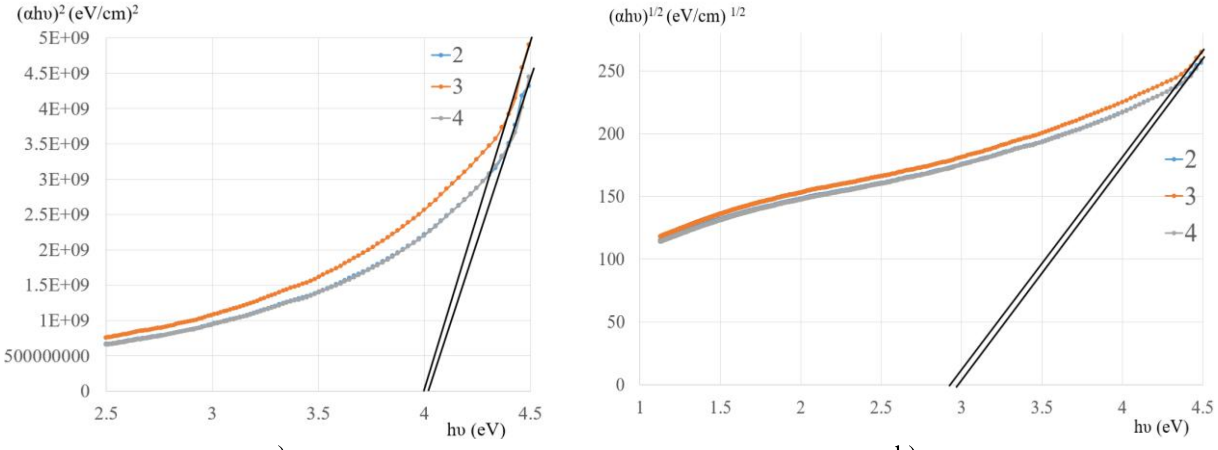

a) b)

Fig.4. Dependency graphs $(\alpha h\nu)^2 = f(h\nu)$ (a) and $(\alpha h\nu)^{1/2} = f(h\nu)$ (b).

The graphs of the dependences of $(\alpha h\upsilon)^2$ and $(\alpha h\upsilon)^{1/2}$ on the parameter hυ are shown in Figure 4. As a result, the values of the band gap were obtained for these graphs: for the graph $(\alpha h\upsilon)^2$/ hυ, the value Eg ~ 4.0 eV was obtained, for the graph $(\alpha h\upsilon)^{1/2}$/ hυ − Eg ~ 2.8-2.9 eV. The value of the optical band gap Eg = 4.12 eV was shown in [26] for nanocrystalline TiN_xO_{1-x} films. This result was obtained from the graph of the dependence $(\alpha h\upsilon)^2$ / hυ. Therefore, this result indicates the synthesis of titanium oxynitride films. However, in [14], the values of the band gap for films of 1.60 eV-1.64 eV were obtained. Therefore, this issue requires further research. It should also be emphasized that similar values of the band gap were obtained for TiO_2 films of the crystalline modification of brookite Eg> 3.5 eV for the $(\alpha h\upsilon)^2$/ hυ graph (direct allowed transitions of TiO_2) and Eg ~ 2.9-3.2 eV for the anatase and rutile modifications of titanium dioxide (indirect allowed transitions) [27]. The difficulty in determining the optical band gap of titanium oxynitride may be due to the fact that titanium oxynitride is represented predominantly by the amorphous phase of this substance. This is indicated by a comparison of the data in the Figure 3, a with the literature data [15].

The electrical resistivity of TiO_xN_y films was measured using a two-probe method (Figure 5). The data obtained for some samples are shown in Table 2. A comparison of the values of specific resistance obtained in the work with literature data was carried out. The results of the comparison showed that the specific resistance of the obtained films is in good agreement with the available literature data [28-30]. In this case, the obtained values of the electrical resistivity of the films corresponded more closely to the values of the resistances of titanium nitride TiN_2 films than titanium oxide TiO_2.

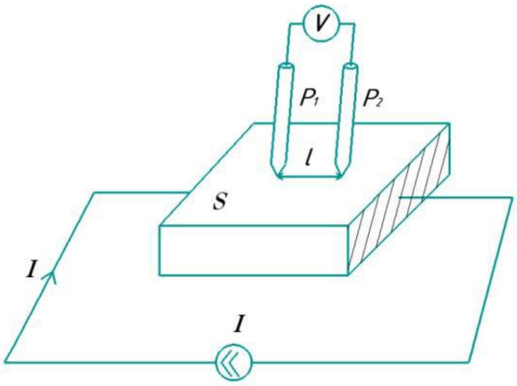

Fig.5. Scheme of measuring specific resistance using the two-probe method:
I - the current flowing through the film under study, S - the area of the films; l - the distance between the probes; U - the measured voltage between the probes.

Table 2. Electrical resistivity of TiO_xN_y films

№, sample	I (mA)	S (m^2)	L, (cm)	U (V)	ρ (Ohm*cm)
2	1.4	$0.18*10^{-6}$	0.4	0.707	$0.227*10^{-3}$
3	1.4	$0.17*10^{-6}$	0.4	2.38	$0.7225*10^{-3}$
4	1.4	$0.18*10^{-6}$	0.4	2.396	$0.766*10^{-3}$

Thus, the conducted studies have shown that in the process of magnetron deposition of titanium in a working chamber with a mixture of argon, nitrogen and oxygen gases, titanium oxynitride films with an amorphous structure were obtained. Analysis of the optical and electrical properties of the obtained films showed that these data correspond to literature data.

4. Conclusion

In this work, thin films of titanium oxynitride on glass and silicon substrates were obtained by magnetron sputtering in an argon atmosphere with the additions of oxygen and nitrogen. It is shown that the type of substrate influences the surface morphology, with films on silicon being characterized by a more uniform and fine-grained structure. Elemental analysis confirmed the presence of Ti, O, and N and their uniform distribution over the surface of the films. The analysis of the optical spectra showed that the obtained films have a predominantly amorphous structure and are similar in their properties to the composition of $TiO_{1.27}N_{0.49}$, which is consistent with the literature data. The estimation of the band gap yielded values comparable to the published results for titanium oxynitride and titanium dioxide films. The measured electrical resistivity values are in good agreement with the known data and are closer to the characteristics of titanium nitride than titanium dioxide. This confirms the intermediate character of the electrophysical properties of titanium oxynitride between the oxide and nitride phases. The scientific novelty of the work lies in the production of TiO_xN_γ films with reproducible optical and electrical properties using a gas mixture similar in composition to atmospheric air.

The practical significance of the results is related to the possibility of using the obtained films in memristor structures. The prospects for further research include optimizing the composition of films and studying their memristive characteristics.

Funding

This work was supported by the Science Committee of the Ministry of Science and Higher Education of the Republic of Kazakhstan [Grant No. AP26103063].

References

1. Song M.-K., Kang J.-H., Zhang X., Ji W., Ascoli A., Messaris I., Demirkol A.S., Dong B., Aggarwal S., Wan W., Hong S.-M., Cardwell S.G., Boybat I., Seo J.-S., Lee J.-S., Lanza M., Yeon H., Onen M., Li J., Yildiz B., del Alamo J.A., Kim S., Choi S., Milano G., Ricciardi C., Alff L., Chai Y., Wang Z., Bhaskaran H., Hersam M.C., Strukov D., Wong H.-S.P., Valov I., Gao B., Wu H., Tetzlaff R., Sebastian A., Lu W., Chua L., Yang J.J., Kim J. (2023) Recent advances and future prospects for memristive materials, devices, and systems. *ACS Nano*, 17(13), 11994–12039. https://doi.org/10.1021/acsnano.3c03505

2. Xu W., Wang J., Yan X. (2021) Advances in memristor-based neural networks. *Front. Nanotech.*, 3, 645995(1–14). https://doi.org/10.3389/fnano.2021.645995

3. Aguirre F., Sebastian A., Le Gallo M. (2024) Hardware implementation of memristor-based artificial neural networks. *Nature Commun.*, 15(1), 1974. https://doi.org/10.1038/s41467-024-45670-9

4. Strukov D.B., Snider G.S., Stewart D.R., Williams R.S. (2008) The missing memristor found. *Nature*, 453, 80–83. https://doi.org/10.1038/nature06932

5. Zimmers A., Aigouy L., Mortier M., Sharoni A., Wang S., West K.G., Ramirez J.G., Schuller I.K. (2013) Role of thermal heating on the voltage induced insulator-metal transition in VO2. *Phys. Rev. Lett.*, 110, 056601. https://doi.org/10.1103/PhysRevLett.110.056601

6. Zhang H., Liu L.F., Gao B., Qiu Y.J., Liu X.Y., Lu J., Han R.Q., Kang J.F., Yu B. (2011) Gd-doping effect on performance of HfO2 based resistive switching memory devices using implantation approach. *Appl. Phys. Lett.*, 98(4), 042105. https://doi.org/10.1063/1.3543837

7. Kim S., Choi Sh.H., Lu W. (2013) Comprehensive physical model of dynamic resistive switching in an oxide memristor. *ACS Nano*, 8(3), 2369–2376. https://doi.org/10.1021/nn405827t

8. Ryndin E., Andreeva N., Luchinin V. (2022) Compact model for bipolar and multilevel resistive switching in metal-oxide memristors. *Micromachines*, 13(1), 98. https://doi.org/10.3390/mi13010098

9. Ju D., Kim S. (2024) Volatile tin oxide memristor for neuromorphic computing. *iScience*, 27(8), 110479(1–13). https://doi.org/10.1016/j.isci.2024.110479

10. Zhu Y.-L., Xue K.-H., Cheng X.-M., Qiao Ch., Yuan J.-H., Li L.-H., Miao X.-Sh. (2021) Uniform and robust TiN/HfO2/Pt memristor through interfacial Al-doping engineering. *Appl. Surf. Sci.*, 550, 149274. https://doi.org/10.1016/j.apsusc.2021.149274

11. Shih Y.-Ch., Wang T.-H., Huang J.-Sh. (2016) Roles of oxygen and nitrogen in control of nonlinear resistive behaviors via filamentary and homogeneous switching in an oxynitride thin film memristor. *RSC Adv.*, 6(66), 61221–61227. https://doi.org/10.1039/c6ra12408a

12. Urazbekov A.E., Troyan P.E., Sakharov Yu.V. (2024) Development of a method for obtaining copper-doped titanium dioxide for the creation of memristive memory elements. *Polzunov Bull.*, 1, 229–233. https://doi.org/10.25712/ASTU.2072-8921.2024.01.029

13. Leng Y.X., Wang Z.H., Huang N. (2011) Structure and Properties of Ti-O-N Films Synthesized by Reactive Magnetic Sputtering. *Physics Procedia*, 18, 40–45. https://doi.org/10.1016/j.phpro.2011.06.054

14. Mucha N.R., Som J., Shaji S., Fialkova S., Apte P.R., Balasubramanian B., Shield J.E., Anderson M., Kumar D. (2020) Electrical and optical properties of titanium oxynitride thin films. *J. Mater. Sci.*, 55(12), 5123–5134. https://doi.org/10.1007/s10853-019-04278-x

15. Naik G.V., Kim J., Boltasseva A. (2011) Oxides and nitrides as alternative plasmonic materials in the optical range. *Opt. Mater. Express*, 1(6), 1090–1099. https://doi.org/10.1364/OME.1.001090

16. Ali Sh., Magnusson R., Pshyk O., Birch J., Eklund P., le Febvrier A. (2023) Effect of O/N content on the phase, morphology, and optical properties of titanium oxynitride thin films. J. Mater. Sci., 58, 10975–10985. https://doi.org/10.1007/s10853-023-08717-8

17. Jia L.W., Lu H.P., Ran Y.J., Zhao S.J., Liu H.N., Li Y.L., Jiang Z.T., Wang Z. (2019) Structural and dielectric properties of ion beam deposited titanium oxynitride thin films. *J. Mater. Sci.*, 54, 1452–1461. https://doi.org/10.1007/s10853-018-2923-y

18. Fabreguette F., Imhoff L., Maglione M., Domenichini B., Marco de Lucas M.C., Sibillot P., Bourgeois S., Sacilotti M. (2010) Correlation between the electrical properties and morphology of low-pressure MOCVD titanium oxynitride thin films grown at various temperatures. *Chem. Vap. Deposition*, 6(3), 109–114. https://doi.org/10.1002/(SICI)1521-3862(200006)6:3%3C109::AID-CVDE109%3E3.0.CO;2-4

19. Guchenko S.A. (2012) Production, structure, and properties of multiphase ion-plasma coatings. *Bull. Karaganda Univ. Ser.: Phys.*, 4(68), 12–25. Available at: https://phs.buketov.edu.kz/apart/srch/2012_physics_4_68_2012.pdf

20. Baikenov M.I., Seldyugaev O.B., Guchenko S.A., Afanasyev D.A. (2024) Reason of pitting corrosion of martensitic steel in sea water. *Euras. Phys. Tech. J.*, 21(1), 38–48. https://doi.org/10.31489/2024No1/38-48

21. Kiseleva E.S. (2016) Physico-mechanical properties and structure of titanium dioxide and oxynitride films deposited by reactive magnetron sputtering. Abstract of diss., Tomsk. [in Russian] Available at: https://portal.tpu.ru/portal/pls/portal/!app_ds.ds_anketa_bknd.download_doc?fileid=3437

22. Dultsev F.N., Svitasheva S.N., Nastaushev Yu.V., Aseev A.L. (2011) Ellipsometric investigation of the mechanism of the formation of titanium oxynitride nanolayers. *Thin Solid Films*, 519(19), 6344–6348. https://doi.org/10.1016/j.tsf.2011.04.034

23. Mergel D., Buschendorf D., Eggert S., Grammes R., Samset B. (2000) Density and refractive index of TiO2 films prepared by reactive evaporation. *Thin Solid Films*, 371(1–2), 218–224. https://doi.org/10.1016/S0040-6090(00)01015-4

24. El-Hossary F.M., Negm N.Z., Abd El-Rahman A.M., Raaif M., Abd Elmula A.A. (2015) Properties of titanium oxynitride prepared by RF plasma. *Advances in Chemical Engineering and Science*, 5, 1–14. http://dx.doi.org/10.4236/aces.2015.51001

25. Pavlov L.P. (1987) Methods for measuring parameters of semiconductor materials. Moscow: Vysshaya Shkola. 239 p. [in Russian] Available at: https://www.studmed.ru/pavlov-lp-metody-izmereniya-parametrov-poluprovodnikovyh-materialov_2b8fe54b8df.html

26. Yang X.G., Li C., Yang B.J., Wang W., Qian Y.T. (2004) Optical properties of titanium oxynitride nanocrystals synthesized via a thermal liquid-solid metathesis reaction. *Chem. Phys. Lett.*, 383(5–6), 502–506. https://doi.org/10.1016/j.cplett.2003.11.037

27. Ievlev V.M., Kushchev S.B., Latyshev A.N., Leonova L.Yu., Ovchinnikov O.V., Smirnov M.S., Popova E.V., Kostyuchenko A.V., Soldatenko S.A. (2014) Absorption spectra of TiO2 thin films synthesized by the reactive radio-frequency magnetron sputtering of titanium. *Semiconductors*, 48(7), 848–858. https://doi.org/10.1134/S1063782614070094

28. Erofeev E.V., Fedin I.V., Kazimirov A.I. (2015) Study of electrophysical parameters of titanium nitride thin films obtained by magnetron sputtering. *Bull. SibSUTIS*, 3, 29–34. Available at: https://vestnik.sibsutis.ru/jour/article/view/506

29. Chris-Okoro I., Cherono Sh., Akande W., Nalawade S. (2025) Optical and plasmonic properties of high-electron-density epitaxial and oxidative controlled titanium nitride thin films. *J. Phys. Chem. C*, 129(7), 3762–3774. https://doi.org/10.1021/acs.jpcc.4c06969

30. Yildiz A., Lisesivdin S.B., Kasap M., Mardare D. (2008) Electrical properties of TiO2 thin films. *J. Non-Cryst. Solids*, 354, 4944–4947. https://doi.org/10.1016/j.jnoncrysol.2008.07.009

AUTHORS' INFORMATION

Makhabayeva, A.T. – PhD student, Master (Sci.), Buketov Karaganda National Research University, Karaganda, Kazakhstan; https://orcid.org/0009-0005-6578-2028; ainurka.mah@bk.ru

Chirkova, L.V. – Candidate of Technical Sciences, Associate Professor, Buketov Karaganda National Research University, Karaganda, Kazakhstan; https://orcid.org/0000-0002-5197-3895; tchlv_53@mail.ru

Guchenko, S.A. – Master (Sci.), Buketov Karaganda National Research University, Karaganda, Kazakhstan; https://orcid.org/0000-0002-9954-5478; guchen@mail.ru

Tuleuov, S.D. – Bachelor (Eng.), Buketov Karaganda National Research University, Karaganda, Kazakhstan; https://orcid.org/0009-0002-6009-1672; serik.tu123@gmail.com.ru

Makhanov, K.M. – Candidate of Physical and Mathematical Sciences, L.N. Gumilyov Eurasian National University, Astana, Kazakhstan; https://orcid.org/0000-0002-1263-0734; makhanov_km@enu.kz

Shakirzyanov, R.I. – PhD., Senior Researcher, L.N. Gumilyov Eurasian National University, Astana, Kazakhstan; https://orcid.org/0000-0001-9908-3034; shakirzyanov_ri@enu.kz

Afanasyev, D.A. – PhD, Associate Professor, Buketov Karaganda National Research University, Karaganda, Kazakhstan; https://orcid.org/0000-0002-0437-5315; a.d.afanasyev2@gmail.com

EURASIAN PHYSICAL TECHNICAL JOURNAL

2025, Volume 22, No. 4 (54)

https://doi.org/10.31489/2025N4/31-38

Received: 23/06/2025 Revised: 14/11/2025 Accepted: 22/12/2025

Research Article

UDC 539.213.32

MODELING OF CLOSE-ORDER FRACTAL STRUCTURES OF METAL-METALLOID ALLOYS WITH CUBIC STRUCTURE

Sereda D.B., Baskevych O.S., Sereda B.P., Kryhliyak I.V.

[1] Dnipro State Technical University, Kamenskoe, Ukraine
[2] Ukrainian State University of Science and Technology, Dnipro, Ukraine
**Corresponding author*: seredabp@ukr.net

Abstract. *Using methods of mathematical physics, a comprehensive simulation of the short-range order in* $Fe_{88}P_{12}$ *and* $Cr_{88}C_{12}$ *alloys produced by electrodeposition was carried out. As the initial configuration for modeling, the crystal structure of the base metal was selected. Numerous experimental studies, including X-ray diffraction and electron microscopy analyses, have indicated that in metal-metalloid alloys, surface microstructures predominantly exhibit ellipsoidal morphologies. Based on these experimental observations, it was hypothesized that the macroscopic ellipsoidal formations observed on the alloy surfaces are composed of clusters with relatively simple geometric configurations, such as spheres or ellipsoids. The results of the simulation revealed that these clusters possess characteristic sizes not exceeding 30-50 angstroms, and their vectorial growth predominantly occurs along a single radial direction relative to the substrate surface. This anisotropic growth behavior is attributed to differences in local atomic bonding energy and diffusion kinetics, which drive the preferential alignment of cluster development. Moreover, it was established that the spatial distribution and size uniformity of the clusters significantly influence the overall mechanical and physicochemical properties of the coatings, including hardness, wear resistance, and corrosion stability. The combination of modeling outcomes with empirical data provides valuable insight into the microstructural evolution mechanisms governing electrodeposited metal-metalloid systems. These findings can serve as a basis for optimizing the electrodeposition parameters to tailor the surface structure and enhance the performance characteristics of functional coatings.*

Keywords: amorphous state, electrodeposition, modeling, clusters.

1. Introduction

Amorphous and nanocrystalline metal alloys obtained by electrodeposition have a set of unusual physical and chemical properties and are a new class of promising materials of undoubted theoretical and practical interest. The structural state of metallic amorphous and nanocrystalline alloys is characterized by close atomic order and, unlike crystals, by the absence of translational symmetry in the arrangement of atoms. All amorphous materials have a short-range order, which is also called topological (or configurational), and the ordered distribution of different kinds of atoms is called the chemical (compositional) short-range order. Since it is problematic to obtain pure metals in an amorphous state, metalloid atoms are introduced to produce them. In the case of two- and multi-component systems, the concept of "near order" includes the spatial distribution of atoms regardless of the grade and mutual distribution of different-grade atoms [1-3]. The creation of promising and improvement of existing metal alloys for protective coatings using electrolytic deposition is impossible without establishing the mechanism of their formation and growth. Currently, there is no single theory of deposition of metal alloys depending on the conditions of their formation, which leads to great difficulties in interpreting the properties of these materials. Numerous experiments on the electrodeposition of metal alloys show that the surface structures have different geometric shapes: two-dimensional surface shapes, and in some cases, three-dimensional (three-dimensional) shapes. It is known that one of the most important properties of the surfaces of fractal systems is the self-similarity property. If you select a small area in the surface area occupied by a fractal cluster, the cluster areas will be similar to the shape of this cluster. For clusters with random arrangements of atoms, it is necessary to use statistical particle sizes. During electrodeposition, the growth of such clusters is observed mainly in the direction opposite to the movement of metal ions and amorphizing elements [4-6]. The research of deposited metal pyrites with body-centered cube grill (BCC) showed that the surfaces have ellipsoidal forms of fractal structure and can be studied by means of fractal geometry, X-ray diffraction analysis and electron microscopy (Fig. 1-3). It has been found that the shape that the surface takes during crystallization is very sensitive to the crystallization conditions, and therefore it is impossible to establish the mechanism of surface growth from the growth of bulk forms. During electrodeposition, an atomic deposition occurs, which forms clusters with different shapes that depend on the orientation of the faces and the conditions of their growth in a certain direction. Surface fractal structures influence various physical objects and phenomena, in particular, to explain the corrosion resistance and wear resistance from the surface shape.

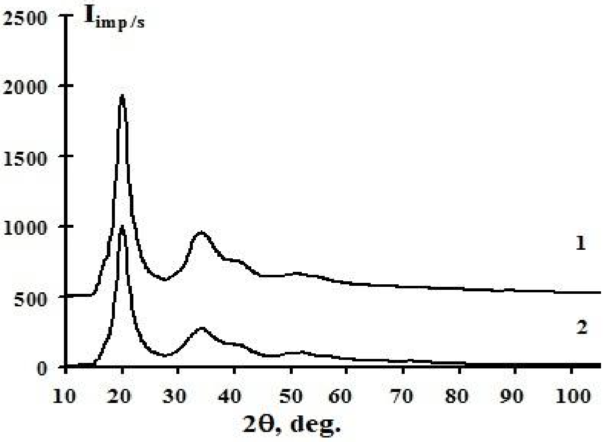

Fig. 1. X-ray diffractogram of $Cr_{88}C_{12}$ (1) and $Fe_{88}P_{12}$ (2) Mo-K_α radiation.

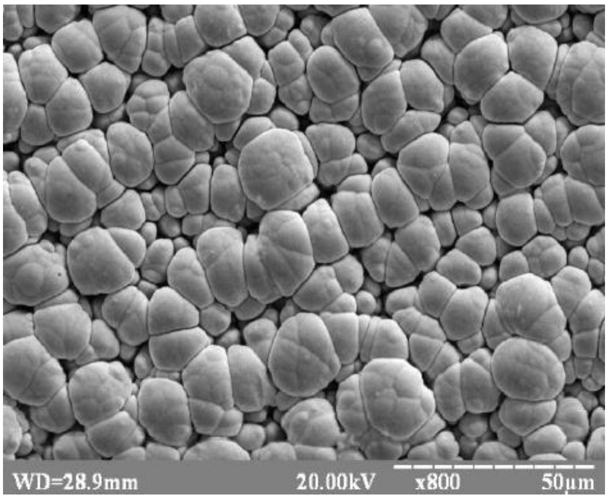

Fig.2. Surface morphology of $Cr_{88}C_{12}$ alloy (REMMA-102-2)

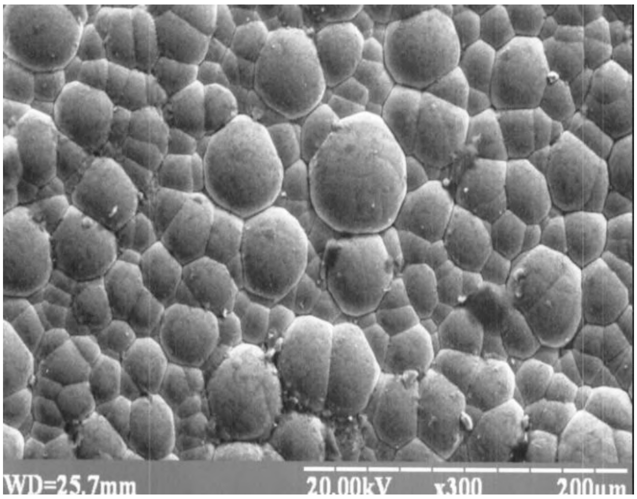

Fig.3. Surface morphology of $Fe_{88}P_{12}$ alloy (REMMA-102-2)

2. Material and methods of research

$Cr_{88}C_{12}$ alloys were obtained from an electrolyte of the following composition: $KCr(SO_4)_2 \cdot 12H_2O$ — 0.5 M, K_2BO_3 — 0.5 M, $(NH_4)_2SO_4$ — 2 M, HCOOH — 0.75 M, with pH adjusted to 3.0 and a temperature of 298 K. $Fe_{88}P_{12}$ alloys were obtained from an electrolyte of the following composition (in g/L): $FeSO_4 \cdot 7H_2O$ — 280, H_3BO_3 — 30, NaH_2PO_2 — 8×12. The pH was adjusted to 2.0–2.5 by the addition of a 5% H_2SO_4 solution. Deposition was performed using a unipolar pulsed current (i = 15–25 A/dm^2) with a pulse repetition rate (f = 2–16 Hz) and a pulse duty cycle (Q = 2–4).

The identification of crystalline phases was carried out using X-ray diffractometry. X-ray diffractograms were obtained on a DRON-3.0 diffractometer with monochromatic Mo-Kα radiation (using a curved LiF monochromator) at measurement points with an interval of 0.1 degrees and an exposure time of less than 100 seconds per point, followed by averaging across five scattering intensity curves.

The quantitative composition and surface morphology were investigated using a REMMA-102-2 scanning electron microscope (SELMI), and the coating thickness was measured using a NU-2 optical microscope (Carl Zeiss).

3. Results and discussion

Numerous experiments on the electrodeposition of alloys with volume-centered cubic lattices have shown that ellipsoidal fractal forms grow (figs. 2 and 3). To establish the mechanism of fractal growth and their structure, we will use the Brave-Donneuil-Harker rule, which states that the crystal habitus is formed with the simplest plane indices, or the faces with the highest reticular atomic density have the lowest energy. For the case of materials with the OCC structure, the bounding planes are the (110) and (200) faces. When deposition by electric current occurs in the direction opposite to the action of the electric current, the deposition process has one growth vector, and other growth directions are of secondary importance. Consider the growth of a fractal structure in terms of the crystal structure of the base metal. As a result of deposition, crystallization centers appear on the substrate, which determine the further growth of clusters. As a result, additional crystallization centers appear on the formed clusters, which again form clusters of a similar shape. The shapes of the clusters and their close order can be determined by modeling the main peak of the structural factor. Since in this case, the deposition of Cr-C and Fe-P alloys has an amorphous structure (Fig. 1), it is necessary to determine their close order and the most likely cluster shape.

It is well known that during the formation of nanocrystalline and amorphous alloys, changes in their physical and chemical properties are observed. This always happens when approaching a certain critical size. The research of the close order of amorphous and nanocrystalline Cr-C and Fe-P alloys with a volume-centered cubic lattice structure allows us to establish the stability and sequence of crystallization processes. To determine the close order of amorphous Cr-C and Fe-P alloys, a methodology for its modeling based on the profile of the main peak of the structural factor is proposed. The profile of the main peak of the structural factor was approximated using the model of the cluster structure of the amorphous state. According to the chosen model, the expression for the diffraction peak profile takes into account the finiteness of the ordering regions, their size distribution, and the relative rms displacements of atoms from the equilibrium position and is defined by eq. [7-12]:

$$i(s_0) = \frac{Q_2 Q_3}{d_{hk}} \exp\left(-\frac{u^2 s_0^2}{2}\right) \int_{-\infty}^{\infty} V(t) \cdot g(L,t) \cdot e^{-\gamma(t)} \cos(s_0 t) dt, \quad (1)$$

where Q_2 and Q_3- coefficients that take into account the effect of relative rms displacements of atoms from equilibrium positions ($\bar{u}^2$) within the reflection plane on the height of the main peak of the structural factor, $g(L, t)$ - distribution of clusters by size, L- size of clusters, V(t)- unction of shape, γ - coefficient, which determines the effect of the relative root mean square static displacements of atoms in the direction perpendicular to the reflection plane (during isothermal annealing $\gamma \rightarrow 0$), t - normal to a number of atomic planes that reflect radiation within the investigated diffraction peak, $s_0 = |s - s_{\max}|$- modulus of the scattering vector.

The function $V(\vec{t})$ is defined by the expression [9-11, 14]:

$$V(\vec{t}) = V^{-1} \int \sigma(\vec{x}) \sigma(\vec{x} + \vec{t}) d^3\vec{x}, \quad (2)$$

where V is volume of the cluster, and the function:

$$\sigma(\vec{x}) = \begin{cases} 1, x \in V \\ 0, x \notin V \end{cases}, \tag{3}$$

If the scattering region has ν planar grids perpendicular to the primary beam, then the intensity of the structural factor in the primary beam region (2) is converted to:

$$i(0) = \text{const}\left(1 + 2\sum_{p=1}^{v}\left(1 - \frac{p}{v}\right)\right) = \text{const} \cdot v, \tag{4}$$

For the scattering regions of disordered systems, the height of the main peak of the structural factor will be lower than that of crystalline and volume-centered cubic lattice nanalloys, and their height will be proportional to the size of this region. The coefficients Q_i for the volume-centered cubic lattice structure are equal Q_2=0,9881 i Q_3=0,9766 [9, 11, 15-20].

The need to introduce a function of cluster size $g(L)$ distribution is dictated by the presence of clusters of different sizes in real nonequilibrium alloys. In order to take into account the function of cluster distribution by size, the profile of the main peak of the structural factor can be represented by the relation [9-10]:

$$i(s_0) = \int_0^{\infty} i(s_0, L) g(L) dL, \tag{5}$$

The distribution of clusters by size according to (5) takes into account scattering both on clusters and on individual atoms and can be found by taking into account the energy of cluster formation:

$$E(L,P) = A \cdot \exp\left[-\frac{U(L) + E(P)}{kT}\right], \tag{6}$$

where *U(L)* is fraction of the cluster energy associated with its size and the energy of pairwise interaction of atoms [13-14], *E(P)* is kinetic energy of the order region associated with the relative rms static displacements of atoms relative to their position in the crystalline state. To express the energy (6.7), the distribution function approaches the Gaussian distribution [9]:

$$g_G(L) = \frac{1}{\sigma_L\sqrt{2\pi}} \exp\left[-\frac{(L - \langle L \rangle)^2}{2\sigma_L^2}\right], \tag{7}$$

where

$$\sigma_L^2 = \bar{L}^2 \left[\frac{\Gamma\left(\frac{3n+2}{6}\right)\Gamma\left(\frac{3n+6}{6}\right)}{\Gamma\left(\frac{3n+4}{6}\right)} - 1\right], \tag{8}$$

$\Gamma(x)$ - gamma Euler function.

Relationship (5) cannot be directly used to analyze the profile of the main peak of the structural factor, since neither the distribution parameters $g(L)$, nor the shape of the cluster areas. In this regard, the function of distribution of clusters by size is used:

$$g(L,t) = \mu \cdot \langle L \rangle \cdot e^{-\beta t^2}, \tag{9}$$

where the variables μ and β are determined by normalizing (9), and $\langle L \rangle$ is average size of the clusters.

Then (7) is transformed to the form:

$$i(s_0) = \frac{Q_2 Q_3}{d_{hkd}} \cdot \mu \cdot \langle L \rangle \cdot \exp\left(-\frac{u^2 s_0^2}{2}\right) \int_{-\infty}^{\infty} V(t) \cdot e^{-(\beta t^2 + \gamma t)} \cos(s_0 t) dt \tag{10}$$

Expression (10) is a function of the main physical parameters of the close-order amorphous system that characterizes the clusters, and the value $\langle L \rangle$ is determined in the process of modeling the profile of the main peak of the cluster structural factor. The values of the gaps (δ) between clusters in nonequilibrium alloys are not constant, however, as a first approximation, we assume them to be the same for clusters of different sizes if their shape remains constant [9]. The average size of a cluster is used to determine its average volume $\langle (L+d)^3 \rangle$ i and the average volume that falls on the same number of atoms in the volume $\langle (L+d+\delta)^3 \rangle$.

Table 1. The function of the shape *V(t)* and dimensions L of the reflection {110} of the OCC structure [14].

Cluster shape	*V(x)*	*I*	*L*	*Multiplicity*
tetrahedral bipyramid	$\mathbf{1 - \frac{3}{2}t + \frac{3}{8}t^2 + \frac{1}{8}t^3}$ 1) 2) $(\mathbf{1 - t})^3$	$I_0 - \frac{3}{2}I_1 + \frac{3}{8}I_2 + \frac{1}{8}I_3$ $I_0 - 3I_1 + 3I_2 - I_3$	$\mathbf{a\sqrt{2}}$ $\mathbf{a\sqrt{2}}$ $\mathbf{a\sqrt{2}}$	4 2
cuboctahedron	$\mathbf{1 - \frac{9}{5}t + \frac{4}{5}t^2}$	$I_0 - \frac{9}{5}I_1 + \frac{4}{5}I_2$	$\mathbf{a\sqrt{2}}$	$\mathbf{a\sqrt{2}}$

Table 2. Parameters of $Cr_{88}P_{12}$ and $Fe_{88}P_{12}$, alloy clusters obtained by modeling the profile of the main peak of the structural factor.

Alloy	Main form of clusters	*a, nm*	*Δa, nm*	*U^2, nm^{-2}*	*δ, nm*	*<L>, nm*	*$Δ_L$, nm*
$Cr_{82}C_{12}$	cuboctahedron	0,28693	0,00216	0,0110	0,1510	3,4563	0,134
$Fei_{88}P_{12}$	cuboctahedron	0,28521	0,00254	0,0113	0,1321	2,5412	0,145

To determine the gaps between clusters, use the equation:

$$\frac{\langle (L+d)^3 \rangle}{\langle (L+d+\delta)^3 \rangle} = \frac{D_{\text{m/alloy}}}{D_{\text{m/cluster}}} \tag{11}$$

where $D_{\text{m/alloy}}$ is macroscopic density of the alloy, $D_{\text{m/cluster}}$ is density of the clusters, δ is average gap between clusters.

We calculate the shape function based on the Bravé principle, which states that the crystal faces with the highest reticular atomic density have the lowest surface energy. Let us consider the near-order models of the densest lattices such as the volume-centered cubic lattice, where the total number of atoms in a cluster remains constant, and the distance between parallel planes should be larger, the greater the reticular density and the interplane distances with small indices. Suppose that the growth of the cluster occurs through a series of successive states of equilibrium of the cluster with the surrounding atoms, i.e., at any given time, the surface energy of the crystal has the lowest value for a given volume (Brave-Donneuil-Harker rule) [14, 21] by virtue of the assumptions, it is possible to choose cluster shapes for the structure of a volume-centered cubic lattice bounded by planes (110), (200) or a set of these planes. Table 1 shows the shape functions *V(x)* and the peak profiles of the structural factors *i(s)* of the reflections (110) of the volume-centered cubic lattice structure.

In Table 1: a - means the length of the polyhedron edge, *L*- size of the cluster, and the length of the side edge $\mathbf{a\sqrt{\frac{3}{2}}}$ For these forms of clusters of the volume-centered cubic lattice structure, there are several orientations that lead to reflection from the {110} faces, but which have different functions *V(x)*. Table 1 shows the multiplicity of such orientations. If the multiplicity of *$V_1(x)$* is 4 and, *$V_2(x)$* is - 2, then

$i(s_0) = (4i_1(s_0) + 2i(s_0))/6$ due to the fact that the clusters do not have predominant orientations in the sample volume. Considering these assumptions, it is possible to calculate the profile of the main peak of the structural factor in an analytical form:

$$i(s_0) = \frac{Q_2 Q_3}{d_{hkl}} \cdot \mu \cdot \langle L \rangle \cdot \exp\left(-\frac{u^2 s_0^2}{2}\right) \cdot l, \qquad (12)$$

where the values of the sub-integral expression I в in equation (12) are given in Table 1, and the values I_n are determined by Eq:

$$I_n = \left(\frac{-1}{2\beta}\right)^n \sqrt{\frac{\pi}{\beta}} \exp\left(\frac{\gamma^2 - s_0^2}{4\beta}\right)^{E\left(\frac{n}{2}\right)} \sum_{k=0} \frac{n!}{(n-2k)!\,k!} \beta^k$$

$$\sum_{\mathrm{j}=0}^{n-2k} \binom{n-2k}{\mathrm{i}} \cdot \gamma^{n-2k-j} s_0 \cdot \cos\left(\frac{s_0 \gamma}{2\beta} + \frac{\pi}{2}\mathrm{j}\right)$$

where $E(n/2)$ - an integer part of a real number, $n/2$, and

$$\binom{n-2k}{i} = \frac{(n-2k)\cdot(n-2k-1)\ldots(n-2k-i+1)}{1\cdot 2\cdot 3\ldots i}, \binom{n-2k}{0} = 1$$

The modeling of the structure and average size of the clusters showed that the most realistic results are obtained when the component of the external impulse is close to one. This indicates that the clusters do not participate in translational and oscillatory motions, and one degree of freedom can be attributed to the radial momentum of the cluster, since during electrodeposition the clusters grow in the form of ellipsoids. This fact is confirmed by the analysis of the microstructure of $Cr_{88}P_{12}$ and $Fe_{88}P_{12}$ alloys (Fig. 2 - 3), which shows that during electrodeposition, the structure grows in the radial direction (under these conditions, ellipsoidal formations on the surface). The modeling of the main peak of the structural factor showed that the near-order of alloy clusters with volume-centered cubic lattice crystal lattices of the main metal have shapes close to cuboctahedra, and their sizes do not exceed 30-50 nm ((Fig. 4 - 5 and Table 2).

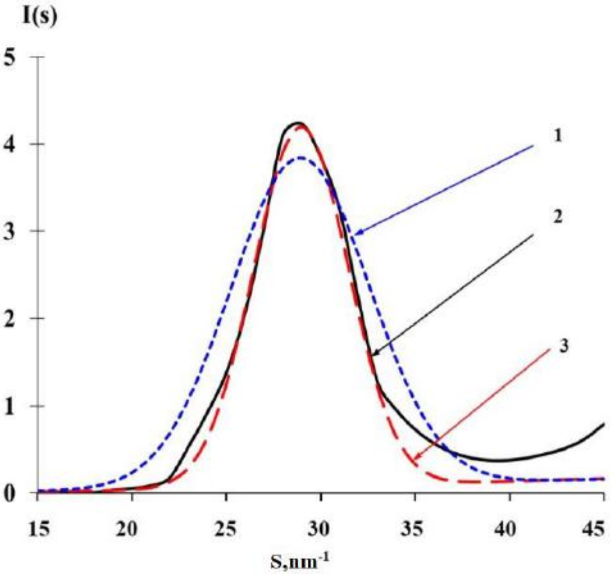

Fig. 4. Modeling the profile of the main peak of the amorphous $Cr_{88}C_{12}$ alloy:
1 - tetrahedral bipyramid, 2 - experimental peak of the structural factor, 3 - cuboctahedron

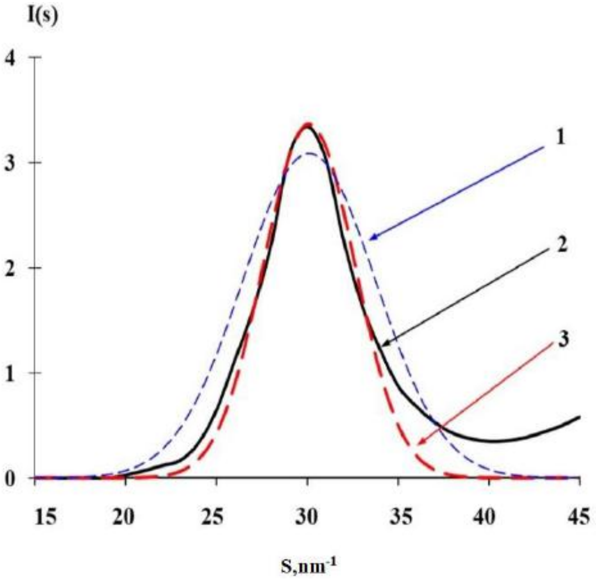

Fig. 5. Modeling of the main peak profile of the amorphous $Fe_{88}C_{12}$:
1 - tetrahedral bipyramid, 2 - experimental peak of the structural factor, 3 - cuboctahedron.

4. Conclusions

The conducted research focused on modeling the short-range order in amorphous $Cr_{88}C_{12}$ and $Fe_{88}P_{12}$ alloys has established that the most probable form of clusters in coatings based on metals with a body-centered cubic structure is the cuboctahedron. It was revealed that the shape and size distribution of $Cr_{88}C_{12}$ and $Fe_{88}P_{12}$ clusters within the surface structures are influenced by the deposition conditions, which ultimately determine the morphology of the resulting coatings. It was also determined that during the deposition process, the vector growth of clusters predominantly occurs in the radial direction, leading to the formation of ellipsoidal microstructures. Understanding the mechanisms of cluster formation opens up new opportunities for the development of advanced materials with enhanced performance and unique properties, which can be effectively utilized across various industrial sectors.

Conflict of interest statement

The authors declare that they have no conflict of interest in relation to this research, whether financial, personal, authorship or otherwise, that could affect the research and its results presented in this paper.

CRediT author statement

Sereda D.B: Conceptualization, Data Curation; **Baskevych O.S.:** Writing Original Draft; Methodology; **Kruglyak I.V.:** Investigation; **Sereda B.P.:** Supervision, Writing Review & Editing. The final manuscript was read and approved by all authors.

References

1 Danilov F.I., Protsenko V.S., Butyrina T.E., Krasinskii V.A., Baskevich A.S., Kwon S., Lee D.Y. (2011) Electrodeposition of nanocrystalline chromium coatings from Cr(III)-based electrolyte using pulse current. *Protection of Metals and Physical Chemistry of Surfaces*, 47(5), 598–605. https://doi.org/10.1134/S2070205111050066

2 Protsenko V.S., Danilov F.I., Gordienko V.O., Baskevich A.S., Artemchuk V.V. (2012) Improving hardness and tribological characteristics of nanocrystalline Cr-C films obtained from *Cr(III)* plating bath using pulsed electrodeposition. *International Journal of Refractory Metals and Hard Materials*, 35, 281–283.

3 Hu Y. C., Li F.X., Li M.Z., Bai H.Y., Wang W.H. (2015) Five-fold symmetry as an indicator of dynamic arrest in metallic glass-forming liquids. *Nature Communications,* 6, 8310. https://doi.org/10.1038/ncomms9310

4 Protsenko V. S., Bobrova L. S., Baskevich A. S., Korniy S. A., Danilov F. I. (2018) Electrodeposition of chromium coatings from a choline chloride based ionic liquid with the addition of water. *Journal of Chemical Technology and Metallurgy*, 53(5), 906–915. Available at: https://journal.uctm.edu/node/j2018-5/15_17-130_p906-915.pdf

5 Wu Z.W., et al. (2015) Hidden topological order and its correlation with glass-forming ability in metallic glasses. *Nature Communications*, 6, 6035. https://doi.org/10.1038/ncomms7035

6 Ding J., Ma E. (2017) Computational modeling sheds light on structural evolution in metallic glasses and supercooled liquids. *Computational Materials*, 3, 9. https://doi.org/10.1038/s41524-017-0007-1

7 Protsenko V. S., Bobrova L.S., Baskevich A.S., Korniy S.A., Danilov F.I. (2018) Electrodeposition of chromium coatings from a choline chloride based ionic liquid with the addition of water. *Journal of Chemical Technology and Metallurgy*, 53(5), 906–915.

8 Kuzmann E., Felner I., Sziráki L., Stichleutner S., Homonnay Z., El-Sharif M.R., Chisholm C.U. (2022) Magnetic anisotropy and microstructure in electrodeposited quaternary Sn–Fe–Ni–Co alloys with amorphous character. *Materials*, 15(9), 3015. https://doi.org/10.3390/ma15093015

9 Feng J., Chen P., Li M. (2018) Absence of 2.5 power law for fractal packing in metallic glasses. *Journal of Physics: Condensed Matter,* 30(25), 255402. https://doi.org/10.1088/1361-648X/aac45f

10 Cheng Y.Q., Ma E. (2011) Atomic-level structure and structure-property relationship in metallic glasses. *Progress in Materials Science*, 56, 379–473. https://doi.org/10.1016/j.pmatsci.2010.12.002

11 Chen D. Z., An Q., Goddard W.A., Greer J.R. (2017) Ordering and dimensional crossovers in metallic glasses and liquids. *Physical Review B,* 95(2), 024103. https://doi.org/10.1103/PhysRevB.95.024103

12 Sereda B.P., Krugliak I.V., Baskevych O.S., Belokon Y.O., Krugliak D.O., Sereda D.B. (2019) The superficial strengthening of construction materials using composition saturant environments [*Monograph*]. DDTU. 246 p. ISBN 978-966-175-187-2.

13 Chen D.Z., Wen X.D., Lu J., Wang Q.M., Wang W.H. (2015) Fractal atomic-level percolation in metallic glasses. *Science,* 349(6254), 1306–1310. https://doi.org/10.1126/science.aab1233

14 Ding J., Asta M., Ritchie R.O. (2017) On the question of fractal packing structure in metallic glasses. *Proceedings of the National Academy of Sciences,* 114(32), 8458–8463. https://doi.org/10.1073/pnas.1705723114

15 Ma D., Stoica A.D., Wang X.-L. (2009) Power-law scaling and fractal nature of medium-range order in metallic glasses. *Nature Materials*, 8(1), 30–34. https://doi.org/10.1038/nmat2340

16 Sereda B.P., Baskevych O.S., Krugliak I.V., Sereda D.B., Krugliak D.O. (2023) Obtaining protective coatings using complex functionally active charges and electrodeposition. [*Monograph*]. DDTU. 190 p. ISBN 978-966-175-244-2

17 Tang L., Wen T., Wang N., Sun Y., Zhang F., Yang Z., Ho K.-M., Wang C.-Z. (2018) Structural and chemical orders in $Ni_{64.5}Zr_{35.5}$ metallic glass by molecular dynamics simulation. *Physical Review Materials*, 2(3), 033601. https://doi.org/10.1103/PhysRevMaterials.2.033601

18 Wu Z. W., Huo C. W., Li F. X., et al. (2016). Critical scaling of icosahedral medium-range order in CuZr metallic glass-forming liquids. *Scientific Reports*, 6, 35967. https://doi.org/10.1038/srep35967

19 Zhuravel I., Mychuda L., Zhuravel Y. (2020) Localization of steel fractures based on the fractal model of their metallographic images. *Ukrainian Journal of Mechanical Engineering and Materials Science*, 6(2), 12–22. https://doi.org/10.23939/ujmems2020.02.012

20 Lu Z., Li H., Lei Z., Chang C., Wang X., Lu Z. (2018) The effects of metalloid elements on the nanocrystallization behavior and soft magnetic properties of FeCBSiPCu amorphous alloys. *Metals,* 8(4), 283. https://doi.org/10.3390/met8040283

21 Huang B., Ge T. P., Liu G. L., Luan J. (2018) Density fluctuations with fractal order in metallic glasses detected by synchrotron X-ray nano-computed tomography. *Acta Materialia, 155*, 236–244. https://doi.org/10.1016/j.actamat.2018.05.064

AUTHORS' INFORMATION

Sereda, Dmytro B. – PhD, Associate Professor, Department of Industrial Mechanical Engineering, Dnipro State Technical University, Kamenskoe, Ukraine; Scopus Author ID: 36667256600; https://orcid.org/0000-0003-4353-1365; etohardcore@gmail.com

Baskevych, Oleksandr S. – Candidate of Physical and Mathematical Sciences, Senior Researcher, Ukrainian State University of Science and Technology, Dnipro, Ukraine; Scopus Author ID: 57202232885; https:// orcid.org/0000-0002-3227-5637; abaskevich@ukr.net

Kruglyak, Irina V. – Doctor of Technical Sciences, Professor, Head of the Industrial Mechanical Engineering Department, Dnipro State Technical University, Kamenskoe, Ukraine; Scopus Author ID: 35196308100; https://orcid.org/0000-0001-8872-6778; irina6878@ukr.net

Sereda, Borys P. – Doctor of Technical Sciences, Professor, Head of the Department of Automobiles and Transportation and Logistics Systems, Dnipro State Technical University, Kamenskoe, Ukraine; Scopus Author ID: 26428911900; https://orcid.org/0000-0002-9518-381X; seredabp@ukr.net

EURASIAN PHYSICAL TECHNICAL JOURNAL

2025, Volume 22, No. 4 (54)

https://doi.org/10.31489/2025N4/39-45

Received: 12/09/2025 Revised: 24/11/2025 Accepted: 22/12/2025

Research Article

UDC 539.261, 539.193, 539.194

THEORETICAL STUDY OF ELECTRONIC AND STRUCTURAL PROPERTIES OF N-(2-OXO-2H-CHROMEN-3-CARBONYL)CYTISINE

Turdybekov D.M.[1], Ibrayev N.Kh.[2], Kopbalina K.B.[1,2*], Kishkentayeva A.S.[3],
Pankin D.V.[4], Smirnov M.B.[4]

[1] Abylkas Saginov Karaganda Technical University, Karaganda, Kazakhstan
[2] Karaganda National Research University named after academician E.A. Buketov, Karaganda, Kazakhstan
[3] School of Pharmacy, Karaganda Medical University, Karaganda, Kazakhstan
[4] Saint Petersburg State University, Saint Petersburg, Russia Federation
*Corresponding author: kopbalinakymbat@mail.ru

Abstract. *New compounds based on cytisine and coumarin are of interest to the pharmaceutical industry due to their promising biological activity. This activity, in turn, is closely related to the structure of the compound, which is manifested in its specific electronic properties. This paper presents the results of a theoretical study of the electronic and structural properties of recently synthesized N-(2-oxo-2H-chromen-3-carbonyl)cytisine. The molecular structure of the ground and first excited states is established. Their structural features are considered, taking into account their conformational diversity. The probabilities of vertical electronic transitions, which determine the intensities of bands in the emission spectrum, are calculated. The obtained theoretical results are compared with the measured luminescence spectrum of ethanol solution.*

Keywords: cytisine, coumarin, complex, density functional theory, Ultraviolet–visible spectroscopy, luminescence spectroscopy.

1. Introduction

Coumarin derivatives possess unique electronic properties, primarily manifested in their pronounced, intense luminescence, which allows them to serve as luminescent markers including luminescent probes [1], bioimaging marker [2], specific sensor [3, 4]. Another important feature is the biological activity exhibited by coumarin derivatives. Among other potential applications, the antidiabetic [5], antimicrobial [6,7] anti-inflammatory [8] and activity of a number of coumarin derivatives can be highlighted. The use of molecular hybridization with other biologically active substances opens up prospects for the creation of new compounds, thereby expanding the applications of coumarin derivatives. Of particular interest are compounds containing cytisine, a natural alkaloid with a pronounced affinity for binding to neuronal nicotinic acetylcholine receptors (nAChRs) [9]. This substance is considered an important factor playing a significant role in the study of central nervous system functioning [9]. As has been shown previously (see, for example, [10]), the biological activity of such complexes is closely linked to their molecular structure. Therefore, an important issue is the consideration of the complex's properties, taking into account its possible conformational diversity [9, 11, 12]. The object of study in this work is the recently obtained N-(2-oxo-2H-chromene-3-carbonyl) complex [13]. In previous works [13, 14], its structure and optical properties were investigated both in the crystalline state (vibrational properties, absorption in the UV-visible range) and in ethanol solution (NMR spectra and absorption in the UV-visible range). At present, the luminescent properties of this compound remain unexplored.

The important reason for choosing luminescence spectra as research objects for the compounds containing a coumarin moiety is the presence of coumarin strong luminescence that is sensitive to its state [15]. This makes these compounds sensitive luminescent markers and probes [16]. This is especially important in drug research, as it allows us to understand, for example, where they accumulate, whether they undergo any reactions, or how they interact with proteins and enzymes. In this case, structure-sensitive luminescence will serve to understand the state of the molecule, i.e., as a state indicator.

In this regard, the present work aims to theoretically study using quantum chemical approach the structure of the molecule in its first excited state, the emission spectrum to the ground state, and compare it with the experimental luminescence spectrum. The results obtained will represent a continuation of the research on this substance, begun in the articles [13, 14], demonstrating novelty in the relevant aspects of the electronic structure of the first excited state of this recently synthesized substance.

2. Materials and methods

2.1. Experimental technique

For the measurements, ethanol solutions of N-(2-oxo-2H-chromene-3-carbonyl) cytisine with a concentration of 10^{-3} M were prepared. The starting material was synthesized according to the work [13]. Emission and luminescence excitation spectra were obtained on a Lumina fluorescence spectrometer (Thermo Fisher Scientific) in reflection geometry. Excitation spectra were recorded in the range of 290-420 nm, and luminescence spectra were recorded in the range of 380-700 nm.

2.2. Theoretical approach

Quantum chemical calculations were performed within the framework of the density functional theory with a hybrid exchange-correlation functional and a long-range dispersion correction wb97XD [17]. A doubly split-valence Pople-type basis set ~~c~~ 6-31G(d,p) [18,19] and the Gaussian G09W Rev. C program [20] were used. The calculation was performed for a single molecule in an ethanol medium. The influence of the medium was taken into account within the framework of the polarizable continuum model [21]. Optimization of the considered molecules was carried out for the ground (S_0) and first excited states (S_1) until the standard criteria were met for the maximum and root mean squared residual forces on atoms and atomic displacements.

3. Results and discussion

3.1 Structural peculiarities

The molecule of the complex under study consists of three main moieties: the cytisine moiety, the intermediate moiety, and the coumarin moiety. A previous experimental and theoretical study [14] of the conformational states of the complex in solution revealed the presence of four conformer states that can transform into each other via internal rotations. Specifically, it was shown that the two lowest-energy conformers are formed by rotating the cytisine moiety relative to the coumarin and intermediate moieties. The other two conformers can be obtained from these conformers by rotating the coumarin moiety relative to the cytisine and intermediate moieties. The potential energy of the latter two conformers is higher, making them less populated at thermal equilibrium. Therefore, only the two lowest-energy states are considered in this study. Their geometries in the ground (S_0) and 1st excited state (S_1), determined by the method described in section (2.2), are shown in Figure 1.

To designate the two conformational states under consideration, the notations 1 were additionally introduced for the conformer observed in the crystalline state [13] and 2 for another conformer with a similar energy. The total energies of the S_1-1 and S_1-2 states are -1221.057229 and -1221.041763 Hartree, respectively. Thus, the energy of S_1-1 is lower by approximately 9.7 kcal/mol. Moreover, a comparison of the geometries of the ground (S_0-1) and first excited states (S_1-1) revealed a number of differences. Structural parameters that differ significantly in different conformer states are listed in Table 1.

The most significantly difference are as follows. In the S_1-1 state, the cytisine ring bordering the transition region is significantly distorted. This is manifested by longer C2C5 and C13C10 bonds and a shorter C5N9 bond and correlates with shorter O4H11 and O8H7 contacts. Much more significant changes occur in the intermediate moiety and the α-pyrone ring of the coumarin moiety.

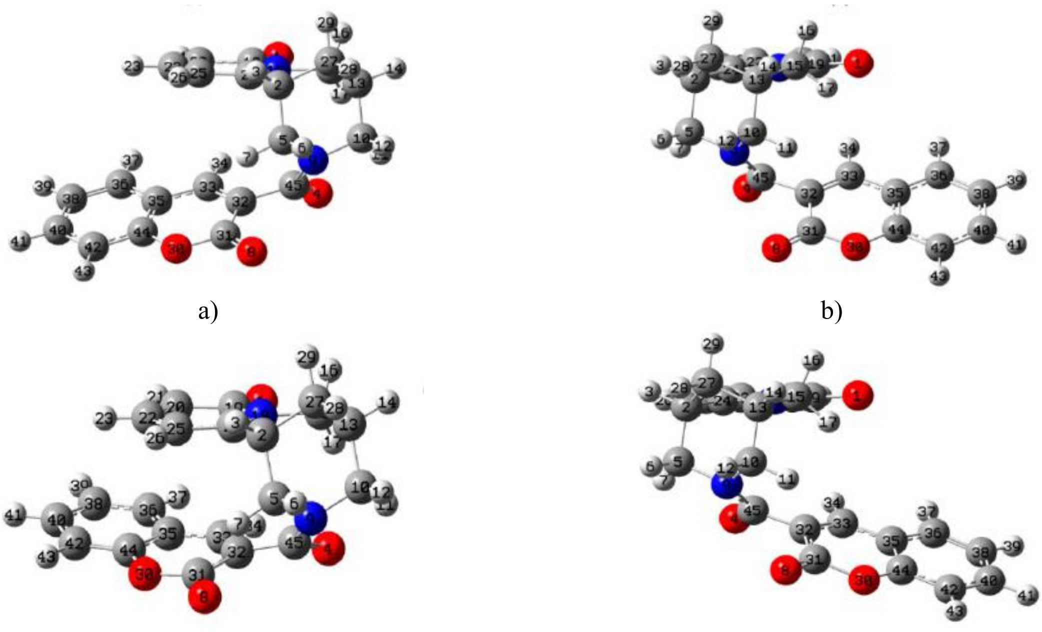

a) b)

c) d)

Fig.1. Optimized geometries of S_0-1 (a), S_0-2 (b), S_1-1 (c), and S_1-2 (d) using the wb97XD/6-31G(d,p) method for the case of a single molecule in an ethanol medium, which is taken into account within the framework of the polarizable continuum model.

Table 1. Selected structural parameters for conformers 1 and 2 in ground (S_0) and excited (S_1) states.

Parameter*	Conformer and state			
	S_0-1	S_1-1	S_0-2	S_1-2
C2C5	1.545	1.559	1.546	1.547
C13C10	1.536	1.543	1.536	1.536
C5N9	1.456	1.447	1.456	1.457
C10N9	1.460	1.461	1.458	1.459
N9C45	1.360	1.394	1.358	1.359
C45O4	1.228	1.237	1.227	1.238
C45C32	1.505	1.474	1.507	1.480
C32C31	1.462	1.418	1.462	1.425
C31O8	1.211	1.229	1.211	1.219
C32C33	1.350	1.429	1.349	1.429
C31O30	1.368	1.398	1.367	1.414
O30C44	1.365	1.370	1.366	1.345
C33C35	1.436	1.400	1.438	1.391
O4H11 (O4H7)**	2.292	2.198	2.299	2.286
O8H7 (O8H11)**	2.262	2.031	2.960	2.505
C10N9C45	119.06	116.04	124.71	123.93
C9N45O4	123.04	118.44	123.39	122.55
C45C32C31	120.48	126.44	117.93	121.28
C32C31O8	125.59	128.97	125.19	128.45
C10N9C45O4	5.92	19.14	-168.70	-161.21
N9C45C32C31	-62.26	-44.93	74.58	55.24
C45C32C31O30	-178.93	172.54	175.01	173.40
C32C31O30C44	-1.03	-2.61	1.65	3.86
C33C32C31O30	-2.78	-9.96	-0.25	4.01
C44C35C33C32	-2.68	-6.09	1.99	6.61

* for two atoms, the bond length is given in Å, for three atoms, the planar angle is given in degrees (°), for four atoms, the dihedral angle is given in degrees (°).

** in some cases, similar structural parameters for S0-2 and S1-2 are given in brackets.

A rotation of the coumarin moiety's ring plane relative to the cytisine moiety's ring plane takes place due to the flexible intermediate moiety. In the S_1-1 state, a more negative charge is observed on the N9 and O4 atoms, which correlates with the longer C45N9 and C45O4 bonds and with an increase in the C10N9C45O4 dihedral angle. At the same time, a rotation of the coumarin moiety leads to a decrease in the O8H7 contact length. This is manifested by the larger absolute value of the dihedral angle N9C45C32C31. For the S_1-1 state, a greater deviation of the α-pyrone ring from planar geometry is observed. This is manifested by a greater deviation of the dihedral angles C45C32C31O30, C32C31O30C44, C33C32C31O30, and C44C35C33C32 from 180° or 0° in S_1-1. This ring contains longer oxygen-carbon bonds (C44-O30, O30-C31, and C31=O8).

When comparing the optimized geometries of S_0-2 and S_1-2, a number of the following features can be noted. In the cytisine moiety, similar structural parameters are observed between S_0-2 and S_1-2, in contrast to S_0-1 and S_1-1. The C45C32 and C45O4 bonds are shorter in S_1-2 compared to S_0-2 while the C45N9 bonds are approximately the same. Just as in S_1-1, S_1-2 has a longer C32C33 bond and a shorter C32C31 bond compared to similar bond lengths in the ground state. In addition, S_1-2 also exhibits a greater deviation from the planar character of the α-pyrone ring in the coumarin moiety. A significant difference of S_1-2 is the longer hydrogen contacts O4H7 and O8H11, which is also manifested in a smaller value of the dihedral angle N9C45C32C31.

3.2 Electronic properties

For the optimized S_1-1 and S_1-2 states, the vertical transition energies and corresponding oscillator strengths were calculated. The longest-wavelength transition is to the ground state, i.e., $S_1\text{-}1 \rightarrow S_0\text{-}1$ and $S_1\text{-}2 \rightarrow S_0\text{-}2$, which is of practical interest in studying luminescence properties.

For the molecule the investigation of molecular orbitals plays the important role in understanding the electronic processes [22]. For S_1-1, the shortest-wavelength transition is the singlet-singlet transition between the 95 → 96 molecular orbitals (the orbital contribution is 98%, see Figure 2a). Its energy difference is 2.9109 eV, which corresponds to a wavelength of 425.93 nm, the oscillator strength is moderate, 0.0769.

For S_1-2, the shortest-wavelength transition is between the 94 → 96 orbitals (the orbital contribution is 96%). Its energy difference is significantly higher, 3.5964 eV, which corresponds to a wavelength of 344.74 nm, and the oscillator strength is 0.509. It should be noted that for S_1-1, a similar higher-energy transition between the same orbitals is also observed (94 → 96, the orbital contribution is 92%). However, its energy difference is significantly higher than 3.7607 eV, corresponding to a wavelength of 329.68 nm, and the oscillator strength is less than 0.3347. As part of this study, an experimental investigation of the luminescence properties of the complex was also conducted. Figure 3 shows the luminescence emission spectrum, which has a maximum at 453 nm (2.7373 eV). The luminescence excitation spectrum for this band was then obtained. The maximum in this spectrum is at 372 nm.

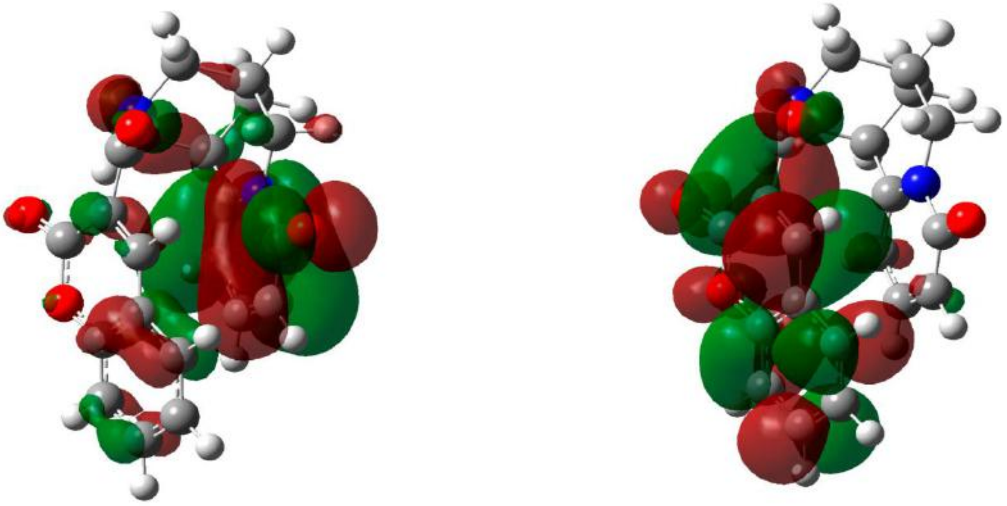

a) b)

Fig.2. View of the 95(HOMO) and 96(LUMO) molecular orbitals for S_1-1.

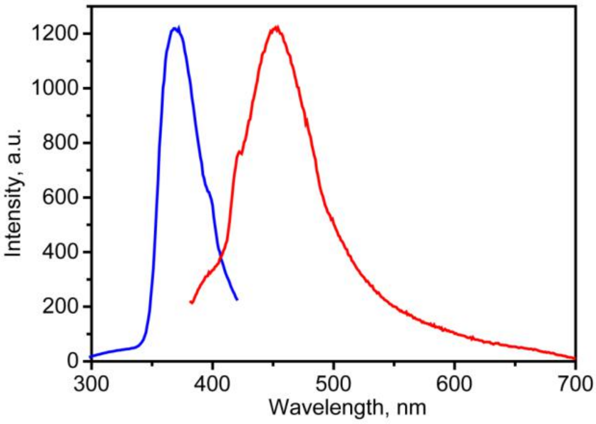

Fig.3. Luminescence emission spectrum at 453 nm (red) and luminescence excitation spectrum at 372 nm (blue).

The obtained theoretical estimates of the wavelength of the singlet-singlet transition from S_1-1 for conformational state 1 show a calculated value (426 nm) quite close to the experimentally observed luminescence maximum (453 nm). Based on this theoretically calculated transition, the radiative (luminescence) rate constant $\mathbf{k_r}$ was estimated according to the Strickler–Berg formula (1), [23]:

$$k_{r,i}\,(S_i \rightarrow S_0) = 2^{-i/2} f(S_i \rightarrow S_0) E^2 (S_i \rightarrow S_0)\,, \tag{1}$$

where *i* is the excited state number, $f(S_i\text{->}S_0)$ is the transition oscillator strength, $E(S_i \rightarrow S_0)$ is the electron transition energy (in cm^{-1}). For the case under consideration (*i*=1) the corresponding value $k_r=3 \cdot 10^7$.

The considered case of molecules corresponds to the case of addition of the intermediate part at atom 3 according to the IUPAC numbering of carbon atoms in the molecule of unsubstituted coumarin [24]. As an example of synthesized compounds with addition through the 3rd atom in the coumarin part, one can cite [25-27]. In these studies, it was noticed the presence of the strong luminescence in the experimental spectrum in the close region 460-480 nm. Nevertheless, it should be noted that the actual emission wavelength is quite sensitive to the structural peculiarities of the molecule as well as pH value or metal cation presence.

4. Conclusion

In this work, density functional theory methods were used to search for and optimize the geometry of the first excited state for two conformations of the N-(2-oxo-2H-chromen-3-carbonyl) cytisine molecule in an ethanol solution. Their energies were calculated. It was found that the first excited state of the conformer corresponding to the crystal structure is the most stable. A structural difference between the ground and first excited states was revealed. The wavelength of the transition from the first excited state to the ground state was calculated. The theoretical estimate of the luminescence maximum in the spectrum of the most stable conformer was 426 nm versus the value of 453 nm established experimentally. In addition, the radiation rate constant $k_r = 3 \cdot 10^7$ was estimated. An interpretation of this electronic transition is proposed based on an analysis of the molecular orbitals involved.

Conflict of interest statement

The authors declare that they have no conflict of interest in relation to this research, whether financial, personal, authorship or otherwise, that could affect the research and its results presented in this paper.

CRediT author statement

Turdybekov D.M.: Validation, Formal Analysis, Visualization, Supervision, Writing – Review & Editing; **Ibrayev N.Kh.:** Conceptualization, Investigation, Resources, Data Curation; **Kopbalina K.B.:** Conceptualization, Methodology, Software, Formal Analysis, Data Curation, Writing – Original Draft; **Kishkentayeva A.S.:** Validation, Investigation, Writing – Original Draft, Writing – Review & Editing;

Pankin D.V.: Conceptualization, Methodology, Software, Formal Analysis, Data Curation, Writing – Original Draft; **Smirnov M.B.:** Methodology, Software, Writing – Review & Editing.
The final manuscript was read and approved by all authors.

Funding

This work was supported by the Science Committee of the Ministry of Science and Higher Education of the Republic of Kazakhstan (grant "Spatial structure and stereochemistry of derivatives of quinolizidine alkaloids and guaiane sesquiterpenoids", IRN AP23487966).

Acknowledgements

The authors express their gratitude to the Research Park of St. Petersburg State University (Project No. 125021702335-5)

References

1. Tian G., Zhang Z., Li H., Li D., Wang X., Qin C. (2020) Design, Synthesis and Application in Analytical Chemistry of Photo-Sensitive Probes Based on Coumarin. *Critical Reviews in Analytical Chemistry*, 51, 565–581. https://doi.org/10.1080/10408347.2020.1753163
2. Wang L., Li W., Zhi W., Ye D., Wang Y., Ni L., Bao X. (2017) A Rapid-Responsive Fluorescent Probe Based on Coumarin for Selective Sensing of Sulfite in Aqueous Solution and Its Bioimaging by Turn-on Fluorescence Signal. *Dyes and Pigments*, 147, 357–363. https://doi.org/10.1016/j.dyepig.2017.07.021
3. Li J., Zhang C.-F., Yang S.-H., Yang W.-C., Yang G.-F. (2014) A Coumarin-Based Fluorescent Probe for Selective and Sensitive Detection of Thiophenols and Its Application. *Analytical Chemistry*, 86, 3037–3042. https://doi.org/10.1021/ac403885n
4. Ray D., Bharadwaj P.K. (2008) A Coumarin-Derived Fluorescence Probe Selective for Magnesium. *Inorganic Chemistry*, 47, 2252–2254. https://doi.org/10.1021/ic702388z
5. Kenchappa R., Bodke Y.D., Chandrashekar A., Aruna Sindhe M., Peethambar S.K. (2017) Synthesis of Coumarin Derivatives Containing Pyrazole and Indenone Rings as Potent Antioxidant and Antihyperglycemic Agents. *Arabian Journal of Chemistry*, 10, S3895–S3906. https://doi.org/10.1016/j.arabjc.2014.05.029
6. Annunziata F., Pinna C., Dallavalle S., Tamborini L., Pinto A. (2020) An Overview of Coumarin as a Versatile and Readily Accessible Scaffold with Broad-Ranging Biological Activities. *International Journal of Molecular Sciences*, 21, 4618. https://doi.org/10.3390/ijms21134618
7. Alam M., Alam M.J., Azaz S., Parveen M., Park S., Ahmad S. (2018) DFT/TD-DFT Calculations, Spectroscopic Characterizations (FTIR, NMR, UV–Vis), Molecular Docking and Enzyme Inhibition Study of 7-Benzoyloxycoumarin. *Computational Biology and Chemistry*, 73, 65–78. https://doi.org/10.1016/j.compbiolchem.2018.01.007
8. Srikrishna D., Godugu C., Dubey P.K. (2018) A Review on Pharmacological Properties of Coumarins. *Mini-Reviews in Medicinal Chemistry*, 18, 113–141. https://doi.org/10.2174/1389557516666160801094919
9. Przybył A.K., Maj E., Wietrzyk J., Kubicki M. (2019) Spectroscopic, Structural and Anticancer Activity Studies of (−)-Cytisine Halogenated N-Benzyl Derivatives. *Journal of Molecular Structure*, 1176, 871–880. https://doi.org/10.1016/j.molstruc.2018.09.029
10. Pankin D. (2021) Laser-Induced Twisting of Phosphorus Functionalized Thiazolotriazole as a Way of Cholinesterase Activity Change. *Spectrochimica Acta Part A: Molecular and Biomolecular Spectroscopy*, 246, 118979. https://doi.org/10.1016/j.saa.2020.118979
11. Kopbalina K.B., Makhmutova A.S., Turdybekov D.M., Turdybekov K.M., Tolenova G.K. (2025) Quantum-Chemical Study of the Structure and Properties of Molecule of the Lupinine Alkaloid Derivative. *Bulletin of the Karaganda University. Physics Series*, 105(1), 14–22. https://doi.org/10.31489/2023No4/33-38
12. He L., Xu Q., Liu Y., Wei H., Tang Y., Lin W. (2015) Coumarin-Based Turn-On Fluorescence Probe for Specific Detection of Glutathione over Cysteine and Homocysteine. *ACS Applied Materials & Interfaces*, 7, 12809–12813. https://doi.org/10.1021/acsami.5b01934
13. Kishkentayeva A., Kopbalina K., Shaimerdenova Z., Shults E., Gatilov Y., Pankin D., Smirnov M., Povolotckaia A., Turdybekov D., Mazhenov N. (2025) Investigation of N-(2-oxo-2H-chromen-3-carbonyl)cytisine's Crystal Structure and Optical Properties. *Materials*, 18, 3153. https://doi.org/10.3390/ma18133153
14. Kopbalina K., Adekenova A., Shaimerdenova Zh., Kairatova Zh., Shakarimova K., Pankin D., Smirnov M., Kishkentayeva A., Artykbayeva M., Jalmakhanbetova R. (2025) Investigation of N-(2-oxo-2H-chromen-3-carbonyl)cytisine's Molecular Structure in Solution. *Molecules*, 30(20), 4139. https://doi.org/10.3390/molecules30204139

15. Gawad S.A.A., Sakr M.A.S. (2022) Spectroscopic Investigation, DFT and TD-DFT Calculations of 7-(Diethylamino) Coumarin (C466) *J. Mol. Struct.* 1248, 131413. https://doi.org/10.1016/j.molstruc.2021.131413

16. Tian G., Zhang Z., Li H., Li D., Wang X., Qin C. (2020) Design, Synthesis and Application in Analytical Chemistry of Photo-Sensitive Probes Based on Coumarin. *Crit. Rev. Anal. Chem.* 51, 565–581. https://doi.org/10.1080/10408347.2020.1753163

17. Chai J., Head-Gordon M. (2008) Long-Range Corrected Hybrid Density Functionals with Damped Atom–Atom Dispersion Corrections. *Physical Chemistry Chemical Physics*, 10, 6615–6620. https://doi.org/10.1039/b810189b

18. Ditchfield R., Hehre W.J., Pople J.A. (1971) Self-Consistent Molecular Orbital Methods. 9. Extended Gaussian-Type Basis for Molecular-Orbital Studies of Organic Molecules. *Journal of Chemical Physics*, 54, 724. https://doi.org/10.1063/1.1674902

19. Hehre W.J., Ditchfield R., Pople J.A. (1972) Self-Consistent Molecular Orbital Methods. XII. Further Extensions of Gaussian-Type Basis Sets for Use in Molecular-Orbital Studies of Organic Molecules. *Journal of Chemical Physics*, 56, 2257. https://doi.org//10.1063/1.1677527

20. Frisch M.J., Trucks G.W., Schlegel H.B., Scuseria G.E., Robb M.A., Cheeseman J.R., Scalmani G., Barone V., Mennucci B., Petersson G.A., et al. (2013) *Gaussian 09, Revision D.01.* Gaussian, Inc., Wallingford CT. Available at: https://www.scirp.org/reference/referencespapers?referenceid=2418053

21. Tomasi J., Mennucci B., Cammi R. (2005) Quantum Mechanical Continuum Solvation Models. *Chemical Reviews*, 105, 2999–3093. https://doi.org/10.1021/cr9904009

22. Kopbalina K.B., Makhmutova A.S., Turdybekov D.M., Turdybekov K.M., Tolenova G.K. (2024) Quantum-Chemical Study of the Structure and Properties of Molecule of the Lupinine Alkaloid Derivative. *Eurasian Physical Technical Journal,* 4(46), 33-38. https://doi.org/10.31489/2023No4/33-38

23. Ibrayev N.Kh., Valiev R.R., Seliverstova E.V., Menshova E.P., Nasibullin R.T., Sundholm D. (2024) Molecular phosphorescence enhancement by the plasmon field of metal nanoparticles. *Physical Chemistry Chemical Physics*, 26, 14624-1436. https://doi.org/10.1039/d4cp01281j

24. Sun X.Y., Liu T., Sun J., Wang X.J. (2020). Synthesis and application of coumarin fluorescence probes. *RSC advances*, 10(18), 10826-10847. https://doi.org/10.1039/C9RA10290F

25. Xu Y., Jiang Z., Xiao Y., Bi F.Z., Miao J.Y., Zhao B.X. (2014). A new fluorescent pH probe for extremely acidic conditions. *Analytica chimica acta*, 820, 146-151. https://doi.org/10.1016/j.aca.2014.02.029

26. Chen Y., Clouthier C.M., Tsao K., Strmiskova M., Lachance H., Keillor J.W. (2014). Coumarin-Based Fluorogenic Probes for No-Wash Protein Labeling, *Angew. Chem. Int. Ed.*, 53, 13785–13788. https://doi.org/10.1002/anie.201408015

27. You Q.H., Lee A.W.M., Chan W.H., Zhu X.M., Leung K.C.F. (2014). A coumarin-based fluorescent probe for recognition of Cu 2+ and fast detection of histidine in hard-to-transfect cells by a sensing ensemble approach. *Chemical Communications*, 50(47), 6207-6210. https://doi.org/10.1039/C4CC00521J

AUTHORS' INFORMATION

Turdybekov, Dastan — Candidate of chemical sciences, Head of the Department of Physics, Abylkas Saginov Karaganda Technical University, Karaganda, Kazakhstan; https://orcid.org/0000-0002-0245-022X; turdas@mail.ru

Ibrayev, Niyazbek - Doctor of Physical and Mathematical Sciences, Professor, Buketov Karaganda National Research University, Karaganda, Kazakhstan; https://orcid.org/0000-0002-5156-5015; niazibraev@mail.ru

Kopbalina, Kymbat – PhD, Senior Researcher, Department of Physics and nanotechnology, Buketov Karaganda National Research University, Karaganda, Kazakhstan; https://orcid.org/0000-0001-6378-9756; kopbalinakymbat@mail.ru

Kishkentayeva, Anarkul – PhD, Senior Researcher, Karaganda Medical University, Karaganda, Kazakhstan; https://orcid.org/0000-0002-0194-8739; anar_kish@mail.ru

Pankin, Dmitrii - Candidate of Science in Physics and Mathematics, Professor, St. Petersburg State University, St. Petersburg, Russia; https://orcid.org/0000-0003-3114-3410; dmitrii.pankin@spbu.ru

Smirnov, Mikhail - Doctor of Physical and Mathematical Sciences, Professor, St. Petersburg State University, St. Petersburg, Russia; https://orcid.org/0000-0002-4292-1989; m.smirnov@spbu.ru

EURASIAN PHYSICAL TECHNICAL JOURNAL

2025, Volume 22, No.4 (54)

https://doi.org/10.31489/2025N4/46-52

Received: 07/08/2025 Revised: 30/10/2025 Accepted: 25/12/2025

Original Research Article

UDC 536.8:662.99

STUDYING CHARACTERISTICS OF THE HEAT PIPE OF A LOW-PRESSURE STEAM ELECTRIC HEATER WITH DIFFERENT TYPES OF HEATERS

Buzyakov R.R.*, Mekhtiyev A.D., Neshina Ye.G., Alkina A.D., Bilichenko A.P.

Abylkas Saginov Karaganda Technical University NJSC, Karaganda, Kazakhstan
r.buzyakov@gmail.com

Abstract. *The article deals with developing and analyzing a heat pipe of a low-pressure steam electric heater intended for autonomous heating systems. The object of the study is two types of heating elements: a tubular electric heater with a nichrome spiral and an induction heater. Experimental analysis methods have been used to evaluate the heating characteristics, the temperature distribution and the energy efficiency. It has been established that the induction heater provides a higher heating rate and uniform temperature distribution, while the tubular heater is characterized by stable operation and economy. The obtained results allow proposing the ways to optimize the design of the electric heater to increase its efficiency and reliability. The findings confirm the practical potential of using the devices under study in various types of heating systems.*

Keywords: steam electric heater, heat pipe, energy efficiency, nichrome coil, induction heater, autonomous heating, low pressure.

1. Introduction

Low-pressure steam electric heaters (LPSEH) are one of the promising technologies for autonomous heat supply. Their use is relevant in the context of the need to reduce energy consumption, to transit to environmentally friendly heat sources and to increase reliability of engineering systems in remote or energy-independent facilities. These devices combine high energy efficiency, environmental friendliness and ease of use, and their operation is based on the principle of a heat pipe, a device in which at reduced pressure a phase transition of the coolant occurs: evaporation and subsequent condensation. This process ensures intense heat transfer with minimal energy costs.

Present day developments in the field of heat pipes cover a wide range of issues: selecting design solutions, selecting coolants and the intensifying heat transfer. A generalized review of these areas is presented in work [1], where design varieties and new technical approaches are considered. High thermal conductivity, resistance to temperature fluctuations and operational reliability allow considering heat pipes as the basis for energy-efficient systems, which is emphasized by the authors of studies [2] and [3], who have proposed a design with a simplified evaporator that maintains stable performance with variable power supply. The key advantage of heat pipes, according to work [4], is the capillary liquid circulation without the use of pumps, which makes such systems energy-independent and durable. The authors of work [5] confirm the efficiency of heat pipes when used with low-potential heat sources, demonstrating a fast thermal response and high energy output compared to traditional water heating systems. Work [6] emphasizes low thermal resistance and versatility of heat pipes when working in vacuum and with low-temperature flows.

Similar approaches are actively used in solar energy. Work [7] considers solar water heaters in which heat pipes can significantly increase thermal efficiency and reliability due to phase transitions and operation at reduced pressure. In the context of increasing requirements for energy efficiency and sustainability of energy supply, the LPSEH is becoming a logical alternative to traditional systems. Due to the possibility of autonomous operation without pumping equipment and an extensive pipeline network, they are especially in demand in regions with a harsh climate. The approach to sustainable heat supply is in particular implemented in study [8], where a dual heat source system has been developed that include heat pumps and energy storage devices, providing reliable heating at low operating costs.

This study continues and develops the scientific aspects outlined in works [9–12], where the design parameters of the LPSEH, the vacuum conditions, the weight and geometry of heat pipes, as well as the integration of new types of electric heaters have been analyzed. Based on the accumulated experimental material, the need for a comparative analysis of two types of heating elements: a tubular electric heater with a nichrome spiral and an induction heater used in the LPSEH has been identified. The tubular electric heater is characterized by a simple design, reliability and affordable cost, which makes it suitable for mass application. However, the limited uniformity of heat distribution reduces the overall efficiency of the system. In contrast, the induction heater uses eddy currents for fast and uniform heating which increases the performance of the device. However, its high cost and design complexity limit widespread implementation.

The purpose of this work is to carry out a comparative analysis of the thermal characteristics of the specified types of heaters, to evaluate their impact on the LPSEH efficiency, and to identify the most rational engineering solutions for increasing reliability and energy efficiency of autonomous heating systems.

2. Experiment description

The aim of this study is a comparative analysis of the efficiency of two types of heating elements used in the design of LPSEH vacuum electric heaters. The experiment assessed the effect of the heater type on the rate of thermal response, the temperature distribution along the tube, the energy efficiency of the system and its operational stability at different vacuum pressure levels.

Two heat pipes of identical design that differ only in the heating element used, have been assembled for the tests: the first one used a tubular electric heater with a nichrome spiral, and the second one used an induction heater. Both units operated at the same power of 120 W, which ensured the correctness of the comparative analysis of the operating characteristics. The design of the tubes included two sections of a copper pipe with the diameter of 22 mm and the length of 210 mm, hermetically sealed at the ends. The mass of each tube with the coolant filled was 230 g.

Distilled water with the volume of 15 ml has been used as the coolant. It has been selected due to its high purity and stability of thermophysical properties, eliminating the effect of impurities on the thermal process. Such a choice of liquid, as well as the assessment of its composition effect on the efficiency of heat transfer, have been considered in detail in a number of works, including the study by Barrak et al. [13], where the characteristics of single- and multi-component coolants, including binary mixtures, have been analyzed.

To provide the conditions for an effective phase transition, vacuum pressure in the range of 5–10 kPa (0.05–0.1 atm) has been maintained inside the tubes. Decreasing pressure leads to decreasing the boiling point of water, accelerates the onset of evaporation, and contributes to increasing the intensity of heat transfer. Such dependences between the vacuum level, the coolant flow modes, and the device orientation have been studied in detail in [14], where the optimal operating conditions for pulsating heat pipes have been determined.

The vacuum environment has been provided and stabilized using a DUO 6/M SERIES vane pump (Pfeiffer Vacuum) that is capable of achieving residual pressure of up to 10^{-3} mbar. This ensures reliable maintenance of the specified pressure range throughout the entire experimental cycle, which is critical for the results reproducibility.

The temperature parameters were recorded using digital thermometers Fluke 51 (USA) with a measurement error of ±0.05% + 0.3 °C and HT-9815 (China) with an accuracy of ±0.1%. The wide operating temperature range of the instruments (from –200 °C to +1372 °C) ensured reliable temperature registration under the experimental conditions. In the present study, temperature measurements were performed in the range from 20 °C to 250 °C, corresponding to the operating modes of the low-pressure steam electric heater.

To ensure the multi-point monitoring of thermal distribution along the length of the tube, contact thermocouples connected to the data collection system have been additionally used. This made it possible to record expected temperature non-uniformities, especially in the upper and lower parts of the tube. Both heat pipes have been connected to a single power source with nominal voltage of 220 V. The current power and total energy consumption have been measured using two digital multimeters (UNI-T and UT61B), as well as a JUANJUAN qt01 wattmeter with the error of ±2%.

These measurements allow calculating the efficiency coefficient (EC) that is used as the main criterion for comparative evaluation of the device efficiency. The parameter measurement diagram is shown in Figure 1. The diagram indicates the main components of the heater and displays the heat transfer processes: solid arrows indicate the upward movement of steam, and dotted arrows indicate the reverse flow of condensate downward.

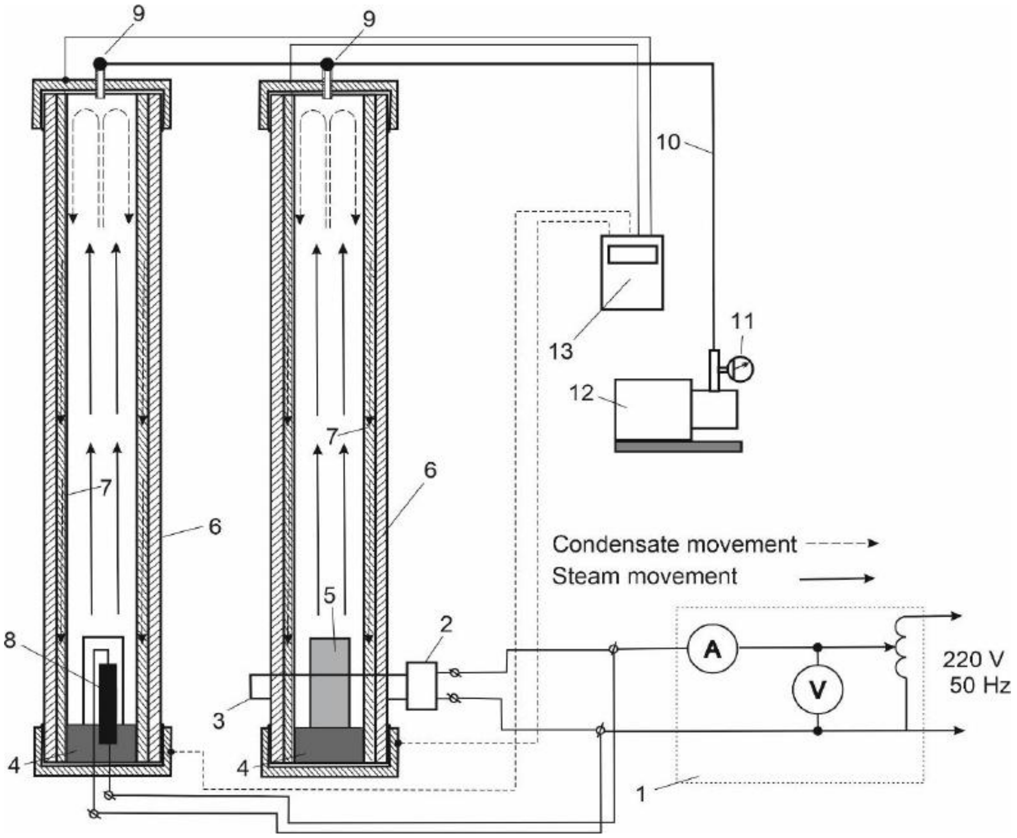

Fig.1. Diagram of measuring the heat electric vacuum tube parameters:
1 – measuring unit with autotransformer; 2 – mini ZVS Low Voltage Induction Heating Power Supply Module; 3 – inductor coil; 4 – coolant; 5 – steel core; 6 – housing of the heat pipe of the LPSEH electric vacuum heater; 7 – drainage porous channel of the regenerator; 8 – tubular electric heater; 9 – check valve for pumping air from the inner cavity of the tube; 10 – air pumping system pipeline; 11 – vacuum gauge; 12 – vacuum pump, 13 – counter.

The experiment has been carried out in the sequence that ensured stable and reproducible conditions. After evacuating the internal volume to pressure of 5–10 kPa, distilled water has been poured into the tube. The valve has been sealed, ensuring pressure stability. From the moment the voltage has been applied, the heating element has been heated either through a nichrome spiral or by inducing eddy currents in a metal core. As a result, the process of evaporation of the coolant has begun, the steam has risen to the upper part of the tube, where it has been condensed, giving off heat to the walls, and then has returned to the lower part as condensate through a drainage channel made of a metal wire structure. Thus, a closed cycle has been formed inside the tube, ensuring continuous and effective heat transfer due to the circulation of steam and liquid in different phase states. The initial operating temperature of the heater casing was reached in less than one minute after switching on, indicating a rapid onset of the heating process. Further temperature increase to higher operating levels occurred during continued heating, as reflected by the experimental temperature–time dependences. A comparative analysis of the thermodynamic characteristics of tubes with different types of heaters has made it possible to identify key differences in the energy output, the uniformity of the temperature field and the overall efficiency of the design.

3. Results and discussion

Experimental studies have shown significant differences in the heat transfer characteristics and energy performance of the two types of heating elements used in the LPSEH design. Based on the data obtained, the temperature dependences on the heater operating time have been plotted (Figure 2). The graph has been plotted and experimental data have been approximated using the Microsoft Excel analysis and visualization tools.

For a quantitative description of the experimental temperature dependences, semi-empirical approximating functions were used, reflecting the temperature rise as a function of heating time. The approximation was performed using third-order polynomial regressions obtained by the least-squares method:

$$T_1(t) = -0.3333t^3 - 4.7619t^2 + 94t - 66.143,$$

$$T_2(t) = -0.5t^3 + 3.2024t^2 + 34.06t - 11.857,$$

where $t$is the heating time, T_1 is the temperature of the induction heater, and T_2 is the temperature of the tubular electric heater. The argument $t$corresponds to the time coordinate (s) shown on the horizontal axis in Figure 2.

The coefficients of determination were R^2=0.9975 for the induction heater and R^2=0.9999 for the tubular heater, indicating a high degree of agreement between the approximating functions and the experimental data.

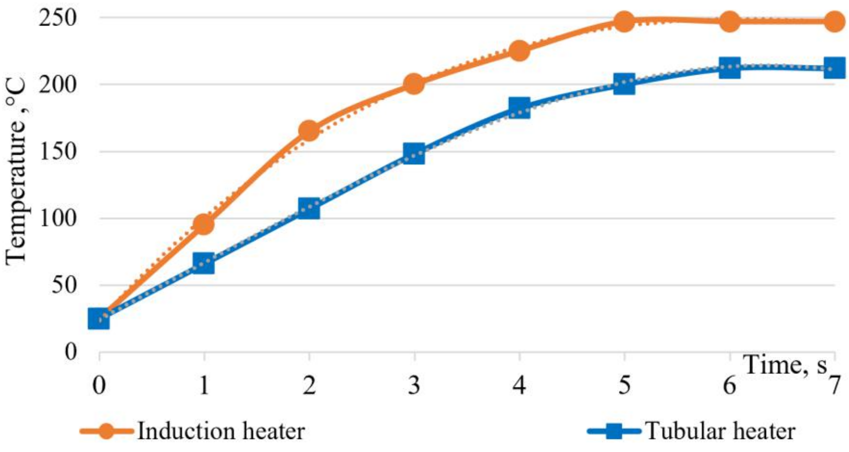

Fig.2. Temperature dependence on the operation time of heaters

The experimental curves were processed using regression analysis. The experimental data were approximated by third-order polynomial regression functions obtained using the least-squares method, which are shown in Figure 2. The high values of the determination coefficients indicate good agreement between the experimental data and the approximating functions. The high reproducibility of the experimental data and the consistency of the obtained temperature trends indicate the reliability of the results and the adequacy of the applied approximation approach.

The maximum temperature reached by the tube with a tubular electric heater has been 212 °C, while for the induction heater this figure has been 247 °C. In addition, the induction heater demonstrated a higher thermal response rate: the average time to reach the temperature of 200 °C has been 3 minutes versus 5 minutes for the tubular heater. This advantage can be explained by a higher heat flux density, characteristic of induction heating, as well as better uniformity of heat distribution along the length of the tube. The analysis of thermal profiles has shown that the induction heater provides a stable temperature field along the entire length of the heat pipe. In particular, a smaller temperature gradient is observed in the upper part of the tube compared to the tubular heater, where local fluctuations and reduced thermal stability have been observed. This indicates a more uniform heat transfer and less local overheating in the case of using the induction method.

The energy efficiency assessment revealed that the efficiency of the induction heater exceeds that of the tubular electric heater by an average of 15%. For a clear comparison of the operational and design features of the investigated heating elements, their main characteristics, summarized on the basis of experimental data and qualitative analysis of the test results, are presented in Table 1.

Table 1. Comparative characteristics of the investigated heating elements.

Characteristic	**Tubular electric heater**	**Induction heater**
Time to reach operating regime	Longer	Shorter
Maximum achieved temperature	Lower than induction	Higher than tubular
Temperature response	Less uniform	More uniform
Energy efficiency	Lower	Higher
Structural complexity	Low	Increased
Cost	Lower	Higher
Technological availability	High	Limited

The data presented in Table 1 clearly demonstrate that induction heating offers advantages in terms of heating rate, temperature uniformity and energy efficiency. These advantages are primarily explained by reduced heat losses due to more targeted energy transfer and the absence of mechanical contact between the heating element and the heated surface. The obtained results are consistent with previously published studies on induction heating systems [15], where high energy efficiency (up to 97.34%) and favorable power factor values (up to 0.81) have been reported for induction-based heaters, confirming the effectiveness of this heating method in high-energy-output applications.

Additional confirmation of the energy and thermal advantages of induction heating is given in [16], where more uniform temperature distribution and increasing of up to 25 °C have also been established compared to resistive elements with equal input power. Thus, experimental and literature data indicate the technological superiority of the induction heating method in the context of energy efficiency and thermal stability.

A comparison of the main operating characteristics of the two types of heaters allows highlighting a number of key differences. Firstly, induction heating provides a higher speed of reaching the target temperature, which makes it preferable for systems with limited warm-up time. Secondly, the temperature field along the tube during induction heating is more uniform, which increases the efficiency of heat transfer and reduces the risk of local overheating. Thirdly, the achieved energy efficiency of the induction element exceeds the resistive analogue by 10-15%, which makes it attractive for use in energy-saving installations.

Another important advantage is the reduced thermal gradient on the tube surface during induction heating, which reduces the risk of overheating and improves the operational safety of the device. However, it should be noted that induction heaters are characterized by greater design complexity, as well as a significantly higher cost, which limits their use in serial and low-cost heating systems.

Thus, the results of the experiment confirm the high efficiency of induction heating in the context of heat transfer, the uniformity of temperature distribution and the overall energy efficiency. These findings are consistent with the theoretical provisions and applied recommendations set out in [17], which summarizes the design principles of induction systems, including frequency parameters, coil configuration and thermal response of materials. Despite this, tubular heaters remain relevant due to their simple design, availability and reliability in operation. In conditions of a limited budget, as well as when mass production of devices is required, resistive elements remain an economically viable solution.

A promising area for further research is optimization of the induction heater design to reduce the cost, simplify the manufacturing technology and increase the technological reliability. The development of hybrid systems with a controlled type of heating can also be of interest for expanding the scope of LPSEH application in energy-efficient engineering systems.

4. Conclusion

The present study was devoted to a comparative analysis of the thermal behavior of a low-temperature steam electric heater employing tubular electric and induction heating elements under identical experimental conditions. The obtained experimental results demonstrated that the type of heating element has a significant influence on the temperature characteristics of the heat pipe and on the formation of the overall thermal regime.

The induction heater exhibited a higher heating rate, a higher maximum operating temperature, and a more uniform temperature distribution along the length of the heat pipe. In particular, the time required to reach the operating regime was shorter, and the temperature gradients along the tube were lower than those observed for the tubular electric heater. Moreover, the energy efficiency of the induction heater exceeded that of the tubular heater by an average of approximately 15%, which confirms its potential for application in energy-efficient autonomous heat supply systems. A comparison of the obtained experimental data with previously published studies [15–17] confirms the key advantages of induction heating under conditions requiring high heating rates, thermal stability, and uniformity of heat transfer.

At the same time, the tubular electric heater demonstrated stable and reproducible operation, adequate thermal performance, and structural simplicity. Its lower cost and high technological availability make this type of heater a practical and economically justified solution for mass production and for applications in which economic and technological constraints play a decisive role. Therefore, the selection of a heating element should be based not only on thermal and energy performance, but also on structural, technological, and economic considerations. Despite the clear operational advantages of induction heating systems, their increased structural complexity and higher cost currently limit their widespread industrial implementation.

The scientific novelty of this work lies in the experimental comparison of heating elements of different physical nature under vacuum heat pipe conditions, which made it possible to identify their key advantages and limitations. The practical significance of the obtained results is associated with the possibility of a well-founded selection of heating elements for specific operating conditions, as well as with the development of recommendations aimed at improving the energy efficiency of low-temperature steam electric heaters.

Further research should focus on optimizing induction heater designs in order to reduce cost, enhance manufacturability, and improve operational reliability. Particular interest is also associated with the development of hybrid heating systems and intelligent control strategies capable of adapting thermal characteristics to changing external conditions and energy efficiency requirements in modern autonomous heat supply systems.

Conflict of interest statement

The authors declare that they have no conflicts of interest in connection with this study, whether financial, personal, authorial or otherwise, that could influence the study and its results presented in this article.

CRediT author statement

Buzyakov R.R.: Conceptualization, Investigation, Formal analysis, Writing – original draft; **Mekhtiyev A.D.:** Methodology, Resources, Writing – review & editing; **Neshina Ye.G.:** Literature review, Theoretical analysis; **Alkina A.D.:** Visualization, Formal analysis; **Bilichenko A.P.:** Data curation, Investigation, Validation. The final version of the manuscript was read and approved by all authors.

Funding

This research is funded by the Science Committee of the Ministry of Education and Science of the Republic of Kazakhstan (Grant No. AP25795573).

References

1 Jose J., Hotta T. K. (2023) A comprehensive review of heat pipe: Its types, incorporation techniques, methods of analysis and applications. *Thermal Science and Engineering Progress, 42*, 101860. https://doi.org/10.1016/j.tsep.2023.101860

2 Jouhara H., Khordehgah N., Almahmoud S., Delpech B., Chauhan A., Tassou S.A. (2018) Waste heat recovery technologies and applications. *Thermal Science and Engineering Progress, 6*, 268–289. https://doi.org/10.1016/j.tsep.2018.04.017

3 Buffone C. (2014) Testing of a low-cost loop heat pipe design. *Journal of Electronics Cooling and Thermal Control, 4*(1), 33–38. https://doi.org/10.4236/jectc.2014.41004

4 Faghri A. (2014) Heat pipes: Review, opportunities and challenges. *Frontiers in Heat Pipes, 5*(1). https://doi.org/10.5098/fhp.5.1

5 Kerrigan K., Jouhara H., O'Donnell G. E., Robinson A.J. (2011) Heat pipe-based radiator for low grade geothermal energy conversion in domestic space heating. *Simulation Modelling Practice and Theory, 19*(4), 1154–1163. https://doi.org/10.1016/j.simpat.2010.05.020

6 Vasiliev L. L. (2005) Heat pipes in modern heat exchangers. *Applied Thermal Engineering, 25*(1), 1–19. https://doi.org/10.1016/j.applthermaleng.2003.12.004

7 Rahimi-Ahar Z., Khiadani M., Rahimi Ahar L., Shafieian A. (2023) Performance evaluation of single stand and hybrid solar water heaters: A comprehensive review. *Clean Technologies and Environmental Policy, 25*, 2157–2184. https://doi.org/10.1007/s10098-023-02556-6

8 Wang Y., Quan Z., Jing H., Wang L., Zhao Y. (2021) Performance and operation strategy optimization of a new dual-source building energy supply system with heat pumps and energy storage. *Energy Conversion and Management, 239*, 114204. https://doi.org/10.1016/j.enconman.2021.114204

9 Mekhtiyev A., Breido I., Buzyakov R., Neshina Y., Alkina A. (2021) Development of low-pressure electric steam heater. *Eastern-European Journal of Enterprise Technologies, 4*(8(112)), 34–44. https://doi.org/10.15587/1729-4061.2021.237873

10 Mekhtiyev A., Buzyakov R., Shapenova Z. (2022) Low-pressure steam electric heater. *Bulletin of Toraighyrov University, 3*(4(89)), 123–134. https://doi.org/10.48081/SYOY6805

11 Mekhtiyev A., Buzyakov R., Kim P., Alkina A. (2021) Research of parameters of an induction electric vacuum heater of a low-pressure steam electric heater. *Proceedings of the University, 3*(4(84)), 262–267. https://doi.org/10.52209/1609-1825_2021_3_262

12 Mekhtiyev A., Buzyakov R. (2023) A low-pressure steam electric heater as the basis of a new generation autonomous heating system. *The Bulletin of KazATC, 5*(128), 474–481. https://doi.org/10.52167/1609-1817-2023-128-5-474-481

13 Barrak A.S., Saleh A.A. M., Naji Z.H. (2019) An experimental study of using water, methanol, and binary fluids in oscillating heat pipe heat exchanger. *Engineering Science and Technology, an International Journal.* https://doi.org/10.1016/j.jestch.2019.05.010

14 Saha N., Das P.K., Sharma P.K. (2014) Influence of process variables on the hydrodynamics and performance of a single loop pulsating heat pipe. *International Journal of Heat and Mass Transfer, 74*, 238–250. https://doi.org/10.1016/j.ijheatmasstransfer.2014.02.067

15 Korepanov A., Lekomtsev P., Niyazov A. (2020) Energy characteristics of induction water heater. *IOP Conference Series: Earth and Environmental Science, 433*, 012035. https://doi.org/10.1088/1755-1315/433/1/012035

16 Szychta E., Szychta L. (2020) Comparative analysis of effectiveness of resistance and induction turnout heating. *Energies, 13*(20), 5262. https://doi.org/10.3390/en13205262

17 Rudnev V., Loveless D., Cook R. (2017) *Handbook of induction heating* (2nd ed.). CRC Press. https://doi.org/10.1201/9781315117485

AUTHORS' INFORMATION

Buzyakov, Rustam – Master, Head of the Commercialization Office, Abylkas Saginov Karaganda Technical University, Karaganda, Kazakhstan; Scopus Author ID: 57346800300; https://orcid.org/0000-0003-2514-5276; r.buzyakov@gmail.com

Mekhtiyev, Ali D. – Candidate of Technical Sciences, Professor, Vice-Rector for Research, Abylkas Saginov Karaganda Technical University, Karaganda, Kazakhstan; Scopus Author ID: 57219935782; https://orcid.org/0000-0002-2633-3976; barton.kz@mail.ru

Neshina, Ye. – Candidate of Technical Sciences, Head of the Department of Energy Systems, Abylkas Saginov Karaganda Technical University, Karaganda, Kazakhstan; Scopus Author ID: 57191724446; https://orcid.org/0000-0002-8973-2958; 1_neg@mail.ru

Alkina, A. – Candidate of Technical Sciences, Senior Lecturer at the Department of Energy Systems, Abylkas Saginov Karaganda Technical University, Karaganda, Kazakhstan; Scopus Author ID: 57160184600; https://orcid.org/0000-0003-4879-0593; alika_1308@mail.ru

Bilichenko, Arkadi – Master, Senior Lecturer at the Department of Energy Systems, Abylkas Saginov Karaganda Technical University, Karaganda, Kazakhstan; Scopus Author ID: 57215327718, https://orcid.org/0000-0002-2132-7016; arkanbili@gmail.com

EURASIAN PHYSICAL TECHNICAL JOURNAL

2025, Volume 22, No.4 (54)

https://doi.org/10.31489/2025N4/53-62

Received: 12/06/2025 Revised: 29/10/2025 Accepted: 25/12/2025

Original Research Article

UDC 536.46:519.63:621.452:004.8

NEURAL NETWORK ACCELERATION OF NUMERICAL SIMULATION OF METHANE COMBUSTION IN A GAS TURBINE ENGINE

Chepurnyi A.V.*, Jakovics A.

Institute of Numerical Modelling, University of Latvia, Riga, Latvia
**Corresponding author*: vasfed12345@gmail.com/

Abstract. *Gas turbines are essential for high-power energy generation, but growing demands to reduce NO_x and CO_2 emissions make traditional combustion chamber design increasingly complex and costly. This work proposes a new modeling paradigm that combines high-fidelity Computational Fluid Dynamics using neural network learning to accelerate emission prediction. A Computational Fluid Dynamics model was developed using the Reynolds-averaged Navier-Stokes equations with the k–ε turbulence model and a non-premixed Probability Density Function approach to simulate turbulent methane combustion. NO_x emissions were calculated post-simulation using the Zeldovich mechanism. Model validation included varying fuel flow, excess air ratio, and wall heat loss. To speed up evaluations, a multilayer perceptron neural network was trained on Computational Fluid Dynamics results to predict NO_x and CO_2 emissions based on key inputs (fuel rate, air excess, temperature, pressure, cooling). The model achieved high accuracy with a coefficient of determination (R^2) of 0.998 for NO_x and 0.956 for CO_2 on an independent test set. Results showed good agreement with both experimental data and a Network of ideal reactors model using detailed kinetic scheme of methane combustion - Mech 3.0. This neural network serves as a fast surrogate model for emissions assessment, enabling rapid optimization of low-emission combustor designs. The approach is suitable for digital twins and combustion control systems and is adaptable to alternative fuels like hydrogen and ammonia.*

Keywords: neural network, combustion, gas turbine engine, numerical simulation.

Abbreviations:

PDF - Probability Density Function (in context - the estimated PDF of the mixture)
RANS - Reynolds-averaged Navier-Stokes equations
RNG k–ε - Turbulent k–ε model with group renormalization
CRN - Network of ideal reactors (method of calculating chemical kinetics)
GRI-Mech 3.0 - Detailed kinetic scheme of methane combustion
MLP - Multilayer Perceptron
ANN - Artificial neural network
PCA - Principal Component Analysis
POD - Method of eigen orthogonal functions
RBF - Radial basis function / radial basis neural network
LES - Large Eddy Simulation
RSM - Reynolds stress model
P1 - Radiation model P1 (first approximation)
SIMPLE - Semi-explicit method for pressure-velocity relationship
MPC - Model-based control (predictive)
CPU - Central Processing Unit
GTE - Gas Turbine Engine
PINN - Physically-informed neural network
CNN - Convolutional Neural Network

1. Introduction

Gas turbine engines (Fig. 1) are widely used in power engineering and aviation, but increasingly stringent NOx and CO_2 regulations require combustion chambers that operate reliably at high pressures and temperatures while producing minimal emissions. The full development cycle of such chambers traditionally relies on expensive experimental stands and resource-intensive Computational Fluid Dynamics (CFD) calculations: modeling turbulent combustion with detailed chemistry takes hours to days, which significantly slows down development. Machine learning, in particular neural networks, offers a way out: a neural network trained on a set of CFD and experimental data instantly predicts flame temperature, product composition, and emission levels. This opens the way to rapid mode selection, optimization, and reduction of design costs.

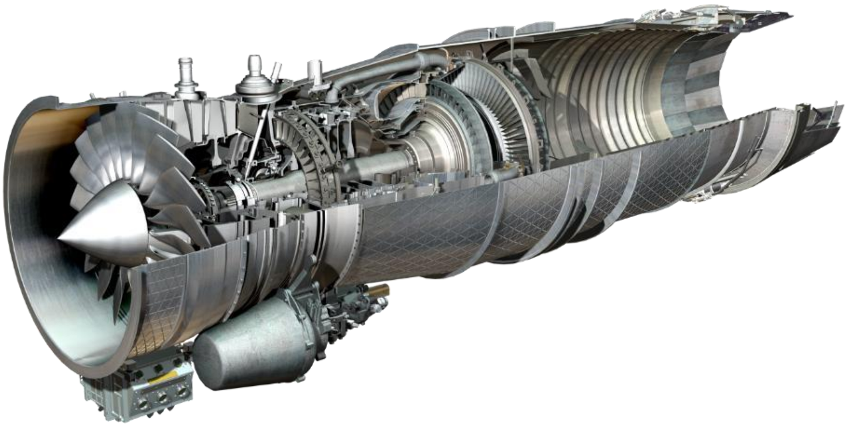

Fig.1. The gas turbine engine - Eurojet EJ200 is a low-bypass turbofan used as the powerplant of the Eurofighter Typhoon (image taken from the official manufacturer's website [https://www.eurojet.de/innovation/])

The aim of the work is to show that a multilayer perceptron trained on a sample of CFD models of methane flame provides engineering-acceptable accuracy of NOx/CO_2 prediction at a computational cost an order of magnitude lower than classical CFD, thereby radically accelerating the process of developing combustion chambers for gas turbine engines.

In recent years, interest in combustion and emissions has increasingly led to the use of neural networks [1]. Wang and Yang showed that such models predict NOx formation significantly more accurately [2, 3]. Earlier work already demonstrated the usefulness of artificial neural networks (ANN) for describing combustion processes [4]. Thus, in [5], a single-layer network predicted NOx emissions, vibrations, and pressure fluctuations based on the operating parameters of a gas turbine engine. Lamont et al. confirmed that ANNs provide accurate estimates of NOx, CO, and chamber outlet temperature with metered fuel supply [6].

“Fast” simplified models are also being developed. Wang et al. created a compact neural network that replaces complex calculations of turbulent combustion and preserves the flow shape with good accuracy [7]. Aversano and colleagues combined principal component analysis and kriging interpolation, constructing a “digital twin” of a burner for a fast parametric study. Similarly, the eigenfunction method in conjunction with the radial basis network made it possible to speed up calculations of a large furnace several times with an acceptable error [8]. For a direct emission forecast, Sun et al. used an RBF network: the maximum errors were $\approx$ 12% for NOx and $\approx$ 3% for CO, the average errors were $<$ 5% and 1%, respectively [9]. The hybrid approach “CFD + network of simple reactors” turned out to be promising. It takes the flow field from CFD and calculates the chemistry in a network of elementary reactors, reducing the NOx discrepancy to $\approx$ 5% (versus 10–20% for pure CFD) [10]. Such a mechanism is implemented, for example, in the ENERGICO energy package, where the CHEMKIN module provides an accuracy of $<$ 5% and reduces the calculation time from weeks to days [11]. Experience shows that neural networks and their combination with classical calculations effectively approximate complex interrelations in combustion and help reduce emissions [12].

In this paper, this approach is developed: detailed CFD modeling is used to train an MLP network that forms an “express model” of methane combustion chamber emissions.

The object of the study is the turbulent non-premix flame of a methane-air mixture in the combustion chamber (Fig. 2) of a gas turbine engine. A steady-state combustion mode is considered: methane (CH_4) is fed through a burnr, mixed with an oxidizer (air) and burns in the chamber. The main reaction during complete combustion is:

$$CH_4 + 2O_2 \rightarrow CO_2 + 2H_2O$$

with the release of heat.

However, in real conditions the flame is turbulent and some of the fuel may not burn completely (CO is formed), and at high temperatures nitrogen oxides are generated from atmospheric nitrogen (thermal NOx by the Zeldovich mechanism). To adequately describe the process, it is necessary to solve a system of coupled equations of gas flow and heat/mass transfer taking into account chemical kinetics.

The gas flow was described by the system of Reynolds-averaged Navier-Stokes (RANS) equations for conservation of mass, momentum, energy, and species transport. The flow was assumed to be steady, turbulent, and chemically reacting.

These equations track how the composition of the gas mixture changes as a result of convection, diffusion, and reactions. For turbulent combustion, a direct solution of a detailed kinetic scheme (including dozens of reactions and intermediate radicals) in conjunction with the Navier–Stokes equations are practically unrealizable due to the enormous computational complexity. Therefore, turbulent combustion models are used that simplify the description of chemistry while preserving the main effects. In this paper, a non-premix combustion approach is used using a variable mixture fraction and the assumption of fast combustion. A scalar value Z is introduced – the fractional content of fuel (mixture) in the gas. The value $Z = 0$ corresponds to a pure oxidizer, $Z = 1$ – to pure fuel. It is assumed that turbulent mixing occurs much slower than the chemical reaction (fast chemical reaction mode), therefore, at each point, chemical equilibrium is established instantly based on the local Z and the mixture formation parameter (for example, enthalpy). Thus, the concentration fields of products (CO_2, H_2O), residual O_2 and main pollutants are calculated assuming local chemical equilibrium at given Z. Turbulent fluctuations of Z are taken into account by means of the assumed PDF (probability density function, Fig. 3) model [13].

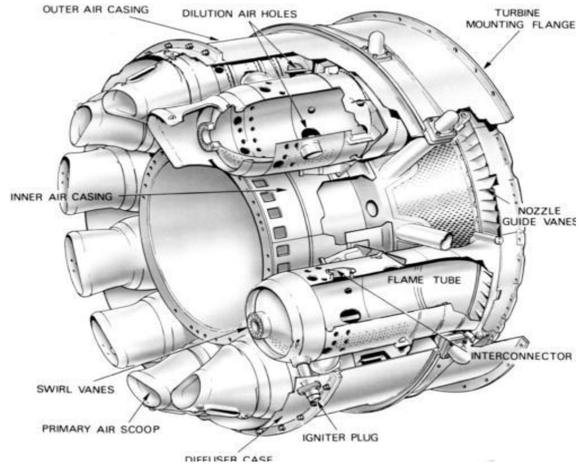

Fig.2. Tubo-annular combustion chamber (Rolls-Royce) [12].

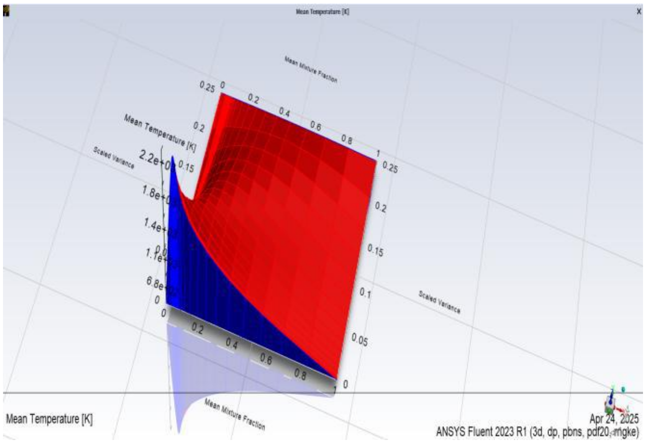

Fig.3. Three-dimensional surface from the flamelet-PDF library generated in the Flamelet-PDF module of ANSYS Fluent for a stationary laminar diffusion flame [14].

The red part of the surface shows hot combustion products (up to ~2250 K) near the optimal fuel-air ratio; blue - cold areas where reactions have not yet begun. The stronger the mixing (the greater the dispersion), the lower the peak temperature: turbulence "stretches" the flame and cools it. The 3-D surface provides a visual representation of how the mixture, turbulence and chemistry work together to form a flame.

A P(Z) distribution within the cell is assumed (usually a beta distribution), allowing the turbulence-averaged product fractions and heat release to be calculated. This approach is known as the unmixed combustion PDF model and is implemented in ANSYS Fluent, among others. It greatly simplifies the calculations by reducing the integration of the rigid kinetics to a preliminary calculation (of a chemical equilibrium table or "flamlet"), and then only the algebraic operations to determine the Z compositions are performed during the CFD solution.

The approach is based on the hypothesis of instantaneous (infinitely fast) combustion, which is true for the main reactants, but NOx formation does not fit into this concept, since NOx formation is a relatively slow process compared to fuel combustion. Therefore, a separate calculation (postprocessing) is used for NOx, taking into account the final reaction rate, as discussed below.

Boundary and initial conditions.

At the chamber inlet, a fuel and air inflow with a certain flow rate and temperature is specified. At the chamber outlet, a boundary condition of the outlet (outlet pressure or ambient condition) is specified. The chamber walls are considered either adiabatic or considering heat exchange. Model validation (see "Verification and validation of models") includes a comparison of variants with heat loss (convective heat removal and radiation) and without it. To summarize, the formulated problem is a stationary turbulent combustion of a methane-air mixture in a direct-flow combustion chamber. The solution method is numerical integration of the averaged Navier-Stokes equations with a turbulent combustion model (mixture model with PDF), supplemented by calculating NOx formation in the postprocessor. The selected turbulence and combustion models and the rationale for their use are described below.

The RNG k–ε turbulence model [15] is used to close the averaged system of flow equations. This is a modification of the standard k–ε model with an additional term in the equation for ε, which increases the accuracy in describing rapidly decaying flows and takes into account the swirl. This is especially important for gas turbine engine combustion chambers, where the flow swirls to stabilize the flame. The model also provides more reasonable values for some constants (e.g., Prandtl numbers) and is able to take into account effects at low Re. Compared to the standard k–ε, RNG k–ε better describes curvilinear and vortex flows with a moderate computational load [15]. The non-premixed PDF approach (see Section 3) is used to describe combustion, where combustion is assumed to be limited by the mixing rate and chemistry is instantaneous. Turbulence affects the flame through fluctuations in the mixture parameter Z, which is described by the beta distribution. The method is suitable for methane diffusion flames, where combustion is determined by the reactant feed.

Since the model assumes instantaneous chemistry, NOx formation is calculated separately after the main calculation, taking into account the final reaction rate according to the Zeldovich mechanism and prompt-NO (the NOx model in Fluent) [16]. When using detailed kinetics directly in the calculation (e.g. via the PDF transport equation), the accuracy can increase to the level of 6% RMS for NOx [17], but this requires significantly more resources. Thus, the combination of RNG k–ε and PDF model is chosen as a balanced solution between accuracy and efficiency, widely used for modeling methane combustion with satisfactory results in terms of temperature and product composition.

Numerical simulation was performed in ANSYS Fluent. The geometry of the flame tube of a typical straight-through tubular-annular combustion chamber with a swirler was built in the SolidWorks' program, the mesh was built in ANSYS Meshing ($\sim 5\times10^5$ cells). A model of almost incompressible gas with the ideal gas equation of state was used. The finite volume method and the Second Order Upwind scheme were applied to approximate the equations (momentum, energy, k, ε, composition). The difference between the 1st and 2nd order schemes on a fine mesh was <2%. The relationship between pressure and velocity was implemented using the SIMPLE algorithm. Convergence criteria: residuals $<10^{-6}$, integral parameters are stabilized with an accuracy of 0.1%. Grid convergence analysis was performed: when doubling the number of cells (to 10^6), the temperature changed by <1%, NOx by ~2%, which confirmed the adequacy of the base grid. A step-by-step strategy was used: first, the main combustion (without NOx) was calculated, then NOx emissions in the postprocessor based on the Zeldovich mechanism (Fluent NO-postprocessor), with recalculation to 15% O_2

Taking into account heat transfer through the walls turned out to be critical: in the base case - adiabatic conditions, then - a scenario with heat loss through convection ($h = 100$ W/m² K, T_ext = 500 K) and radiation (model P1, emission = 0.7).

To ensure the generalization capability of the neural network and meet statistical requirements, the training dataset was expanded to 200 operating points. The dataset covers a wide range of operating conditions characteristic of gas turbine combustion chambers:

- Fuel mass flow rate**:** 0.004 – 0.006 kg/s;
- Air inlet temperature**:** 300 – 600 K;
- Air excess ratio (α): 1.2 – 2.0.

The neural network was trained in MATLAB using the Levenberg-Marquardt algorithm. The dataset was randomly divided into three subsets: Training (70%) for weight adjustment, Validation (15%) to prevent overfitting, and Testing (15%) for independent performance evaluation.

Training dataset structure

Each row in the table corresponds to one unique CFD simulation with its own set of input and output parameters. These parameters are divided into two groups:

Inputs: These are the 4 variables that determined the operating conditions of the combustor in the simulation. The neural network learns from them to make predictions.

mf_fuel_kg_s: mass flow rate of fuel (methane) in kg/s.

mf_air_primary_kg_s: mass flow rate of primary air (for combustion) in kg/s.

mf_air_secondary_kg_s: mass flow rate of secondary air (for cooling) in kg/s.

T_air_in_K: inlet air temperature in Kelvin.

Outputs: these are the 2 target variables that the neural network learns to predict:

Mass fraction NOx - mass fraction of nitrogen oxides (NOx) in the combustion products.

CO2_pct - percentage of carbon dioxide (CO_2) in the combustion products.

The purpose of using this table is to train the neural network (multilayer perceptron) to recognize the complex relationships between the operating parameters of the combustion chamber and the resulting NOx and CO_2 emissions, so that it can make instant predictions without the need for lengthy CFD calculations.

At this stage, 200 CFD calculations may be sufficient for preliminary analysis and creation of the neural network model, this allows to assess the main trends and check what is happening, but it is planned to increase the number of calculations to 500 - 2000 options. The neural network was trained in MATLAB (Neural Network Toolbox): 4 inputs, one hidden layer of 10 neurons, 2 outputs (NOx, CO_2), the backpropagation method (Levenberg–Marquardt algorithm). MSE reached a minimum in ~100 epochs. Calculation of 1 point <0.01 s — comparable to a thousand-fold acceleration compared to CFD. For additional validation, CHEMKIN (via ANSYS Chemkin-Pro) was used — equilibrium composition, verification of the NO formation mechanism. Calculations were also performed in ANSYS Energico — the chamber model as a network of PSR reactors (Fig. 4), the GRI-Mech 3.0 mechanism. NOx values were obtained with an accuracy of 5–10% of the experimental ones, confirming the reliability of the models. Thus, the integrated approach combined the tools of CFD (Fluent), detailed chemistry (Chemkin/Energico) and neural network modeling (MATLAB), which allowed a comprehensive study and validation of the proposed methodology.

2. Materials and Methods

Numerical verification.

To check the numerical stability, a grid convergence analysis was performed on three grids: 0.3, 0.5, and 1.0 million elements. With increasing resolution, the maximum temperature increased (~1940 K → ~2010 K), and NOx increased from 45 ppm to 55 ppm. The changes in the transition from 0.5 to 1 million were ~6%, which is considered acceptable. The base grid (0.5 million) was used further, and the spread was taken into account as an estimate of the discretization error. Approximation schemes were also investigated: the 1st order scheme underestimated the temperature and NOx (1960 K and 48 ppm), so the 2nd order scheme was used in the calculations. Taking into account heat losses (convection and radiation model P1) reduced the temperature by 100–150 K and decreased NOx by ~15%. For example, with an equivalent coefficient of 0.6, the NOx concentration decreased from 50 to ~42 ppm. The main features of the flow were preserved.

Experimental validation.

The numerical data are compared with the results from [18], where NOx ~25 ppm at T_output ~1673 K were obtained in a laboratory chamber on methane. The CFD results (22–30 ppm at ~1650–1700 K) fall within this range. The expected exponential dependence of NOx on temperature, characteristic of the thermal mechanism of its formation, is also confirmed [19]. For example, increasing the temperature from 1500 to 1700 K increased NOx from 10 to 50 ppm.

The temperature distributions in CFD correspond to the laser diagnostics data: the maximum of ~2000 K is localized in the flame above the burner, with a subsequent decrease towards the outlet (~1600 K). The observed recirculation zone behind the swirl is consistent with the literature data for swirling turbulent methane flames [20]. Additionally, a comparison was made with the CRN reactor model using GRI-Mech 3.0. The obtained NOx level (~50 ppm) practically coincides with the CFD results (~52 ppm), confirming the reliability of the model. The CO_2 yield was in the range of 8–10%, which is close to the theoretical value. The CO concentration did not exceed 10 ppm (at the nominal mode), indicating almost complete combustion.

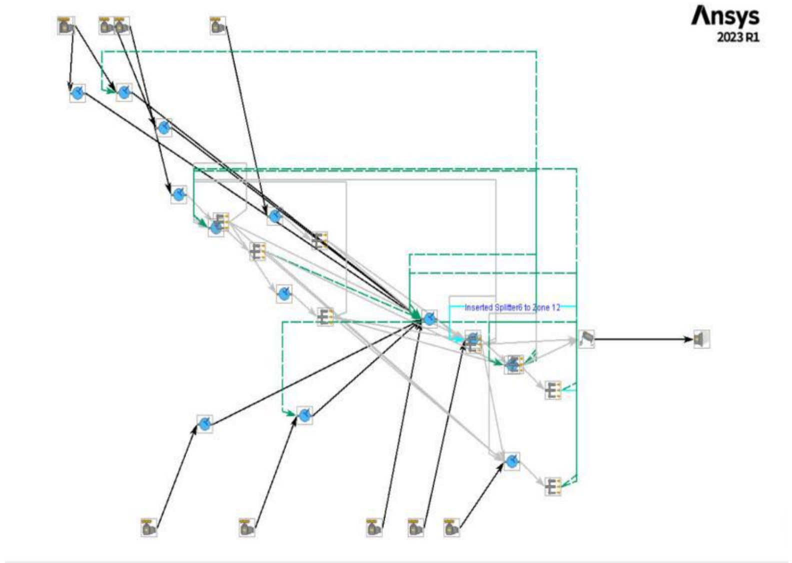

Fig.4. Network of serial/parallel PSR (Perfectly Stirred Reactor) reactors with visual flow grouping tools.

Testing the neural network model.

An extended dataset (200 cases) was used. The prediction performance was evaluated on an independent test set of 30 scenarios (15% of the database). The results are presented in Fig. 5. The model demonstrated high accuracy: the coefficient of determination (R^2) reached 0.998 for NOx and 0.956 for CO_2. The Mean Absolute Error (MAE) and Root Mean Squared Error (RMSE) values confirm that the neural network successfully reproduces the complex non-linear dependencies of pollutant formation without significant overfitting. The maximum deviation for NOx (~10%) was observed in extreme lean modes.

Table 1. Neural network performance metrics on the independent test dataset.

Variable	R² (Determination Coefficient)	MAE (Mean Absolute Error)	RMSE (Root Mean Squared Error)
NOx (ppm)	0.998	1.774	2.450
CO_2 (%)	0.956	0.202	0.263

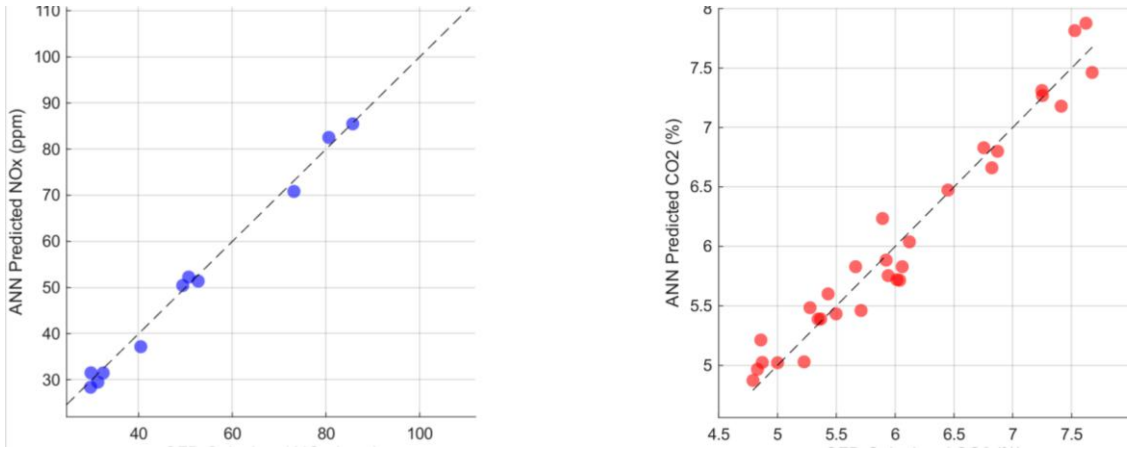

a) b)

Fig.5. Neural Network Validation Results: a) NO_x prediction (R^2=0.998); b) CO_2 prediction (R^2=0.956).

In general, the neural network correctly reproduced the main dependencies (increase in NOx with temperature, decrease in CO_2 with lean mixtures), which corresponds to literature data [9]. This confirms the adequacy of both the CFD model and the neural network trained on its basis.

3. Results and discussion

In Fig. 6 the temperature profile in the combustion chamber is shown under typical conditions (air excess coefficient α ≈ 2.0, close to the nominal load). The maximum temperature reaches ~2100 K in the main flame zone immediately behind the swirl.

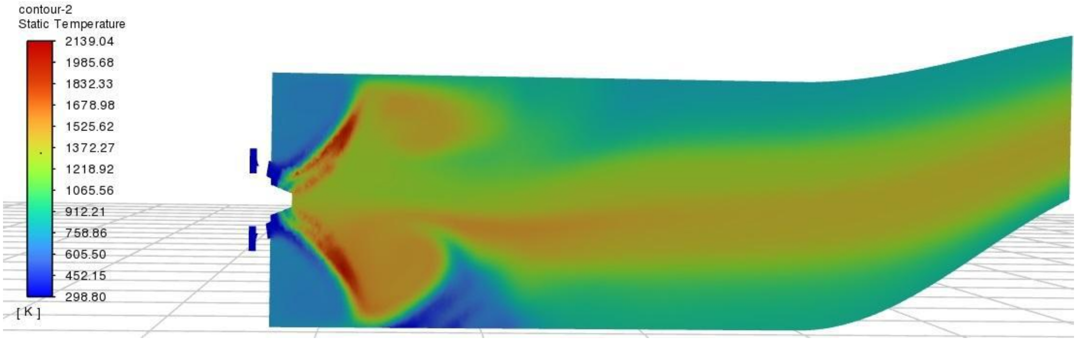

Fig.6. Temperature profile in the flame tube under typical conditions (described in the text)

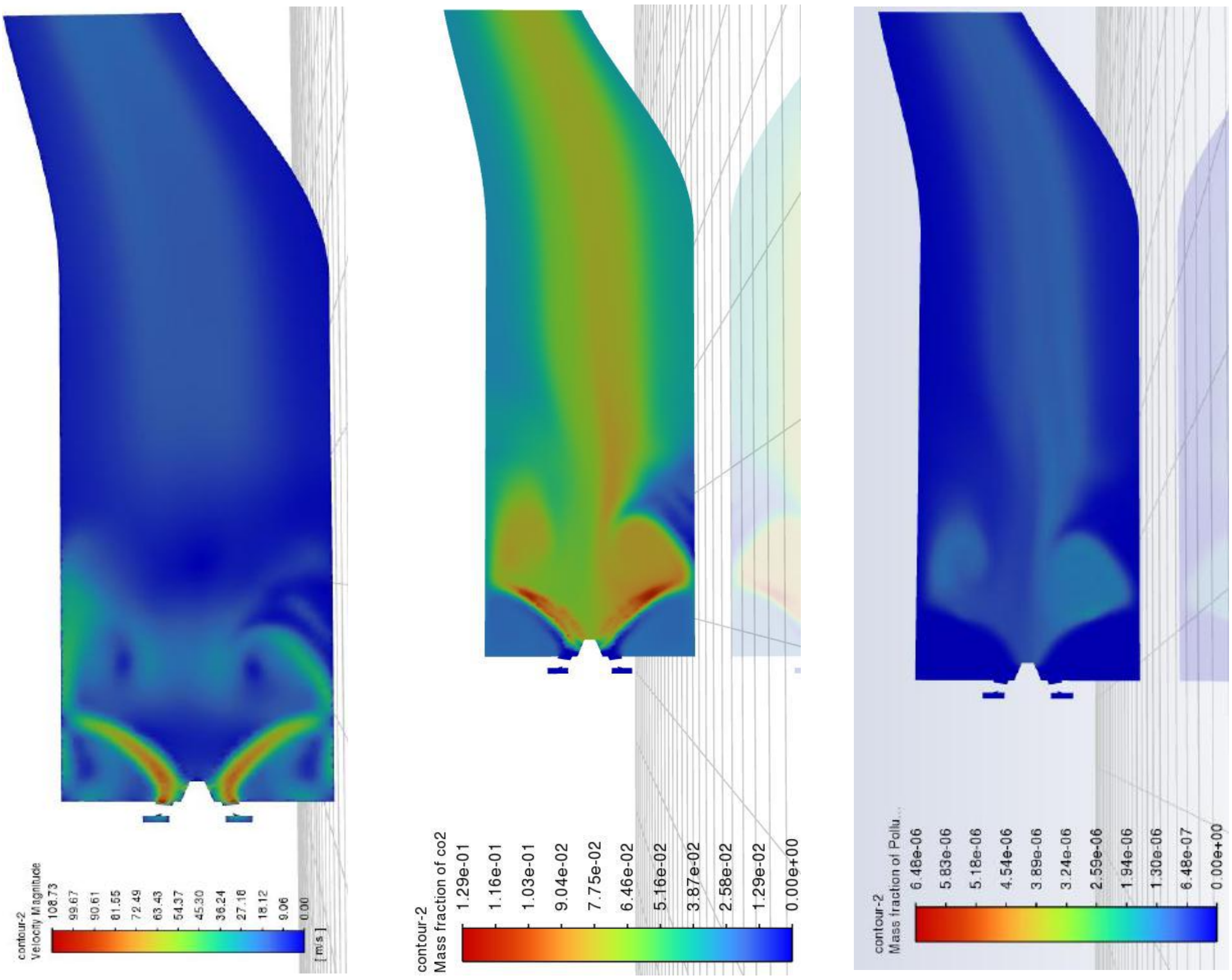

a) b) c)

Fig.7. Distribution along the flame tube of the:

a) velocity magnitude; b) mass fraction of CO2; c) mass fraction of NOx (mode with a "lean" fuel-air mixture).

In the central part of the chamber, a combustion product recirculation zone is formed, which is expressed in an area with an elevated temperature (about 1500 K) – this helps maintain combustion and re-burn unreacted methane, Fig 7. Closer to the walls, the temperature is lower (about 1000 K or less, due to the supply of secondary air), which is important to prevent overheating of the chamber material. Velocity field (Fig 7a) is characterized by a strong swirl of the flow: immediately behind the inlet nozzle, a swirling air flow is visible, creating a toroidal recirculation zone behind the flame plume. This zone captures part of the combustion products and returns them to the base of the flame, promoting stable combustion. Such a structure (the so-called internal recirculation torus) is typical for chambers with vortex stabilization.

The distribution of concentrations of the main products (CO_2, H_2O) exactly repeats the temperature field - the highest concentration of CO_2 is observed in the same place where the temperature is high, confirming that the fuel mainly burns in the torch behind the swirl. Oxygen is almost completely consumed in the flame zone, and ~15% O_2 remains at the outlet (in terms of dry gas, (during fuel combustion, water vapor (H_2O) is formed. But when analyzing the composition of combustion products, it is removed (moisture condenses), and only the dry part of the gas is analyzed - CO_2, CO, O_2, NOx, etc.)) with an excess of air of 2.0, which is consistent with the mass balance), Fig. 7b., Fig. 7c.

The CFD model showed that NOx is formed in the high-temperature flame zone (Fig. 7c, reaching 20–30 ppm behind the combustion zone. The concentration decreases towards the outlet due to dilution. The final emission is ~50 ppm without cooling, ~40–45 ppm with cooling, which corresponds to the standards (temperature <2000 K). An increase in temperature (for example, when α decreases from 2.0 to 1.8) causes a sharp increase in NOx (~15 → 70 ppm), which is due to the exponential dependence according to Arrhenius. The opposite trend is observed for lean mixtures: at α=2.5 – only ~10 ppm. The air temperature at the inlet also has an effect. The neural network successfully reproduces these dependencies, accelerating the analysis of modes. CO_2 prediction and combustion efficiency: at nominal modes, CO_2 is ~3–4%, which indicates complete combustion. At α=3.0, CO_2 drops to ~2%, and CO grows (~5e–6), which reflects deterioration of combustion in a diluted and cooled flame.

4. Conclusions

This paper presents a study aimed at improving the efficiency of numerical modeling of methane combustion in a gas turbine engine combustion chamber by using neural networks. A technique has been developed that combines high-precision CFD modeling of turbulent combustion with subsequent training of a multilayer perceptron for rapid prediction of harmful emissions.

The main conclusions and results are as follows:

1 A CFD model of a methane combustion chamber (flame tube) has been developed based on the RNG k–ε turbulent model and a combustion model assuming fast chemical reaction with PDF.

2 The model has been successfully verified (grid sensitivity analysis, comparison of orders of approximation) and validated against literature data: temperature and concentration distributions, as well as predicted NOx levels (~tens of ppm) are close to those observed experimentally. This confirms the suitability of the selected models for assessing processes in a real chamber.

3 A numerical study of the factors influencing NOx and CO_2 emissions was conducted. It was shown that the key role is played by the combustion temperature regime, determined by the mixture composition (excess air coefficient) and cooling conditions. Thermal NOx increases sharply with an increase in the maximum flame temperature, which corresponds to the exponential nature of its kinetics. Moderate wall cooling can reduce NOx by 10–20% by reducing thermal peaks. Methane combustion efficiency (in terms of CO_2 and CO concentrations) is reduced at too lean mixtures, which limits the ability to minimize NOx by leaning alone. These results are consistent with physical concepts and previously published data on emissions in chamber flare flames [21].

4 A neural network model (MLP) has been developed that approximates the dependence of NOx and CO_2 emissions on the chamber operating mode parameters. The model has been trained on an expanded dataset (200 cases) obtained from CFD and provides a coefficient of determination (R^2) of 0.998 for NOx and 0.956 for CO_2 relative to CFD.

5 In practice, this means that the neural network can replace CFD calculations for emission assessment purposes, producing results in a fraction of a second. Thus, a significant increase in efficiency has been achieved: a quick forecast is possible in real time or during multiple runs during optimization calculations.

6 The neural network reproduces physical patterns: analysis of weights and responses showed that the model captures the exponential nature of NOx growth with temperature, the effect of residence time and oxygen concentration, although these dependencies were not explicitly specified. This demonstrates the ability

of AI tools to identify hidden dependencies in complex multidimensional combustion process data. In essence, the neural network has become a digital twin of the camera, to which various scenarios can be applied and a reliable response estimate can be obtained.

Application prospects. The proposed approach can be directly used in the design of low-emission combustion chambers. A neural network surrogate trained on CFD data can be integrated into optimization algorithms for finding the best configuration (e.g. swirl geometry, flame tube diameter ratio, etc.) based on the criteria of minimizing NOx/CO while maintaining combustion stability. In addition, such a surrogate can serve as the basis for a combustion monitoring and control system: receiving operational sensor data (temperature, flow rate, pressure), the trained network could predict the emission level and signal the need to adjust the mode, which essentially implements the concept of control based on the MPC (Model Predictive Control) model for emissions.

The plan is to move on to modeling ammonia combustion by training a neural network surrogate that simultaneously predicts NO_x, CO, and soot. For this, full-size CFD dumps, and more complex architectures (CNN, PINN) will be used, which will allow reproducing the spatial-temporal structure of the flame and assessing thermoacoustic stability. Additionally, the introduction of AI models directly into the CFD code is being considered to correct for turbulence and reaction rates, providing faster and more accurate calculations.

Conflict of interest statement

The authors declare that they have no conflict of interest in relation to this research, whether financial, personal, authorship or otherwise, that could affect the research and its results presented in this paper.

CRediT author statement

Chepurnyi A.: Conceptualization, Software, Validation, Investigation, Data curation, Writing – original draft, Visualization; **Jakovics A.:** Methodology, Analysis of calculations results and scientific editing of draft. The final manuscript was read and approved by all authors.

Acknowledgement

The author, Andrii Chepurnyi, dedicates this article to his entire large and educated family, who instilled in him a love of science, especially his mother Lyudmila Chepurna, and grandfather Ivan Chepurnyi.

References

1. Aversano G., Bellemans A., Li Z., Coussement A., Gicquel O., Parente A. (2019) Application of reduced-order models based on PCA & Kriging for the development of digital twins of reacting flow applications. *Computers & Chemical Engineering, 121*, 422–441. https://doi.org/10.1016/j.compchemeng.2018.09.022
2. Shao C., Liu Y., Zhang Z., Lei F., Fu J. (2023) Fast prediction method of combustion chamber parameters based on artificial neural network. *Electronics, 12*(23), 4774. https://doi.org/10.3390/electronics12234774
3. Wang Z., Yang X. (2024) NOx formation mechanism and emission prediction in turbulent combustion: A review. *Applied Sciences, 14*(14), 6104. https://doi.org/10.3390/app14146104
4. Ihme M., Chung W.T., Mishra A.A. (2022) Combustion machine learning: Principles, progress and prospects. *Progress in Energy and Combustion Science, 91*, 101010. https://doi.org/10.1016/j.pecs.2022.101010
5. Li S., Zhu H., Zhu M., Zhao G., Wei X. (2021) Combustion tuning for a gas turbine power plant using data-driven and machine learning approach. *Journal of Engineering for Gas Turbines and Power, 143*(3), 031021. https://doi.org/10.1115/1.4050020
6. Lamont W., Roa M., Lucht R. (2014) Application of artificial neural networks for the prediction of pollutant emissions and outlet temperature in a fuel-staged gas turbine combustion rig (Paper No. GT2014-25030). In *Proceedings of ASME Turbo Expo 2014: Turbine Technical Conference and Exposition*. https://doi.org/10.1115/GT2014-25030
7. Wang Q., Hesthaven J.S., Ray D. (2019) Non-intrusive reduced order modeling of unsteady flows using artificial neural networks with application to a combustion problem. *Journal of Computational Physics, 384*, 289–307. https://doi.org/10.1016/j.jcp.2019.01.031
8. Lee W., Jang K., Han W., Huh K.Y. (2021) Model order reduction by proper orthogonal decomposition for a 500 MWe tangentially fired pulverized-coal boiler. *Case Studies in Thermal Engineering, 28*, 101414. https://doi.org/10.1016/j.csite.2021.101414
9. Sun J., Song Y., Shi Y., Zhao N., Zheng H. (2023) Prediction of the pollutant generation of a natural gas-powered coaxial staged combustor. *Journal of Tsinghua University (Science & Technology), 63*, 649–659. https://doi.org/10.16511/j.cnki.qhdxxb.2023.25.014

10. Khodayari H., Ommi F., Saboohi Z. (2021) Multi-objective optimization of a lean premixed laboratory combustor through CFD-CRN approach. *Thermal Science and Engineering Progress, 25*, 101014. https://doi.org/10.1016/j.tsep.2021.101014

11. Fichet V., Kanniche M., Plion P., Gicquel O. (2010). A reactor network model for predicting NOx emissions in gas turbines. *Fuel, 89*(9), 2202–2210. https://doi.org/10.1016/j.fuel.2010.02.010

12. Huang Z., Dai P., Xu C., Tian H., Sun L., Li X. (2025) Optimization of ammonia/methane mixture combustion kinetic model based on artificial neural network. *Applied Thermal Engineering, 264*, 125484. https://doi.org/10.1016/j.applthermaleng.2025.125484

13. Pope S.B. (1985) PDF methods for turbulent reactive flows. *Progress in Energy and Combustion Science, 11*(2), 119–192. https://doi.org/10.1016/0360-1285(85)90002-4

14. Peters N. (1984) Laminar diffusion flamelet models in non-premixed turbulent combustion. *Progress in Energy and Combustion Science, 10*(3), 319–339. https://doi.org/10.1016/0360-1285(84)90114-X

15. Yakhot V., Orszag S.A., Thangam S., Gatski T. B., Speziale C.G. (1992) Development of turbulence models for shear flows by a double expansion technique. *Physics of Fluids A: Fluid Dynamics, 4*(7), 1510–1520. https://doi.org/10.1063/1.858424

16. Hashemi S.A., Fattahi A., Sheikhzadeh G.A., Hajialigol N., Nikfar M. (2012) Numerical investigation of NOx reduction in a sudden-expansion combustor with inclined turbulent air jet. *Journal of Mechanical Science and Technology, 26*(11), 3723–3731. https://doi.org/10.1007/s12206-012-0848-y

17. Zhao X., Haworth D.C., Huckaby E.D. (2012) Transported PDF modeling of nonpremixed turbulent CO/H2/N2 jet flames. *Combustion Science and Technology, 184*(5), 676–693. https://doi.org/10.1080/00102202.2012.660223

18. Sun J., Zhao N., Li Y., Cheng X., Zheng H. (2025) Experimental and numerical study on NOx emissions characteristics in a coaxial staged combustor. *Journal of Engineering for Gas Turbines and Power, 147*(8), 081002. https://doi.org/10.1115/1.4067219

19. Lefebvre A.H. (1984) Fuel effects on gas turbine combustion—liner temperature, pattern factor, and pollutant emissions. *Journal of Aircraft, 21*(11), 887–898. https://doi.org/10.2514/3.45059

20. Bahramian A., Maleki M., Medi B. (2017) CFD modeling of flame structures in a gas turbine combustion reactor: Velocity, temperature, and species distribution. *International Journal of Chemical Reactor Engineering, 15*(4), 20160076. https://doi.org/10.1515/ijcre-2016-0076

21. Xu S., Tu Y., Huang P., Luan C., Wang Z., Shi B. (2020) Effects of wall temperature on methane MILD combustion and heat transfer behaviors with non-preheated air. *Applied Thermal Engineering, 174*, 115282. https://doi.org/10.1016/j.applthermaleng.2020.115282

AUTHORS' INFORMATION

Chepurnyi, Andrii – PhD student, University of Latvia, Riga, Latvia; https://orcid.org/0009-0005-4410-5458; vasfed12345@gmail.com

Jakovics, Andris – Doctor of Physical and Mathematical Sciences, Head of Laboratory of Multiphysical Processes, University of Latvia, Riga, Latvia; https://orcid.org/0000-0003-3410-5081; Andris.Jakovics@lu.lv

EURASIAN PHYSICAL TECHNICAL JOURNAL

2025, Volume 22, No.4 (54)

https://doi.org/10.31489/2025N4/63-73

Received: 20/09/2025 Revised: 12/11/2025 Accepted: 25/12/2025

Original Research Article

UDC 536.46:532.517.4

STUDY OF THE INFLUENCE OF VARIOUS METHODS OF FUEL INPUT THROUGH BURNERS ON COMBUSTION PROCESSES

Askarova A.S.[1], Bolegenova S.A.[1], Nugymanova A.O.[1], Maximov V.Yu.[1], Bolegenova S.A.[1], Ospanova Sh.S.[1]*, Shortanbayeva Zh.K.[1], Aubakirov N.P.[2], Nurmukhanova A.Z.[1]

[1] Al-Farabi Kazakh National University, Almaty, Kazakhstan
[2] Kazakh National Research Agrarian University, Almaty, Kazakhstan
*Corresponding author: Shynar.Ospanova@kaznu.edu.kz

Abstract. *This paper presents new results of computational experiments to study the influence of various methods of fuel input (straight flow and vortex with a flow deflection angle of the pulverized coal stream) across the firing systems on combustion processes utilizing the BKZ-75 boiler combustion chamber case of the Shakhtinskaya TPP (Kazakhstan), fluidized combusting Karaganda coal with high ash content. According to the results of computational combustion modeling, the following results were derived: the total velocity vector distributions, spatial distributions of temperature, and concentrations of carbon oxides and nitrogen dioxide (NO_2) within the full volume through the combustion zone and at the chamber's discharge. It has been appeared that the vortex strategy of providing the discuss blend makes it conceivable to enhance the method in the combustion of high-ash coal, as in this case there's an increment in temperature within the center of the burn and a lower temperature observed at the combustion zone outlet, which features a noteworthy effect on the chemical forms of the arrangement of reaction products formed during combustion. When employing vortex burner devices, the concentration levels at the combustion outlet zone for carbon monoxide (CO) decrease by about 15 %, and for nitrogen dioxide (NO_2) by roughly 20 % relative to direct-flow burner devices. The comes about gotten make it conceivable to create proposals for the advancement of ideal strategies for managing flame structure and combustion dynamics of a pulverized coal burn to extend the productivity of vitality offices and decrease emanations of hurtful substances into the environment.*

Keywords: combustion, simulation, coal-fired power plant, linear-flow and swirling-flow burners, thermal field, carbon monoxide emission, toxic nitrogen compounds.

1. Introduction

Today, energy consumption is the largest source of anthropogenic greenhouse gas emissions, contributing to global warming [1]. According to the International Energy Agency (IEA) for 2022, the world's most significant sources of energy are petroleum, coal, and natural gas (Figure 1) [2]. Just over 16% of global energy comes from low-carbon sources, of which approximately 11% comes from renewable fuels and renewable municipal waste (biofuels and biomass). The remaining clean energy sources include hydropower, geothermal energy, solar energy, wind energy, tidal energy, and wave energy.

The global community is rapidly moving to achieve complete decarbonization of the global economy by 2050, introduce a carbon tax, and strengthen adaptation measures to the impacts of climate change. The Paris Agreement on climate change ignited the carbon neutrality movement, with the European Union, the United Kingdom, Japan, Korea, and more than 110 other countries committing to carbon neutrality by 2050. However, carbon dioxide emissions are still at record levels and are rising rapidly [2].

Despite the growing popularity of alternative sources, electric coal remains the primary method for producing electricity. The IEA indicated that high coal demand will remain stable until 2025. Although Western countries want to reduce coal consumption, it will continue in Asian markets. The world is close to peak fossil fuel use, and coal will be the first to decline, but the world is not there yet. Request for coal waste resolved and is expected to hit record-breaking level this year, expanding worldwide emanations [2].

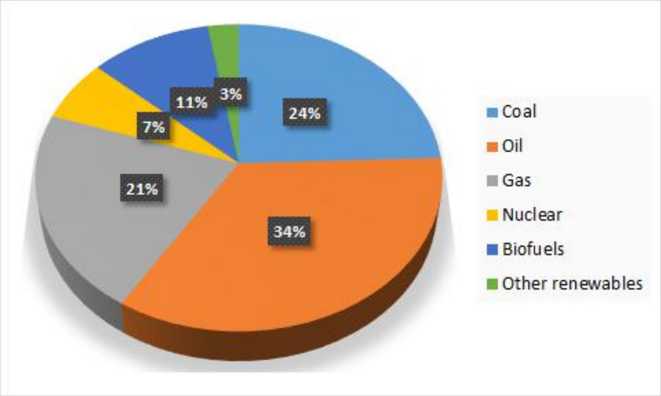

Fig.1. Fuels' share of the world's total primary supply in 2025 [2].

The coal industry faces a paradoxical situation. While the global green transition frames coal as the dirtiest source of electricity, it continues to serve as an affordable and dependable resource with rising demand. Indeed, although driving countries have announced approach to realize carbon nonpartisanship over period 2020-2060, coal generation is impossible to decrease before long. Fueled by tall common gas costs, rising power request, and fast mechanical and vitality division development in India, China, and Southeast Asia, coal is anticipated to preserve its current proportion within the vitality blend for at slightest other 5-10 a long time [3–6].

According to the International Energy Agency (IEA), global coal consumption will likely rise in the coming years. The post-COVID recovery has driven energy demand sharply upward, prompting a resurgence of coal use. In the EU, previously retired coal-fired power plants are being reactivated, while in the United States, coal mining is experiencing its first revival in a decade. This “coal resurgence” started in 2021 in the midst of the vitality emergency, as clean energy demonstrated fewer solid, compelled by both characteristic situations (moo wind and cold climate) and by technological challenges (including the surge in solar panel production). As a result, coal has returned to the global energy mix despite strong opposition from environmentalists [2].

Coal-based power generation continues to play a crucial role in the economies of many countries and in ensuring public welfare [7–11]. In response to global environmental priorities, the industry is working to develop “clean” coal utilization and processing technologies while meeting strict ecological standards. This makes research on combustion processes in power plant chambers and identifying optimal fuel-burning methods especially relevant. Although the share of coal-fired plants is expected to decline, coal will remain the primary fuel for Kazakhstan’s thermal power sector. Subsequently, a key challenge for household control designing is planning and executing ecologically inviting advances at coal-burning facilities in Kazakhstan control that direct toxin arrangement forms and reduce outflows [12-17].

This study presents computational experiments to analyze the influence of different fuel injection methods-direct-flow and vortex, with a specified swirl angle of the pulverized coal stream through burner devices on combustion processes. Environmentally optimal air supply configurations for the combustion chamber were identified. Cutting-edge numerical devices empowered detailed 3D representations of the results, which had been confirmed against test data obtained from a working warm control station [18-21].

2. Materials and methods

Structural and Functional Description of the Combustion Chamber

To implement numerical simulation techniques, we chose the combustion zone of the BKZ-75 steam-generating unit, introduced at the Shakhtinskaya TPP located in Kazakhstan, in which Karaganda coal with ash content 35.1 % is combusted. The object of study is the BKZ-75 vertical water-tube steam boiler, operating at a capacity of 75 t/h (51.45 GCal/h). Figure 2a illustrates a boiler schematic and a finite difference framework used for running computational tests.

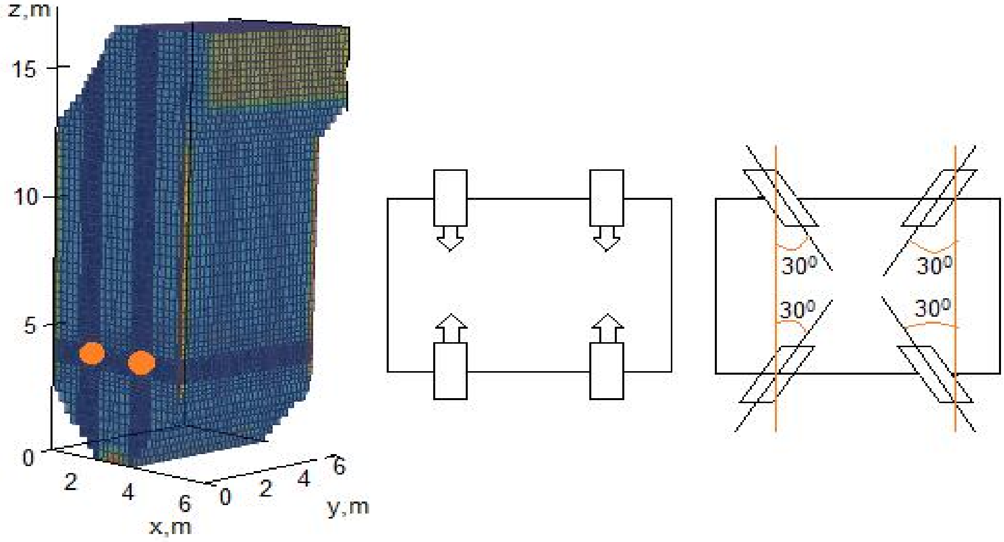

a) b) c)

Fig. 2 Evaporator graph and finite-difference framework (a) and diverse plans of burner gadgets course of action: direct-flow (b) and vortex (c) within the firebox of the BKZ-75 evaporator

The evaporator utilizes four burners for pulverized coal combustion, two introduced at the front side and raised to one level. Figure 2a shows a pot chart and a finite-difference approach for executing computational tests. Below are the comes about of computational tests to think about warm forms, streamlined and analysis of concentration profiles in the combustion zone of the BKZ-75 boiler at the Shakhtinskaya Thermal Power Plant [12-14, 17] for the shown two modes of providing coal powder fuel: 1) direct-flow approach of providing the discuss blend burners are found on inverse side dividers (Figure 4b); 2) vortex approach of providing the discuss blend - burners with a whirl point of the discuss blend stream and a 30-degree tilt toward the boiler's central symmetry (Figure 2c) [22-24].

The initial data for carrying out numerical modeling and numerical experiments on fuel combustion in the combustion chamber of the BKZ-75 boiler, as well as all the necessary parameters of coal dust are presented in Tables 1-2.

Table 1. Composition and initial data of Karaganda coal

Composition of the original coal dust, %		Name of the parameter	Initial data of Karaganda coal		
			Designation	Unit of measurement	Meaning
W	10,60	Type of coal	KR-200	-	-
A	35,10	Fineness of grinding	R_{90}	%	20
S_2	1,04	Density of coal	ρ	kg/m^3	1300
C	43,21				
H_2	3,60				
O_2	5,24	Heat of combustion of coal	Q_L^R	kcal/kg	4433
N_2	1,21				
V	22,00				

Table 2. Calculated performance indicators of the combustion chamber of the BKZ-75 boiler

№	Parameter name	Designation	Unit of measurement	Meaning
1	Nominal steam capacity	D	t/h	75
2	Boiler efficiency	η	%	80.88
3	Height of the combustion chamber	h(z)	m	16.75
4	Firebox width	x	m	6
5	Depth of the combustion chamber	y	m	6.6
6	Number of burners on the boiler	N	pcs.	4
7	Fuel efficiency of one burner	B	t/h	3.2
8	Primary air flow rate to the boiler	V_p	nm^3/t	31797
9	Secondary air consumption for the boiler	V_s	nm^3/t	46459
10	Excess air coefficient in the furnace	α		1.2
11	Hot air temperature	t_h	°C	290
12	Suction cups in the firebox	$\Delta\alpha_t$	-	0.10
13	Estimated fuel consumption for the boiler	B	t/h	12.49
14	Cold air temperature	t_c	°C	30
15	Air mixture temperature	t_{air}	°C	140
16	Wall temperature	t_w	°C	430.15

3. Results

Underneath are the results of a consideration of warm forms, streamlined, and concentration fields in the BKZ-75 boiler combustion chamber at the Shakhtinskaya TPP for two coal feed modes.

3.1. Investigation of the airflow dynamics within the firebox of the BKZ-75 boiler

Figures 3–4 show the optimal design of the firebox of the BKZ-75, specifically the conveyance of the complete velocity vector $v=\sqrt{U^2+V^2+W^2}$ across its different sections. The complete velocity vector is displayed within the figures underneath in the shape of bolts of distinctive colors. The heading of the arrow indicates the course of the medium's speed, and utilizing the color scale, you'll decide its numeric value. The coming about areas of the overall velocity vector empower the investigation of the development of responding streams within the combustion space, as appeared in its different areas, as demonstrated within the illustrations.

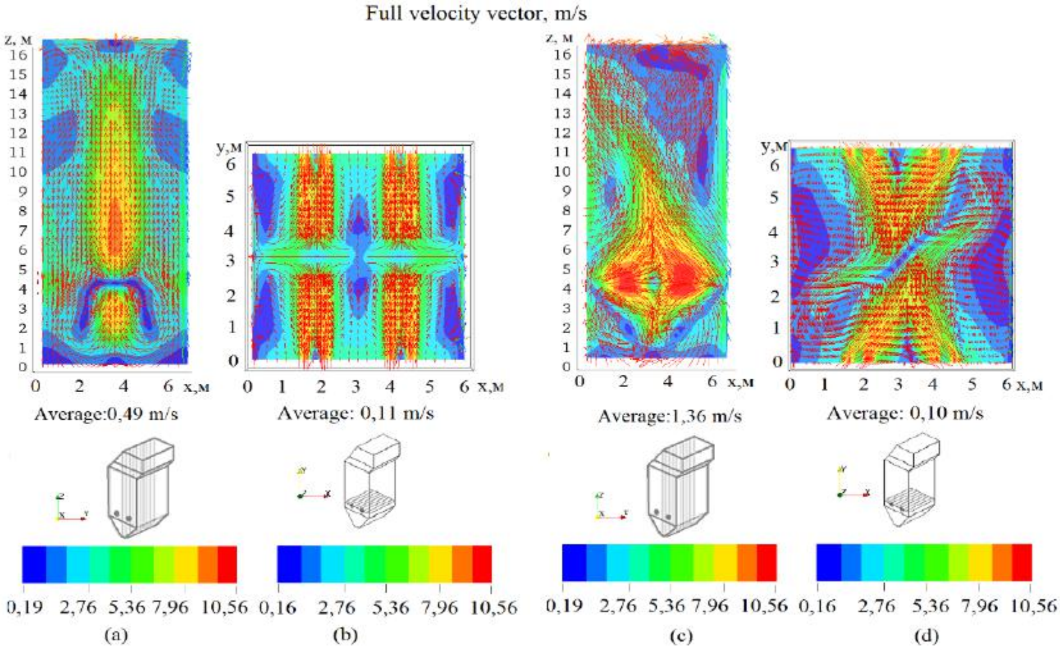

Fig. 3. Conveyance of the entire velocity within the longitudinal (x=3.0 m) and transverse areas of the firebox (burner zone, h=4.0 m) of the BKZ-75 with: direct-flow (a, b), vortex approach of discuss blend supply (c, d)

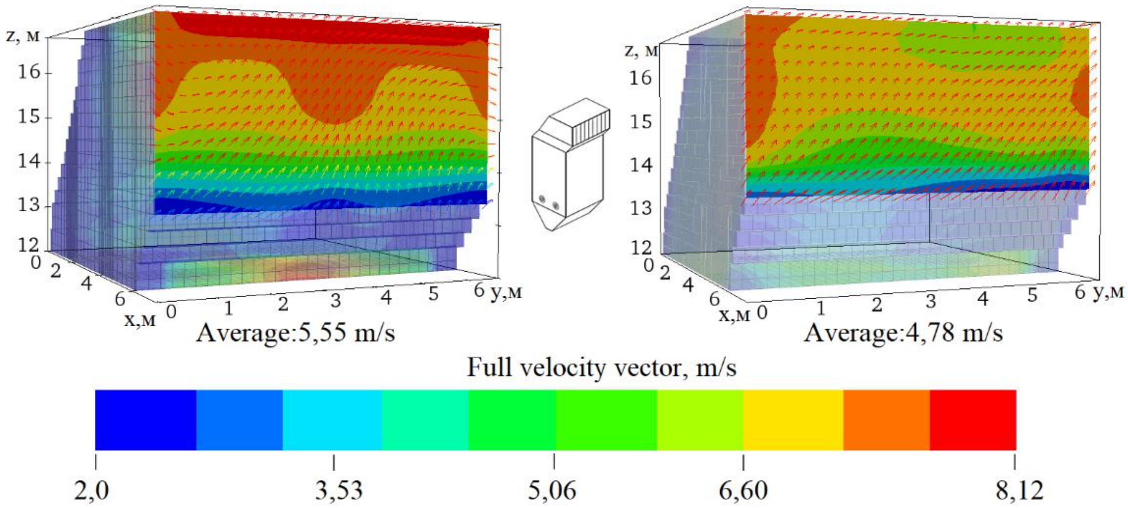

Fig. 4. Conveyance of the entire velocity in cross segments at the outlet (h=16.75 m) from the firebox BKZ-75 with: a) direct-flow and b) vortex approach of providing the discuss blend.

Figure 3 outlines the conveyance of the overall speed vector within the longitudinal (x = 3.0 m) and transverse (h = 4.0 m, burner zone) segments of the firebox BKZ-75 for direct-flow (Fig. 3a, b) and vortex (Fig. 3c, d) air supply approaches. Within the direct-flow setup, planes from restricting burners impact at a right point within the chamber center, part into littler rivulets, and blend into two prevailing streams coordinated for the pipe (Fig. 3a, b).

In contrast, the vortex method generates a markedly different flow structure. Air–fuel jets introduced at a 30° swirl angle create a central vortex within the chamber (Fig. 3c, d). Four swirling streams converge at the chamber center, interact at a 30° angle, and merge into a stronger, unified vortex directed toward the outlet. Comparison of the two modes reveals that the vortex method enhances turbulence, leading to intensified mixing. Incomplete combustion of coal particles is a well-known issue. Some particles are entrained by flue gases as fly ash, while others are removed with slag via the cold funnel, resulting in mechanical heat losses. Examination of the velocity (Fig. 3) shows that the vortex strategy advances more overwhelming circulation of dust gas streams, expanding coal grain residence time in the combustion zone. This reduces the extent of mechanical under burning and contributes to more complete fuel utilization in the BKZ-75 boiler.

Figure 4 presents the velocity distribution in transverse sections at the chamber outlet (h = 16.75 m). As the planes are absent from the burner zone, velocity vectors steadily equalize, the vortex is debilitated, and the stream grows to attain a uniform conveyance over the exhaust cross-section. Notably, the mean outlet velocity for the vortex case (4.78 m/s) is lower than for the direct-flow case (5.55 m/s), suggesting improved energy dissipation and flow uniformity under vortex combustion conditions.

3.2 Investigation of the thermal properties of the combustion chamber

Utilizing computational analysis, temperature areas were gotten in several segments of the firebox BKZ-75 for two discuss supply modes: coordinate stream and vortex (Fig. 5). The 3D plots with temperature scales allow determination of local values throughout the chamber. A clear qualitative difference is observed between the two cases. Quantitatively, the average temperature at the burner level (h = 4.0 m) is 620 °C for the direct-flow method and 854 °C for vortex burners. In both modes, most extreme temperatures happen close the firebox; be that as it may, for direct-flow burners, high-temperature zones move toward the dividers, expanding their warm stack (Fig. 5b). Within the case of vortex burners with a 30° whirl point, the flame core is concentrated within the central part of the firebox (Fig. 5c, d), bringing down the walls' warm stack. This impact emerges from the stronger vortex stream, improving convective warm exchange and expanding the residence time of coal elements within the combustion region.

This slant is affirmed by three-axis (Fig. 6a) and two-axis (Fig. 6b) temperature disseminations along the chamber stature for both air supply modes. The average temperature profiles (Fig. 6a) demonstrate that the vortex method extends the high-temperature zone. The minima observed in the curves (Fig. 6b) corresponds to the burner level (h = 4.0 m), where the entering air mixture has a lower temperature.

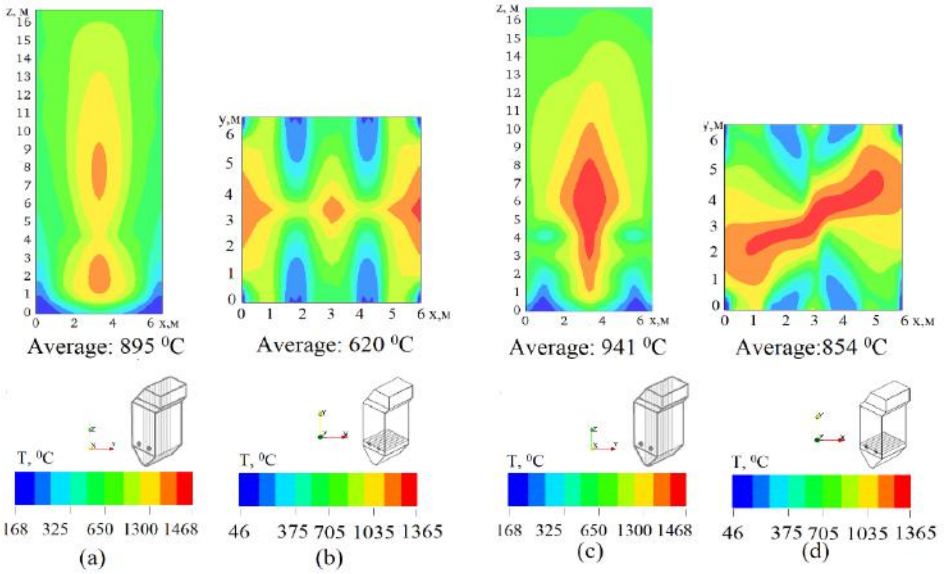

Fig. 5. Temperature dissemination within the longitudinal (x=3.0 m) and cross areas of the firebox (burner region, h=4.0 m) of the BKZ-75 with: direct-flow (a, b) vortex approach of providing the discuss blend (c, d).

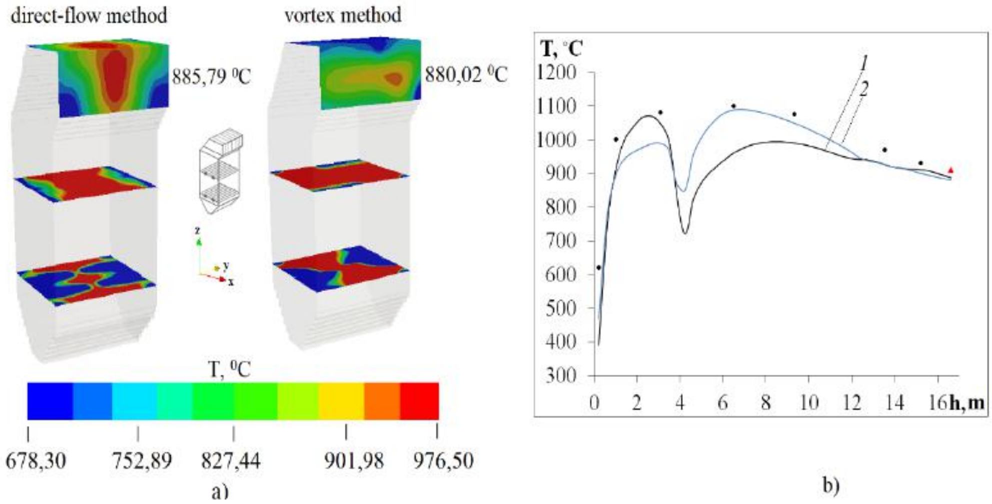

Fig. 6. Three-dimensional a) and two-dimensional b) dispersions of temperature T along the stature of the firebox h of the BKZ-75 kettle with: bend 1 direct-flow and bend 2 vortex strategy of providing the discuss blend;
● exploratory values [25]; ▲hypothetical esteem gotten utilizing the CBTI strategy [17].

At the chamber outlet, the mean temperature is 886 °C for the direct-flow configuration (Fig. 6a, b, curve 1) and 880 °C for the vortex case (Fig. 6a, b, curve 2). Experimental data [25] plotted on the graphs confirm close agreement between simulation and full-scale measurements. Moreover, the outlet temperature for the direct-flow mode is consistent with the theoretical value as predicted by the Central Boiler and Turbine Institute (CBTI) methodology [17], further validating the numerical results.

3.3 Consider the concentration areas of combustion items of pulverized coal fuel in the firebox.

Switching from direct-flow to vortex fuel stock, with jets slanted 30° toward the chamber pivot and conferring a twirl to the air fuel blend, modifies the temperature conveyance inside the firebox and subsequently affects the concentration fields of combustion products. Specifically, extreme temperatures within the fire center and lower amounts at the outlet strongly influence the chemical pathways of product formation [21]. Figures 7-8 present computational results for carbon monoxide (CO) concentration fields in various sections of the BKZ-75 boiler under both air supply modes. Figure 7 shows the CO distribution in longitudinal (x = 3.0 m) and transverse sections at the burner level (h = 4.0 m), comparing direct-flow (a, b) and vortex (c, d) operation. In both cases, maximum CO concentrations are localized near the chamber center, corresponding to the burner region. This zone, where contradicting fuel discusses planes cross, shows strong burning and hoisted temperatures (~1400°C). Beneath these situations, fragmented fossil fuel oxidation happens, and carbon monoxide is effectively formed through chemical reactions between the ground coal and the oxidizing medium. Thus, the air supply method not only modifies flow and temperature fields but also governs the spatial distribution and intensity of CO formation within the burning area.

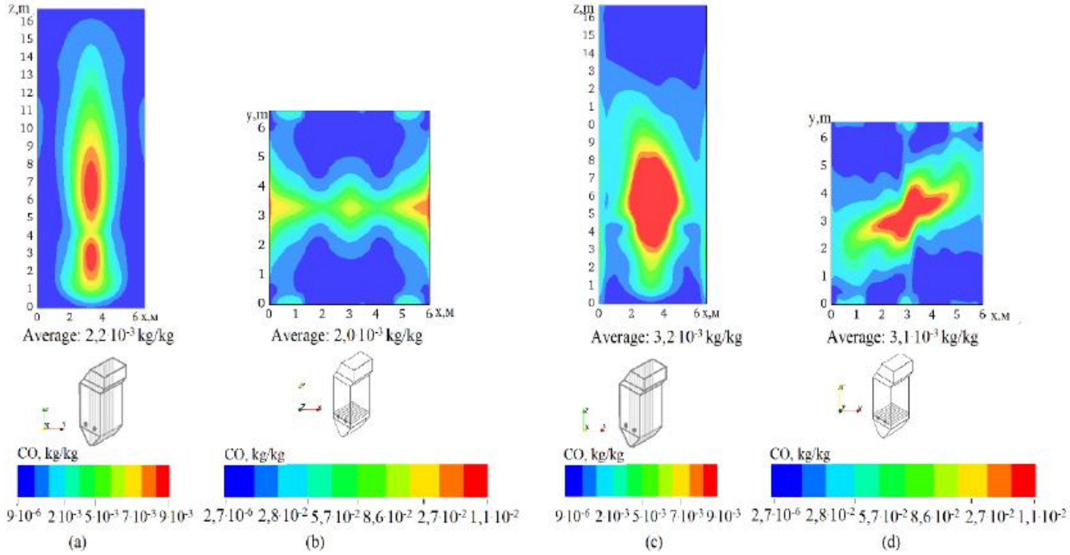

Fig. 7 Dispersion of the concentration of carbon monoxide CO within the longitudinal (x=3.0 m) and cross areas of the firebox (burner range, h=4.0 m) of the BKZ-75 evaporator with: direct-flow (a, b) and vortex strategy of providing the discuss blend (c, d).

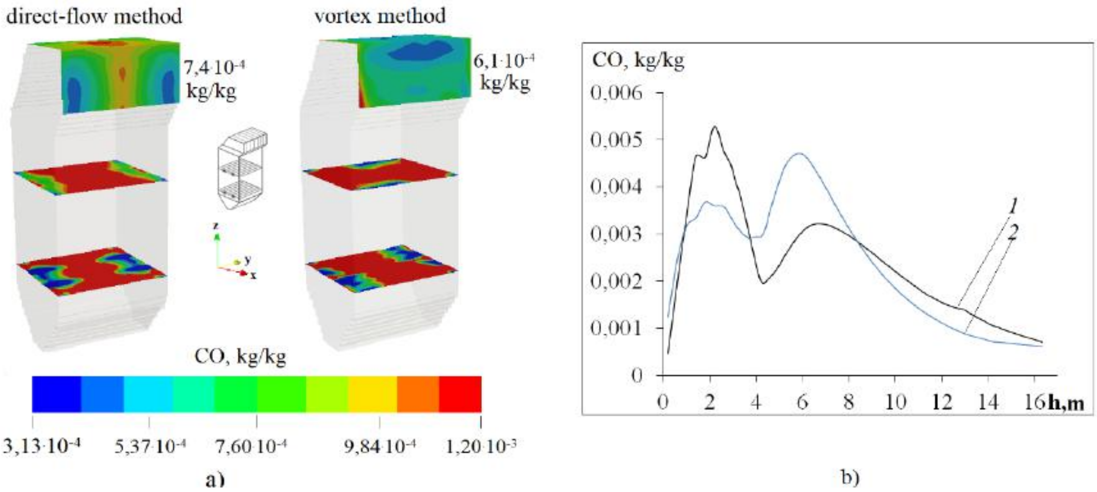

a) b)

Fig. 8. Three-dimensional a) and two-dimensional b) conveyances of concentrations of carbon monoxide CO along the tallness of the combustion chamber h of the BKZ-75 evaporator with: bend 1 - direct-flow and bend 2 - vortex strategy of providing the discuss blend.

Analysis of Figure 8 shows that beneath the vortex, the supply form of carbon monoxide (CO) concentrations is elevated within the central locale of the firebox, especially within the flame region, associated to the direct-flow approach. This increment is ascribed to higher temperatures, forcing combustion responses, and increasing total carbon transformation. At the same time, the higher combustion intensity accelerates the subsequent oxidation of CO to carbon dioxide (CO_2). As a result, CO concentrations are lower at the chamber outlet using the vortex method. This trend is confirmed by the three-dimensional (Fig. 8a) and two-dimensional (Fig. 8b) disseminations of normal CO concentration along the space tallness for both working ways.

When operating in direct-flow mode, the outlet CO concentration is on average 7.4×10^{-4} kg/kg (Fig. 8a, b; curve 1), whereas for the vortex configuration it decreases to 6.1×10^{-4} kg/kg (Fig. 8a, b; curve 2). Thus, the vortex method reduces CO concentration at the exit by approximately 15% relative to direct flow. Overall, the comes about illustrate that vortex burners upgrade combustion effectiveness by powers in-compartment oxidation forms, bringing down poison outflows at the exit associated to customary direct-flow frameworks. Computational tests created NO_2 concentration areas within the longitudinal (x = 3.0 m) and transverse (h = 4.0 m) segments of the firebox BKZ-75 for both air supply modes (Fig. 9).

The results show that maximum NO_2 formation occurs in regions of elevated temperature and strong vortex motion, located near the burners at h = 4.0 m. Enhanced turbulence from vortex burners improves fuel–oxidizer mixing, while high flame-core temperatures promote NO_2 generation. Under these conditions, the average cross-sectional NO_2 concentration reaches 943 mg/nm^3 (Fig. 9d) compared with 493 mg/nm^3 for non-vortex flow mode (Fig. 9b). Figure 10 shows a uniform decrease in NO_2 concentration toward the combustion chamber exit, reflecting reduced oxygen and fuel availability.

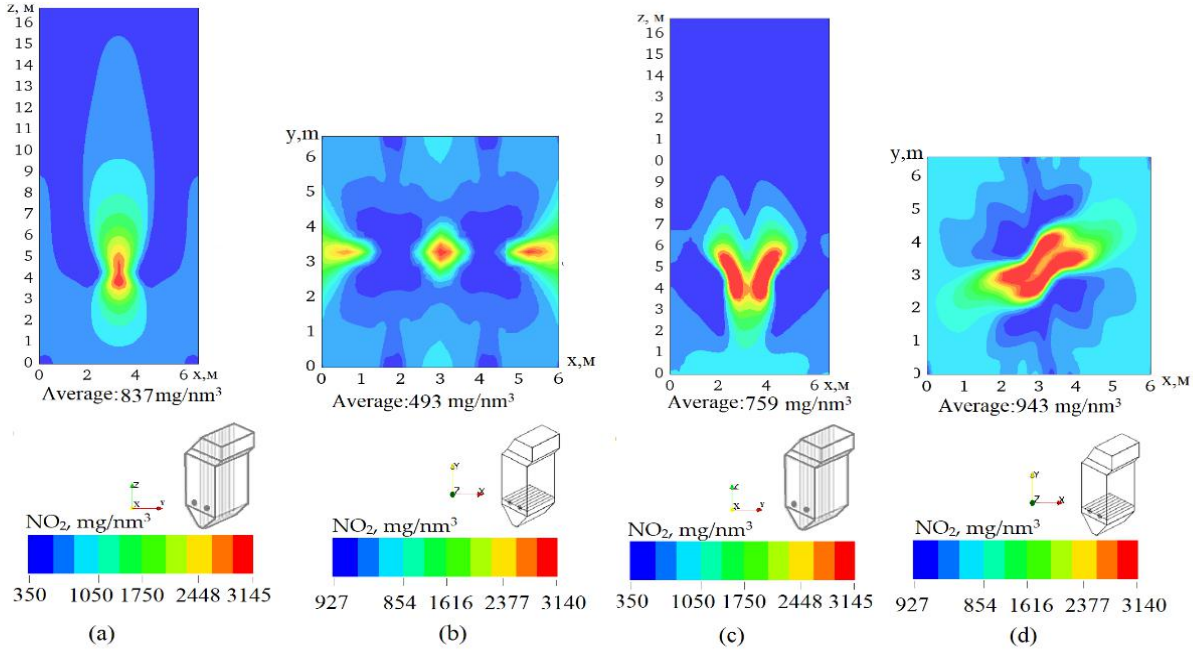

(a) (b) (c) (d)

Fig. 9. Dispersion of nitrogen dioxide NO_2 within the longitudinal (x = 3.0 m) and cross segments of the firebox (burner region, h = 4.0 m) of the BKZ-75 boiler with: direct-flow (a, b) and vortex strategy of providing the discuss blend (c, d).

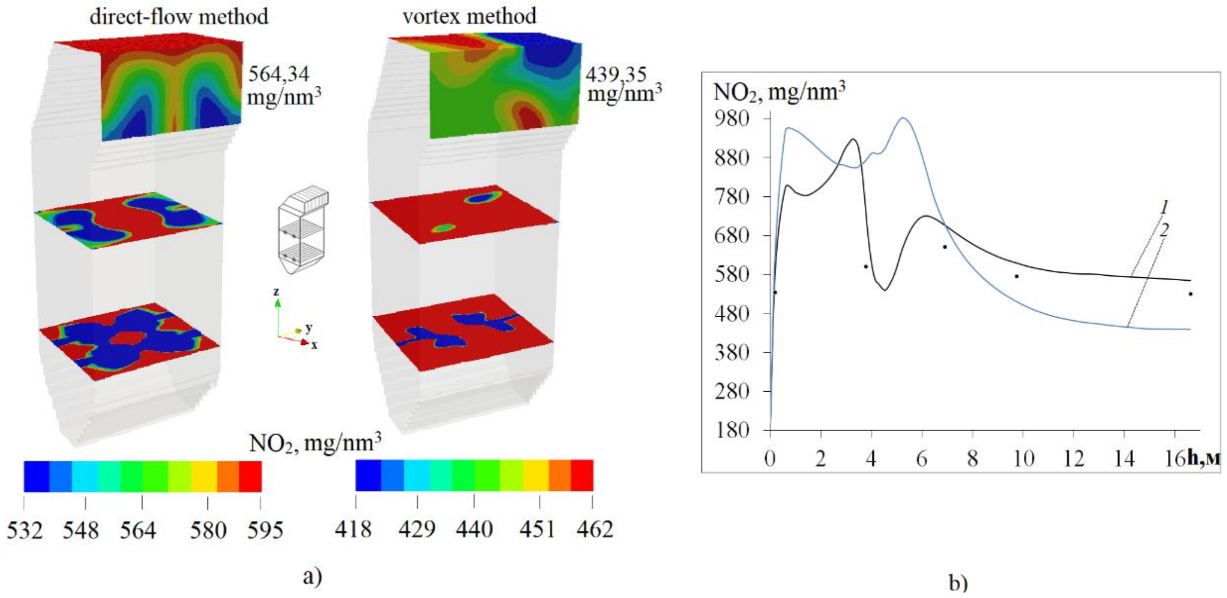

a) b)

Fig. 10. Three-axis a) and two-axis b) conveyance of the nitrogen dioxide NO_2 along the stature of firebox h of the BKZ-75 evaporator with: bend 1 – direct-flow and bend 2 – vortex way of providing the discuss blend; • – exploratory quantities [25].

With vortex burners, the flat temperature falls along the cavity quickly, assisting in smothering the NO_2 arrangement. Under direct-flow conditions, the NO_2 level at the outlet is 564 mg/nm^3, while in vortex mode it decreases to 439 mg/nm³ (Figs. 10a, b; curves 1 and 2), a reduction exceeding 20%. Exploratory information from the firebox BKZ-75 at Shakhtynskaya TPP [32, 36] confirms these results.

4. Comparisons and discussion

Table 3 presents the comes about of numerical tests for the important parameters of the firebox BKZ-75: temperature (T), carbon monoxide (CO) concentration, and nitrogen dioxide (NO_2) concentration, assessed over distinctive areas of the burning interstellar for both direct-flow and vortex discuss supply approaches. Investigation of the information in Table 1 appears that the utilization of burners with a whirling air-fuel blend outstandingly decreases the normal exit concentrations of destructive substances (CO and NO_2)), aligning them with acceptable limits for the BKZ-75 burning Karaganda coal with high ash content.

Table 3. Cross-sectional normal standards of the most features of the fuel burning handle (T, CO, NO2) at different statures h of the firebox BKZ-75 (burner zone, h = 4 m; at the exit from the heater, h = 16.75 m) amid burning, it covers Karaganda coal with high ash content (fiery debris substance 35,1%)

Height h, m	Air mixture supply methods					
	Direct-flow method of supplying an air mixture			Vortex method of supplying an air mixture		
	Unit			Unit		
	T, °C	CO, kg/kg	NO_2, mg/nm^3	T, °C	CO, kg/kg	NO_2, mg/nm^3
4	620,56	$2.0 \cdot 10^{-3}$	492.48	854.52	$3.1 \cdot 10^{-3}$	943.60
16.75	885.79	$7.4 \cdot 10^{-4}$	564.34	880.02	$6.1 \cdot 10^{-4}$	439.35

Linked with direct-flow jets, vortex burners lower outlet CO levels by about 15% and NO_2 levels by 20%. These discoveries emphasize the viability of vortex jet in improving high-dust coal burning in control plant heaters whereas at the same time diminishing toxin outflows into the atmosphere.

5. Conclusions

1. Mathematical demonstration of warm and mass exchange forms within the firebox of a Kazakhstan warm control plant was achieved for distinctive fuel supply strategies (direct-flow and vortex with a 30° whirl point of the coal-dust stream). A computational demonstration of the BKZ-75 evaporator at the Shakhtinskaya TPP was created, precisely speaking, under the genuine conditions of characteristics of low-rank coal combustion.
2. The influence of pulverized coal swirl on combustion characteristics was scrutinized, counting stream streamlined features (velocity), temperature dispersion, and focuses of burning items (CO and NO_2). Relative comes about are displayed for the direct-flow mode (jets on inverse dividers) and the vortex mode (burners slanted at 30° for the evaporator pivot).
3. Vortex supply of the air–fuel mixture was found to extend the high-temperature zone, increase the flame-core temperature, and reduce outlet temperatures, significantly influencing the chemistry of combustion product formation. This effect is attributed to intensified vortex motion, enhanced convective transfer, and longer residence time of coal particles in the furnace.
4. Vortex burners reduce CO outlet concentrations by ~15% and NO_2 by ~20% compared with direct-flow burners.
5. The close agreement between experimental measurements and numerical predictions confirms the reliability of the proposed combustion chamber model and the methodology for simulating high-temperature reactive flows in real boiler geometries.
6. The results provide a basis for developing recommendations on optimizing pulverized coal combustion, with the dual objectives of improving power plant efficiency and reducing pollutant emissions.

Conflict of interest statement

The authors declare that they have no known competing financial interests or personal relationships that could have appeared to influence the work reported in this paper.

CRediT author statement

Askarova A.S.: Conceptualization, Funding acquisition; **Bolegenova S.A.:** Resources, Supervision; **Nugymanova A.O.:** Visualization, Investigation, Data curation, Writing-Original draft preparation; **Maximov V.Yu.:** Data curation, Methodology; **Bolegenova S.A.:** Software, Validation; **Ospanova Sh.S.:** Writing-Reviewing and Editing; **Shortanbayeva Zh.K.:** Validation; **Aubakirov N.P.:** Software, Writing-Reviewing and Editing; **Nurmukhanova A.Z.:** Supervision.

Funding:

This work has been funded financially by the Science Committee of the Ministry of Education and Science of the RK (Grant No. AP23490571).

References

1 Pan J., Liu G., Chen L., Xu Q. (2025) Coal dust exposure hazards and prevention technology: A review, *Process. Saf. Environ. Prot.,* 202(B), 107756. https://doi.org/10.1016/j.psep.2025.107756

2 Zhakiyev N., Burkhanova D., Nurkanat A., Zhussipkaliyeva Sh., Sospanova A., Khamzina A. (2025) Green energy in grey areas: The financial and policy challenges of Kazakhstan's energy transition, *Energy Res. Soc. Sci.,* 124, 104046. https://doi.org/10.1016/j.erss.2025.104046

3 Tang R., Cheng S. (2023). Combustion chemistry of unsaturated hydrocarbons mixed with NO_x: a review with a focus on their interactions, *Energies,* 16(13), 4967. https://doi.org/10.3390/en16134967

4 Bartela L., Gladysz P., Ochmann J., Qvist S., Sancho L.O. (2022). Repowering a coal power unit with small modular reactors and thermal energy storage, *Energies.* 15(16), 5830. https://doi.org/10.3390/en15165830

5 Messerle V.E., Askarova A.S., Bolegenova S.A., Maximov V.Yu., Nugymanova A.O. (2019) 3D-modelling of Kazakhstan low-grade coal burning in power boilers of thermal power plant with application of plasma gasification and stabilization technologies, *J. Phys. Conf. Ser.*, 1261(1), 012022. https://doi.org/10.1088/1742-6596/1261/1/012022

6 Abbas Q., Yaqoob H., Uzair S., Ali H.M., Jamil M.M. (2025) Utilization of local coal in Pakistan's oil-fired power plants and future clean technologies for power generation, *Case Stud. Chem. Environ. Eng.,* 11, 101132. https://doi.org/10.1016/j.cscee.2025.101132

7 Askarova A., Bolegenova S., Mazhrenova N., Manatbayev R., Ospanova Sh., Berezovskaya I., Maximov V., Nugymanova A., Shortanbayeva Z. (2016) 3D modelling of heat and mass transfer processes during the combustion of liquid fuel, *Bulg. Chem. Commun*., 48(E2), 229 – 235. Available at: http://www.bcc.bas.bg/BCC_Volumes/Volume_48_Special_E_2016/Special%20Issue%20E/Statii/Pages229-235.pdf

8 Gao M., Hong F., Yan G., Liu J., Chen F. (2019) Mechanism modelling on the coordinated control system of a coal-fired subcritical circulating fluidized bed unit, *Appl. Therm. Eng.,* 146, 548-555. https://doi.org/10.1016/j.applthermaleng.2018.09.119

9 Hongxin W., Chenyi S., Haidn O., Askarova A., Manfletti Ch., Slavinskaya N. (2023) A joint hydrogen and syngas chemical kinetic model optimized by particle swarm optimization, *Fuel*, 332, 125945. https://doi.org/10.1016/j.fuel.2022.125945

10 Messerle V., Karpenko E.I., Lavrichshev O.A., Ustimenko A. (2013) Plasma preparation of coal to combustion in power boilers, *Fuel Process. Technol.,* 107, 93-98. https://doi.org/10.1016/j.fuproc.2012.07.001

11 Askarova A., Georgiev A., Bolegenova S., Beketayeva M., Maximov V., Bolegenova S. (2022) Computational modeling of pollutants in furnaces of pulverized coal boilers of the Republic of Kazakhstan, *Energy,* 258, 124826. https://doi.org/10.1016/j.energy.2022.124826

12 Liu Ya., Lin B., Liu T., Hao Zh. (2025) Conjugate heat transfer characteristics of crushed coal rock mass under axial compression: Coupling numerical analysis based on CT reconstruction and FEM, *Int. J. Heat Mass Transf.,* 242, 126788. https://doi.org/10.1016/j.ijheatmasstransfer.2025.126788

13 Ustimenko A.B., Messerle V. (2018) Plasma Gasification Energy Conversion Systems, *Comp. Energy Syst.,* 4, 1026-1064. https://doi.org/10.1016/B978-0-12-809597-3.00444-2

14 Liu J., Yu P., Li Y., Wan Ch., Du D. (2022) Numerical simulation on convective heat transfer characteristics in porous media based on the digital rock technology. *Int. J. Heat Mass Transf., 196*, 123323. https://doi.org/10.1016/j.ijheatmasstransfer.2022.123323

15 Feng X.-B., Liu Q., He Ya-L. (2020) Numerical simulations of convection heat transfer in porous media using a cascaded lattice Boltzmann method, *Int. J. Heat Mass Transf.,* 151, 119410. https://doi.org/10.1016/j.ijheatmasstransfer.2020.119410

16 Liu Q., Zhong W., Yu A. (2025) Study on the gas-solid flow and reaction characteristics of oxy-fuel co-firing of coal and biomass in a pressurized fluidized bed by 3D Eulerian-Lagrangian modelling, *Powder Technol.,* 456, 120808. https://doi.org/10.1016/j.powtec.2025.120808

17 Liu X., Tan H., Wang Y., Yang F., Mikulčić H., Vujanović M., Duić N. (2018) Low NOx combustion and SCR flow field optimization in a low volatile coal fired boiler, *J. Environ. Manag.,* 220, 30 - 35.

https://doi.org/10.1016/j.jenvman.2018.05.009

18 Choi M., Park Ye., Li X., Kim K., Sung Y., Hwang T., Cho G. (2021) Numerical evaluation of pulverized coal swirling flames and NO_x emissions in a coal-fired boiler: Effects of co- and counter-swirling flames and coal injection modes, *Energy,* Vol. 217, 119439. https://doi.org/10.1016/j.energy.2020.119439

19 Xia Z., Chen C., Bi J., Li K., Jin Ya. (2016) Modeling and simulation of catalytic coal gasification in a pressurized jetting fluidized bed with embedded high-speed air jets, *Chem. Eng. Sci.,* 152, 624–635. https://doi.org/10.1016/j.ces.2016.06.052

20 Klimanek A., Bigda J. (2018) CFD modelling of CO_2 enhanced gasification of coal in a pressurized circulating fluidized bed reactor, *Energy,* 160, 710 – 719. https://doi.org/10.1016/j.energy.2018.07.046

21 Zhong W., Yu A., Zhou G., Xie J., Zhang H. (2016) CFD simulation of dense particulate reaction system: approaches, recent advances and applications, *Chem. Eng. Sci.,* 140, 16-43. https://doi.org/10.1016/j.ces.2015.09.035

22 Messerle V., Ustimenko A. (2020) Modeling of Coal Ignition in Plasma-Fuel Systems with an Electric Arc Torch, *IEEE Trans. Plasma Sci.,* 48(2), 344 – 349. https://doi.org/10.1109/TPS.2019.2956847

23 Askarova A.S., Bolegenova S.A., Maximov V.Yu., Beketayeva M.T. (2018) Modeling of Heat Mass Transfer in High-Temperature Reacting Flows with Combustion, *High Temp.,* 56(5), 738–743. https://doi.org/10.1134/S0018151X1805005X

24 Wu X., Hu F., Ding C., Yang Y., Yang Ch., Liao H., Lu K., Li B., Liu T., Liu Ch., Li P., Liu Zh. (2024) Progress in numerical simulations and fundamental characteristics of pulverized coal co-firing with ammonia, *Int. J. Hydrog. Energy,* 82, 740 – 758. https://doi.org/10.1016/j.ijhydene.2024.07.456

25 Askarova A.S., Bolegenova S.A., Georgiev A., Bolegenova S.A., Maximov V.Yu., Manatbayev R.K., Yergaliyeva A.B., Nugymanova A.O., Baizhuma Zh.T. (2018) The use of a new “clean” technology for burning low-grade coal in on boilers of Kazakhstan TPPs, *Bulg. Chem. Commun.,* 50, 53 – 60. Available at: http://bcc.bas.bg/BCC_Volumes/Volume_50_Special_G_2018/BCC_50G_PD_2018.Or.pdf#page=51

AUTHORS’ INFORMATION

Askarova, Aliya Sandybayevna – Doctor of Physical and Mathematical Sciences, Professor, Department of Thermophysics and Technical Physics, al-Farabi Kazakh National University, Almaty, Kazakhstan; SCOPUS Author ID: 6603209318; https://orcid.org/0000-0003-1797-1463; Aliya.Askarova@kaznu.edu.kz

Bolegenova, Saltanat Alikhanovna - Doctor of Physical and Mathematical Sciences, Professor, Department of Thermophysics and Technical Physics, al-Farabi Kazakh National University, Almaty, Kazakhstan; SCOPUS Author ID: 57192917040; https://orcid.org/0000-0001-5001-7773; Saltanat.Bolegenova@kaznu.edu.kz

Nugymanova, Aizhan Olzhabekkyzy – PhD, Senior Lecturer, Department of Thermophysics and Technical Physics, al-Farabi Kazakh National University, Almaty, Kazakhstan; SCOPUS Author ID: 57193723169; https://orcid.org/0000-0003-0393-5672; nugymanova.aizhan@kaznu.kz

Maximov, Valeriy Yuryevich – PhD, Professor, Department of Thermophysics and Technical Physics, al-Farabi Kazakh National University, Almaty, Kazakhstan; SCOPUS Author ID: 57130389500; https://orcid.org/0000-0003-4120-1071; valeriy.maximov@kaznu.kz

Bolegenova, Symbat Alikhanovna – PhD, Associate Professor, Department of Thermophysics and Technical Physics, al-Farabi Kazakh National University, Almaty, Kazakhstan; SCOPUS Author ID: 57195694754; https://orcid.org/0000-0003-1061-6733; bolegenova.symbat@kaznu.kz;

Ospanova, Shynar Sabitovna– PhD, Acting Associate Professor, Department of Thermophysics and Technical Physics, al-Farabi Kazakh National University, Almaty, Kazakhstan; SCOPUS Author ID: 55988678700; https://orcid.org/0000-0001-6902-7154; Shynar.Ospanova@kaznu.edu.kz

Shortanbayeva, Zhanar Kairzhanovna – Master (Sci.), Senior Lecturer, Department of Thermophysics and Technical Physics, al-Farabi Kazakh National University, Almaty, Kazakhstan; SCOPUS Author ID: 56943453700; https://orcid.org/0000-0002-1148-6865; Zhanar.Shortanbaeva@kaznu.kz

Aubakirov, Nurymzhan Parzhanovich - PhD, Senior Lecturer, Kazakh National Research Agrarian University, Almaty, Kazakhstan; SCOPUS Author ID: 58645049000; https://orcid.org/0000-0002-7340-2735; aubakirov.nurimzhan@yandex.ru

Nurmukhanova, Alfiya Zeinullovna – Candidate of Technical Sciences, Senior Lecturer, Department of Thermophysics and Technical Physics, al-Farabi Kazakh National University, Almaty, Kazakhstan; SCOPUS Author ID: 57217224044; https://orcid.org/0000-0002-0289-3610; alfiyanurmukhanova7@gmail.com

EURASIAN PHYSICAL TECHNICAL JOURNAL

2025, Volume 22, No. 4(54)

https://doi.org/10.31489/2025N4/74-81

Received: 22/04/2025 Revised: 15/10/2025 Accepted: 22/12//2025

Research Article

UDC 53/087; 654.9; 629.7

A STUDY OF DEPENDENCE RESONANCE FREQUENCIES OF DIFFERENTIAL CAPACITIVE SENSOR ON TIME

Nabiyev R.N., Garayev G.I., Rustamov R.R. *

National Aviation Academy of the Azerbaijan, Baku, Azerbaijan
**Corresponding author*: rrustamov@naa.edu.az

Abstract. *The article notes that airport perimeter security is considered one of the preventive measures in aviation security and the need to stimulate innovative devices led to the need to improve the sensors uses in perimeter security-warning systems. It emphasizes that the most widely used sensor in perimeter security-warning systems is the capacitive sensor and the importance of adapting to environmental changes is shown. Therefore, the article emphasizes that the purpose is to explore the environmental dependence of the frequency changes of two auto-generators built on digital logic elements applied as differential capacitive sensors. For this purpose, it is described the results from investigations of frequency variations of two auto-generators built on digital logic elements used as differential capacitive sensors in perimeter security-warning systems, as well as their synchronous operation in relation to each other's dependence on time. The mathematical expectation and dispersion of the variation values of the resonance frequencies of auto-generators which were connected to sensitive elements of different lengths were calculated in experiments, and it was found that the frequencies of the auto-generators changed more synchronously with each other. As a result, it is determined experimentally that, taking into account the time drift of the resonant frequency of auto-generators with sensitive elements of two meters length in laboratory conditions, the discreteness of the measured parameters allows us to determine the weight of the approaching object, and in all cases, the resonant frequencies of both auto-generators change approximately equally in both directions with a small difference depending on time.*

Keywords: aviation security, airport, perimeter, security-warning system, differential capacitive sensor, resonance frequency, sensitive element, dispersion.

1. Introduction

Early detection of an intruder within the airport area is considered a significant issue from a aviation security perspective [1-3]. An intruder intending to unlawfully enter the area first crosses the physical guarding fence installed around the perimeter of the area [4, p. 182-183]. With this in mind, the project of the guarding fence, as well as the effectiveness and reliability of the security-warning system installed along the perimeter, must be commensurate with the assessed risk of acts of unlawful interference that may be directed against civil aviation [5, p. 16, 25].

It is possible to reduce the damage caused by acts of terrorism and unlawful interference by detecting the intruder through special sensors installed in the security-warning system, generating an alarm signal regarding the intrusion, and delaying the intruder for a certain period of time in the physical guarding fence [6-8]. At the same time, the maximum sensitivity distance of the perimeter security-warning system should be increased and the probability of generating false warning signals in the system should be reduced as much as possible [9-11].

One of the top five challenges for aviation security is the proper use of methods for the "expansion of technical resources and stimulation of innovation" [12, p. 23]. As preventive measures in aviation security start with perimeter protection, the stimulus of innovation results in improving the sensors used for the perimeter security-warning systems of the airport. There is an urgent need to improve capacitive sensors, which are increasingly used in warning and perimeter protection systems in order to adapt to the environment [13, 14]. Capacitive sensors used in airport perimeter security-warning systems consist of sensitive elements that have a certain capacitance relative to the ground. When sensitive elements are approached or touched, the change in capacitance causes the frequency of the sensor's auto-generator to change and it was generated warning signal [15]. Since the frequency variations of the auto-generator differ depending on the length of the sensitive elements and the weights of the intruders, the sensitivity distance of the capacitive sensor and the frequency of the auto-generator's output signal also differ [16, 17].

Work objective. The dependence of the frequency variations of two auto-generators built on digital logic elements applied as differential capacitive sensors on the environment has been determined. Therefore, the synchronous operation of two auto-generators, each of which has simultaneously connected HEs of equal length, and the time dependence of the frequency distance were studied under various conditions. A metal case with auto-generators built on logic elements was grounded. Experiments were carried out with the lengths of sensitive elements measuring 2, 5, 6, 10, and 50-m.

2. Problem statement

The experiments carried out in both indoor and outdoor spaces on different days are described below.

In Fig. 1, as indoor space there is a metal box and laboratory room [16]. As for outdoor space, the VOR-DME is used (VOR - Omni-directional distance; DME - distance measuring equipment) in Fig. 1a, 1b.

a) b)

Fig. 1. Experiments in outdoor territories: a) in the territory of NAA, b) in the territory of VOR-DME.

To determine the dependence of frequency variations of auto-generators on time, the frequency variation diapasons within five- and one-hour durations were explored. Each of the first of five experiments lasted five hours; four of them were carried out in laboratory and one in the territory of of NAA (Table 1).

Table 1. Experiments to study the frequency variations of auto-generators.

Experiments	Location	Antenna length, m	During five hours with hourly -intervals	During one hour with five- minute – intervals
1	Case	-	+	+
2	Lab.	-	+	+
3	---	2	+	+
4	---	5	+	+
5	in the territory of NAA	10	+	+
6	in the territory of VOR-DME	50	-	+

3. Experimental technique

The values of the auto-generators frequency variations were measured using two eight-digit devices with the model number "SKU00653" and recorded with a video camera (Fig. 2).

Fig. 2. Auto-generators in a metal case

The accuracy of frequency counters has been tested with a "Tektronix AFG3102C" Function Generator and they were found to have high accuracy [18].

4. Results and discussion

4.1. Experiments lasting five hours

These experiments were carried out by registering the frequencies with an hourly interval during five hours.

In order to determine the individual resonance frequency diapasons of auto-generators in the 1st and 2nd experiments, the sensitive elements were not connected to them. In order to eliminate side effects in Experiment 1, the auto-generators are placed in a metal (screened) case. Under the same conditions, Experiment 2 was carried out without the use of a metal case.

The graphs in Fig. 3a and Fig. 3b illustrate the frequency variations of auto-generators according to Experiments 1 and 2, respectively. Although the frequency values slightly differ, in some graphs they are the same for both auto-generators (◆ -1st auto-generator, ■ - 2nd auto-generator). In circles within the Fig.3, certain parts of the graphs are enlarged to show the direction of the frequency axes.

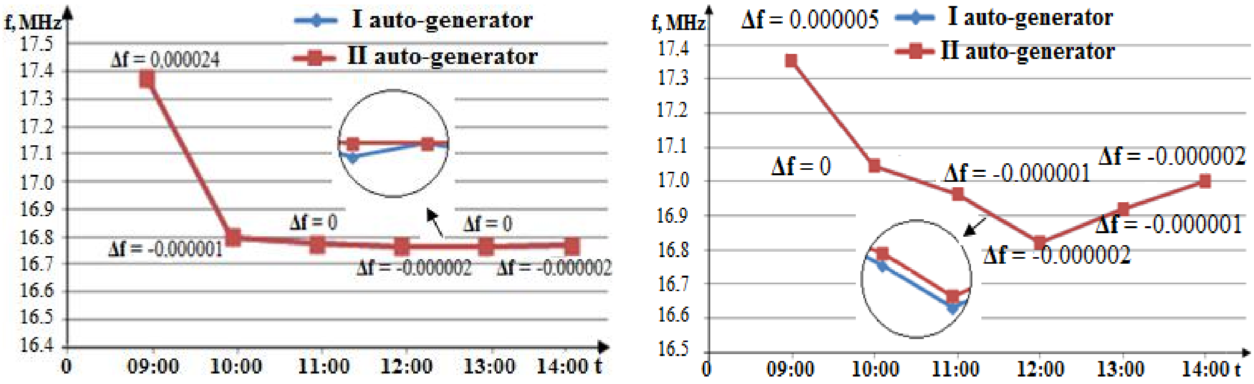

a) b)

Fig. 3. Frequency variations of auto-generators:
a) in a metal case under laboratory conditions, b) under laboratory conditions.

The graphs show that the difference between the resonance frequencies decreases over the time and becomes quite small, even zero in some cases.

Resonance frequency values for the 1st and 2nd auto-generators while running are respectively: in Experiment 1, f_1 = 17.374754 MHz, f_2 = 17.374778 MHz (Fig. 3, a): in Experiment 2: f_1 = 17.354630 MHz, f_2 = 17.354635 MHz (Fig. 3, b). In Experiments 3 and 4, for determination of - the effects of SEs on resonance frequencies, they were not initially connected to auto-generators. In this case, the recorded values of the frequencies are respectively: in Experiment 3, f_1 = 16.615353 MHz and f_2 = 16.615354 MHz; in Experiment 4, f_1 = 16.333898 MHz and f_2 = 16.333913 MHz.

In turn, two wires were connected separately to the auto-generators as SEs. In all experiments carried out with connected SEs, the lengths of the wires by which they consist were identical. The wires were attached to the dielectric supports in parallel to each other and to the floor. The distance between them was 10 cm, the altitude from the floor was 1 m, and the lengths were 2 m and 5 m in Experiments 3 and 4, respectively. After connecting the SEs: in Experiment 3, f_1 = 13.599993 MHz and f_2 = 13.599989 MHs and in Experiment 4, f_1 = 10.459934 MHz and f_2 = 10.459942 MHs. Such frequency variations were expected; adding the capacitance of SE to input capacitance will result in a reduction in the frequency of auto-generators. The graphs of the frequency variations according to Experiments 3 and 4 are illustrated in Fig. 4a and Fig. 4b respectively.

In the first four experiments, the maximum values of the variations of the resonance frequencies of the 1st and 2nd auto-generators are:

in Experiment 1, 0.605620 MHz and 0.605646 MHz;
in Experiment 2, 0.351823 MHz and 0.351830 MHz;
in Experiment 3, 0.113939 MHz and 0.1131936 MHz;
in Experiment 4, 0.1119920 MHz and 0.1119911 MHz, respectively.

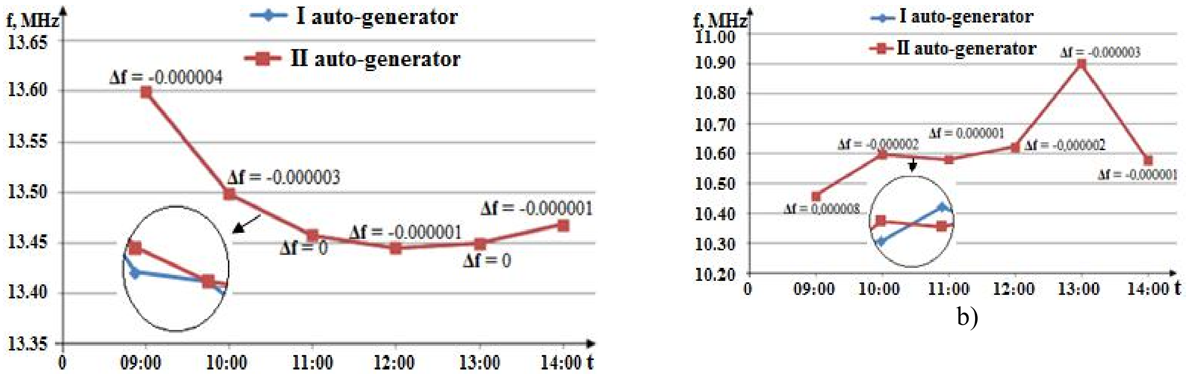

a) b)

Fig. 4. Frequency variations of SE connected auto-generators of 2 m (a) and 5 m (b) lengths.

Experiment 5 was carried out in the NAA territory, at an environment of temperature 8ºC, atmospheric pressure of 775 mm of mercury, and relative humidity of 70-80%, according to the report of the Ministry of Ecology and Natural Resources, February 5, 2019. Two wires each 10 m in length as SEs, were connected to the auto-generators and attached to dielectric supports in parallel to each other and to the surface of the Earth. The distance between the wires and their altitude from the surface of the Earth was equal to 1 m (Fig. 5). Each SE was connected to the auto-generators via a coaxial cable of 5 m in length. Screen coverage of coaxial cables was grounded, on the side where they are connected to auto-generators.

When the SEs were not connected, the values of the resonance frequencies of the auto-generators were f_1 = 17.709108 MHz and f_2 = 17.709110 MHz, respectively, and f_1 = 19.353318 MHz and f_2 = 19.353322 MHz after connection of the SEs. As seen, the frequency variation is not as expected. Such variations in frequency (i.e., increases) when connecting SEs may occur due to various reasons.

For example, SEs may increase the input potential of an auto-generator by receiving electromagnetic waves as an antenna in an outdoor space and by collecting electrical charges in the total input capacity. This corresponds to the reduction of the value of the total input capacity which in turn increases the frequency of the auto-generator. The total input capacitance of the auto-generator is determined by the capacitances of auto-generator input, the coaxial cable, and SEs. The experiments outlined below, which were carried out in the territory of VOR-DME, indicate that when the SE is 6 m in length and the frequency of the auto-generator is repeatedly higher than the value without SE, we can suggest that this is related to the resonance phenomena. Since it is not the object of our research, however, we have not carried out its analysis is not carried out.

Fig. 5 shows the graphs of frequency variations after connecting the SEs. As seen from the graphs, during the five-hour experiments and with regard to the initial values, the final value of the frequency increased by 0.095692 MHz in the 1st auto-generator and 0.095689 MHz in the 2nd auto-generator. The difference in frequencies is quite small at different hours, and the maximum difference (at 09:00) is 0.000004 MHz.

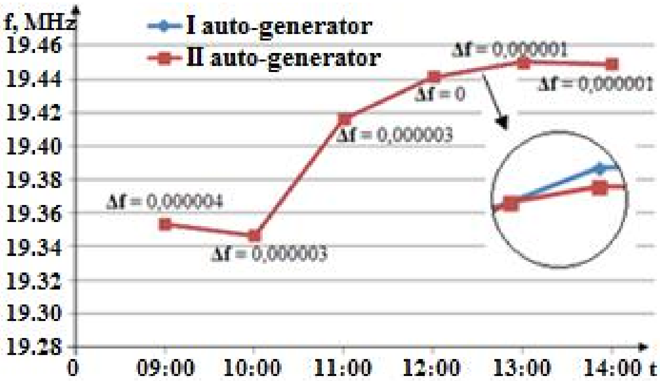

Fig. 5. Frequency variation of the 10m long SE connected auto-generators during five hours.

In all experiments, the recorded values of the resonance frequencies of the auto-generators are random. Comparison of the recorded values shows that the difference between the resonance frequencies of the auto-generators at the beginning of the experiment (09:00) were: in Experiment 1, Δf = 0.000024 MHz; in Experiment 2, Δf = 0.000005 MHz; in Experiment 3, Δf = 00.000004 MHz; in Experiment 4, Δf = 0.000008 MHz; and in Experiment 5, Δf = 0.000004 MHz which is more than the differences that occurred in other hours. These values can be ignored as the rough error that occurred at the beginning of the experiment. The estimated values of the mathematical expectation, dispersion and mean quadratic deviation of possible values of random numbers Δf for the five experiments during five hours, excluding initial values are provided in the following table (Table 2):

Table 2. The values of the mathematical expectation, dispersion and mean quadratic deviation of random numbers Δf.

No.	$M_N(\Delta f)$	$D_N(\Delta f)$	$\sigma_N(\Delta f)$
1	-10^{-6}	$8\cdot10^{-13}$	$89\cdot10^{-7}$
2	$-1.2\cdot10^{-6}$	$5.6\cdot10^{-13}$	$7.48\cdot10^{-7}$
3	-10^{-6}	$12\cdot10^{-13}$	$10.95\cdot10^{-7}$
4	$-1.4\cdot10^{-6}$	$18.4\cdot10^{-13}$	$13.56\cdot10^{-7}$
5	$1.6\cdot10^{-6}$	$14.4\cdot10^{-13}$	$120\cdot10^{-7}$

4.2. One-hour experiments

The frequency values in these experiments were recorded during one hour with five-minute of intervals. All conditions remained the same as in the five-hour experiments. In addition, one experiment was carried out with 50 m length wires in the territory of VOR-DME (Fig.1b). On that day, the environment was at a temperature of 22-24ºC and there was atmospheric pressure of 758 mm of mercury and relative humidity of 50-60 %. Values are based on data from the press service of the Ministry of Ecology and Natural Resources of May 5, 2019. The frequency variations of the auto-generators are illustrated in graphs in Fig.6a and Fig. 6b, in accordance with the 1st and 2nd Experiments. As seen from the graphs, the resonance frequencies of the auto-generators decreased during an hour at an approximately equal rate (Fig.7). The difference between the frequency values is significantly small (Δf ≤ 0.000003 MHz). This difference even accounts for Δf = 0.000001 MHz.

The frequency variations of the auto-generators in 3rd and 4th Experiments are illustrated in the respective graphs (Fig. 7a and Fig. 7b). As seen in the graphs, the resonance frequencies of the auto-generators vary over time. Comparison of the values shows that the difference between the values of the auto-generator resonance frequencies is quite small, i.e., Δf ≤0.000002 MHz in Experiment 3, Δf ≤ 0.000003 MHz in Experiment 4. This difference even equals zero in some cases.

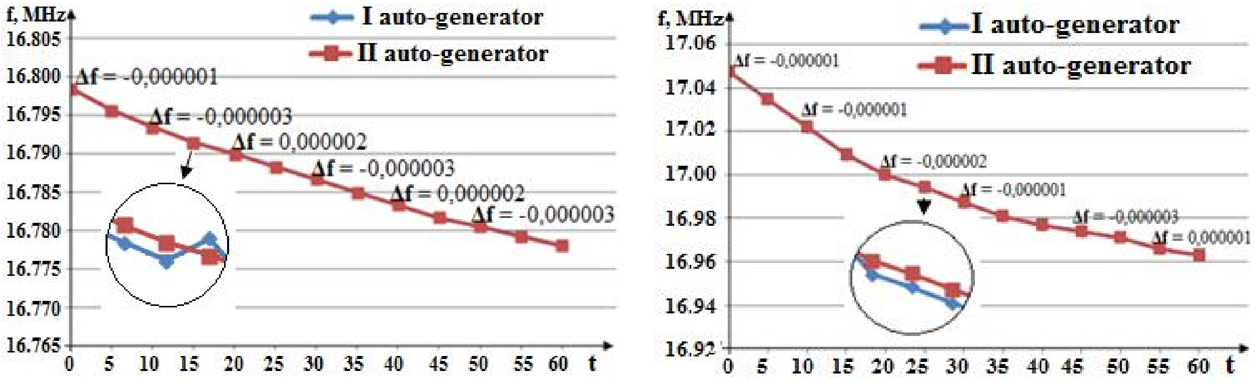

a) b)

Fig.6. Variations of resonance frequencies of the auto-generators within one hour: a) in a metal case, b) in a room.

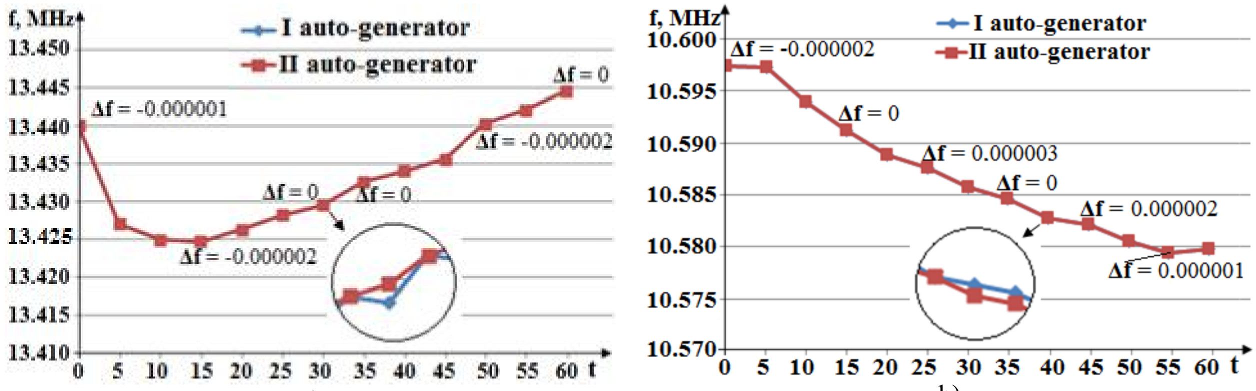

a) b)

Fig.7. Variations of resonance frequencies of the auto-generators within one hour connected to SEs with lengths 2 m (a) and 5 m (b).

The drift of frequency values on time during one hour is:

In Experiment 3, for the 1st auto-generator, $\Delta f_{zI} = \pm 0.009965$ MHz (13.429734 MHz ÷ 13.449664 MHz); for the 2nd auto-generator, $\Delta f_{zII} = \pm 0.009966$ MHz (13.429732 MHz ÷ 13.449664 MHz);

In Experiment 4, for the 1st auto-generator, $\Delta f_{zI} = \pm 0.0090275$ MHz (10.579381 MHz ÷ 10.597436 MHz); for the 2nd auto-generator, $\Delta f_{zII} = \pm 0.009026$ MHz (10.579382 MHz ÷ 10.597434 MHz). The variation diapason - Δf_z determines the degree of discreteness of the measurement system.

The graphs for frequency variations of the auto-generators in accordance with Experiments 5 and 6 are shown in Fig. 8a and Fig. 8b, respectively.

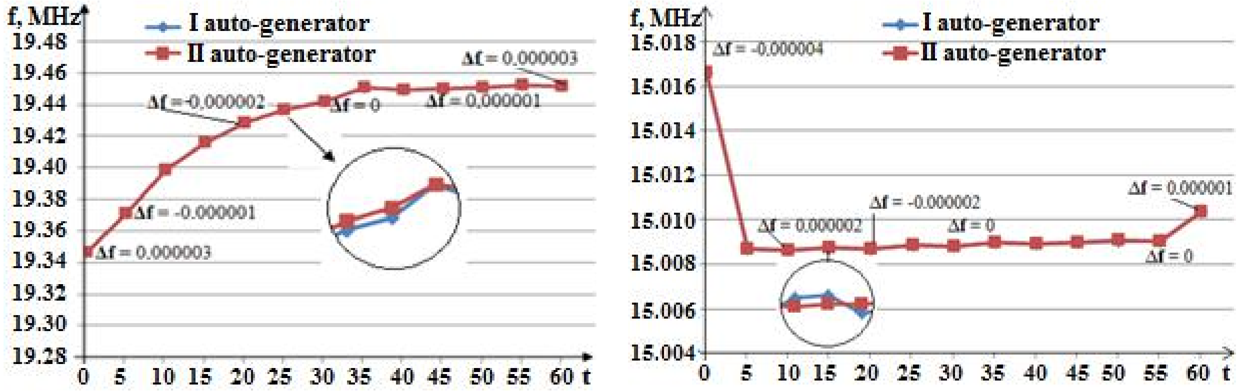

a) b)

Fig.8. Variations of resonance frequencies of the auto-generators during one hour connected to Ses with lengths 10 m (a) and 50 m (b).

Comparison of these values shows that the difference between the frequencies is quite small, and they are $\Delta f \le 0.000003$ MHz in Experiment 5 (Fig. 8a) and $\Delta f \le 0.000004$ MHz in Experiment 6 (Fig. 8b). This difference equals zero in both experiments at the half hour. As seen from the graphs, the resonance frequencies of the auto-generators vary in the same way.

Fig. 8a shows that the resonance frequencies of both auto-generators increase for 35 minutes after being turned on and subsequently, they vary up until the end of the hour with small differences, by increasing or decreasing. Within an hour, the resonance frequencies increase by 0.105322 MHz on both auto-generators. Fig. 8b shows that the resonance frequencies of both auto-generators decrease for five minutes after turning on and subsequently, they vary up until the end of the hour for 55 minutes with small differences, by increasing or decreasing. During one-hour experiment, the final values of the frequencies of the 1st and 2nd auto-generators decreased by 0.006271 MHz and 0.006266 MHz, respectively, with regard to the initial values. The maximum value of the variations of resonance frequencies of the auto-generators during one hour are:

1) On the 10 m length of SEs, $\Delta f_{zI} = \pm\ 0.052964$ MHz (19.346528 MHz ÷ 19.452456 MHz) for the 1st auto-generator, and $\Delta f_{zII} = \pm\ 0.0529635$ MHs (19.346531 MHs ÷ 19.452458 MHs) for the 2nd auto-generator;

2) On the 50 m length of SEs, $\Delta f_{zI} = \pm 0.004001$ MHs (15.008618÷15.016619 MHs) for the 1st auto-generator, and $\Delta f_{zII} = \pm 0.003998$ MHs (15.008620÷15.016615 MHs) for the 2nd auto-generator.

5. Conclusion

Taking into account the time-dependent drift ($\Delta f_{zI} = \pm\ 0.009965$ MHz and $\Delta f_{zII} = \pm\ 0.009966$ MHz) of resonance frequencies values of auto-generators with sensitive elements of 2 m in length, under laboratory conditions, the discreteness value of the measured parameters on both auto-generators was $n_m = 15$, which allowed for determination of the weight of the approaching object.

Comparisons of the dispersions ($D_1(\Delta f) = 8 \cdot 10^{-13}$; $D_2(\Delta f) = 5.6 \cdot 10^{-13}$; $D_3(\Delta f) = 12 \cdot 10^{-13}$ $D_4(\Delta f) = 18.4 \cdot 10^{-13}$ and $D_5(\Delta f) = 14.4 \cdot 10^{-13}$) of random values Δf_i showed that, in the experiments carried out, the value of the dispersion calculated in Experiment 2 was much smaller than in others. The calculated ratio between the dispersions in Experiments 4 and 2 ($D_4\ (\Delta f)\ /\ D_2\ (\Delta f) \approx 3.3 \cdot 10^{-13}$) was approximately 3. This also indicates that frequency variations of auto-generators in Experiment 2 were more synchronous.

The results of the experiments showed that, in all cases, the resonance frequencies of both auto-generators varied with a small difference in both sides (either increasing or decreasing) depending on time. The difference in resonance frequencies decreased over the time, accounting for a quite small value, even zero. In all experiments, the recorded values of the resonance frequencies of the auto-generators were random.

Conflict of interest statement

The authors declare that they have no conflict of interest in relation to this research, whether financial, personal, authorship or otherwise, that could affect the research and its results presented in this paper.

CRediT author statement

Nabiyev R.N.: Conceptualization, Methodology, Supervision; **Qarayev Q.I.:** Software, Writing-Original draft preparation, Validation; **Rustamov R.R.:** Data curation, Investigation, Visualization, Writing- Reviewing and Editing. The final manuscript was read and approved by all authors.

References

1 Nabiyev R.N., Ramazanov K.Sh., Rustamov R.R. (2019) Mathematical model of advanced security-warning system. *Scientific Journal National Aviation Academy,* 1(21), 132-140. [in Azerbaijani]. https://doi.org/10.30546/EMNAA.2019.21.1.132

2 Zaikov D.E. (2024) Airport border security: retrospective analysis and legal regulation prospects. *Transport law and security. Russian University of Transport,* 4(52), 31-40. Available at: https://trans-safety.ru/tpb/articles/ 2025/pdf/52/02_zaikov.pdf [in Russian].

3 Anyukhin S.G., Proshutinsky D.A, Permyakov M.P. (2020) New approaches to building detection systems for object protection. *International Scientific-Technical Conference "Safety Systems",* Moscow, 9, 231-233. [in Russian]. Available at: https://www.elibrary.ru/item.asp?id=45631025

4 *Doc. 8973 – Restricted. Aviation Security Manual of ICAO.* (2022) Montreal, 13. 946. Available at: https://store.icao.int/en/aviation-security-manual-doc-8973

5 Ganiyev SH.F. (2021) Sistema sertifikatsii v oblasti aviatsionnoy bezopasnosti. ID Akademii Zhukovskogo, Moscow, 48. [in Russian] Available at: http://storage.mstuca.ru/xmlui/bitstream/handle/123456789/9099/%21T_%D0%A3%D0%9F%20%D0%93%D0%B0%D0%BD%D0%B8%D0%B5%D0%B2%20%D0%A8.%D0%A4.%20%D0%A1%D0%B8%D1%81%D1%82.%20%D1%81%D0%B5%D1%80%D1%82%D0%B8%D1%84.pdf

6 Chinyakova E.V. (2020) Analysis and development of technologies in the system of preventing acts of illegal interference in the activities of civil aviation of the Russian Federation. *Bulletin of Science and Education. Scientific and methodological journal, Russian Federation*. 9(87), 1, 27-31. [in Russian]. Available at: https://scientificjournal.ru/ images /PDF/2020/87/VNO-9-87-I-.pdf

7 Sokolov V.M., Kezhov A.A., Nishanbayev Z.T. (2023) Design of a multi-sphere multispectral internal affairs bodies installation protection system on the basis of the perimeter security system “Radar-IQ”. *Scientific and technical journal I-methods, Russia, Saint Petersburg*. 15(2) 1-19. [in Russian]. Available at: http://intech-spb.com/wp-content/uploads/archive/2023/2/Sokolov.pdf

8 Nabiyev R.N., Abdullayev A.A., Qarayev Q.I. (2024) On-board control-measurement system for micro convertiplane-type unmanned aerial vehicles. *Eurasian Physical Technical Journal*. 21, 2(48). https://doi.org/10.31489/2024No2/61-69

9 Ivanov E. (2022) Air transport infrastructure perimeter security systems. *Security systems*. 6(166). 66-67. [in Russian] Available at: http://cs.groteck.ru/SS_6_2022/70/

10 Tushko I. (2022) Engineering security equipment for protecting transport facilities perimeter. *Security systems*. 6. 166. 67-68. Available at: http://cs.groteck.ru/SS_6_2022/70/

11 Teixidó P., Gómez-Galán,J. A., Caballero R., Pérez-Grau F. J., Hinojo-Montero J. M., Muñoz-Chavero F., Aponte, J. (2021) Secured perimeter with electromagnetic detection and tracking with drone embedded and static cameras. *Sensors*. 21(21), 7379. DOI: https://doi.org/10.3390/s21217379.

12 *Doc 10118. Global aviation security plan of ICAO*. (2024) Montreal, 2. 34. Available at: https://www.icao.int/Security/Documents/GLOBAL%20AVIATION%20SECURITY%20PLAN%202nd%20Ed.EN.pd

13 Endang S.A., Nunuk P., Rinosa A.W., Dini W. (2023) Airport perimeter security system readiness analysis (case study at Budiarto Curug-Tangerang Airport). *Siber Journal of Transportation and Logistics*. 1(2), 64-71. DOI: https://doi.org/10.38035/sjtl.v1i2.42.

14 Heško F., Fiľko M., Novotňák J., Kašper P. (2021) Perimeter protection of the areas of interest. *Acta Avionica*. 23, 45, 2, 31-44. https://doi.org/10.35116/aa.2021.0014.

15 Pashayev A.M. Nabiyev R.N., Garayev G.I., Rustamov R.R. (2022) *Differential capacitive sensor*, Patent (Invention), İ 2022 0033, Intellectual Property Agency of the Republic of Azerbaijan, Patent and Trademark Examination Center. No.8, Publ. 31.08.2022. Available at: https://patent.copat.gov.az/files//21292216552597822637 ixtira% 2008.2022.pdf

16 Nabiyev R.N., Garaev G.I., Rustamov R.R. (2021) The study of dependence of the resonance frequencies of differential sensor on the intruder’s approaching. International Scientific and Practical Conference International Trends in Science and Technology. Warsaw, Poland. 28, 3-8. DOI: https://doi.org/10.31435/rsglobal_conf/30042021/7526.

17 Makeeva O.V., Oleshko V.S., Fedorov A.V., Yurov V.M. (2020) Development of a device for determining work electron output. *Eurasian Physical Technical Journal.* 17, 1(33), 127-131. DOI 10.31489/2020No1/127-131.

18 Nabiyev R.N., Garayev G.I., Rustamov R.R. (2022) Differential-capacitory device with two autogenerators. *Izvestiya SFedU. Engineering Sciences, Scientific, technical and practical journal, Taganrog*. 2(226), 145-153. [in Russian] DOI 10.18522/2311-3103-2022-2-145-153.

AUTHORS’ INFORMATION

Nabiyev, Rasim Nasib – Doctor of of Techn. Sciences, Professor; Head of Aviation Electronics Department; Scientific Research Institute of the National Aviation Academy of Azerbaijan, Baku, Azerbaijan; Scopus Author ID: 57217116540; https://orcid.org/0000-0002-1727-0360; rnabiyev@naa.edu.az

Garayev, Gadir Isaxan – PhD (Eng.), Scientific Researcher, Aviation Electronics Department; Scientific Research Institute of the National Aviation Academy of Azerbaijan, Baku, Azerbaijan; https://orcid.org/0000-0001-7232-669X; qadir.qarayev@naa.edu.az

Rustamov, Ruslan – PhD (Eng.), Senior Teacher, Aviation Security Department, National Aviation Academy of Azerbaijan, Baku, Azerbaijan; https://orcid.org/0000-0001-6969-6796; rrustamov@naa.edu.az

EURASIAN PHYSICAL TECHNICAL JOURNAL

2025, Volume 22, No. 4(54)

https://doi.org/10.31489/2025N4/82-93

Received: 16/09/2025 Revised: 27/10/2025 Accepted: 22/12/2025

Research Article

UDC 53.083.7:621.396

MODELING AND MEASUREMENT OF ANTENNA CHARACTERISTICS OF A SATELLITE STATION BASED ON SOFTWARE-DEFINED RADIO

Baktybekov K.S.[1]*, Ashurov A. E.[2], Ivanov A. V.[1], Kelgenbayev A. Zh.[1], Zhapanova A. S.[3], Sailaubaiuly S.[1]

[1] Ghalam LLP, Astana, Kazakhstan
[2] L.N. Gumilyov Eurasian National University, Astana, Kazakhstan
[3] S. Seifullin Kazakh Agrotechnical Research University, Astana, Kazakhstan
**Corresponding author*: k.baktybekov@ghalam.kz

Abstract. *This study investigates the characteristics of a parabolic satellite antenna designed for communication with low Earth orbit satellites in the S-band. The choice of the S-band is motivated by the significantly lower power consumption of the radio link compared to the X-band. The S-band (2–4 GHz) is less sensitive to adverse weather effects than the X-band (8–12 GHz). These factors are critical for nanosatellites during Earth observation (EO) data transmission. Particular attention is given to measurements of the radiation pattern of the parabolic antenna in the S-band. These measurements provide essential data for optimizing the antenna design and parameters, thereby enhancing the overall efficiency of the communication system. During testing, both simulated and experimental radiation patterns of the gain were obtained, along with key antenna parameters such as Equivalent Isotopically Radiated Power, Input Power Flux Density, and the Gain-to-Noise Temperature Ratio. A comparison between measured and calculated results, including measurement accuracy and error budgets, demonstrated good agreement.*

Keywords: radiation pattern, parabolic antenna, S-band, ground station, gain measurement, modeling.

1. Introduction

Modern low Earth orbit (LEO) satellite systems play a crucial role in the development of global communication networks, offering low latency and high throughput, which are particularly valuable in applications such as the Internet of Things (IoT), Earth observation, and broadband access [1-2]. However, effective communication with rapidly moving LEO satellites requires antenna systems with high directivity that can adapt to dynamically changing link geometries. Parabolic antennas remain one of the most widely used solutions for ground stations due to their ability to focus electromagnetic energy into a narrow beam, ensuring high gain and minimal losses [3]. The main challenges in operating with LEO satellites are related to continuous tracking and compensation of atmospheric distortions, particularly in the X-band (8-12 GHz), where weather effects become significant [4]. In contrast, the S-band (2-4 GHz) is less affected by precipitation but requires a larger aperture size to achieve comparable directivity, complicating mechanical control [5]. Previous studies [6-7] have highlighted the importance of optimizing the reflector shape and feed system to minimize sidelobe levels, which is critical for reducing interference in dense satellite constellations.

Modern approaches to enhancing the efficiency of parabolic antennas include hybrid solutions that combine mechanical scanning with electronic beam steering using phased arrays [8]. However, as noted in [9], most research has been focused on geostationary satellites, while the specific challenges of LEO orbits-such as short visibility windows and frequent beam reorientation-remain insufficiently explored. This paper presents a comprehensive analysis of the directional characteristics of a parabolic antenna in the S-band, including radiation pattern modeling, gain evaluation, and both simulation and measurement of Equivalent Isotropically Radiated Power (EIRP), Input Power Flux Density (IPFD), and the Gain-to-Noise Temperature Ratio (G/T). The results are compared with recent studies on adaptive algorithms [10], providing recommendations for the design of next-generation ground stations.

In recent years, significant attention has been devoted to optimizing the directional characteristics of parabolic antennas for LEO satellites. Research indicates that in the X-band, achieving a gain of 50–55 dBi requires extremely high reflector surface accuracy (RMS ≤ 0.25 mm) and careful feed design [11]. In the S-band, however, challenges remain in reducing cross-polarization distortions and adapting to varying satellite orientations, which is often addressed through circular polarization [12]. It was also shown in [12] that a developed software-defined radio (SDR) transceiver based on field-programmable gate arrays (FPGA) provides greater flexibility, enabling operation across multiple frequency bands, filtering schemes, and adaptive modulation and coding techniques without major hardware modifications.

Within this research, both radiation pattern modeling and gain evaluation were carried out, and the results were compared against experimental measurements. Particular emphasis was placed on measuring the radiation pattern of the parabolic antenna in the S-band, designed for receiving payload data and telemetry as well as transmitting command signals. These measurements provide essential insights for optimizing antenna design and parameters, thereby improving the overall performance of the communication system.

2. Structural scheme of the device under test and radiation pattern simulation results

The device under test is a prime-focus parabolic reflector antenna developed for operation in the frequency range 2.025 - 2.300 GHz with right- and left-hand circular polarizations. The parabolic reflector has a diameter of 3.7 meters and is equipped with a dual-band waveguide feed. The dual-band feed is installed at the prime focus of the reflector and provides simultaneous reception in the X-band as well as both transmission and reception in the S-band [13]. The S-band receive chain includes a low-noise amplifier (LNA) with a gain of 30 dB at 2.226 GHz for downlink (DL) and 2.060 GHz for uplink (UL). For measurement purposes, a test coupler (BDC 1018-30/20S, S-band downlink) was added to the scheme.

The bandpass filter, directional coupler, and LNA are integrated into the feed assembly. The LNA is powered via a supply unit located in the enclosure assembly (downlink). A test cable is routed between the output of the power supply and the switch on the DUT positioner. The modem unit is a functional subsystem that consists of an SDR modem and a control computer. The SDR performs the primary signal processing tasks-modulation, demodulation, filtering, and frequency conversion. The control computer operates the SDR, implements communication protocols, processes data, and provides interfacing with external systems [13].

The S-band transmit chain (enclosure assembly uplink), including a preamplifier and a high-power amplifier (HPA) with an output power of 30 W, amplifies the RF signal generated by the SDR. The amplified signal is transmitted through the chain with consideration for circular cross-polarization isolation (S-band uplink). The signal is then fed into the antenna feed and radiated by the antenna at 2060 MHz. The structural scheme of the testing device is shown in Figure 1.

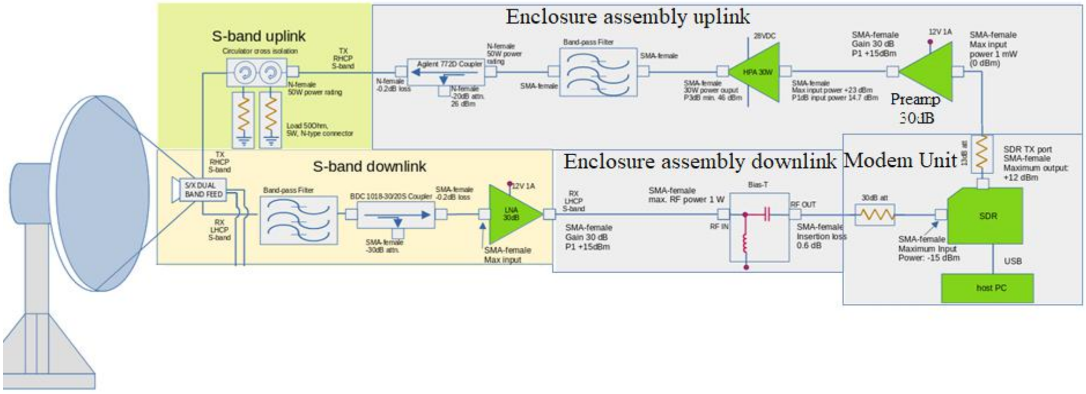

Fig.1. Structural scheme of testing device.

Prior to testing, the antenna geometry was modeled in CAD, and simulations were conducted in Ansys HFSS. The calculated radiation pattern of the antenna in the S-band at 2060 MHz is presented in Figure 2.

The contour plot of the calculated radiation pattern of the antenna in the S-band at 2060 MHz is shown in Figure 3.

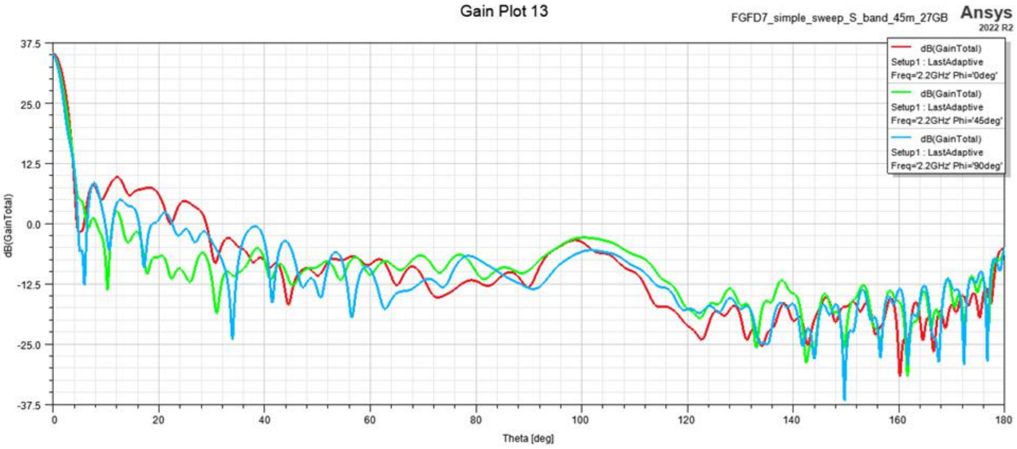

Fig.2. Calculated radiation pattern of the antenna in the S-band.

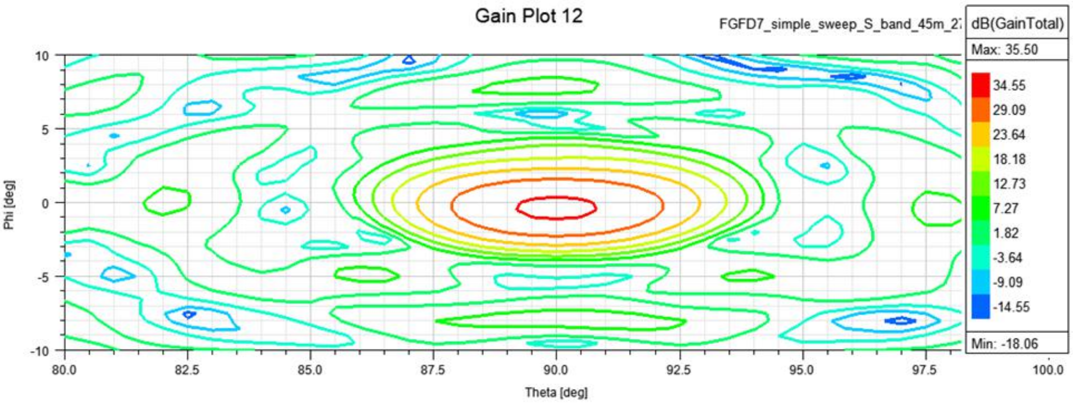

Fig.3. Contour plot of the calculated radiation pattern of the antenna in the S-band.

According to the modelling results in ANSYS HFSS, the antenna Gain should be 35.5dBi maximum, and beamwidth around 2.5 degrees at -3dB. Side-lobes are at level -25dB.

3. Antenna radiation pattern measurements

The radiation pattern measurements were performed using the “on-the-fly” method, in which the measurement axis (AZ or EL) of the DUT positioner is continuously scanned over a predefined angular range without stopping at each grid point. The measurement is conducted during the motion sequence when the DUT positioner passes through one of the specified grid points. The applied DUT positioner supports radiation pattern measurements in both receive (DL) and transmit (UL) modes, enabling a comprehensive analysis of antenna characteristics. For the present study, the antenna radiation pattern was measured in receive mode.

The RF budget of the antenna radiation pattern at 2.226 GHz is presented in Table 1. The experimental setup for radiation pattern measurement is shown in Figure 4. The test setup for radiation pattern measurements consists of three sections: the Feed room, Measurement room, and Operator room. Each section represents a dedicated space housing specific equipment. The Feed room includes the feed positioner 30R99 and the equipment rack 30R01. The Measurement room contains the DUT positioner 10R99 and equipment racks 10R01 and 10R02. The Operator room hosts the equipment rack 20R01 and the operator’s workstation.

The transmit subsystem comprises an RF synthesizer (1) located in rack 30R01, as well as power amplifiers (2), a broadband directional coupler (5), and a PIN switch (6). The latter is used to switch between two linear polarization ports of the feed (7) and operates up to 40 GHz (30R99). Port switching is controlled by the measurement system controller (13) and PC1 software. The receiver (13), controller (14), and PC1 are installed in the Operator room. A frequency distribution converter, Mixer 1 (3), is located in the Feed room (30R99) to handle the RF reference signal.

Table 1. RF budget of the antenna radiation pattern at 2.226 GHz

F, MHz	Gen out, dBm	Gen out-PA in, path loss, dB	HPA #1, gain dB	J05 F-Feed, dB	Tx feed, Gain, dBi	Free-space Loss, dB	Antenna Gain, dBi	Filter, dB	DUT coupler, dB	DUT coupler-LNA in, loss, dB	ASCU LNA, input, dBm	LNA, gain, dB	Rx Mixer, dBm
2226	-30	-3,5	42	-1,5	12	-64,90	35	-1	-30	-4,5	-46,40	25,7	20,7

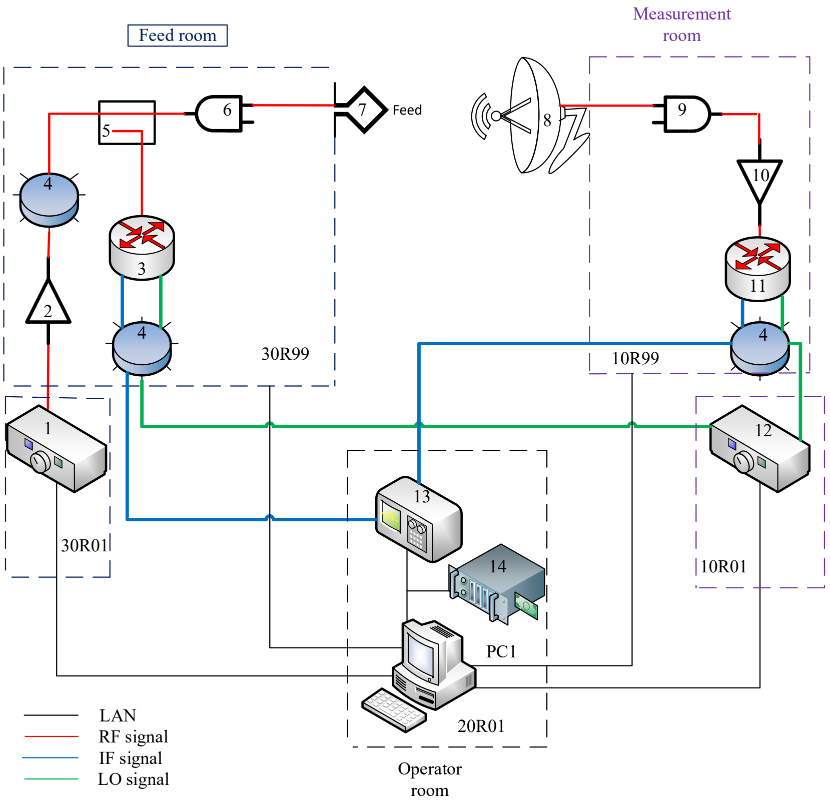

Fig.4. Experimental setup for radiation pattern measurement.

The RF signal is generated by the synthesizer, with frequency and power levels controlled at a fixed reference level using the microwave receiver (13) and PC software via the IEEE bus from PC1. The transmitted and amplified RF signal is radiated through the feed (7). Along the signal path, several coaxial switches are employed, including an IF switch block (4) for Tx/Rx mode selection. The reference signal coupler (5) is connected to the reference mixer Mixer 1 (3), which operates in the main mixing mode, ensuring extended dynamic range and thus higher measurement accuracy.

The receive subsystem consists of the antenna under test (8), a 2-port PIN switch (9), a low-noise amplifier (LNA) (10), Mixer 2 (11), coaxial IF switch block (4), and an LO synthesizer (12). The intermediate frequency signal from the IF switch is routed to port 2 of the receiver (13), where it is processed and read using the software on PC1. The system controller (14) performs synchronization, distributing trigger pulses from the position encoder to the measurement equipment (RF/LO sources, receiver, and PIN switches) as the DUT passes through the specified points, ensuring precise timing coordination of the measurements.

4. Antenna Gain Measurements

The application of the three-antenna gain measurement methods is generally infeasible due to the large size of the antenna and the limited space in the feed room. Furthermore, the antenna's dimensions do not allow for disassembly or replacement with other antennas on the feed positioner, which is required for applying the three-antenna techniques. Therefore, the power measurement method (PMM) [14] was employed in the experimental setup. This method is well established and widely used. Determining the gain with a power meter is both flexible and efficient, making it particularly suitable for large satellite antennas. The described method provides a measurement accuracy of ±0.25 dB.

In the measurement software was added gain measurement method utilizing two power sensor heads. This enables measurements of the absolute gain of the DUT. By measuring the output power of the feed, the input power of the antenna, and accounting for free-space losses as well as the feed gain, the gain of the device under test can be readily calculated using the following equation:

$$\frac{P_r}{P_t} = \left(\frac{\lambda}{4\pi R}\right)^2 \cdot G_t \cdot G_r; \tag{1}$$

where: Pt - transmitted power; Pr - received power; Gt - transmitting antenna gain; Gr - receiving antenna gain; R - free-space distance; λ - wavelength.

Table 2 presents the radio frequency (RF) link budget of the antenna gain at 2.226 GHz.

Table 2. Radio frequency (RF) link budget of the antenna gains at 2.226 GHz.

F, MHz	Gen out, dBm	Gen out-HPA in path los, dB	HPA#1 Gain, dB	J05F-Feed, dB	Tx feed Gain, dBi	Free-space Loss, dB	Antenna Gain, dBi	Filter, dB	DUT coupler, dB	DUT coupler LNA in, dB	ASCU LNA in, dBm	LNA Gain, dB	Rx Mixer, dB
2226	-38,5	-3,5	42	-6,4	12	-64,84	34	-1	-30	-4,5	-63,7	25,7	-38,04

Figure 5 shows the block diagram of antenna gain measurement in the receive mode (DUT Rx).

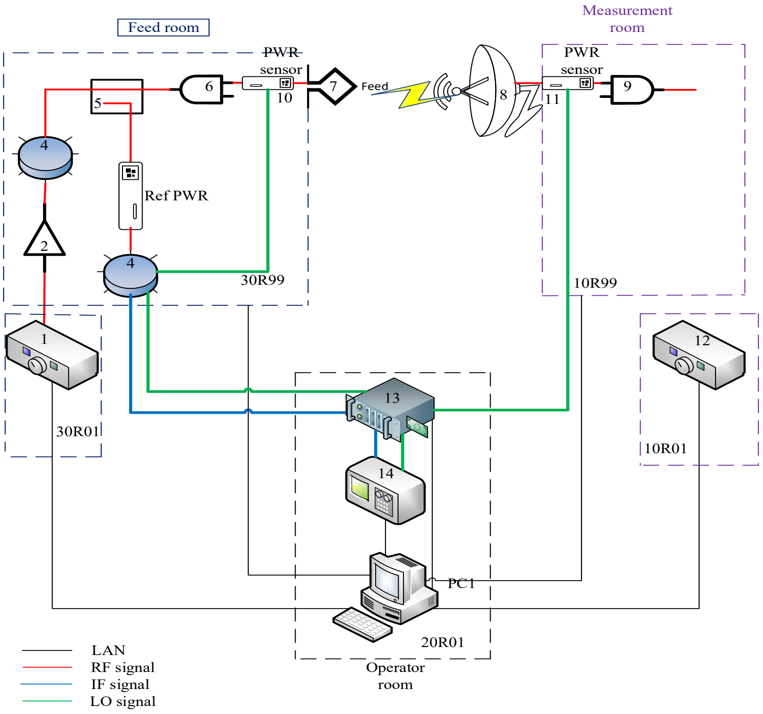

Fig.5. Block diagram of antenna gain measurement.

In this mode, the PC1 software, together with power sensors (10, 11) connected via the controller (13), provides automatic switching between power measurements at the input port (11), connected to the antenna (8), and the output port (10), connected to the feed (7). The measured power values from both ports are fed into the power meter (14) and then transferred via the IEEE interface to the personal computer (PC1), where they are processed by the software in accordance with the previously presented equation. The measured value of 31 dBi then should be corrected by adding 3dB due to the applied method and hardware. The measurement feeds are operating in linear polarization, whereas the DUT feed in circular. Therefore the resulted Gain is equal to 34 dBi.

5. Equivalent Isotropically Radiated Power (EIRP) Measurement

The Equivalent Isotropically Radiated Power (EIRP) is defined as the product of the transmitting antenna gain (G_{TX} in given direction and the input power applied to the antenna (P_{TX}):

$$\mathrm{EIRP} = G_{TX} \cdot P_{TX} \tag{2}$$

For EIRP measurement, a formula based on the Friis transmission equation is applied, where the parameters of the range feed antenna are used instead of those of the device under test (Tx antenna):

$$\mathrm{EIRP} = \frac{P_{RX,feed} \cdot LP_{down}}{G_{RX,feed}}; \tag{3}$$

$$LP_{down} = (4\pi R/\lambda)^2; \tag{4}$$

where: LP_{down}- free-space path loss, $G_{RX,feed}$- range feed gain; $P_{RX,feed}$ - received power at the range feed; λ - wavelength of the test signal; R - free-space distance (distance between the device under test and the range feed).

The RF budget of the EIRP at 2.060 GHz is presented in Table 3. The antenna must be aligned with the symmetry axis of the measurement zone (Measurement Room). The input signal is applied as a synthesized continuous wave (CW) (1) with a sufficient level to saturate the transponder (10R02). The transmitted and received power are measured using power meters (3) and (11), and based on the known antenna characteristics and the distance to the Range Feed antenna, the EIRP is calculated.

Table 3. RF budget of the EIRP at 2.060 GHz.

F, MHz	Prx (PM), dBm	Cable path D/L Loss, dB	D/L Range feed Gain, dBi	Free space Loss, dB	dBm to dBW	EIRP, dBW
2060	12,75	-6,4	11,6	-64,23	30	41,78

Note: EIRP and IPFD tests are typically performed under payload saturation conditions, i.e., at its maximum output power. Two methods are commonly used to determine saturation [15]:

- by measuring the maximum output power using power meters (3) and (11);
- by analyzing the carrier-to-noise ratio using the signal analyzer (9).

Figure 6 illustrates the schematic diagram for the EIRP test.

6. The Input Power Flux Density (IPFD) Measurement

The Input Power Flux Density (IPFD) is defined as the power flux density required to saturate the device under test, and can be expressed as [16]:

$$\mathrm{IPFD} = P_{TX,feed} \cdot G_{TX,feed} \cdot \left(\frac{1}{4\pi R2}\right), \tag{5}$$

where: $G_{TX,feed}$ is the range feed gain; $P_{TX,feed}$ is the transmitted power of the range feed; R is the free-space distance (i.e., the distance between the device under test and the range feed); $(1/4\pi R^2)$ is the free-space distribution factor.

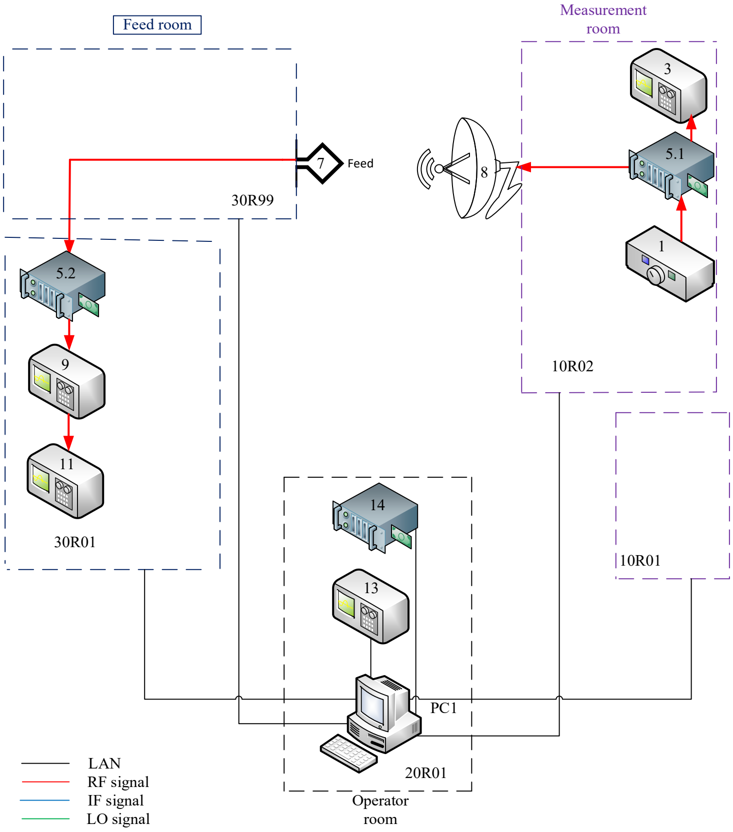

Fig.6. EIRP testing scheme.

The RF budget of the IPFD at 2.060 GHz is presented in Table 4. To determine the IPFD, the testing antenna (Measurement Room) must be aligned with the axis of the measurement zone at the maximum of its radiation pattern. A synthesized CW signal (1) is applied through the feed (7), ensuring saturation of the payload of the antenna (Measurement Room). The required input power saturation level at the antenna can be measured using the power meter (10). With the known feed gain and the distance **R**, the IPFD can then be calculated using the aforementioned equation in the PC1 software. Figure 6 presents the schematic diagram of the IPFD test.

Table 4. RF budget of the IPFD at 2.060 GHz.

F, MHz	Power Meter Tx, dBm	Cable path U/L reference, dB	Tx Power dBm	U/L cable path 7m loss, dB	U/L Range antenna gain, dBi	Spreading loss, dB	dBm to dBW	IPFD, dBW/ m^2	IPFD circular estimation
2060	-36	-16	-20	-6	12	-36,44	30	-50,44	-53,44

7. Measurement of Receiver Chain Figure of Merit (G/T)

The principle of the test setup for G/T is shown in Figure 7. The determination of G/T is performed by measuring three different power levels [17]:

– P_1 - the noise power level of the receiving test equipment. For this purpose, the feed (7) is terminated with a 50 Ω load, and the test equipment (10R02) is disconnected from the antenna. The intrinsic noise of the test equipment P_1 (10) is then measured;

– P_2 - the noise power level of the receiving test equipment, including the internal noise of the measurement equipment (10R02);

– P_3 - the power level of the receiving test equipment (10R02), including the antenna noise and the power from the feed.

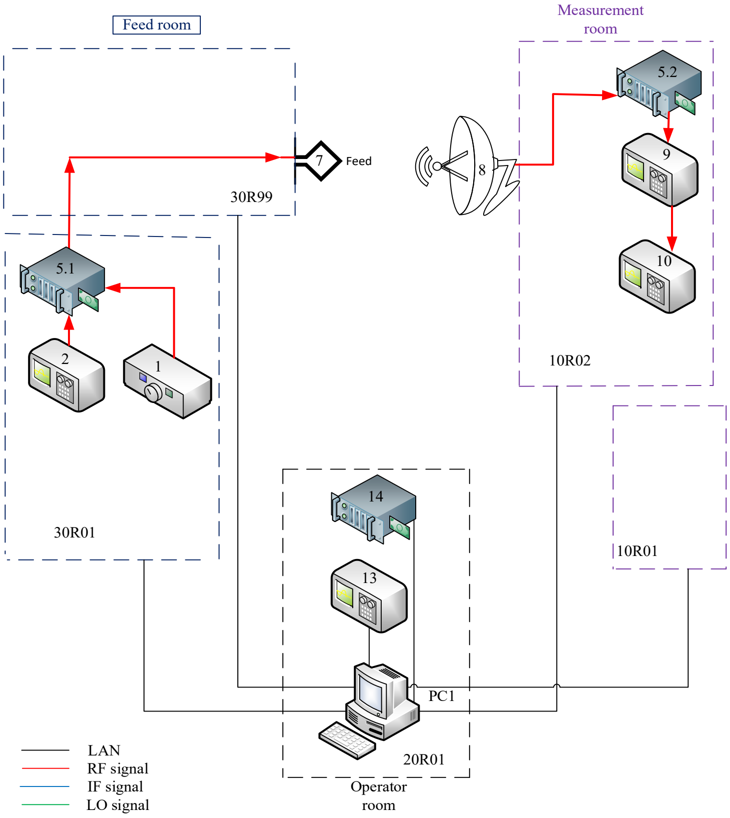

Fig.7. Schematic diagram of the IPFD and G/T test.

After the power levels are measured, the stored data are processed in the PC1 software, where the G/T value is automatically calculated using the following equation [18].

$$\frac{\mathrm{G}}{\mathrm{T}} = \left(\frac{k\cdot \mathrm{B}*\cdot LP}{EIRP}\right)\cdot\left(\frac{\mathrm{P3}-\mathrm{P2}}{\mathrm{P2}-\mathrm{P1}}\right), \tag{6}$$

where: LP - is the free-space path loss; k - is the Boltzmann constant; B - is the resolution bandwidth.

Table 5. RF budget of G/T at 2.060 GHz.

F, MHz	Ptx, dBm	Cable path U/L, dB	U/L range antenna	EIRP Tx	Free space, dB	P1, dBm	P2, dBm	P3, dBm
2226	-40	-6	12	-34	-64,90	-49,8	-49,79	-39,38

Y1, dB	Y1 lin	Y1-1	Y2, dB	Y2 lin	Y2-1	k, dBW/Hz/K	k, dBm/Hz/K	NBW, Hz	NBW dBHz	G/T
0,01	1,00251	-26,5738	10,41	10,9901	9,99561	-226,6	-199,6	942000	59,74050901	-5,65884

8. Results and discussion of the experiment

The proposed system provides Fundamental RF mixing up to 18 GHz and then Low-Harmonic RF mixing (3rd harmonic) up to 40 GHz and therefore sufficient measurement speed, sensitivity and dynamic range without the use of large amounts of coherent integration or very small IF bandwidths. Fundamental and Low-Harmonic mixing also minimizes the accuracy problems associated with RF and LO harmonics when measuring wide-band antennas. Due to the design of the Distributed Frequency Converter, and the internal design of the IF processing Unit, system stability and accuracy improve significantly. The system stability is a key factor in achieving high levels of measurement repeatability.

The excellent accuracy means antenna patterns can be measured over an extremely wide dynamic range with less than 0.1 dB of uncertainty due to the instrumentation.

The system uses an industrial standard measurement system in our modified configuration. A RF multiplexing is applied with the switches to extend the number of measurement channels. Only a single mixer (reference mixer type is used) is required, allowing use of a single rotary joint in the positioner. Furthermore, the sources and receiver are triggered using a TTL handshake, resulting in a higher frequency switching speed. The receiver operates in fast - CW mode and stores the measured data in its internal point buffer, from where it is transferred to the control computer in an asynchronous fashion. This configuration minimizes overhead and makes maximum use of the high speed of the individual components.

The graphs below present the results of the normalized three-dimensional radiation pattern (Fig. 8), the antenna gain (Fig. 9), and the normalized contour plot of the gain (Fig. 10).

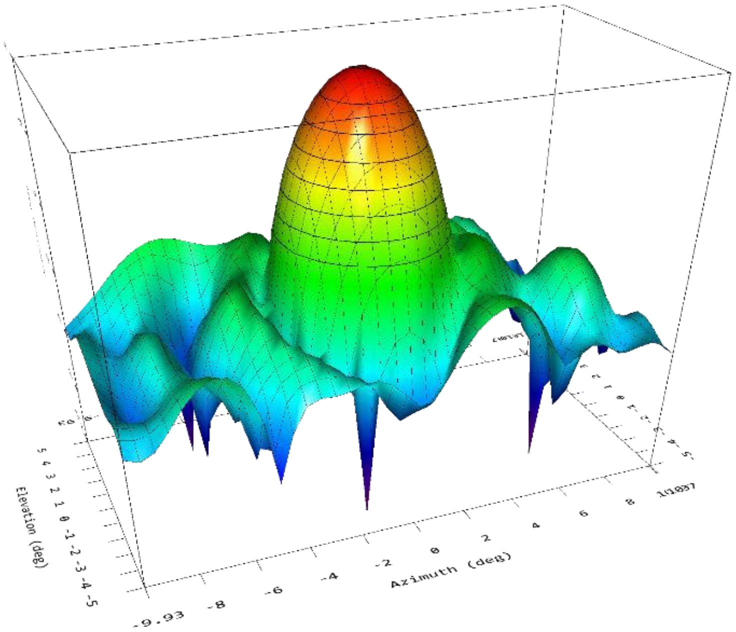

Fig.8. Three-dimensional radiation pattern.

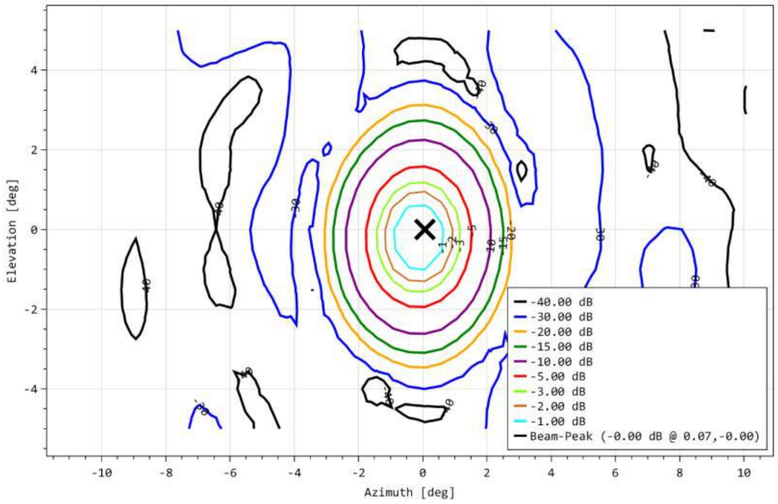

Fig.9. Contour graph of the gain.

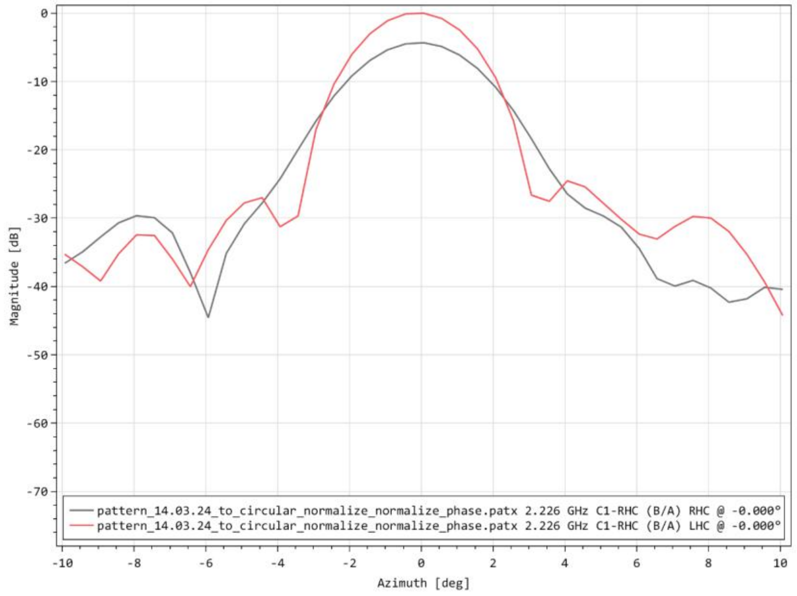

Fig.10. Antenna Gain versus Direction.

As seen from the plots, the pattern width at -3dB is around 2.4 degrees, which is very close to the expected from modelling (2.2 deg.). The total Gain of the tested antenna is 34 dBi, and side-lobes at level -25dB, which is very close to the expected value.

Overall, the observed results are consistent with the calculated values obtained from Ansys simulations. Minor discrepancies may be attributed to inaccuracies in the CAD model, as well as inaccuracy in manufacturing and fastening of the antenna feed to the reflector. The test results are presented below in Table 6. The test results show that the measured parameters of EIRP, IPFD, and G/T are generally consistent with the preliminary simulations. The most significant deviation is observed in the EIRP values, which requires further analysis to determine the reasons for exceeding the design specifications.

Table 6. Test results with payload.

DL Frequency / DL, MHz	UL Frequency / UL, MHz	Power Budget calculations			Measurement results		
		EIRP	IPFD	G/T	EIRP	IPFD	G/T
2220	2058	41.78	-50.44	-5.02	43.23	-50.32	-5.04
2226	2060	41.78	-50.44	-3.64	45.06	-50.1	-3.69
2230	2062	41.78	-50.44	-3.69	44.84	-50.17	-3.75

The IPFD and G/T parameters demonstrate a high degree of agreement with the calculated models, confirming the reliability of the receiving chain characteristics and the antenna's noise properties. These data can be further used for evaluating the compliance of the antenna and payload with the design requirements.

9. Conclusion

Tests of the S-band channel of the earth station's antenna system for receiving and transmitting signals from low Earth orbit (LEO) satellites were conducted. As part of the antenna and payload testing, procedures for measuring and collecting experimental data were developed. Namely, the proposed system achieves high accuracy, stability, and speed by combining Fundamental and Low-Harmonic RF mixing with an optimized Distributed Frequency Converter architecture. The modified industrial-standard setup provides increased channel capacity using RF multiplexing, while the minimized overhead and the maximized component speed are achieved through TTL triggered fast-CW data acquisition.

Accordingly, a CAD model of the parabolic antenna was created, and calculations of parameters such as equivalent isotropically radiated power (EIRP), input power flux density (IPFD), and the gain-to-noise-temperature ratio (G/T) were performed. Simulations were carried out in ANSYS HFSS. Experimental measurements of these parameters showed good agreement with the calculated results. These results indicate that the developed antenna system is ready for use in the satellite-communications earth station, and that the antenna test range is ready for further operation.

Conflict of interest statement

The authors declare that they have no conflict of interest in relation to this research, whether financial, personal, authorship or otherwise, that could affect the research and its results presented in this paper.

CRediT author statement

Baktybekov K.S.: Conceptualization, Supervision - Original Draft; **Ashurov A. E.:** Writing - Review & Editing; **Zhapanova, A.S.:** Data Curation – Writing; **Ivanov, A. V.:** Data Curation – Writing; **Kelgenbayev, Al. Zh.:** Writing – Review; **Sailaubaiuly S.:** Writing – Review. The final manuscript was read and approved by all authors.

Funding

This research has been/was/is funded by the Aerospace Committee of the Ministry of Digital Development, Innovations and Aerospace Industry of the Republic of Kazakhstan (BR 21982462)

References

1 Li Ye., Wang M., Hwang K., Li Z., Ji T. (2023) LEO Satellite Constellation for Global-Scale Remote Sensing with On-Orbit Cloud AI Computing. IEEE Transactions on Aerospace. *IEEE Journal of Selected Topics in Applied Earth Observations and Remote Sensing*, 16, 9369 – 9381. https://doi.org/10.1109/JSTARS.2023.3316298

2 Cedric Westphal, Lin Han, Richard Li. (2023) LEO satellite networking relaunched: Survey and current research challenges. *ITU Journal on Future and Evolving Technologies*, 4, 4, 711-744. https://doi.org/10.52953/LWXC1928

3 Manuel Arrebola., Leandro de Haro, Jose A Encina. (2008) Analysis of Dual-Reflector Antennas with a Reflectarray as Subreflector. *IEEE Antennas and Propagation Magazine*, 50, 6, 39 – 51. https://doi.org/10.1109/MAP.2008.4768921

4 Taeyoung Kim. (2024) An Analysis of Issues Related to Attenuation by Atmospheric Factors in the Frequency Bands for Radar Systems. *Journal of the Korean Military Science and Technology Society*, 27, N6, 657- 664. https://doi.org/10.9766/KIMST.2024.27.6.657

5 Dhanush S., Sreelakshmi K., Ranjit G., Dora K., Susarla Hari. (2023) LNA Design for LEO Space S-Band Applications. Proceeding of the 6th International Conference on Computation System and Information Technology for Sustainable Solutions (CSITSS), Bangalore, India. *IEEE Xplore*. https://doi.org/10.1109/CSITSS57437.2022.10026407

6 Rodrigues G., Angevain J.C, Santiago-Prowald J. (2013) Shape optimization of reconfigurable antenna reflectors. *CEAS Space J.,* 5, 221–232. https://doi.org/10.1007/s12567-013-0038-5

7 Evans G.E., Schrank H.E. (2024) A Planar Series-Feed Antenna Array with an Extremely Low Sidelobe Level. October 2024. *IEEE Antennas and Wireless Propagation Letters,* 1 - 5. https://doi.org/10.1109/LAWP.2024.3483269

8 Rui Chen, Zhenyang Tian, Wen-Xuan Long, Xiaodong Wang, Wei Zhang (2023) Hybrid Mechanical and Electronic Beam Steering for Maximizing OAM Channel Capacity. *IEEE Transactions on Wireless Communications*, 22, 1, 534 - 549. https://doi.org/10.1109/TWC.2022.3195988.

9 Marco Lisi (2002) Phased arrays for satellite communications: a system engineering approach. *Proceedings of the 2000 IEEE International Conference on Phased Array Systems and Technology (Cat. No.00TH8510). IEEE Xplore*. https://doi.org/10.1109/PAST.2000.858938

10 Raúl Igual, Carlos Medrano, Inmaculada Plaza Carlos Orrite (2013) Adaptive tracking algorithms to improve the use of computing resources. *IET Computer Vision,* 7(6), 415 – 424. https://doi.org/10.1049/iet-cvi.2012.0016

11 Pedram Mousavi, Lotfollah Shafai, Veidt B., Dewdney P. (2001) Feed-Reflector design for large adaptive reflector antenna (LAR). *IEEE Transactions on Antennas and Propagation*, 49(8), 1142 – 1154. https://doi.org/10.1109/8.943309

12 Zhao P., Chen N., Li Y., Feng C. (2023) Cross-Polarization Interference Cancellation in Satellite Communication. *Proceedings of the 5th International Conference on Electronic Engineering and Informatics (EEI*), Wuhan, China, 391 – 395. https://doi.org/10.1109/EEI59236.2023.10212784

13 Baktybekov K.S., Bochkova E.N., Korol V.V., Murushkin M.S., Zhumazhanov B.R. (2024) Design of Software Defined Radio of Ground Station for Receiving Nanosatellites Image Data in S-band. *Eurasian Physical Technical Journal.* 21, 4(50), 79 – 87. https://doi.org/10.31489/2024No4/79-87

14 Fasold D. (2006) Measurement Performance of Basic Compact Range Concepts. *Proceedings of the 21st Antenna Measurement Technical Association (AMTA)*, Europe, 2006. https://doi.org/10.1109/RAST.2015.7208382

15 Hunscher C., Hartmann J. (2007) Satellite Antenna Measurements. *Proceedings of the 2nd International ITG Conference on Antennas*, Munich, Germany, 25 – 32. https://doi.org/10.1109/INICA.2007.4353925

16 Velasco C., Tipantuña C. (2017) Meteorological picture reception system using software defined radio (SDR). *Proceeding of the IEEE 2nd Ecuador Technical Chapters Meeting*, 1-6. https://doi.org/10.1109/ETCM.2017.8247551

17 Farrar A. (1985) Computer Models for Determination of Satellite Power-Flux-Density Limits. *Proceeding of the 6th Symposium and Technical Exhibition on Electromagnetic Compatibility*. Zurich, Switzerland, 315 – 320. https://doi.org/10.23919/EMC.1985.10798853

18 Ohmaru K., Mikuni Y. (1984) Direct G/T Measurement for Satellite Broadcasting Receivers. *IEEE Transactions on Broadcasting*. BC-30, 2, 38 – 43. https://doi.org/10.1109/TBC.1984.266529

AUTHORS' INFORMATION

Baktybekov, Kazbek Suleimenuly - Doctor of Physical and Mathematical Sciences, Professor, Payload and Research Department, Research Associate, Ghalam LLP, Astana, Kazakhstan; Scopus Author ID:8926833000; https://orcid.org/0000-0002-6401-8053; k.baktybekov@ghalam.kz

Ashurov, Abdikul Erkulovich - PhD, Head of the Department of Space Engineering and Technology, L.N. Gumilyov Eurasian National University, Astana, Kazakhstan; Scopus Author ID: 57942248600; https://orcid.org/0000-0001-6044-5579 ; ashurov_ae@enu.kz

Ivanov, Anton Vladimirovich – Engineer, Head of Electrical Test Department, AITC Ghalam LLP, Astana, Kazakhstan; https://orcid.org/0009-0009-1037-1108; a.ivanov@ghalam.kz

Kelgenbayev, Almas Zhabaykhanuly – Engineer, Chief Engineer of Electrical test department, Ghalam LLP, Astana, Kazakhstan; https://orcid.org/0009-0000-2734-8988; a.kelgenbayev@ghalam.kz

Zhapanova, Ainur Shaizadanovna – Master (Sci.), Senior Lecturer at the Department of Radio Engineering, Electronics, and Telecommunications, S. Seifullin Kazakh Agrotechnical Research University, Astana, Kazakhstan; https://orcid.org/0009-0000-9012-2703; zhapanovaainur@gmail.com

Sailaubaiuly, Serikbol – Master (Sci.), Nazarbayev University, Astana, Kazakhstan; https://orcid.org/0009-0002-5597-2408; serikbolsailaubaiuly@gmail.com

EURASIAN PHYSICAL TECHNICAL JOURNAL

2025, Volume 22, No. 4(54)

https://doi.org/10.31489/2025N4/94-100

Received: 07/10/2025 Revised: 13/11/2025 Accepted: 22/12/2025

Research Article

UDC 533.6:66.095:66.047

INVESTIGATION OF THE EFFECT OF ELECTROPHYSICAL PARAMETERS OF THE HIGH-VOLTAGE SHORT-PULSE ELECTROHYDRAULIC DISCHARGE SYSTEM AND A NANOCOMPOSITE CATALYST ON OIL SLUDGE DESTRUCTION

Satybaldin A.Zh.[1], Shaimerdenova K.M.[1], Zhandybaev B.B.[1], Bakibaev A.A.[2], Alpyssova G.K.[1], Seitzhan R.[1], Tyanakh S. [1]

[1] Buketov Karaganda National Research University, Karaganda, Kazakhstan
[2] Tomsk State University, Tomsk, Russian Federation
*Corresponding author: zhandybaevb@gmail.com

Abstract. *This paper presents the results of a study on oil sludge processing using high-voltage short-pulse electrohydraulic discharge. The influence of key parameters, such as discharge voltage, capacitor bank capacitance, processing time, electrode gap, and catalyst concentration, on the yield of light and medium petroleum fractions is analyzed. Experiments have shown that the optimal conditions for achieving the maximum fraction yield (up to 36.4%) are: a processing time of 6 minutes, an electrode gap of 10 mm, a capacitor bank capacitance of 0.125 μF, and a nanocomposite catalyst concentration of 1%. It has been established that the use of a catalyst enhances the destruction of high-molecular compounds, while optimization of the electrophysical parameters improves the energy efficiency of the process. The obtained results can be used to develop energy-efficient technologies for oil waste disposal.*

Keywords: oil sludge, nanocatalyst, high-voltage short-pulse electrohydraulic discharge, light and middle fractions.

1. Introduction

Oil production, crude oil processing, and its transportation through main pipelines are accompanied by the accumulation of large amounts of petroleum-containing waste, among which oil sludge (OS) occupies a significant place. Oil sludge formed during the operation of enterprises in the oil industry is a multicomponent system that includes water, organic compounds, and mineral impurities. Due to the presence of pathogenic microorganisms, parasites, and heavy metals, such waste has a negative impact on ecosystems and poses a threat to human health. Oil sludge also contains a solid inert fraction. According to estimates, the annual global volume of oil sludge generation exceeds one billion tons, meaning that up to seven tons of such contaminated material may be produced per ton of extracted crude oil [1]. Traditional methods of handling oil sludge—such as storage in sludge pits or subsequent incineration—lead to the loss of a significant portion of valuable hydrocarbons and are accompanied by harmful effects on ecosystems. Therefore, the processing of oil sludge with the aim of recovering oil for further economic use is considered a more efficient, economical, and environmentally justified option. Various technologies for extracting oil from oil sludge have been studied to date, including freezing methods [2], solvent extraction [3], microwave irradiation [4], centrifugation [5], ultrasonic treatment [6], and pyrolysis [6, 7]. However, most existing methods thermal, biological, mechanical, chemical, and physicochemical are unable to ensure sufficient environmental safety and a high degree of recovery of petroleum products from sludge. An additional challenge is that these technologies rely on expensive, fully imported equipment requiring skilled technical maintenance, as well as significant reagent costs (polyurethane compositions, various resins, liquid glass, cement materials). As a result, the overall environmental burden associated with oil sludge processing remains high. One of the most promising approaches to minimizing harmful impacts is the extraction of valuable hydrocarbon components from oil sludge followed by their processing into commercial products, which significantly reduces the amount of residual waste. In recent years, companies in the oil production sector have been actively implementing new technological solutions aimed at more efficient utilization of waste generated at the stages of oil extraction and refining. However, as follows from the conducted analysis of published studies [1–7], to date there is no universal technology for neutralizing and processing oil sludge that simultaneously meets all environmental, technical, and economic requirements. Centrifuges and separation units used in industry—both foreign and domestic—allow effective water removal and reduce the impact of solid mechanical impurities while practically preserving the hydrocarbon fraction of the raw material. According to study [8], combined oil sludge processing technologies based on mechanical and physicochemical methods followed by a biological post-treatment stage are considered more environmentally safe and provide enhanced efficiency in the treatment of petroleum waste. Such processing methods require significantly lower costs compared to direct incineration of oil sludge, and their efficiency is considerably higher. An additional challenge is that these technologies rely on expensive, fully imported equipment that requires qualified technical maintenance, as well as substantial expenditures on reagents (polyurethane compounds, various resins, liquid glass, cement materials). As a result, the overall environmental burden of oil sludge processing remains high.

Consequently, a global trend has emerged toward a decline in the growth rate of conventional hydrocarbon reserves, including crude oil. In this regard, special attention is being paid to the rational use of petroleum resources and the active search for alternative and unconventional sources of hydrocarbons. The search for efficient technologies for oil sludge processing and utilization is therefore an urgent scientific and practical challenge. This issue becomes increasingly important as the availability of conventional hydrocarbon resources decreases and the need to expand the raw material base through unconventional sources grows. However, the processing of such feedstocks is associated with several difficulties due to their high viscosity, the presence of resin–asphaltene compounds, metals, and other impurities, which significantly complicate the treatment process [9, 10]. One of the most promising methods for processing petroleum waste is the application of high-voltage short-pulse electrohydraulic discharge (HVED) to heavy hydrocarbon organic matter. This method is based on the generation of high-energy pulses in a liquid medium, which produce shock-wave effects and create localized extreme conditions—high temperatures, pressures, and cavitation. As a result, complex hydrocarbon structures are destroyed, leading to the formation of lighter fractions [11, 12]. The use of HVED technology improves the physicochemical properties of petroleum residues, reduces their viscosity, enhances fluidity, and increases the yield of light and middle hydrocarbon fractions that are in demand as fuels and petrochemical feedstocks. Additional advantages of this method include its relative energy efficiency, environmental friendliness (due to the absence of aggressive chemical reagents), and the possibility of integration with catalytic processes. In our previous studies [13, 14], the effectiveness of the developed nanocomposite catalyst based on bentonite coated with nickel, in combination with the impact of HVED, was examined. It was shown that the introduction of the catalyst contributes to the intensive destruction of chemical bonds in heavy hydrocarbon C-C compounds and leads to an increased yield of light and middle fractions. The obtained results confirmed the feasibility of using the developed nanocomposite catalysts based on nickel-coated bentonite to enhance the efficiency of oil sludge processing.

A promising direction for further research is the study of the effect of HVED discharges and the addition of the nanocomposite catalyst based on zeolite, coated with nickel as developed by the authors, in order to increase its catalytic activity. Zeolites, due to their unique crystalline structure and surface properties, provide high efficiency in processing heavy hydrocarbon feedstocks and contribute to the increased yield of low-molecular-weight products. Additionally, zeolites exhibit significant thermal stability, which allows their use in the treatment of petroleum residues under high-temperature conditions [15].

The application of HVED in combination with nanocomposite catalysts based on zeolites opens up new possibilities for the efficient processing of oil sludge. In particular, studying the effect of a catalyst composed of a mixture of activated zeolite and bentonite clay impregnated with nickel on the oil sludge treatment process can serve as a foundation for the development and implementation of new nanocatalysts for the thermal cracking of heavy hydrocarbon feedstocks. This approach enhances processing efficiency, increases the yield of target products, and simultaneously contributes to solving the problem of industrial waste utilization.

2. Materials and methods of research

The oil sludge used in this study was obtained from the inner surfaces of the Atasu–Alashankou main oil pipeline. To increase the processing efficiency, a nickel-coated zeolite catalyst was additionally introduced into the oil sludge. The catalyst concentration in the treated sludge varied from 0.0 to 1.5% (0.5%, 1.0%, and 1.5%). The catalyst was introduced in the form of a fine powder immediately before the start of the electrohydraulic treatment. The fractional composition of the processed products was determined by thermal distillation. The main criterion for evaluating process efficiency was the percentage yield of light and middle hydrocarbon fractions at temperatures up to 200 °C and 300 °C, respectively, for the analyzed oil sludge.

To determine the optimal parameters and develop a mathematical model of the oil sludge processing process formed on the inner surfaces of the Atasu–Alashankou oil pipeline under the influence of HVEDs, laboratory experiments were carried out using the probabilistic–deterministic experimental design method. The applied methodological approach made it possible to evaluate the combined effect of the key parameters of the HVED system and the nanocatalytic additive. The list of the studied factors and their levels is presented in Table 1. Since the dependence of the yield of target products from oil sludge on the considered parameters exhibits a nonlinear character, the experimental data were processed using the method of experimental design based on the principles of nonlinear multiple correlation. The design matrix is presented in Table 2. Each row of the matrix corresponds to a specific set of experimental conditions. The matrix structure was developed in such a way that, in the full set of experiments, each level of any factor is combined exactly once with every level of the remaining parameters.

Table 1. Studied electrophysical parameters of the HVED system and the added nanocomposite catalyst

X1 (%)	0	0,5	1	1,5
X2(μF)	0,125	0,25	0,5	0,75
X3(min)	5	6	7	8
X4(mm)	7	8	9	10

Note: The variable X_1 represents the amount of added nanocomposite catalyst (%), X_2-the capacitance of the capacitor bank in the HVED system (μF), X_3-the treatment time (min) under electrohydraulic discharges, and X_4-the electrode gap (mm).

Table 2. Experimental design matrix and the influence of various HVED system factors and added catalyst on the yield of light and middle fractions after treatment.

No.	X_1, %	X_2, μF	X_3, min	X_4, mm	y_{avg}, %
1	0	0,125	5	7	20,3
2	0,5	0,25	6	8	29,9
3	1	0,5	7	9	24,9
4	1,5	0,75	8	10	21,3
5	0	0,25	7	10	18,1
6	0,5	0,125	8	9	21,1
7	1	0,75	5	8	13,33
8	1,5	0,5	6	7	29,61
9	0	0,5	8	8	21,46
10	0,5	0,75	7	7	15,4
11	1	0,125	6	10	36,4
12	1,5	0,25	5	9	30,09
13	0	0,75	6	9	9,18
14	0,5	0,5	5	10	23,68
15	1	0,25	8	7	25,8
16	1,5	0,125	7	8	20,9

3. Results and discussion

Based on the constructed experimental design matrix, histograms were plotted to illustrate the influence of the main parameters on the yield of light and middle hydrocarbon fractions. Figure 1 shows the dependence of the yield of these fractions on the duration of the HVED treatment and the electrode gap during the processing of oil sludge formed on the inner surface of the Atasu–Alashankou oil pipeline. As shown in Figure 1, the highest yield of light and middle fractions is achieved at a treatment duration of 6 minutes and an electrode gap of 10 mm. Under these conditions, the yield reaches 36.4% of the initial oil sludge mass. This result can be explained by the combined effect of two factors-the optimal duration of the HVED treatment and the interelectrode distance-which ensure the most stable formation of the pulsed discharge, thereby promoting the destruction of high-molecular-weight hydrocarbon compounds.

When the treatment time exceeds 6 minutes (up to 7–8 minutes), a decrease in the yield of target fractions is observed, which is associated with the redistribution of discharge energy and possible secondary compaction of the reaction products. Similarly, reducing the electrode gap below 10 mm decreases process efficiency due to discharge channel instability and local overheating of the medium. Figure 2 shows the influence of the capacitor bank capacitance of the HVED system and the treatment duration on the yield of light and middle fractions from the oil sludge. The highest yield of light and medium fractions is observed at the minimum capacitance of the capacitor bank - 0.125 μF. Under six minutes of exposure, the yield reaches its maximum value of 36.4 %.

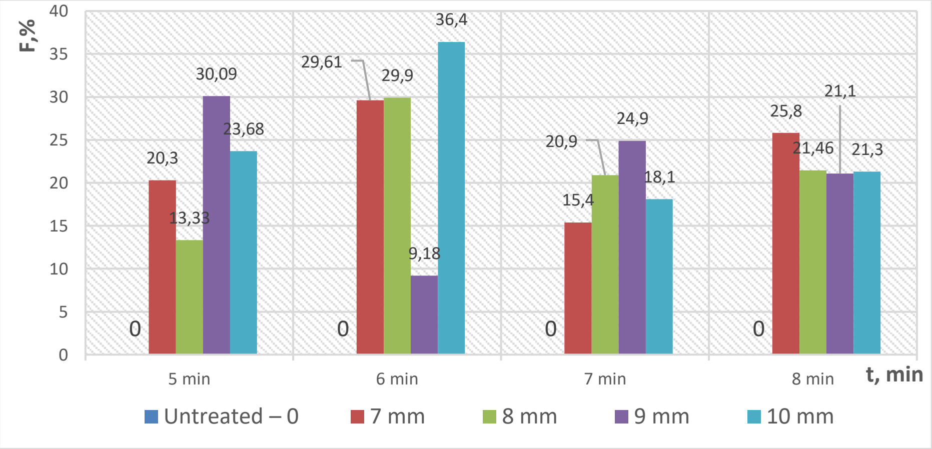

Fig.1. Influence of HVED treatment time and electrode gap on the yield of light and middle fractions

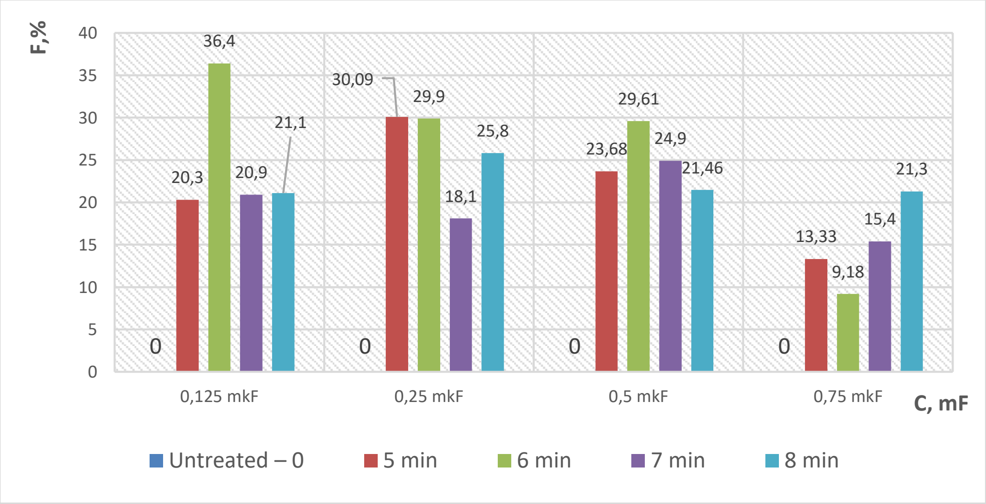

Fig.2. Influence of the capacitor bank capacitance of the HVED system on the yield of light and middle fractions

This result indicates that at low capacitance values, more powerful and concentrated discharge pulses are formed, providing effective destruction of complex hydrocarbon structures. With an increase in capacitance (0.25–0.75 μF), a gradual decrease in yield is observed, which is associated with the elongation of the pulse over time and a reduction in the specific energy transferred to the reaction zone. At the same time, the influence of treatment duration also becomes evident: increasing the exposure time to 7–8 minutes leads to stabilization of the results; however, a significant increase in yield is not observed. Experimental data showed that the maximum yield of light and medium fractions is achieved at a nanocatalyst concentration - zeolite impregnated with nickel - of 1% and a treatment duration of 6 minutes (Fig. 3).

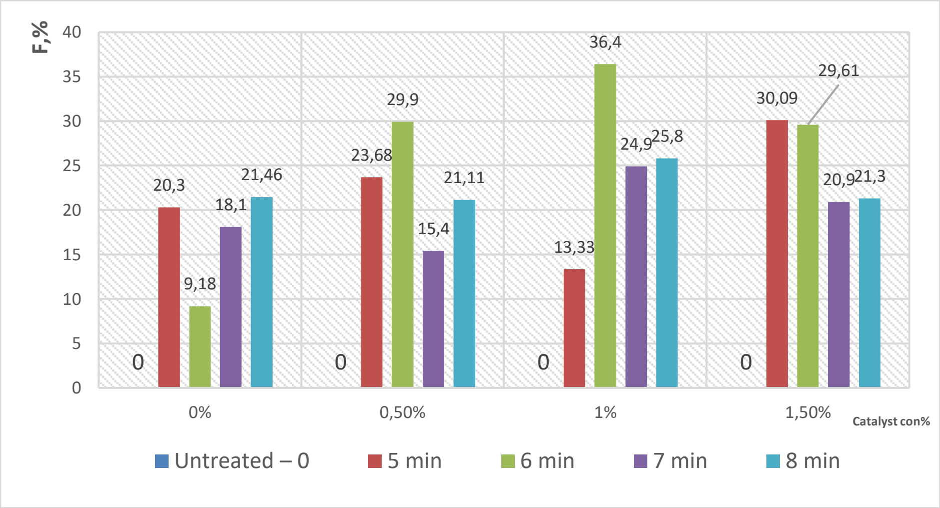

Fig.3. Influence of the amount of nickel-coated zeolite nanocatalyst on the yield of light and medium fractions

Further increase in the amount of catalyst leads to a decrease in the yield of target products, which may be associated with the sorption of active components or the restriction of mobility in the organic medium. This confirms the necessity of accurately determining the optimal catalyst content to achieve maximum process efficiency. As shown in Fig. 4, the following graphs illustrate the influence of discharge voltage (kV) and capacitor bank capacitance (μF) on the yield of light and medium oil sludge fractions (%) during processing by the HVED method.

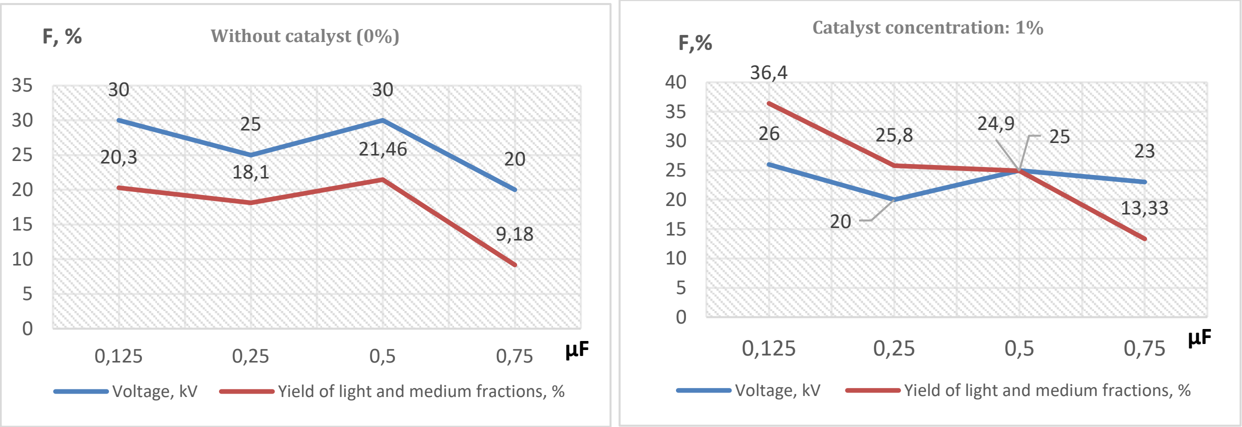

a) b)

Fig. 4. Influence of discharge voltage on the yield of light and medium fractions from oil sludge:
(a) without catalyst; (b) with 1% catalyst content.

In experiments conducted without the use of a catalyst (0%), it was found that increasing the capacitance of the capacitor bank from 0.125 to 0.25 μF leads to a decrease in discharge voltage, recorded by the kilovoltmeter, from 30 to 25 kV. This is accompanied by a reduction in the yield of light and medium fractions — from 20.3% to 18.1%. With a further increase in the capacitance of the HVED system up to 0.5 μF, the opposite trend is observed: the voltage rises to 30 kV, and the proportion of light and medium fractions increases to 21.46%. Thus, the capacitance of the capacitor bank has a significant effect on the intensity of the destruction of high-molecular-weight hydrocarbon compounds present in oil sludge.

At a catalyst content of 1%, the dependence becomes more pronounced: the maximum yield (36.4%) is observed at a capacitance of 0.125 μF, while the kilovoltmeter reading is 26 kV. When the capacitance increases to 0.5 μF, the voltage drops to 20 kV, and the yield of target fractions decreases from 36.4% to 25.8%. This behavior can be explained by the fact that at lower capacitance values of the capacitor bank, higher pulse voltages are generated in the system, ensuring the intensive occurrence of physical-chemical destruction processes. In the presence of a catalyst, these processes proceed more efficiently due to the accelerated breaking of molecular C–C bonds in heavy hydrocarbons.

4. Conclusion

As a result of the experimental studies, it was established that the use of HVED technology in combination with a nickel-coated zeolite nanocatalyst enhances the efficiency of processing oil sludge formed on the inner surfaces of the Atasu–Alashankou oil pipeline. It was determined that the yield of light and medium hydrocarbon fractions is significantly influenced by the electrophysical parameters of the process: the capacitance of the HVED system's capacitor bank, the interelectrode gap, the treatment duration, and the catalyst content.

The kilovoltmeter readings, which reflect the actual discharge voltage, together with the capacitance of the HVED capacitor bank and the catalyst concentration, determine the efficiency of the electrohydraulic destruction process of high-molecular-weight compounds in oil sludge.

The maximum fraction yield of 36.4% is achieved under optimal conditions: treatment duration of 6 minutes, interelectrode distance of 10 mm, capacitor capacitance of 0.125 μF, and catalyst concentration of 1.0%. The introduction of the zeolite-based catalyst increases the energy efficiency of the process, confirming the potential of combining HVED technology with catalytic methods for oil waste processing.

Conflict of interest statement

The authors declare that they have no conflict of interest in relation to this research, whether financial, personal, authorship or otherwise, that could affect the research and its results presented in this paper.

CRediT author statement

Satybaldin A. Zh.: Supervision, Funding acquisition, Writing – review & editing, **Shaimerdenova K. M.**: Methodology, **Zhandybaev B.B.**: Writing –original draft, Investigation, **Bakibayev A.A.**: Formal analysis, **Seitzhan R.**: Data curation, **Berdibayev D.N.**: Investigation, **Alpysova G.K.**: Data curation. The final manuscript was read and approved by all authors.

Funding Information

This research was funded by the Science Committee of the Ministry of Science and Higher Education (Grant No. AP23483556).

References

1. Niu A., Sun X., Lin C. (2022) Trend in research on characterization, environmental impacts and treatment of oily sludge: A systematic review. *Molecules*, 27, 7795. https://doi.org/10.3390/molecules27227795
2. Lin C., He G., Li X., Peng L., Dong C., Gu S., Xiao G. (2007) Freeze/thaw induced demulsification of water-in-oil emulsions with loosely packed droplets. *Separation and Purification Technology*, 56, 175–183. https://doi.org/10.1016/j.seppur.2007.01.035
3. Al-Zahrani S.M., Putra M.D. (2013) Used lubricating oil regeneration by various solvent extraction techniques. *Journal of Industrial and Engineering Chemistry*, 19, 536–539. https://doi.org/10.1016/j.jiec.2012.09.007
4. Fortuny M., Oliveira C.B.Z., Melo R.L.F.V., Nele M., Coutinho R.C.C., Santos A.F. (2007) Effect of salinity, temperature, water content, and pH on the microwave demulsification of crude oil emulsions. *Energy & Fuels*, 21, 1358–1364. https://doi.org/10.1021/ef0603885
5. Cambiella A., Benito J. M., Pazos C., Coca J. (2006) Centrifugal separation efficiency in the treatment of waste emulsified oils. *Chemical Engineering Research and Design*, 84, 69–76. https://doi.org/10.1205/cherd.05130

6. Shishkin Y.L. (2006) Fractional and component analysis of crude oils by the method of dynamic microdistillation–differential scanning calorimetry coupled with thermogravimetry. *Thermochimica Acta,* 441, 162–167. https://doi.org/10.1016/j.tca.2005.12.011

7. Chen J. B., Mu L., Jiang B., Yin H., Song, X., Li A. (2015) TG/DSC-FTIR and Py-GC investigation on pyrolysis characteristics of petrochemical wastewater sludge. *Bioresource Technology*, 192, 1–10. https://doi.org/10.1016/j.biortech.2015.05.031

8. Hu G.J., Li J. B., Zeng G.M. (2013) Recent development in the treatment of oily sludge from petroleum industry: A review. *Journal of Hazardous Materials*, 261, 470–490. https://doi.org/10.1016/j.jhazmat.2013.07.069

9. Zhukova E.M. (2008) Effect of high-voltage electrohydraulic discharge on the physicochemical properties of oil and petroleum products. Doctoral Dissertation, Saratov State University named after N.G. Chernyshevsky. Saratov, Russia. 145. Available at: https://www G.K..dissercat.com/content/vozdeistvie-vysokovoltnogo-elektrogidravlicheskogo-razryada-na-fiziko-khimicheskie-svoistva [in Russian]

10. Nikolaev A. I., Peshnev B. V., Ismail A.M.H. (2022) Cavitation treatment of water-containing petroleum products. *Izvestiya Vysshikh Uchebnykh Zavedenii. Series Chemistry and Chemical Technology*, *65*(7), 94–99. https://doi.org/10.6060/ivkkt.20226507.6611 [in Russian]

11. Balakaeva G., Kalmenova G. (2023) Development of an application for thermal processing of oil sludge to prevent environmental pollution in the industrial oil and gas sector. *Bulletin of Abai Kazakh National Pedagogical University. Series of Physical and Mathematical Sciences*, *81*(1), 136–144. https://doi.org/10.51889/2959-5894.2023.81.1.015

12. Bodykov D. U., Salakhov R.Kh. (2020) Oil processing using the electrohydraulic effect. *Combustion and Plasma Chemistry*, *18*, 29–36. https://doi.org/10.18321/cpc343

13. Satybaldin A. Zh., Shaimerdenova,K. M., Baikenov,M. I., Zhandybayev,B. B., Tyanakh S. (2025) Influence of nanocatalyst and HVED on the yield of fractions from oil sludge. *Bulletin of Toraighyrov University*, *2*, 289–302. https://doi.org/10.48081/BMGX4755

14. Satybaldin A., Zhakipbaeyev B., Tusipkhan A., Baykenov M., Khalikova Z., Alpyssova G. (2021) The influence of a high-voltage discharge on the oil bottom sediments formed at the oil storage facilities of the atasu-alashankou station. *Eurasian Physical Technical Journal*, *18*(3(37), 71–75. https://doi.org/10.31489/2021No3/71-75

15. Ivanova I.I. (2017) Zeolite catalysts: Synthesis, activation, catalysis, and deactivation. In *International Symposium "Diffraction Methods in the Characterization of New Materials"* (May 31 – June 2, 2017). Conference presentation [Electronic resource]. Available at: https://istina.msu.ru/conferences/presentations/607587

AUTHORS' INFORMATION

Satybaldin, Amangeldy Zharlygassynovich – Candidate of Chemical Sciences, Associate Professor, Faculty of Physics and Technology, Buketov Karaganda National Research University, Karaganda, Kazakhstan; https://orcid.org/0000-0002-0846-4665; satybaldin.1975@mail.ru

Shaymerdenova, Kulzhan Meiramovna - Candidate of Technical Sciences, Professor, Faculty of Physics and Technology, Buketov Karaganda National Research University, Karaganda, Kazakhstan; https://orcid.org/0000-0002-9588-4886; gulzhan.0106@mail.ru

Zhandybayev, Beken Bakhytbekuly - PhD student, Faculty of Physics and Technology, Buketov Karaganda National Research University, Karaganda, Kazakhstan; https://orcid.org/0000-0001-5719-9549; zhandybaevb@gmail.com

Bakibayev, Abdigali Abdimanapovich – Doctor of Chemical Sciences, Professor, Faculty of Chemistry, Tomsk State University, Tomsk, Russian Federation; https://orcid.org/0000-0002-3335-3166 ; bakibaev@mail.ru

Alpyssova, Gulnur Kenzhebekovna – PhD, Associate Professor, Faculty of Physics and Technology, Buketov Karaganda National Research University, Karaganda, Kazakhstan; https://orcid.org/0000-0002-7164-218; gulnur-0909@mail.ru

Seitzhan, Raikhan – Master, Senior Lecturer, Faculty of Chemistry, Buketov Karaganda National Research University, Karaganda, Kazakhstan; https://orcid.org/0000-0003-2362-6383; Raikhan.Seitzhan@mail.ru

Tyanakh, Sairagul – PhD, Senior Lecturer, Faculty of Chemistry, Buketov Karaganda National Research University, Karaganda, Kazakhstan; https://orcid.org/0000-0001-5343-4695 ; Saika_8989@mail.ru

EURASIAN PHYSICAL TECHNICAL JOURNAL

2025, Volume 22, No.4 (54)

https://doi.org/10.31489/2025N4/101-116

Received: 13/05/2025 Revised: 26/10/2025 Accepted: 22/12/2025

Original Research Article

UDC 53.01

COMPUTATIONAL ANALYSIS OF INFORMATION-THEORETIC MEASURES AND OSCILLATOR STRENGTHS IN QUANTUM SYSTEMS VIA THE NIKIFOROV–UVAROV METHOD

Inyang E.P.[1] *, Okoi P.O.[2], Nwachukwu I.M.[1]

[1] Department of Physics, Faculty of Science, National Open University of Nigeria, Jabi-Abuja, Nigeria
[2] Department of Physics, Faculty of Physical Science, University of Calabar, Calabar, Nigeria
Corresponding Author: etidophysics@gmail.com;einyang@noun.edu.ng

Abstract. *This study investigates Fisher and Shannon entropies in one- and three-dimensional systems under the Radial Scalar Power Potential. Using the Nikiforov–Uvarov method combined with the Greene–Aldrich approximation, we derived energy eigenvalues and normalized wavefunctions. The results demonstrate that Shannon and Fisher entropies satisfy fundamental quantum information inequalities, including the Białynicki–Birula–Mycielski and Stam–Cramér–Rao bounds, across different spatial dimensions. Rényi entropy was also analyzed in both position and momentum spaces, revealing its dependence on the screening parameter and highlighting the complementarity in measurement precision between conjugate domains. In particular cases, the Radial Scalar Power Potential reduces to the Kratzer potential, allowing the computation of energy spectra for methylidyne (CH) and nitrogen (N_2) molecules. Energy increases with angular momentum, affecting molecular stability and spectroscopic transitions, while calculated oscillator strengths are in agreement with previous results, thereby validating the Radial Scalar Power Potential model for applications in both quantum information theory and molecular spectroscopy.*

Keywords: Schrödinger equation, Oscillator strength, Nikiforov-Uvarov method; Diatomic molecules; Entropic uncertainty.

1. Introduction

Quantum information theory studies the transfer and manipulation of information within quantum systems by combining principles from quantum mechanics, computer science, and information theory. It focuses on understanding and controlling how information is stored in quantum states. Among the various metrics used in this field, Shannon entropy and Fisher information have been widely applied [1, 2], as they provide a rigorous way to quantify uncertainty in atoms and molecules. Over the years, information-theoretic measures in quantum systems have attracted significant attention [3], largely due to their applications in probability density functions and computational analyses, offering deeper insights into the behavior of quantum mechanical systems. These measures have been applied across diverse areas, including physical and chemical sciences [4]. The entropic uncertainty relation serves as an alternative formulation to the Heisenberg uncertainty principle [5]. In both position and momentum spaces, information-theoretic tools have been extensively employed to study the distribution of quantum states under various potential models [1-5]. In quantum mechanics, the Heisenberg uncertainty principle (HUR) [6] was later reformulated in terms of entropies by Białynicki-Birula and Mycielski (BBM) [7], extending its application to both position and momentum spaces. However, Hirschman [8] was the first to introduce an entropic approach to the position-momentum uncertainty relation, and Beckner [9] provided a formulation equivalent to BBM, highlighting the crucial role of entropy in capturing the intrinsic uncertainty of quantum systems. This entropic relation is expressed as:

$$S(\rho_{nl}) + S(\gamma_{nl}) \geq D(1 + ln\,\pi) \tag{1}$$

The number of spatial dimensions is denoted by D. This relationship has been shown to surpass the Heisenberg Uncertainty Relation (HUR) in sophistication, as it can accommodate greater complexity. The Shannon entropy, a key metric in this framework, is defined as:

$$S(\rho_{nl}) = -\int_{R^D} \rho_{nl}(r_q)\, ln\, \rho_{nl}\,(r_q) dr_q \tag{2}$$

,

and

$$S(\gamma_{nl}) = -\int_{R^D} \gamma_{nl}(p)\, ln\, \gamma_{nl}\,(p) dp\ , \tag{3}$$

where $S(\rho_{nl})$ is the position space Shannon entropy, $S(\gamma_{nl})$ is the momentum space Shannon entropy, R^Drepresent integrating over real space and D is the dimensions which could be 1,2 or 3.

The probability densities (PD) in position and momentum spaces are provided in Equations (4) and (5), respectively.

$$\rho_{nl}(r_q) = \left|\psi(r_q)\right|^2 \tag{4}$$

and

$$\gamma_{nl}(p) = |\psi(p)|^2 \tag{5}$$

$\boldsymbol{\psi(p)}$ represents the momentum-space wave function, obtained by applying the Fourier transform (FT) to $\boldsymbol{\psi(r_q)}$**.** This concept is related to Shannon entropy and reflects the degree to which a system is localized or spread out in space [10]. In contrast, Fisher information (FI), a purely local measure, primarily investigates local variations in the probability density (PD) and is expressed as follows [11]:

$$I(\rho) = \int_{R^D} \frac{\left|\nabla \rho_{nl}(r_q)\right|^2}{\rho_{nl}(r_q)} dr_q \tag{6}$$

$$I(\gamma) = \int_{R^D} \frac{|\nabla \rho_{nl}(p)|^2}{\rho_{nl}(p)} dp \quad . \tag{7}$$

Fisher information inequality becomes [11]

$$I(\rho)I(\gamma) \geq 9\left[2 - \frac{2l+1}{l(l+1)}|m|\right]^2 \geq 36\,. \tag{8}$$

The Rényi entropy [12] in coordinate spaces can be expressed as

$$R_q(\rho_r) = \frac{1}{1-q}\text{In}\left(\int_{R^D}\left|\rho(r_q)\right|^q dr_q\right) \tag{9}$$

$$R_q(\phi_p) = \frac{1}{1-q}\text{In}\left(\int_{R^D}|\phi(p)|^q\, dp\right) \tag{10}$$

The concept of Rényi entropy introduces an index parameter q, which characterizes the sensitivity of a system to deviations from equilibrium. When q=1, Rényi entropy reduces to Shannon entropy, representing the equilibrium distribution and reflecting the balance of uncertainty in the system. For q>1, Rényi entropy decreases, indicating increased knowledge about the system, whereas for q<1, the entropy rises, reflecting reduced information. The parameter q is always non-negative and lies within the range 0<q<∞ [13]. Previous studies have applied information-theoretic measures to molecular systems. Amadi et al. [14] investigated

Shannon entropy and Fisher information in three-dimensional molecular systems under the Deng-Fan and Eckart potentials for diatomic molecules, finding that Shannon entropy exhibited localization, while Fisher information indicated delocalization in both position and momentum spaces. Both measures satisfied the BBM and Stam–Cramér–Rao (SCR) inequalities. Similarly, Onyeaju et al. [15] analyzed Shannon and Rényi entropies in molecular potentials, validating the Heisenberg Uncertainty Principle (HUP) through expectation values in both position and momentum spaces. Laguna et al. [16] further explored information-theoretic measures using Gaussian-type functions.

Oscillator strength, which quantifies the probability of an electron transition between energy levels in atoms or molecules, is critical for understanding spectral line intensities and matter–radiation interactions [17,18]. For instance, Hibbert [19] described oscillator strength as a measure of electric dipole emission during electron transitions, using the dipole approximation and selection rules. This measure has been widely applied in stellar spectroscopy, where atomic transitions involve energy absorption or emission. Studies on oscillator strengths in different potential models have produced diverse trends. Ikot et al. [20] found that oscillator strength decreased with increasing potential parameters in the enhanced molecular Manning–Rosen potential, while Varshni [21] observed a similar decrease under the Hulthén potential. In contrast, Hassanabadi et al. [22] reported an increase in oscillator strength for the generalized Pöschl–Teller potential as potential parameters were raised. Numerous other studies have examined potential models in quantum systems [23–25].

However, to the best of our knowledge, no previous work has applied the Radial Scalar Power Potential (RSPP) to investigate Fisher information, Shannon and Rényi entropies, or oscillator strengths in coordinate spaces. The RSPP provides a valuable framework for analyzing quantum state behavior, calculating information-theoretic measures, and determining transition probabilities, which are essential for advancing quantum information theory and understanding oscillator strengths. Accordingly, this study investigates Shannon, Fisher, and Rényi entropies, oscillator strength, and the energy spectra of methylidyne (CH) and nitrogen (N_2) diatomic molecules within the context of the RSPP.

2. The solutions for the eigenvalues and wavefunctions.

In this study, we employ the Nikiforov-Uvarov (NU) method [26], a systematic technique for solving second-order differential equations of the hypergeometric form. For a comprehensive derivation and detailed methodology, refer to Appendix A. When examining a quantum system governed by a defined potential, the Schrödinger equation (SE) is represented as [27]:

$$\frac{d^2R_{nl}(r_q)}{dr_q{}^2}+\frac{2\mu}{\hbar^2}\left(E_{nl}-V(r_q)-\frac{l(l+1)\hbar^2}{2\mu r_q{}^2}\right)R_{nl}(r_q)=0 \tag{11}$$

where l is the angular momentum quantum number, μ is the reduced mass , r_q is the particle distance, and $\hbar$ is the Planck constant.

The RSPP is of the form [28]

$$V(r_q)=a_0r_q+b_0r_q{}^2+d_0-\frac{g_0}{r_q}+\frac{k_0}{r_q{}^2} \tag{12}$$

where $a_0, b_0, d_0, g_0,$ and k_0 are potential strength.

The RSPP has valuable practical and experimental implications in quantum mechanics, atomic physics, and molecular systems. It offers a more precise model for studying particle interactions in central force fields, especially in cases where traditional potentials like the Coulomb or harmonic oscillator fall short in capturing interaction details. Experimentally, this potential helps predict energy spectra and analyze the behavior of diatomic molecules, quarkonium systems, and nanoscale particles. Its flexibility makes it ideal for fitting experimental data more accurately, leading to a deeper understanding of complex physical phenomena like the information theory.

Inserting Eq. (12) into (11) gives

$$\frac{d^2R_{nl}}{dr_q{}^2}+\frac{2\mu}{\hbar^2}\left(E_{nl}-a_0r_q-b_0r_q{}^2-d_0+\frac{g_0}{r_q}-\frac{k_0}{r_q{}^2}-\frac{l(l+1)\hbar^2}{2\mu r_q{}^2}\right)R_{nl}(r_q)=0\,, \tag{13}$$

.

Equation (13) cannot be solved exactly with the inserted potential model. The Greene-Aldrich approximation scheme ${r_q}^{-2} \approx \alpha^2(1-e^{-\alpha r_q})^{-2}; {r_q}^{-1} \approx \alpha(1-e^{-\alpha r_q})^{-1}$ is employed to address the centrifugal barrier. This approximation provides a reliable estimate for the centrifugal term and is applicable within the range specified by $\alpha << 1$, [29]. The Greene-Aldrich approximation is selected for its simplicity and effectiveness in solving Schrödinger equation with specific potential forms. However, its limitations arise in higher-dimensional scenarios due to reduced accuracy in capturing the intricate coupling of angular momentum and potential terms, which may lead to deviations in energy eigenvalues and wavefunction behavior. By applying a variable transformation from $r_q \to x_d$, our new coordinate is expressed in terms of the parameter $x_d = e^{-\alpha r_q}$, which enables the simplification of Eq. (13), ultimately leading to Eq. (14).

$$\frac{d^2\psi(x_d)}{dx_d{}^2} + \frac{1-x_d}{x_d(1-x_d)}\frac{d\psi(x_d)}{dx_d} + \frac{1}{[x_d(1-x_d)]^2}\begin{bmatrix} -A(1-x_d)^4 - B(1-x_d)^3 \\ -\varepsilon(1-x_d)^2 + C(1-x_d) - D - \gamma \end{bmatrix}\psi(x_d) = 0, \tag{14}$$

where

$$\left.-\varepsilon = \frac{2\mu E_{nl}}{\alpha^2\hbar^2} - \frac{2\mu d_0}{\alpha^2\hbar^2}, \quad A = \frac{2\mu a_0}{\alpha^4\hbar^2}, \quad B = \frac{2\mu b_0}{\alpha^3\hbar^2}, \quad C = \frac{2\mu g_0}{\alpha\hbar^2}, D = \frac{2\mu k_0}{\hbar^2},, \quad \gamma = l(l+1)\right\}. \tag{15}$$

Equation (14) contains terms of order ${x_d}^3$ *and* ${x_d}^4$. To simplify and obtain an approximate analytical solution, we neglect these terms by assuming to $\alpha r_q \prec 1$ [30]. Truncation of higher-order terms simplifies mathematical models, making them more computationally efficient while retaining physically realistic outcomes. This approach reduces complexity, enhances interpretability, and enables practical application in systems where lower-order terms dominate, ensuring accurate predictions without unnecessary computational overhead, especially in well-defined parameter regimes with minimal influence from higher-order contributions. Consequently, Eq. (14) reduces to

$$\frac{d^2\psi(x_d)}{dx_d{}^2} + \frac{1-x_d}{x_d(1-x_d)}\frac{d\psi(x_d)}{dx_d} + \frac{1}{[x_d(1-x_d)]^2}\begin{bmatrix} -(\varepsilon+6A+3B){x_d}^2 \\ +(2\varepsilon+4A+3B-C)x_d \\ -(\varepsilon+A+B-C+D+\gamma) \end{bmatrix}\psi(x_d) = 0, \tag{16}$$

The comparison of Eq. (16) and Eq. (A1) of Appendix A, the following polynomials are gotten;

$$\begin{aligned} &\tilde{\tau}(x_d) = 1 - x_d; \ \sigma(x_d) = x_d(1-x_d); \ \sigma^{/}(x_d) = 1 - 2x_d, \\ &\sigma^{//}(x_d) = -2; \sigma(x_d) = -(\varepsilon+6A+3B){x_d}^2 \\ &+(2\varepsilon+4A+3B-C)x_d - (\varepsilon+A+B-C+D+\gamma) \end{aligned} \tag{17}$$

Inserting the polynomials given into Eq. (A9) of Appendix A, gives

$$\pi(x_d) = -\frac{x_d}{2} \pm \sqrt{(A_1 - K){x_d}^2 + (K + A_2)x_d + A_3},$$

where

$$A_1 = \left(\frac{1}{4} + \varepsilon + 6A + 3B\right), \quad A_2 = -(2\varepsilon + 4A + 3B - C), \quad A_3 = (\varepsilon + A + B - C + D + \gamma).$$

The NU method stipulates that the discriminant of the quadratic equation must be equal to zero. By using the discriminant, we can solve for the constant k to determine the two roots. In this particular analysis, we concentrate on the negative square root, expressed as:

$$K = -(A_2 + 2A_3) - 2\sqrt{A_3}\sqrt{A_3 + A_2 + A_1}. \tag{18}$$

We then put Eq. (18) into $\pi(x_d) = -\frac{x_d}{2} \pm \sqrt{(A_1 - K){x_d}^2 + (K + A_2)x_d + A_3}$, and obtain, $\pi(x_d)$has the most suitable expression given as

$$\pi(x_d) = -\frac{x_d}{2} - \left[\left(\sqrt{A_3} + \sqrt{A_3 + A_2 + A_1}\right)x_d - \sqrt{A_3}\right], \tag{19}$$

Using the polynomials and Eq. (17). Therefore, we obtain $\tau(x_d)$ and $\tau^{/}(x_d)$ as follows:

$$\tau(x_d) = 1 - 2x_d - 2\sqrt{A_3}x_d - 2\sqrt{A_3 + A_2 + A_1}x_d + 2\sqrt{A_3}, \tag{20}$$

$$\tau^{/}(x_d) = -2\left[1 + \sqrt{A_3} + \sqrt{A_3 + A_2 + A_1}\right],. \tag{21}$$

Referring to Eq. (A10) and Eq. (A11) of Appendix A, the following expressions for λ_n and λ are as follows:

$$\lambda_n = n^2 + \left[1 + 2\sqrt{A_3} + 2\sqrt{A_3 + A_2 + A_1}\right]n, (n = 0,1,2,\ldots), \tag{22}$$

$$\lambda = -\frac{1}{2} - \sqrt{A_3} - \sqrt{A_3 + A_2 + A_1} - (A_2 + 2A_3) - 2\sqrt{A_3}\sqrt{A_3 + A_2 + A_1}, \tag{23}$$

The eigenvalues of the RSPP is obtained by equating Eqs. (22) and (23) and incorporating Eq. (15)

$$E_{nl} = \frac{\alpha^2\hbar^2 l(l+1)}{2\mu} + \frac{a_0}{\alpha^2} - \alpha g_0 + \alpha^2 k_0 + d_0 + b_0 - \frac{\alpha^2\hbar^2}{8\mu}\left[\frac{\left(n+\frac{1}{2}+\sqrt{\left(l+\frac{1}{2}\right)^2+\frac{6\mu a_0}{\alpha^4\hbar^2}+\frac{2\mu b_0}{\alpha^3\hbar^2}+\frac{2\mu k_0}{\hbar^2}}\right)^2-\frac{4\mu a_0}{\alpha^4\hbar^2}-\frac{2\mu b_0}{\alpha^3\hbar^2}-\frac{2\mu g_0}{\alpha\hbar^2}+\frac{4\mu k_0}{\hbar^2}+l(l+1)}{n+\frac{1}{2}+\sqrt{\left(l+\frac{1}{2}\right)^2+\frac{6\mu a_0}{\alpha^4\hbar^2}+\frac{2\mu b_0}{\alpha^3\hbar^2}+\frac{2\mu k_0}{\hbar^2}}}\right]^2 \tag{24}$$

The derivation of energy eigenvalues in Eq. (24) follows a precise and methodical approach, incorporating standard approximation techniques and ensuring mathematical rigor. It systematically applies boundary conditions, and potential terms, yielding results that align with established theory. The derivation effectively captures essential physical behavior while maintaining mathematical consistency.

The wave function (WF) for the ground state and the first excited state, along with their normalization constants, are presented in Eqs. (25) and (26).

$$\psi_{0l}\left(r_q\right) = \sqrt{\frac{\alpha\,\Gamma\,[2(1+A+B)]}{\Gamma\,[2A]\,\Gamma\,[2+2B]}} \times (e^{-\alpha r_q})^A \times (1 - e^{-\alpha r_q})^{B+\frac{1}{2}} \tag{25}$$

$$\psi_{1l}\left(r_q\right) = \sqrt{\frac{2A(3+2A+2B)\alpha\,\Gamma\,[2(1+A+B)]}{(3+2B)\,\Gamma\,[2+2A]\,\Gamma\,[2+2B]}} \times \left(e^{-\alpha r_q}\right)^A \times (1 - e^{-\alpha r_q})^{B+\frac{1}{2}} \times \mathrm{P}_1^{(2A,2B)}\left(1 - 2e^{-\alpha r_q}\right), \tag{26}$$

where

$$A = \sqrt{l \times (l+1) - \frac{2m}{\alpha^2 h^2} \times (E_{nl} - a) - \frac{2m}{\alpha^2 h^2}}\,; \quad B = l + \frac{1}{2}$$

P_1 and $\mathit{\Gamma}$ are Jacobi and Gamma functions respectively

The wave function in momentum space is expressed as

$$\Psi_{00}(p) = \sqrt{\frac{1}{2\pi}}\sqrt{\frac{\alpha\,\Gamma\,[2(1+A+B)]}{\Gamma\,[2A]\,\Gamma\,[2+2B]}}\int_0^\infty (e^{-\alpha r_q})^A \times (1 - e^{-\alpha r_q})^{B+\frac{1}{2}} e^{-ip\,r_q}\, d\,r_q \tag{27}$$

$$\Psi_{00}(p) = \sqrt{\frac{\alpha\,\Gamma\,[2(1+A+B)]}{\Gamma\,[2A]\,\Gamma\,[2+2B]}} \times \frac{\Gamma\,[\frac{3}{2}+B]\,\Gamma\,[A+\frac{ip}{\alpha}]}{\sqrt{2\pi}\alpha\,\Gamma\,[\frac{3}{2}+A+B+\frac{ip}{\alpha}]} \quad . \tag{28}$$

The eigenfunction corresponding to the SE in spherical polar coordinates is expressed as:

$$\Psi_{nlm}\left(r_q,\theta_{r_q},\phi_{r_q}\right)=\frac{R_{nl}\left(r_q\right)}{r_q}Y_{lm}\left(\theta_{r_q},\phi_{r_q}\right). \tag{29}$$

The spherical harmonics $Y_{lm}(\theta,\phi)$ is defined by

$$Y_{lm}(\theta,\phi)=(-1)^m\sqrt{\frac{2l+1(l-m)!}{4\pi(l+m)!}}P_l^m(\cos\theta)e^{im\phi} \tag{30}$$

where the function $P_l^m(Cos\theta)$ is the associated Legendre function.

The wave function in momentum space is represented by the Fourier transform [31].

$$\Psi_{nlm}(p,\theta_p,\phi_p)=\frac{1}{(2\pi)^{3/2}}\int_{\mathbb{R}^3}\Psi_{nlm}\left(r_q,\theta_{r_q},\phi_{r_q}\right)e^{-i\bar{p}.\bar{r}}\,d^3r_q \tag{31}$$

The notation $d^3r_q=\left(r_q^2\,dr_q\right)sin\theta d\theta d\phi$ is the volume element. The plane-wave expansion for $e^{-i\bar{p}.\overline{r_q}}$ is given as

$$e^{-i\bar{p}.\overline{r_q}}=(2\pi)^{3/2}\sum_{l=0}^{\infty}\sum_{m=-l}^{l}i^{-l}\frac{J_{l+1/2}\left(p\,r_q\right)}{\sqrt{p\,r_q}}\,\mathrm{Y}_{lm}(\theta_p,\phi_p)\mathrm{Y}_{lm}^{*}\left(\theta_{r_q},\phi_{r_q}\right)\ [32] \tag{32}$$

Given the axial symmetry, only the m = 0 terms remain, which simplifies the plane-wave expansion significantly.

$$e^{-i\bar{p}.\overline{r_q}}=(2\pi)^{3/2}\mathrm{Y}_{lm}(\theta_p,\phi_p)\sum_{l=0}^{\infty}i^{-l}\frac{J_{l+1/2}\left(p\,r_q\right)}{\sqrt{p\,r_q}}\,\mathrm{Y}_{l0}^{*}\left(\theta_{r_q},\phi_{r_q}\right) \tag{33}$$

Substituting equations (30) and (33) into equation (32) yields

$$\Psi_{nlm}(p,\theta_p,\phi_p)=i^{-l}\mathrm{Y}_{lm}(\theta_p,\phi_p)\int_0^{\pi}\int_0^{2\pi}\mathrm{Y}_{l0}\left(\theta_{r_q},\phi_{r_q}\right)\mathrm{Y}_{l0}^{*}\left(\theta_{r_q},\phi_{r_q}\right)sin\theta d\theta d\phi$$

$$\times\int_0^{\infty}\frac{R_{nl}\left(r_q\right)}{r_q}\frac{J_{l+1/2}\left(p\,r_q\right)}{\sqrt{p\,r_q}}r_q^2\,dr_q \tag{34}$$

For the ground state, the orthonormality condition of the spherical harmonics is applied to simplify the analysis.

$$\Psi_{000}(p,\theta_p,\phi_p)=\frac{\mathrm{Y}_{00}(\theta_p,\ \phi_p)}{\sqrt{p}}F_{00}(p) \tag{35}$$

where,

$$F_{00}(p)=\int_0^{\infty}\sqrt{r_q}\,R_{00}\left(r_q\right)J_{1/2}\left(p\,r_q\right)dr_q \tag{36}$$

The momentum space wave function is obtained using MATHEMATICA software, as given by:

$$\Psi_{000}(p,\theta_p,\phi_p)=\frac{(-1)^{1/4}e^{-\frac{i\pi}{4}}\Gamma\left[\frac{3}{2}+B\right]\sqrt{\frac{\alpha\Gamma[2(1+A+B)]}{\Gamma[2A]\Gamma[2+2B]}}\left(-\frac{i\Gamma\left[A-\frac{ip}{\alpha}\right]}{\Gamma\left[\frac{3}{2}+A+B-\frac{ip}{\alpha}\right]}+\frac{i\Gamma\,\mathrm{a}\left[A+\frac{ip}{\alpha}\right]}{\Gamma\left[\frac{3}{2}+A+B+\frac{ip}{\alpha}\right]}\right)}{p\sqrt{2\pi}\alpha}\mathrm{Y}_{00}(\theta_p,\ \phi_p) \tag{37}$$

2.1 Oscillator Strength

Oscillator strength is a dimensionless quantity that represents the probability of a system, like an atom or molecule, absorbing or emitting electromagnetic radiation. It represents the intensity of transitions between energy states, with higher values corresponding to more significant transitions. This parameter is crucial for analyzing spectra and atomic/molecular interactions. The expression is given by:

$$f_{ij}^{l} = \frac{2M}{3\hbar^2}\left(E_j - E_i\right)\left|\langle\psi_j|r|\psi_i\rangle\right|^2 \tag{38}$$

where E_j *and* ψ_j are at a higher state than the respective E_i *and* ψ_i. The M represents an electronic mass. The notation $\left|\langle\psi_j|r|\psi_i\rangle\right|$ is the matrix element and $\left(E_j - E_i\right)$ is the energy difference [19].

2.2. Expectation values and the Heisenberg Uncertainty principle

The expression for the expectation value (EV) of $\boldsymbol{r_q}$, $\boldsymbol{r_q}^{\mathbf{2}}$, and $\hat{\mathbf{p}}^{\mathbf{2}}$ are as follows [1].

$$\langle r_q\rangle_n = \int_0^\infty R_{n\ell} r_q R_{.n\ell}\, dr_q \tag{39}$$

$$\langle {r_q}^2\rangle_n = \int_0^\infty R_{.n\ell} {r_q}^2 R_{n\ell} dr_q \tag{40}$$

$$\langle \hat{p}^2\rangle_n = \int_0^\infty R_{n\ell}\hat{p}^2 R_{.n\ell} dr_q = -\int_0^\infty R_{nl}(r)\frac{d^2}{dr_q^2}R_{n.l}^{*}(r)dr_q \tag{41}$$

The uncertainties in both position and momentum are evaluated using Equations (42) and (43) [1].

$$\Delta r_q = \sqrt{\langle r_q^2\rangle - \langle r_q\rangle^2} \tag{42}$$

$$\Delta p = \sqrt{\langle p^2\rangle - \langle p\rangle^2} \tag{43}$$

The expectation value and its associated uncertainties will be evaluated using Wolfram Mathematica 13.

3. Case Study: Diatomic Molecules

Formed through the covalent bonding of two atoms, diatomic molecules are fundamental to numerous physical and chemical phenomena. Their importance spans diverse fields, from atmospheric chemistry to molecular spectroscopy and quantum mechanical modeling. Recent studies [2,24-26,33] have significantly enriched our understanding of their intrinsic properties, providing advanced theoretical models and experimental data that offer deeper insights into their structure, dynamics, and interactions. The potential utilized in our study enables the investigation of diatomic molecules by setting $g_0 = 2D_e r_e, k_0 = D_e r_e^2, a_0 = b_0 = d_0 = 0$ of Eq. (12), we have the Kratzer potential and the energy equation is given as Eq.(44), when $\alpha = 0$. The Kratzer potential has emerged as a key model in atomic and molecular physics, particularly in the study of vibrational and rotational spectroscopy [34]. Its relevance in molecular physics is both substantial and widely acknowledged.

$$E_{nl} = -\frac{2\mu_a}{\hbar^2}D_e^2 r_e^2\left[n + \frac{1}{2} + \sqrt{\left(l + \frac{1}{2}\right)^2 + \frac{2\mu_a D_e r_e^2}{\hbar^2}}\right]^{-2} \tag{44}$$

4. Results and Discussion

The NU method was employed to derive the energy spectrum of the Schrödinger equation under the RSPP, retaining terms up to the second order. This approximation ensures accuracy in position space, which is critical because information-theoretic measures such as Fisher information, Shannon entropy, and Rényi entropy are highly sensitive to the precision of the underlying wavefunctions. Fisher information, which characterizes the localization or sharpness of a probability distribution, responds strongly to even minor variations in eigenvalues. Similarly, Shannon and Rényi entropies, which quantify the uncertainty and spread of quantum states, are directly influenced by the accuracy of the eigenfunctions and their corresponding spectra. Consequently, enhancing the precision of eigenvalue approximations significantly improves the reliability and fidelity of these entropy-based analyses in both coordinate and momentum representations, offering deeper insights into the fundamental behavior of quantum systems. Table 1 reports the one-dimensional ground-state Shannon entropy for various values of the screening parameter α. As α increases, entropy in position space rises, while it decreases in momentum space, illustrating the trade-off between

.

precision in conjugate variables and confirming compliance with the BBM inequality. A similar pattern is observed in Table 2, which presents the three-dimensional ground-state Shannon entropy over the range α=0.01to 0.09. In all cases, the total entropy exceeds the BBM bound of 6.4343, reaffirming the fundamental quantum constraint on simultaneous measurements of position and momentum.

Table 1. Numerical Values of Position and Momentum Shannon Entropies for the One-Dimensional Ground State using parameters $a_0, = 1.9, b_0 = 1.7, d_0 = 1.8, g_0 = 1.1, k_0 = 0.02, \mu = 1, \hbar = 1$

α	$S(\rho)$	$S(\gamma)$	$S(\rho) + S(\gamma) \geq 2.14473$
0.01	2.014582633	0.130538251	2.145120884
0.02	2.017227462	0.129000744	2.146228206
0.03	2.016882987	0.12872739	2.145610377
0.04	2.024335028	0.121969552	2.14630458
0.05	2.038506689	0.108715548	2.147222237
0.06	2.061039402	0.087358576	2.148397978
0.07	2.093779221	0.05611188	2.149891102
0.08	2.138926224	0.012875116	2.15180134
0.09	2.199166310	-0.044868907	2.154297403

Table 2. Numerical Values of Position and Momentum Shannon Entropies for the three-dimensional Ground State using parameters $a_0, = 1.9, b_0 = 1.7, d_0 = 1.8, g_0 = 1.1, k_0 = 0.02, \mu = 1, \hbar = 1$

α	$S(\rho)$	$S(\gamma)$	$S(\rho) + S(\gamma) \geq 6.4342$
0.01	2.356488661	4.210105084	6.566593745
0.02	0.127911327	6.438681244	6.566592571
0.03	-1.136590993	7.703183368	6.566592375
0.04	-2.023404187	6.058972249	4.035568062
0.05	-2.707005078	9.273597358	6.566592279
0.06	-3.263379488	9.829971751	6.566592263
0.07	-3.732534727	10.29912698	6.566592253
0.08	-4.138146485	10.70473873	6.566592247
0.09	-4.495392354	11.06198460	6.566592243

Table 3 displays the one-dimensional ground-state Fisher information for various values of α. As expected, the product of Fisher information in position and momentum spaces satisfies the SCR inequality. Increasing α enhances position-space Fisher information reflecting improved localization while reducing momentum-space information, demonstrating the intrinsic limits imposed by the uncertainty principle.

Table 3. Numerical Values of Position and Momentum Fisher Information for the One-Dimensional Ground State using parameters $a_0, = 1.9, b_0 = 1.7, d_0 = 1.8, g_0 = 1.1, k_0 = 0.02, \mu = 1, \hbar = 1$

α	$I(\rho)$	$I(\gamma)$	$I(\rho)I(\gamma) \geq 4$
0.01	0.30313370	13.19549806	4.000000150
0.02	0.30406752	13.1550108	4.000011510
0.03	0.302969164	13.20285708	4.000058572
0.04	0.298904296	13.38283435	4.000186677
0.05	0.291090195	13.74304620	4.000466004
0.06	0.278928026	14.34422399	4.001006078
0.07	0.262046936	15.27201902	4.001985792
0.08	0.240366064	16.65674436	4.003716087
0.09	0.214192951	18.70638388	4.006775559

This inverse relationship persists in three dimensions, as shown in Table 4. As α increases, position-space Fisher information becomes more pronounced, indicating sharper localization, whereas momentum-space information decreases. These trends not only comply with the SCR inequality but also highlight how α influences the fundamental trade-off between precision in conjugate observables.

Table 5 presents numerically computed Rényi entropies for the index parameter q=0.5. The data show that increasing α leads to higher entropy in both coordinate and momentum spaces, emphasizing the role of screening in enhancing the system's overall uncertainty.

Table 4. Numerical Values of Position and Momentum Fisher Information for the three-Dimensional Ground State using parameters $a_0, = 1.9, b_0 = 1.7, d_0 = 1.8, g_0 = 1.1, k_0 = 0.02, \mu = 1, \hbar = 1$

α	$I(\rho)$	$I(\gamma)$	$I(\rho)I(\gamma) \geq 36$
0.01	13.1768	3.642751741	47.99981114
0.02	58.2168	0.824488281	47.99906934
0.03	135.2568	0.354872211	47.99887971
0.04	244.2968	0.196477482	47.99882003
0.05	385.3368	0.124563430	47.99887357
0.06	558.3768	0.085961509	47.99891224
0.07	763.4168	0.062873883	47.99897888
0.08	1000.4568	0.047977061	47.99897643
0.09	1269.4968	0.037809514	47.99905749

Table 5. Numerical Values of Position and Momentum Renyi information using parameters $a_0, = 1.9, b_0 = 1.7, d_0 = 1.8, g_0 = 1.1, k_0 = 0.02, \mu = 1, \hbar = 1$

α	$R_{0.6}(\rho)$	$R_3(\gamma)$	$R_{0.6}(\rho) + R_3(\gamma) \geq 2.057915$
0.01	2.017227462	-0.096433416	2.057944483
0.02	2.014582633	-0.095156679	2.058045411
0.03	2.016882987	-0.097403422	2.058208962
0.04	2.024335028	-0.104780595	2.058441418
0.05	2.038506689	-0.118856345	2.058749655
0.06	2.061039402	-0.141272364	2.059146266
0.07	2.093779221	-0.173875004	2.05965288
0.08	2.138926224	-0.218864514	2.060306226
0.09	2.19916631	-0.278926653	2.061169497

Furthermore, as the index q increases, Rényi entropy also rises, confirming its sensitivity to the shape of the underlying probability distribution. This behavior supports the use of Rényi entropy as a generalized measure for exploring quantum delocalization, coherence, and complexity. In Table 6, the expectation values $\langle r\rangle$, $\langle r^2\rangle$, and $\langle p^2\rangle$ are reported for the ground state. These values provide additional insight into the average behavior of quantum observables and reinforce the Heisenberg Uncertainty Principle by illustrating the inherent limits on the simultaneous accuracy of position and momentum measurements.

Table. 6: Numerical Values of Expectation values and Heisenberg uncertainty using parameters $a_0, = 1.9, b_0 = 1.7, d_0 = 1.8, g_0 = 1.1, k_0 = 0.02, \mu = 1, \hbar = 1$

α	$\langle r\rangle$	$\langle r^2\rangle$	$\langle p^2\rangle$	$\Delta r\Delta p \geq 0.5$
0.01	194.1635691	37702.79139	0.075783437	0.500073000
0.02	97.02067465	9416.303916	0.076016882	0.500293610
0.03	64.82897404	4206.10529	0.075742291	0.500662210
0.04	48.93699129	2398.190572	0.074726074	0.501186938
0.05	39.6153286	1572.835561	0.072772549	0.501884149
0.06	33.62556095	1134.303532	0.069732006	0.502783536
0.07	29.58801336	879.3269599	0.065511734	0.503935848
0.08	26.82459241	723.8098833	0.060091516	0.505427125
0.09	24.97346852	628.4821408	0.053548238	0.507405668

Table 7 shows that, as α increases, oscillator strengths decrease. This decline reflects reduced interaction between the electric field and electronic states, leading to lower transition probabilities. These trends are consistent with previous studies using other potential models, highlighting the robustness of the observed behavior.

.

Table. 7: Numerical Values of Oscillator Strength for the Radial Scalar Power Potential, using parameters $a_0, = -20, b_0 = 3, d_0 = 4.8, g_0 = 2, k_0 = 1, \mu = 1, \hbar = 1$

Transition	α	f_{ij}^{l}
1s – 2p	0.0250	150.7654321
	0.0500	149.8765432
	0.0750	148.9876543
	0.1000	148.0987654
	0.1500	147.2098765
1s – 3p	0.0250	2900.123456
	0.0500	1450.234567
	0.0750	950.3456789
	0.1000	710.4567890
	0.1500	460.5678901

By imposing specific boundary conditions, the RSPP was reduced to the Kratzer potential, facilitating an accurate analytical treatment. Table 8 summarizes the spectroscopic parameters for CH and N_2 molecules, chosen for their relevance in previous studies and practical applications. Using these parameters in Eq. (44), energy eigenvalues were computed and are presented in Table 9.

Table 8. Spectroscopic properties of the chosen diatomic molecules [35].

Molecules	$D_e(eV)$	$r_e(\dot{A})$	$\mu(amu)$
CH	31838.081490	1.1198	0.929931
N_2	11.938193820	1.0940	7.003350

Table 9: Comparison of bound-state energy (in eV) for different ℓ quantum numbers across various diatomic molecules while keeping n constant.

n	l	CH	CH [40]	N_2	N_2 [40]
0	0	0.083223	0.08322383	0.054436	0.05443655
1	0	0.241150	0.24115051	0.162076	0.16207644
	1	0.244408	0.24440882	0.162565	0.16256502
2	0	0.389589	0.38958988	0.268260	0.26826045
	1	0.392654	0.39265445	0.268742	0.26874244
	2	0.398767	0.39876758	0.269706	0.26970629
3	0	0.529286	0.52928690	0.373014	0.37301474
	1	0.532172	0.53217281	0.373490	0.37349025
	2	0.537929	0.53792974	0.374441	0.37444116
	3	0.546528	0.54652818	0.375867	0.37586721
4	0	0.660914	0.66091486	0.476364	0.47636485
	1	0.663635	0.66363571	0.476834	0.47683401
	2	0.669063	0.66906360	0.477772	0.47777219
	3	0.677171	0.67717107	0.479179	0.47917917
	4	0.687917	0.68791738	0.481054	0.48105461
5	0	0.785083	0.78508342	0.578335	0.57833578
	1	0.787651	0.78765158	0.578798	0.57879869
	2	0.792775	0.79277502	0.579724	0.57972438
	3	0.800428	0.80042821	0.581112	0.58111263
	4	0.810573	0.81057320	0.582963	0.58296310
	5	0.823160	0.82316019	0.585275	0.58527534

The results show strong agreement with alternative analytical methods [35]. For a fixed principal quantum number n, increasing the angular momentum quantum number ℓ leads to higher energy levels, reflecting the centrifugal contribution to the effective potential and its implications for molecular stability and spectroscopic behavior. Beyond the Kratzer limit, the full RSPP model reveals deeper physical trends. The results show that the screening parameter directly affects the spatial confinement of the system. Stronger screening leads to more localized wavefunctions, larger energy spacings, and reduced overlap between states, which lowers oscillator strengths and reduces transition probabilities. These changes are reflected in information-theoretic measures as well, with Fisher information increasing in position space and Shannon and Rényi entropies capturing the redistribution of uncertainty between conjugate variables. These results demonstrate that the potential shape influences measurable spectroscopic properties and the quantum information content of the states, highlighting the practical significance of our findings for understanding and predicting transition behaviors in the system.

Figures 1(a) and 1(b) illustrate wavefunction profiles and corresponding probability densities for ℓ=1. As n increases, wavefunctions become more oscillatory, with higher amplitudes and additional nodes, indicating the emergence of distinct quantum states. The associated probability densities display Gaussian-like peaks, supporting the quantized nature of the system and confirming compliance with the BBM inequality. Figures 2(a) and 2(b) extend this analysis to ℓ=2, further confirming the influence of the potential on wavefunction structure and spatial localization.

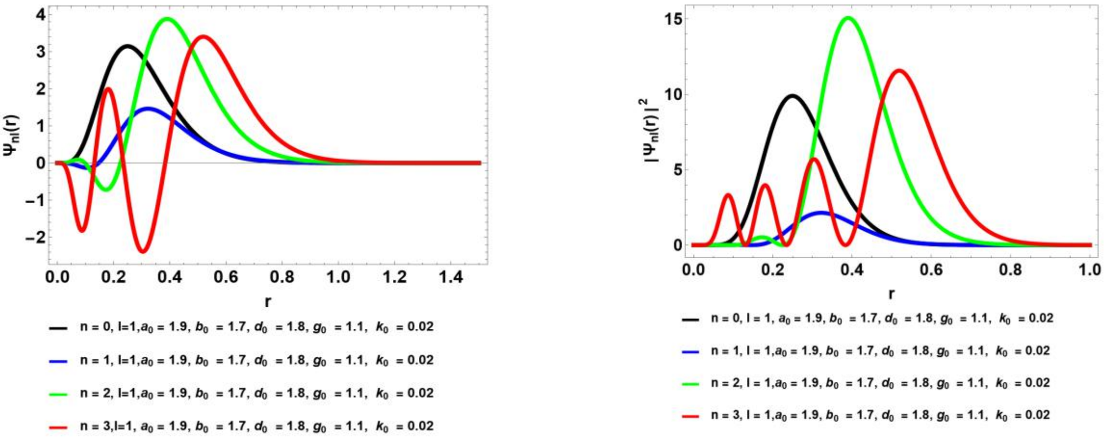

a) b)

Fig.1. *(a)* Radial wave functions and *(b)* corresponding probability density functions for various principal quantum numbers n, at *l* =1

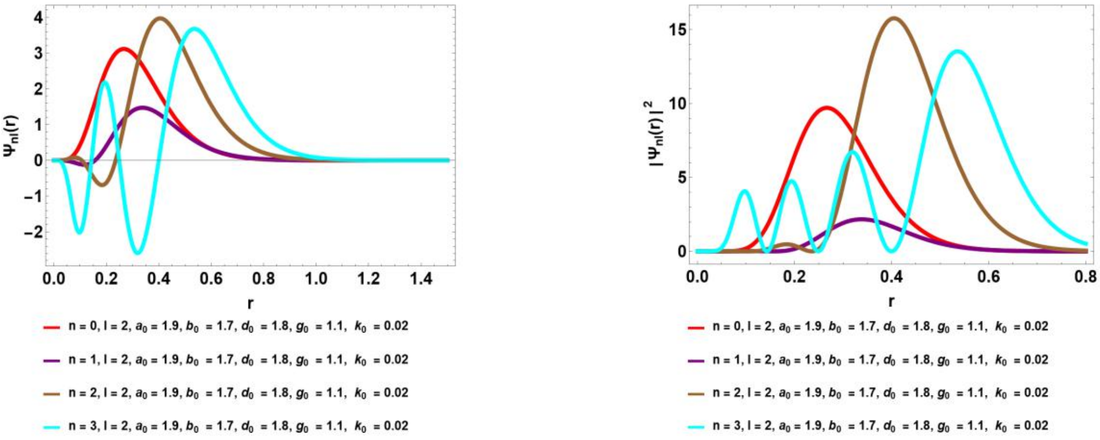

a) b)

Fig. 2. *(a)* Radial wave functions and *(b)* corresponding probability density functions for various principal quantum numbers, at *l* =2

Figures 3(a) and 3(b) show the variation of Shannon entropy with respect to α. An increase in α leads to a decline in position-space entropy and a corresponding rise in momentum-space entropy, reinforcing the uncertainty principle.

.

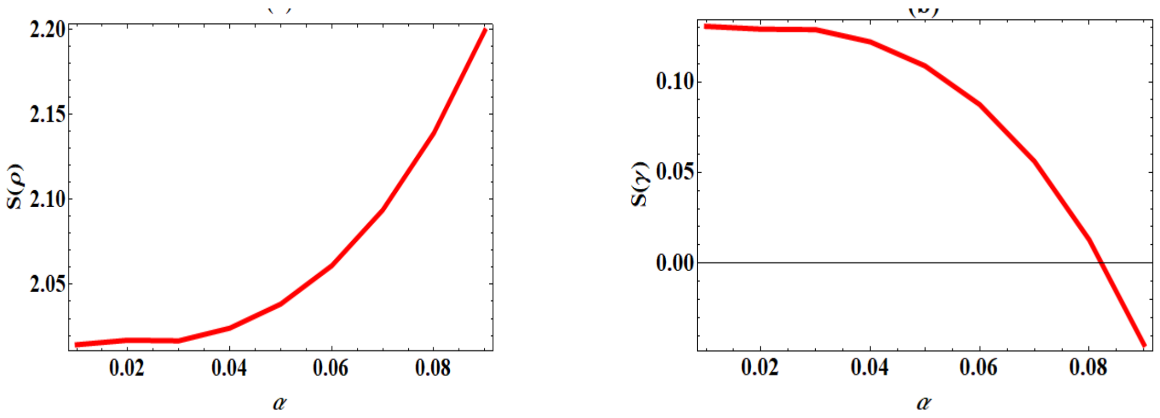

a) b)

Fig 3. (a, b): Variations of Shannon entropies with α parameter

Figures 4(a) and 4(b) depict Fisher information under the same variation. As α increases, Fisher information in position space rises, signifying enhanced sensitivity to parameter changes, while it declines in momentum space, reflecting decreased sensitivity in that domain. Finally, Figures 5(a) and 5(b) illustrate Rényi entropy trends with respect to α. As α increases, Rényi entropy decreases in momentum space while increasing in position space. This duality highlights the system's evolving structure and localization as a function of the screening parameter.

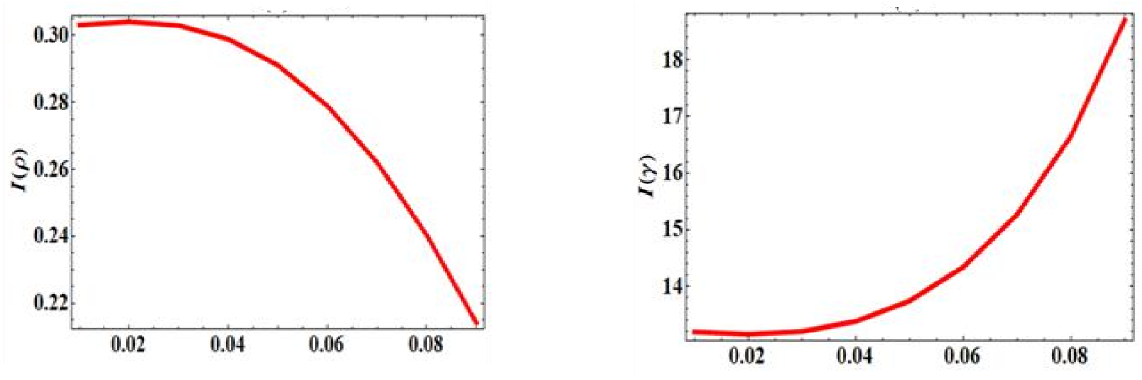

a) b)

Fig. 4. (a, b): Variations of Fisher information with α parameter

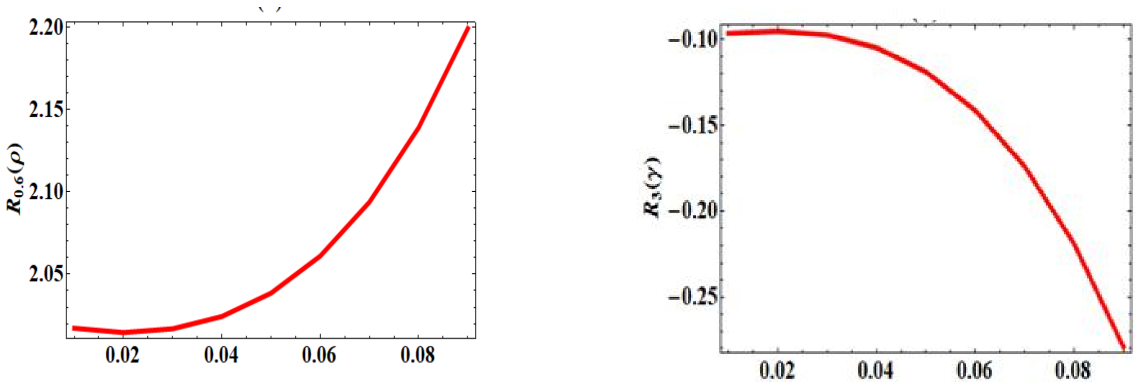

a) b)

Fig. 5. (a, b): Variations of Renyi entropy with α parameter

These complementary behaviors in position and momentum representations are in full agreement with the uncertainty principle, illustrating the balance between information content in conjugate domains. This integrated analysis not only reinforces the foundational constraints of quantum mechanics but also enhances our understanding of how information is distributed between conjugate variables, providing valuable insights for quantum measurement, coherence, and the design of quantum technologies.

5. Conclusions

In this study, the Schrödinger equation for the Radial Scalar Power Potential (RSPP) was solved analytically using the NU method, applying the Greene–Aldrich approximation and an appropriate coordinate transformation. This allowed us to obtain energy eigenvalues and normalized wavefunctions, which were then used to compute expectation values, Shannon entropy, Fisher information, Rényi entropy, and oscillator strengths in both position and momentum spaces.

Our results confirm that Shannon entropy and Fisher information satisfy the BBM and SCR inequalities in one- and three-dimensional cases, reaffirming the quantum mechanical limits on the simultaneous precision of conjugate observables. Wavefunction and probability density analyses for $\ell=1$ and $\ell=2$ demonstrate an inverse behavior of Fisher information: increases in one space correspond to decreases in the other, reflecting the uncertainty equilibrium inherent in quantum systems.

By imposing specific boundary conditions, the RSPP reduces to the Kratzer potential, enabling accurate computation of energy eigenvalues for methylidyne (CH) and nitrogen (N_2) molecules. Energy levels rise with increasing angular momentum quantum number, highlighting the centrifugal contribution to the effective potential and its relevance for molecular stability and spectroscopic transitions. Additionally, oscillator strengths decrease with higher screening parameters, indicating reduced electron–field interaction and lower transition probabilities, in agreement with prior studies. These findings provide a clear physical interpretation of the relationships between potential parameters, wavefunction localization, and information-theoretic measures. They emphasize the connection between quantum uncertainty and measurable quantities, such as transition energies and oscillator strengths. The results have practical implications for molecular spectroscopy, modeling of diatomic systems, and the design of quantum sensors, offering a framework for further exploration in quantum information theory and related technological applications.

Conflict of interest statement

The authors declare that they have **no conflict of interest** in relation to this research, whether financial, personal, authorship or otherwise, that could affect the research and its results presented in this paper.

CRediT author statement

Inyang E.P.: Conceptualization, Methodology, Writing-Original draft preparation, Funding acquisition; **Nwachukwu I. M.**: Software Funding acquisition; **Okoi P.O.**: Visualization, Validation, Funding acquisition. The final manuscript was read and approved by all authors.

Funding

This research was supported by the 2025 Senate Research Grant from the National Open University of Nigeria: with grant number NOUN/DRA/SRG/AW/035.

Acknowledgements

The authors, expresses appreciation to the National Open University of Nigeria for the 2025 Senate Research Grant.

References

1 Inyang E.P., Omugbe E., Abu-shady M., William E.S. (2023) Investigation of quantum information theory with the screened modified Kratzer and a class of Yukawa potential model. *Eur Phys J Plus*, 138 (11), 969. https://doi.org/10.1140/epjp/s13360-023-04617-7

2 Inyang E. P. (2025) Quantum expectation values and Shannon entropy in diatomic molecular systems. *Journal of Mathematical Chemistry*. https://doi.org/10.1007/s10910-025-01738-5

3 Inyang E.P., Aouami A.E.L., Ali N., Endut R., Ali N.R., Aljunid S.A. (2024) Information entropies with Varshni-Hellmann potential in higher dimensions. *Phys Open,* 100220. https://doi.org/10.1016/j.physo.2024.100220

4 Dong S., Sun G.H., Dong S.H., Draayer J.P. (2014) Quantum information entropies for a squared tangent potential well. *Phys Lett A*, 378(3), 124–130. https://doi.org/10.1016/j.physleta.2013.11.020

5 Pooja, Kumar R., Kumar G., Kumar R., Kumar A. (2016) Quantum information entropy of Eckart potential. *Int J Quantum Chem,* 116(19), 1413–1418. https://doi.org/10.1002/qua.25197

.

6 Heisenberg W. (1927) Über den anschaulichen Inhalt der quantentheoretischen Kinematik und Mechanik. *Z Phys*, 43, 172–198. https://doi.org/10.1007/BF01397280

7 Białynicki-Birula I., Mycielski J. (1975) Uncertainty relations for information entropy in wave mechanics. *Commun Math Phys,* 44, 129–132. https://doi.org/10.1007/BF01608825

8 Hirschman I.I. (1957) A note on entropy. *Am J Math,* 79(1), 152–156. https://doi.org/10.2307/2372390

9 Beckner W. (1975) Inequalities in Fourier analysis. *Ann Math,* 102(1):159–182. https://doi.org/10.2307/1970980

10 Esquivel Olea R.O., Molina Espíritu M., López Rosa S. (2023) 3D information-theoretic analysis of the simplest hydrogen abstraction reaction. *J Phys Chem A*,127(30), 6159–6174. https://doi.org/10.1021/acs.jpca.3c01957

11 Omugbe E., Osafile O.E., Okon I.B., Eyube E.S., Inyang E.P., Okorie U.S., Onate C.A. (2022) Non-relativistic bound state solutions with α-deformed Kratzer-type potential using the supersymmetric WKB method: Application to theoretic-information measures. *Eur Phys J D,* 76(4), 72. https://doi.org/10.1140/epjd/s10053-022-00395-6

12 Rényi A. (1960) On measures of information theory. In: Neyman J., ed. *Proc 4th Berkeley Symp Math Stat Probab*, I, 547–561. Berkeley, CA: Berkeley Univ. Press.

13 Njoku I.J., Onyenegecha C.P. (2024) Global and local information-theoretic measures of the inversely quadratic Hellmann–Kratzer potential. *Chin J Phys*, 88, 594–608. https://doi.org/10.1016/j.cjph.2023.10.014

14 Amadi P.O., Ikot A.N., Rampho G.J., Okorie U.S., Abdullah H.Y., Lütfüoğlu B.C. (2020) Information entropies for H_2 and ScF diatomic molecules with Deng-Fan-Eckart potential. *Rev Mex Fis*; 66(6), 742–748. https://doi.org/10.31349/revmexfis.66.742

15 Onyeaju M.C., Omugbe E., Onate C.A., Okon I.B., Eyube E.S., Okorie U.S., et al. (2023) Information theory and thermodynamic properties of diatomic molecules using molecular potential. *J Mol Model,* 29(10), 311. https://doi.org/10.1007/s00894-023-05708-z

16 Laguna H.G., Salazar S.J., Sagar R.P. (2022) Information theoretical statistical discrimination measures for electronic densities. *J Math Chem,* 60(7), 1422–1444. https://doi.org/10.1007/s10910-022-01363-6

17 Njoku I.J., Onyeocha E., Onyenegecha C.P., Onuoha M., Egeonu E.K., Nwaokafor P. (2023) Quantum information of the modified Mobius squared plus Eckart potential. *Int J Quantum Chem,* 123(6), e27050. https://doi.org/10.1002/qua.27050

18 Estañón C.R., Montgomery H.E. Jr, Angulo J.C., Aquino N. (2024) The confined helium atom: An information–theoretic approach. *Int J Quantum Chem*, 124(4), e27358. https://doi.org/10.1002/qua.27358

19 Hibbert A. (1975) Developments in atomic structure calculations. *Rep Prog Phys*, 38(11), 1217. https://doi.org/10.1088/0034-4885/38/11/001

20 Ikot A.N., Hassanabadi H., Obong H.P., Umoren Y.C., Isonguyo C.N., Yazarloo B.H. (2014) Approximate solutions of Klein–Gordon equation with improved Manning–Rosen potential in D-dimensions using SUSYQM. *Chin Phys B*, 23(12), 120303. https://doi.org/10.1088/1674-1056/23/12/120303

21 Varshni Y.P. (1990) Eigenenergies and oscillator strengths for the Hulthén potential. *Phys Rev A,* 41(9), 4682. https://doi.org/10.1103/PhysRevA.41.4682

22 Hassanabadi H., Hoda Y.B., Lu L.L. (2012) Approximate analytical solutions to the generalized Pöschl–Teller potential in D dimensions. *Chin Phys Lett*, 29(2), 020303. https://doi.org/10.1088/0256-307X/29/2/020303

23 Inyang E. P., Nwachukwu I. M., Ekechukwu C.C., Ali N., Lawal K.M. (2025) Variance-based approach to quantum information measures and energy spectra of selected diatomic molecules. *Journal of the Korean Physical Society*. https://doi.org/10.1007/s40042-025-01483-7

24 Inyang E.P., Obisung E.O., Amajama J., Bassey D.E., William E.S., Okon I.B. (2022) The effect of topological defect on the mass spectra of heavy and heavy-light quarkonia. *Eurasian Phys Tech J,* 19(4), 78–87. https://doi.org/10.31489/2022No4/78-87

25 Inyang E.P., Nwachukwu I.M., Ekechukwu C.C., Ekong I.B., William E.S., Lawal K.M., et al. (2024) Analytical solution of the class of inversely quadratic Yukawa potential with application to quantum mechanical systems. *Eurasian Phys Tech J*, 21(4), 118–130. https://doi.org/10.31489/2024No4/118-130

26 Nikiforov S.K., Uvarov V.B. (1988) Special functions of Mathematical Physics, Birkhauser, Basel. Available at: https://link.springer.com/book/10.1007/978-1-4757-1595-8

27 William E.S., Inyang E.P., Thompson E.A. (2020) Arbitrary l-solutions of the Schrödinger equation interacting with Hulthén–Hellmann potential model. *Rev Mex Fis*, 66(6), 730–741. https://doi.org/10.31349/RevMexFis.66.730

28 Inyang E.P., Ali N., Endut R., Rusli N., Aljunid S.A. (2024) The radial scalar power potential and its application to quarkonium systems. *Indian J Phys*, 1–10. https://doi.org/10.1007/s12648-024-03335-9

29 Greene R.L., Aldrich C. (1976) Variational wave functions for a screened Coulomb potential. *Phys Rev A,* 14(6), 2363. https://doi.org/10.1103/PhysRevA.14.2363

30 Tas A., Aydogdu O., Salti M. (2017) Relativistic spinless particles with position dependent mass: Bound states and scattering phase shifts. *J Korean Phys Soc*, 70(10), 896–904. https://doi.org/10.3938/jkps.70.896

31 Kota V.K.B. (2014) *Embedded random matrix ensembles in quantum physics*. Vol. 3, Heidelberg: Springer.

32 Inyang E.P., William E.S., Obu J.O., Ita B.I., Inyang E.P., Akpan I.O. (2021) Energy spectra and expectation values of selected diatomic molecules through the solutions of Klein–Gordon equation with Eckart–Hellmann potential model. *Mol Phys*, 119(23), e1956615. https://doi.org/10.1080/00268976.2021.1956615

33 Inyang E.P., Ali N.R., Aljunid S.A. (2024) Energy spectra, expectation values, and thermodynamic properties of HCl and LiH diatomic molecules. *Eurasian Phys Tech J*; 21, 124–137. https://doi.org/10.31489/2024No1/124-137

34 Inyang E.P., Ntibi J.E., Obisung E.O., William E.S., Ibekwe E.E., Akpan I.O., Inyang E.P. (2022) Expectation values and energy spectra of the Varshni potential in arbitrary dimensions. *Jordan J Phys*, 15(5), 509. https://doi.org/10.47011/15.5.7

35 Rani R., Bhardwaj S.B., Chand F. (2018) Bound state solutions to the Schrödinger equation for some diatomic molecules. *Pramana J Phys,* 91, 46. https://doi.org/10.1007/s12043-018-1622-1

AUTHORS' INFORMATION

Inyang, Etido Patrick – Dr. (Sci.), Department of Physics, Faculty of Science, National Open University of Nigeria, Abuja, Nigeria; ORCID iD: 0000-0002-5031-3297; etidophysics@gmail.com

Okoi, Peter Obeten - Mr. (Sci.), Department of Physics, Faculty of Physical Science, University of Calabar, Calabar, Nigeria; ORCID iD: 0000-0001-9147-425X; okoipeter7@gmail.com

Nwachukwu, Iheke Michael – Dr. (Sci.), Department of Physics, Faculty of Science, National Open University of Nigeria, Abuja, Nigeria; ORCID iD: 0000-0003-2237-7805; inwachukwu@noun.edu.ng

.

APPENDIX A: Review of Nikiforov-Uvarov (NU) method

The NU method was proposed by Nikiforov and Uvarov [31] to transform Schrödinger-like equations into a second-order differential equation via a coordinate transformation $s = s(r)$, of the form

$$\psi''(s)+\frac{\tilde{\tau}(s)}{\sigma(s)}\psi'(s)+\frac{\tilde{\sigma}(s)}{\sigma^{2}(s)}\psi(s)=0 \tag{A1}$$

where $\tilde{\sigma}(s)$, and $\sigma(s)$ are polynomials, at most second degree and $\tilde{\tau}(s)$ is a first-degree polynomial. The exact solution of Eq.(A1) can be obtain by using the transformation.

$$\psi(s)=\phi(s)y(s) \tag{A2}$$

This transformation reduces Eq.(A1) into a hypergeometric-type equation of the form

$$\sigma(s)y''(s)+\tau(s)y'(s)+\lambda y(s)=0 \tag{A3}$$

The function $\phi(x)$ can be defined as the logarithm derivative

$$\frac{\phi'(s)}{\phi(s)}=\frac{\pi(s)}{\sigma(s)} \tag{A4}$$

With $\pi(\mathrm{s})$ being at most a first-degree polynomial. The second part of $\psi(s)$ being $y(\mathrm{s})$ in Eq. (A2) is the hypergeometric function with its polynomial solution given by Rodrigues relation as

$$y(s)=\frac{B_{nl}}{\rho(s)}\frac{d^{n}}{ds^{n}}\left[\sigma^{n}(s)\rho(s)\right] \tag{A5}$$

where B_{nl} is the normalization constant and $\rho(s)$ the weight function which satisfies the condition below;

$$\left(\sigma(s)\rho(s)\right)'=\tau(s)\rho(s) \tag{A6}$$

where also

$$\tau(s)=\tilde{\tau}(s)+2\pi(s) \tag{A7}$$

For bound solutions, it is required that

$$\tau^{/}(\mathrm{s})<0 \tag{A8}$$

The eigenfunctions and eigenvalues can be obtained using the definition of the following function $\pi(s)$ and parameter λ, respectively:

$$\pi(s)=\frac{\sigma'(s)-\tilde{\tau}(s)}{2}\pm\sqrt{\left(\frac{\sigma'(s)-\tilde{\tau}(s)}{2}\right)^{2}-\tilde{\sigma}(s)+k\sigma(s)} \tag{A9}$$

and

$$\lambda=k_{-}+\pi'_{-}(s) \tag{A10}$$

The value of k can be obtained by setting the discriminant in the square root in Eq. (A9) equal to zero. As such, the new eigenvalues equation can be given as

$$\lambda+n\tau'(s)+\frac{n(n-1)}{2}\sigma''(s)=0,(n=0,1,2,...) \tag{A11}$$

EURASIAN PHYSICAL TECHNICAL JOURNAL

2025, Volume 22, No.4 (54)

https://doi.org/10.31489/2025N4/117-122

Received: 08/08/2025 Revised: 21/10/2025 Accepted: 22/12/2025

Original Research Article

UDC 531.19; 520.8; 524.3-54

FLUCTUATION-DISSIPATION CORRELATION OF THE SIGNAL OF STARS OF THE FS CMA TYPE

Zhanabaev Z.Zh., Imanbayeva A.K., Akniyazova A.Zh., Ashimov Ye.K.*

Al-Farabi Kazakh National University, Almaty, Kazakhstan
**Corresponding author:* ashimov.yeskendyr@kaznu.kz

Abstract. *Due to the importance of stellar evolution, new theories and approaches to the study of stars are constantly being developed. This study presents novel results obtained through the application of the fluctuation-dissipation theorem. According to this theorem, fluctuations within a system give rise to dissipation in the form of thermal equilibrium. The spectral correlation function of fluctuations is related to the degree of photon dissipation. In this work, the evolutionary stage of stars is determined by analyzing the relationship between dissipation and fluctuation in complex FS CMa-type systems.*

Keywords: Fluctuation-dissipation analysis, FS CMa-type stars, binary stars, photon dissipation.

1. Introduction

Stellar evolution is an extremely complex and lengthy process that plays a key role in the dynamics and development of the Universe. Stars form from dense clouds of gas and dust and pass through several stages of their existence, each accompanied by unique physical phenomena. Stars are primarily composed of hydrogen and helium, which are the main elements present in their cores and atmospheres. Understanding stellar evolution is crucial for interpreting observational data, refining theories of stellar development, and understanding the complex interactions between stars under various astrophysical conditions [1]. Thus, the study of stellar evolution contributes to a broader understanding of the formation, evolution, and dynamics of stars and galaxies in the Universe.

FS CMa-type stars represent a distinct subclass of eruptive objects that exhibit characteristics of both B[e]-type stars and systems with signs of accretion and mass loss. These objects are characterized by strong emission lines (notably $H\alpha$), often with double-peaked profiles indicative of rotating disks or collimated outflows, and a pronounced excess of radiation in the near- and mid-infrared ranges, pointing to the presence of circumstellar dust [2]. Unlike classical B[e] stars, FS CMa objects are not associated with high-mass supernova progenitors or young stellar clusters, which complicates their classification within standard evolutionary frameworks [3]. It is assumed that most FS CMa objects are binary systems, in which the interaction between the components plays a key role in shaping the observed spectral features and energy distributions [4]. The mechanisms of dust formation, particularly near hot B-type stars, can be explained by interactions within close binary systems, where matter transferred from one component to the other cools and condenses into a dust shell or disk. Thus, the study of FS CMa-type stars opens a new avenue for investigating interacting binaries, transitional stages of stellar evolution, and the conditions for dust formation in extreme environments.

There are various methods used to study stellar evolution, such as the observation of star clusters, asteroseismology, numerical modeling and the construction of evolutionary tracks, spectroscopy and photometry, the study of variable stars, and so on [5–8]. In our study, statistical methods will be applied to astrophysical processes. One of the key tools of statistical physics is the fluctuation-dissipation relation (FDR). The FDR emerged within the framework of nonequilibrium statistical physics and kinetic theory, and its formalism was thoroughly developed in the works of Klimontovich [9, 10], L.D. Landau and E.M. Lifshitz [11], and Kubo [12]. These theoretical foundations form the basis of modern analysis techniques for open systems, including astrophysical applications. The use of the FDR allows for the extraction of physically meaningful parameters from fluctuation spectra, and has found wide application in plasma physics, quantum optics, biophysics, and astrophysics [13, 14]. In addition, the information-entropy method for astrophysical phenomena, as used in the works of Zhanabaev Z.Zh. [15–17], will also be considered. In our article, we will analyze the evolutionary stage and physical properties of binary stars and FS CMa-type systems using the FDR to quantitatively describe the connection between radiation fluctuations and dissipative processes in stars with complex structures. These methods provide insight into the dynamics of binary star systems through the equilibrium between fluctuations and dissipation.

The stellar data used in this study were obtained from the PolarBase database, as it operates with high-resolution telescopes employed for spectro-polarimetric observations of stars, specifically the Bernard Lyot Telescope (since 2006) and the Canada-France-Hawaii Telescope (since 2005) [18].

2. Spectral correlation functions of diffusion of concentration in a fluctuating medium.

We will use terms and notations of books (article) of Y.L.Klimontovich "Statistical Physics", "Physics of Open Systems" and others [9, 10]. The Einstein-Smoluchowski equation with random force $\mathrm{y(t)}$ (Langevin source) for the sensor output voltage $\delta\mathrm{V}(\mathrm{t},\vec{\mathrm{r}})$ (denoting fluctuations through δ means also δ is Dirac function):

$$\frac{\delta\mathrm{V}(\mathrm{t},\vec{\mathrm{r}})}{\partial\mathrm{t}} = \mathrm{D}\frac{\partial^2}{\partial\mathrm{r}^2}\delta(\mathrm{t},\vec{\mathrm{r}}) + \mathrm{y}(\vec{\mathrm{r}},\mathrm{t}) \tag{1}$$

where D is the diffusion coefficient. From equation (1) through Fourier-transformation in frequency ω and in wave number $\vec{\mathrm{k}}$ we have

$$\mathrm{y}(\omega,\vec{\mathrm{k}}) = \delta\mathrm{V}(\omega,\vec{\mathrm{k}})(\mathrm{i}\omega + \mathrm{Dk}^2). \tag{2}$$

The correlation function (correlator) of white noise, the random force $y(t)$, does not depend on frequency. Therefore,

$$\langle y_i y_j \rangle_{\vec{k}} = 2Dk^2 \tag{3}$$

where the coefficient 2 takes into account the modulus delta-collision function $|\mathrm{y}|^{\mathrm{n}} = 2\delta(\mathrm{y})$, where n is any number.

From formula (2), the observed values $\delta\mathrm{V}(\omega,\vec{\mathrm{k}})$ represent correlators (i.e., matrix products) involving the modulus $(\mathrm{i}\omega + \mathrm{Dk}^2)$. The correlator is given by:

$$\langle \delta\mathrm{V}_{\mathrm{i}}\delta\,\mathrm{V}_{\mathrm{j}} \rangle_{\omega_{\mathrm{i}}\vec{\mathrm{k}}}, (\omega^2 + \mathrm{D}^2\mathrm{k}^4). \tag{4}$$

Considering (3) from (2), (4) we write down

$$\langle \delta\mathrm{V}_{\mathrm{i}}\delta\,\mathrm{V}_{\mathrm{j}} \rangle_{\omega_{\mathrm{i}}\vec{\mathrm{k}}} = \frac{2\mathrm{D}^2\vec{\mathrm{k}}^2}{\omega^2+\mathrm{D}^2\vec{\mathrm{k}}^4} \tag{5}$$

The expression $D\vec{\mathrm{k}}^2$ has the frequency dimension $[\mathrm{D}] = \frac{\mathrm{m}^2}{\mathrm{c}}, [\mathrm{k}^2] = \frac{1}{\mathrm{m}^2}$. Therefore, in the description of experiments $\overrightarrow{\mathrm{kk}}^2 = \Delta\omega$ is used as a measure of the broadening of the spectrum due to collisions of gas and air particles.

For air, the frequency dimension is approximately $\mathrm{D} \sim 10^{-4}\frac{1}{\mathrm{c}}$, while for semiconductor materials, $\mathrm{D} \sim (10^{-4} \div 10^{-9})\frac{1}{\mathrm{c}}$. The fundamental (resonant) frequency ω_0, highlighted in formula (5), is used in the so-called Lorentz spectrum, defined as

$$\mathrm{f}(\omega, \omega_0, \Delta\omega) = \frac{2(\Delta\omega/2)}{(\omega-\omega_0)^2+(\Delta\omega/2)^2} \tag{6}$$

The function $\mathrm{f}(\omega, \omega_0, \Delta\omega)$ is one of the representations of the Dirac delta function δ, satisfying the normalization condition:

$$\frac{1}{\pi}\int_{-\infty}^{\infty} f(\omega, \omega_0, \Delta\omega)d\omega = 1. \tag{7}$$

$\Delta\omega$ is determined from the experiment as "half-width of the spectrum" i.e. the value of $\Delta\omega = \omega_0 - \omega(\mathrm{f} = 1/2)$, equal at the point where $\mathrm{f} = 1/2$. For modelling, $\mathrm{Dk}^2 = \Delta\omega$ is used as a frequency-independent parameter.

For modelling $\mathrm{f}(\mathrm{c}, \omega, \omega_0)$ considering gas concentration C_0, the parameter $\omega_0\mathrm{C}_0$ is introduced instead of $\Delta\omega$. And also $\omega_0\mathrm{C}$ is also frequency independent. We will now consider the Lorentz spectrum as a function of C. In dimensionless form $\omega = \omega_0\frac{\mathrm{C}}{\mathrm{C}_*}$, where C_* is the characteristic concentration by fluctuations, equation (6) has the following form:

$$f(\omega, \omega_0, C/C_*) = \frac{1}{\pi}\frac{\frac{\omega_0 C}{2C_*}}{(\omega-\omega_0)^2+\left(\frac{\omega_0 C}{2C_*}\right)^2} \tag{8}$$

With a change in the impurity concentration C_0, the mass density within the volume also changes. Fluctuation interactions between particles in the volume lead not only to oscillations, but also to rotational motions. Based on the fluctuation-dissipation relation, the following equation can be written:

$$f_{\text{Л}}(\omega, \omega_0, \mathrm{C}) = \alpha(\omega_0) * \mathrm{cth}\left(\frac{\mathrm{C}\hbar\omega}{2kT}\right) \tag{9}$$
$$\alpha(\omega_0) = \mathrm{const}$$

Let us introduce the notation:

$$\mathrm{C}_* = \frac{2kT}{\hbar\omega_0}, \text{ for the power spectrum } \mathrm{C} = \frac{\mathrm{C}}{\mathrm{C}_*} \tag{10}$$

Let $\alpha(\omega_0) \sim \omega_0$. The proportionality coefficient is incorporated into the normalization condition, i.e., into the value of $f(c)_{\max}$, the Lorentz spectrum is summed over the frequency ω (with ω ranging from 100 to 200). The hyperbolic cotangent function describes the emission process, while the absorption is characterized by the hyperbolic tangent (i.e., the inverse function). Equation (9) therefore takes the following form:

$$f_{\text{Л}}(\omega, \omega_0, \mathrm{C}/\mathrm{C}_*) = \alpha(\omega_0)\mathrm{th}\left(\frac{C\hbar\omega_0}{2kT}\right) \tag{11}$$

The value of concentration, $C_{*_0} = \mathrm{C}_*/2$ corresponding to the saturation of the sensor signal, we determine from the equality of fluctuation coherent quantum ($\hbar\omega_0/2$) and dissipation thermal (kT) factors:

$$C_{*_0} = 2kT/\hbar\omega_0. \tag{12}$$

Telescope observations are represented through the emission wavelength λ:

$$\omega_0 = k * c = 2\pi * \mathrm{c}/\lambda, \tag{13}$$
$$x = \mathrm{C} * \hbar\omega/2kT = \mathrm{C} * \hbar kc/2kT = \mathrm{C} * (\hbar c * 2\pi)/(\lambda_0 * 2kT) \tag{14}$$

.

where c is the speed of light, C is the elemental concentration, T is the temperature of the star, $h\omega_0 = 2.11\text{eV}$ is the energy of the He photon, kT is the thermal energy, k is Boltzmann's constant.

The algorithm of the fluctuation-dissipative stellar analysis has been demonstrated above, and the formulae necessary to fulfil the purpose of the study have been summarized. The next section reflects the results obtained from this work and draws a conclusion based on these results.

3. Results and Discussion

The fluctuation-dissipation method provides a relationship between the dissipation power and the fluctuation intensity of He elements in the stellar atmosphere. Equation (11) describes the equality between the probability density of the concentration and the probability of dissipation. The saturation values of dissipation at C/C_* may serve as an indicator of the evolutionary stage of the stars. Saturation curves as a function of relative concentration were modeled for each star, starting from zero. It was found that in early-type stars (e.g., HD 210839, type O9.5 Iab). He saturation is reached rapidly due to the high temperature and ionization potential. In main-sequence stars (e.g., Vega, A0 V), the saturation process is moderate, whereas in blue supergiants (e.g., P Cygni, B1-2 Ia-0ep), He saturates slowly and the $H\alpha$ intensity persists longer, which corresponds to a more rarefied atmosphere. Figure 1 shows the variation of the dissipation function (11) for HD 210839, Vega, and P Cygni, with their corresponding saturation points as follows: $\mathrm{C}_* = 0.75$, $\mathrm{C}_* = 1.2$, $\mathrm{C}_* = 2$, respectively. As we can see, C_* is smaller for younger stars and increases for stars that are in the middle or later stages of their evolution.

For comparison, the corresponding Lorentzian functions are also shown in Figure 1 as dashed lines, using the same color scheme. The Lorentzian approximation exhibits a broader profile, especially in the case of P Cygni, which may be attributed to enhanced turbulence and pressure in its extended atmosphere.

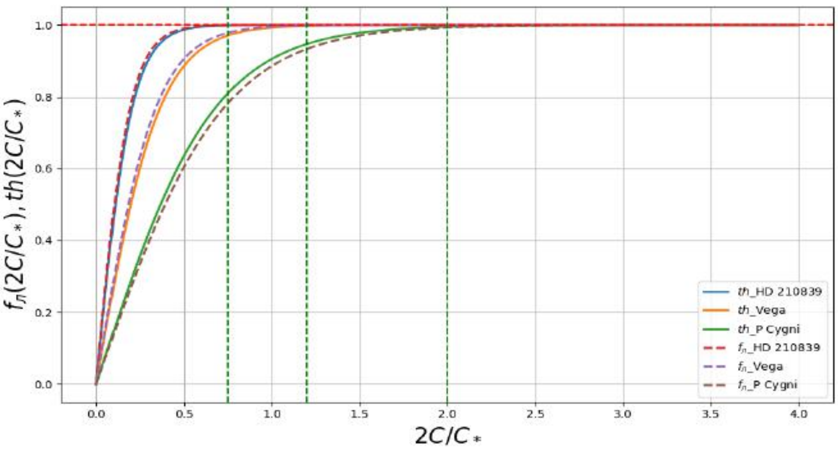

Fig.1. Dissipation function versus normalized concentration for the stars HD 210839, Vega, and P Cygni for the He (λ5875) spectral line, along with the integral of the Lorentzian function.

For the star HD 210839 (blue line), saturation is reached more rapidly (a steep rise in the function), reflecting the high level of ionization in the hot atmosphere of an O-type star. Vega (orange line) shows similar behavior but with a less pronounced rise, consistent with the cooler atmosphere of an A-type star. For P Cygni (green line), saturation occurs significantly more slowly, reflecting the typical characteristics of the rarefied atmosphere of a B-type supergiant. The green vertical dashed lines indicate characteristic threshold concentration values at which the transition to saturation occurs in the model. These values may correspond to different excitation regimes of He in the star's atmosphere.

A similar analysis was carried out for FS CMa-type stars, objects characterized by strong emission, dusty envelopes, and unstable circumstellar processes, as shown in Figure 2. Among these, MWC 645 exhibited the most rapid He saturation, likely due to the high density and temperature of its circumstellar environment. In contrast, 3 Pup shows a significantly slower saturation process, reflecting a more stable and evolved envelope. The characteristic He related dependencies observed in these objects are consistent with current understanding of their evolutionary stages, as well as with the differences in intensity and profiles of the corresponding spectral lines. On the fluctuation-dissipation plots for FS CMa-type stars MWC 645, MWC 728, and 3 Pup, the corresponding saturation points are: $C_* = 1, C_* = 1.4, C_* = 2.5$. A visual comparison of the tangent and Lorentzian curves highlights that the dissipation model provides a better description of sharp saturation transitions in hot stars, whereas the Lorentzian model may be useful for capturing smoother behavior in the atmospheres of stars.

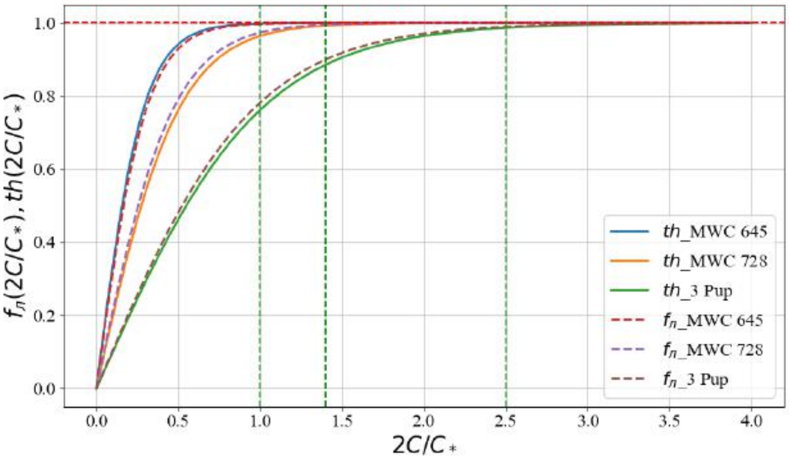

Fig.2. Dissipation function versus normalized concentration for the stars MWC 645, MWC 728, and 3 Pup for the *He* (λ5875) spectral line, along with the integral of the Lorentzian function.

Thus, the proposed method, based on the fluctuation-dissipation approach, provides a qualitative description of the saturation behavior of emission lines and can be applied to assess the evolutionary status of shell stars. This methodology opens up prospects for a quantitative analysis of elemental saturation and its comparison with results from spectrophotometric observations.

4. Conclusion

In the present study, a new methodology for analyzing the evolutionary state of stars was developed and tested using the fluctuation-dissipation relation. The core of the method lies in the relationship between spontaneous fluctuations in the stellar atmosphere and dissipative processes, manifested through the saturation of emission lines, particularly the *Hα* and *He* lines. The fluctuation-dissipation relation (FDR) is expressed as an integral of the Lorentzian function over frequency, taking into account the frequency shift caused by the presence of *Hα* and *He* element concentrations. Dissipation is represented as the absorption of photons, i.e., the inverse of the photon Bose condensation number, described via the hyperbolic tangent function (tanh).

Modeling results indicate that young, massive stars of early spectral types (e.g., HD 210839) reach saturation more rapidly than more evolved objects, such as Vega or P Cygni. Similarly, among FS CMa-type stars, the differences in C_* values are consistent with independent assessments of their structural properties, circumstellar environment density, and envelope activity levels. The observed patterns confirm that dissipation saturation serves as a sensitive indicator of the thermodynamic and dynamic state of a star's atmosphere.

The proposed fluctuation-dissipation analysis method represents an effective tool for determining the evolutionary characteristics of stars, particularly in cases where traditional approaches provide limited information. Future prospects include expanding the sample of studied objects, applying the method to spectral lines of other elements, and integrating the results with findings from astrophysical and polarimetric observations.

Conflict of interest statement

The authors declare that they have no conflict of interest in relation to this research, whether financial, personal, authorship or otherwise, that could affect the research and its results presented in this paper.

CRediT author statement

Zhanabaev Z.Zh.: Conceptualization, Methodology, Supervision; **Imanbayeva A.K.:** Writing – review & editing, text correction and proofreading; **Akniyazova A.Zh.:** Investigation, Writing – original draft, Data validation; **Ashimov Ye.K.:** Formal analysis, Visualization, Writing – review & editing. The final manuscript was read and approved by all authors.

.

References

1 Kippenhahn R., Weigert A., Weiss A. (2012) *Stellar Structure and Evolution*. Springer. https://doi.org/10.1007/978-3-642-30304-3

2 Miroshnichenko A.S., et al. (2007) A new group of B[e] stars: unclassified FS CMa type objects. *The Astrophysical Journal*, 671(2), 828. https://doi.org/10.1086/523036

3 de la Fuente D., Najarro F., Trombley C., Davies B., Figer D.F. (2015) First detections of FS Canis Majoris stars in clusters. *A&A*, 575, A10. https://doi.org/10.1051/0004-6361/201425371

4 Miroshnichenko A.S.; Zharikov S.V.; Korčaková D., Manset N., Mennickent R., Khokhlov S.A., Danford S., Raj A., Zakhozhay O.V. (2020) Binarity among objects with the Be and B[e] phenomena. *Contributions of the Astronomical Observatory Skalnaté Pleso*, 50 (2), 513-517. https://doi.org/10.31577/caosp.2020.50.2.513

5 Salaris M., Cassisi S. (2005) *Evolution of Stars and Stellar Populations*. Wiley https://doi.org/10.1002/0470033452

6 Aerts C., Christensen-Dalsgaard J., Kurtz D.W. (2010). *Asteroseismology*. Springer. https://doi.org/10.1007/978-1-4020-5803-5

7 Paxton B., et al. (2011) Modules for Experiments in Stellar Astrophysics (MESA). *Astrophysical Journal Supplement Series*, 192(1), 3. https://doi.org/10.1088/0067-0049/192/1/3

8 Gray D.F. (2005). *The Observation and Analysis of Stellar Photospheres*. Cambridge University Press. https://doi.org/10.1017/CBO9781316036570

9 Wei Wu, Jin Wang. (2020) Generalized Fluctuation-Dissipation Theorem for Non-equilibrium Spatially Extended Systems. *Frontiers in Physics,* 8, id.*567523,* 18. https://doi.org/10.3389/fphy.2020.567523

10 Seifert U., Speck T. (2010) Fluctuation-dissipation theorem in nonequilibrium steady states. *EPL Europhysics Letters,* 89, 10007. https://doi.org/10.1209/0295-5075/89/10007

11 Sarracino A., Vulpiani A. (2019) On the fluctuation-dissipation relation in non-equilibrium and non-Hamiltonian systems. Chaos Interdiscip. *J. Nonlinear Sci.*, 29, 083132. https://doi.org/10.1063/1.5110262

12 Kubo R. (2019) Fluctuation-dissipation theorem revisited. *Prog. Theor. Exp. Phys*., 12, 123I01. https://doi.org/10.1166/rits.2014.1023

13 Caprini L., Puglisi A., Sarracino A. (2021) Fluctuation–Dissipation Relations in Active Matter Systems. *Symmetry*, 13(1), 81. https://doi.org/10.3390/sym13010081

14 Coghi F., Buffoni L., Gherardini S. (2023) Convergence of the integral fluctuation theorem estimator for nonequilibrium Markov systems. *Journal of Statistical Mechanics: Theory and Experiment*, 063201. https://doi.org/10.1088/1742-5468/acc4b2

15 Zhanabaev Z.Zh., Ussipov N.M. (2023) Information-entropy method for detecting gravitational wave signals. *Eurasian Physical Technical Journal*, 20, 2 (44), 79-86. https://doi.org/10.31489/2023NO2/79-86

16 Zhanabaev Z.Zh., Ussipov N.M. (2019) Scale – invariance of many galaxies. *Recent Contributions to Physics* 2(69), 27-32. https://doi.org/10.26577/rcph-2019-i2-4 (In Kaz.).

17 Zhanabaev Z.Zh., Grevtseva T.Yu. (2014) Physical fractal phenomena in nanostructured semiconductors. *Reviews in Theoretical Science*, 2(3), 211-259. https://doi.org/10.1166/rits.2014.1023

18 Hurley J.R., Tout C.A., Pols O.R. (2002) Evolution of binary stars and the effect of tides on binary populations. *Monthly Notices of the Royal Astronomical Society*, 329(4), 897-928. https://doi.org/10.1046/j.1365-8711.2002.05038.x

---

AUTHORS' INFORMATION

Zhanabaev, Zeinulla – Doctor of Phys. and Math. Sciences, Professor, al-Farabi Kazakh National University, Almaty, Kazakhstan; Scopus Author ID: 15840905700; https://orcid.org/0000-0001-5959-2707, Zeinulla.Zhanabaev@kaznu.edu.kz

Imanbayeva, Akmaral – Candidate of Phys. and Math. Sciences, Senior Lecture, al-Farabi Kazakh National University; Almaty, Kazakhstan; Scopus Author ID: 15054326000; https://orcid.org/0000-0001-9900-9782, akmaral@physics.kz

Akniyazova, Aigerim – PhD student, Department of Physics and Technology, al-Farabi Kazakh National University, Almaty, Kazakhstan; Scopus Author ID: 59194078400; https://orcid.org/0000-0002-9185-3185, aigerimakniyazova@gmail.com

Ashimov, Yeskendyr – PhD student, Department of Physics and Technology, al-Farabi Kazakh National University, Almaty, Kazakhstan; Scopus Author ID: 57694992000; https://orcid.org/0000-0002-1316-0156, ashimov.yeskendyr@kaznu.kz

EURASIAN PHYSICAL TECHNICAL JOURNAL

2025, Volume 22, No.4 (54)

https://doi.org/10.31489/2025N4/123-131

Received: 25/06/2025 Revised: 28/11/2025 Accepted: 22/12/2025

Original Research Article

UDC 537.533,535.31

COLLIMATOR AND TELESCOPIC MODES OF A CATHODE LENS

Trubitsyn A.A.*, Grachev E.Yu., Kochergin E.G., Serezhin A.A.

Ryazan State Radio Engineering University named after V.F. Utkin, Ryazan, Russia
Corresponding author: assur@bk.ru

Abstract. *One way to improve the performance of emission systems (electron microscopes, microfocus X-ray tubes, etc.) is to reduce cathode lens aberrations. Such a reduction is only possible through a thorough theoretical analysis of their electron-optical schemes. This research attempts to develop tools for modeling a cathode lens with a virtually arbitrary electrode configuration in the paraxial approximation, and the conditions for implementing the collimator and telescopic modes have been determined. The relationship between the parameters that provide the specified operating modes of the lens has been studied. Electron-optical schemes have been developed that guarantee collimator and telescopic modes of a cathode lens of a real (non-idealized) design.*

Keywords: electron optics, electrostatic lens, paraxial optics, potential distribution.

1. Introduction

A cathode lens (immersion objective, electron gun) is used for the primary formation and acceleration of the electron flow in charged particles sources of emission systems [1-3], such as electron spectrometers, electron microscopes, microfocus X-ray tubes, electron lithographs, etc. The diameter of the probe (focal spot) of the emission system depends on the quality of the device's output optics, while the magnitude of the generated probe current is determined by the source brightness [4]. Source brightness is the most important parameter [5]. To approach the theoretically limiting (Langmuir) brightness [6, 7], reducing the aberrations of the cathode lens is primarily necessary. However, despite numerous studies on the numerical modeling of electron guns [8-10] and quantitative improvement of their parameters, the cathode lens, even in the paraxial approximation, remains virtually unstudied. This is primarily due to the overestimation of the capabilities of numerical experiments by modern researchers. This paper attempts to develop and advance tools for studying the paraxial properties of a cathode lens and apply these tools to lenses with arbitrary electrode geometries.

A cathode lens is characterized by the fact that the cathode is immersed in an electric field created by potentials on the anode and the focusing electrode. The paper considers low-current lenses, i.e. those whose perveance does not exceed 10^{-2} μA/V$^{3/2}$ [11].

Numerical analysis of a low-current cathode lens, when the space charge can be neglected during calculating the field and single trajectories of charged particles, does not cause any problems. However, the capabilities of numerical analysis are limited by the enumeration of various design options, and therefore the only advantage of numerical experimentation in creating new devices is the reduction in the cost of development. Discovering a new quality of the designed device is possible only by means of theoretical analysis. Theoretical optics includes paraxial optics and the theory of aberrations.

2. Theoretical technique

The fundamental equation of paraxial electron optics is a second-order linear differential equation, which in the cylindrical coordinate system $r0z$ for axially symmetric systems has the form [12]

$$r'' + \frac{\Phi'}{2\Phi} r' + \frac{\Phi''}{4\Phi} r = 0. \tag{1}$$

The general solution of equation (1) for a known potential distribution $\Phi=\Phi(z)$ on the axis of symmetry will be the particle trajectory $r=r(z)$. In the case of common types of electron lenses, such as immersion, Einzel, and aperture lenses, this equation is solved by standard numerical methods. When modeling a cathode lens, difficulties arise in calculating the trajectories of electrons in the region where they start from the cathode. In the paraxial approximation (1), these difficulties are due to a mathematical singularity in the potential distribution function on the surface $z=z_c$ of the cathode C, since $\Phi_c=\Phi(z_c)=0$, and $\Phi'_c\neq 0$. From here on in the article, we will use the subscript "c" for the values of all functions on the cathode surface. Fortunately, a sufficiently developed theory [13] for solving second-order equations with this type of singularity allows us to find both particular solutions, where one of the particular solutions of equation (1), $p=p(z)$, is an analytic function, and the second solution, $g=g(z)$, has the following expression in terms of analytic function

$$g = \sqrt{\Phi} q, \tag{2}$$

where $q=q(z)$ is an analytical function, which, as follows from (1) and (2), satisfies the equation

$$q'' + \frac{3}{2}\frac{\Phi'}{\Phi} q' + \frac{3}{4}\frac{\Phi''}{\Phi} q = 0. \tag{3}$$

It can be shown that the functions $p(z)$ and $q(z)$ satisfy the same boundary conditions

$$p_\text{c} = q_\text{c} = 1, \qquad p'_\text{c} = q'_\text{c} = -\frac{\Phi''_\text{c}}{2\Phi'_\text{c}}, \tag{4}$$

and the particular solutions $p(z)$ and $g(z)$ are related to each other by the relation

$$\sqrt{\Phi}(pg' - gp') = \frac{1}{2}\Phi'_\text{c}, z > z_c$$

Partial solutions are key functions in paraxial optics and allow us to calculate electron trajectories, determine magnification, cardinal elements, and more. The general solution, which is the trajectory equation in our case, can be expressed as a linear combination of linearly independent partial solutions

$$r(z) = ap(z) + bg(z),$$

where the constants a and b are determined from the initial conditions on the cathode surface. In the uniquely significant work [14], expressions for a and b for a cathode lens were obtained and the equation for the paraxial trajectory was written

$$r(z) = r_\text{c} \cdot p(z) + \frac{2\sqrt{\varepsilon}}{\Phi'_\text{c}} \sin\vartheta_\text{c} \cdot g(z), \tag{5}$$

where ε is the energy of an electron emitted from the cathode and it is a mathematical quantity of the second order of smallness, r_c is the radius of the electron's start from the surface of the cathode, ϑ_c is the initial angle of movement relative to the axis of symmetry.

In the following calculations, the expression for the first derivative $r'(z)$ will be used, which is found by differentiating equation (5):

$$r'(z) = r_\mathrm{c} \cdot p'(z) + \frac{2\sqrt{\varepsilon}}{\Phi'_\mathrm{c}} \sin\vartheta_\mathrm{c} \cdot g'(z). \tag{6}$$

To date, cathode lenses have been little studied, even in the paraxial approximation, especially since elements of the theory of aberrations of this lens [14] are awaiting their time. Almost all the available results of studying the paraxial cathode lens are presented in [15], using the approximation of infinitely small interelectrode gaps. In this approximation, the axial distribution of the potential $\Phi(z)$ was obtained using the method of separation of variables.

3. Numerical experiment

The main drawback of the variable separation method is that it can only describe potential distribution functions in idealized electron-optical systems (EOS) with simple electrode configurations. Our theoretical approach, presented in this paper, allows us to study a wide range of cathode lenses with virtually arbitrary boundaries. To analyze the paraxial properties and calculate the aberrations of real (non-idealized) cathode lenses, the software FOCUS CL [16] has been developed and is being promoted.

The software FOCUS CL contains 1) a graphical editor for inputting the cathode lens design, 2) a block for calculating the axial potential distribution using the boundary element method and visualizing it, 3) a block for calculating particular solutions $p(z)$, $g(z)$ using the Runge-Kutta method and constructing trajectories $r(z)$. The boundary element method is used to solve the external Dirichlet problem, where each electrode is represented by a closed contour with a given potential on it. It should be noted that obtaining the integral equation relating the potentials of the simple and double layers [17] is based on the second Green's formula. The integral equation in this formulation provides the possibility of solving the field problem for systems with electrodes of arbitrary thickness and shape, having corners and kinks. The axial potential distribution function $\Phi(z)$ is defined in a set of discrete nodes. The software has a built-in option for smoothing the nodal values $\Phi(z)$ using the sliding polynomial method [18]. The derivatives $\Phi'(z)$, $\Phi''(z)$, $p'(z)$ and $g'(z)$ are calculated using six-node numerical differentiation formulas [19].

It should be noted that well-known methods such as the finite difference method (FDM) and the finite element method (FEM) are not very suitable for calculating the axial potential distribution. These methods require calculating the field over the entire analyzed region and only then extracting the axial distribution. This means that the time required to solve the problem using these methods is orders of magnitude higher than using the BEM. Therefore, using the FDM and FEM for solving cathode lens synthesis problems is impractical. Note that the unique modes of the cathode lens [15] can be detected by analyzing equations (5) and (6). The collimator mode, characterized by the transformation of the flow emitted by a point source (r_c=0) into a parallel flow $r'(z)$=0 at the exit of the lens in image space at $z \geq z_\mathrm{im}$, as can be seen from (6), is determined by the system

$$\begin{cases} r_\mathrm{c} = 0, \\ g'(z) = 0, z \geq z_\mathrm{im}, \end{cases} \tag{7}$$

whereas the telescopic mode, which causes the transformation of the parallel flow ($\sin\vartheta_\mathrm{c} = 0$) of electrons emitted from a flat cathode into a parallel $r'(z)$=0 at the exit from the lens at $z \geq z_\mathrm{im}$, will be fixed by the system of expressions

$$\begin{cases} \sin\vartheta_\mathrm{c} = 0, \\ p'(z) = 0, z \geq z_\mathrm{im}, \end{cases} \tag{8}$$

The left boundary z_im of the image space coincides with the boundary of the region of the uniform field, which is located at a distance from the center of the lens approximately equal to the inner diameter *d* of the cylindrical electrodes. Searching for the parameters at which the lens switches to the collimator or telescopic mode by checking the second condition of (7) and (8) is convenient because the form of particular solutions $g(z)$ and $p(z)$ does not depend on the initial values of the electron energy ε and the angle ϑ_c, but is determined only by fixed boundary conditions (4), which in turn are associated with the distribution $\Phi(z)$ of a particular EOS. Of practical interest are three-electrode cathode lenses (Fig. 1), consisting of a grounded cathode C, in the simplest case disk-shaped, and control and accelerating cylindrical electrodes with potentials *V* and V_acc, respectively. Given the same diameter *d* of the cylindrical electrodes and a significant excess of length over

.

the diameter of the accelerating electrode, the specific form of $\Phi(z)$ will be determined by the length l and the potential V of the control electrode.

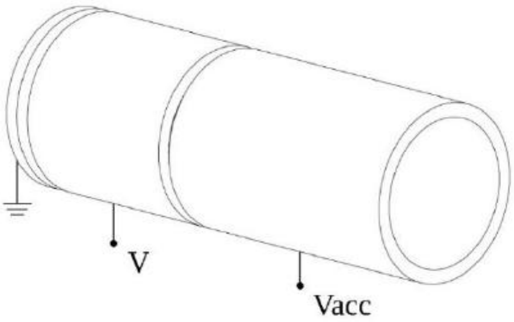

Fig.1. A three-electrode cathode lens consisting of a grounded cathode, a control electrode with potential V, and an accelerating electrode with potential V_{acc}

This article, firstly, tests the proposed methodology for studying a three-electrode cathode lens with a numerically determined axial potential distribution in the two specific modes mentioned above—collimator and telescope ones. Secondly, it presents lens designs with actual interelectrode gap sizes and defines the criteria for both lens modes. Presenting the criteria of the two modes in one article allows for their comparative evaluation. Since the results of the lens study in telescope mode have been previously published [20] and are publicly available, this mode for a real lens design is considered in less detail.

3.1 Collimator mode of the three-electrode cathode lens

Fig. 2, a demonstrates the collimator mode of a three-electrode cathode lens. Electrons are emitted by a point source in the range of initial angles $\vartheta_c = -70°$ to $+70°$ with a step of 10°. The relative initial energy of the particles is $\varepsilon/V_{acc} = 10^{-3}$, the relative length of the control electrode is $l/d = 1$, and its relative potential is $V/V_{acc} = 0.49$. The selected range of angles $\vartheta_c = -70°$ to $+70°$ allows us to exclude uninformative "tails" in the angular distributions of electrons, which appear in calculations near the boundaries of the full range of angles -90° and +90°. An additional argument in favor of choosing a slightly reduced range of initial angles ϑ_c in calculations is the cosine distribution of electrons by angles during emission from a solid, which sharply reduces the number of particles emitted by the cathode just near ±90°.

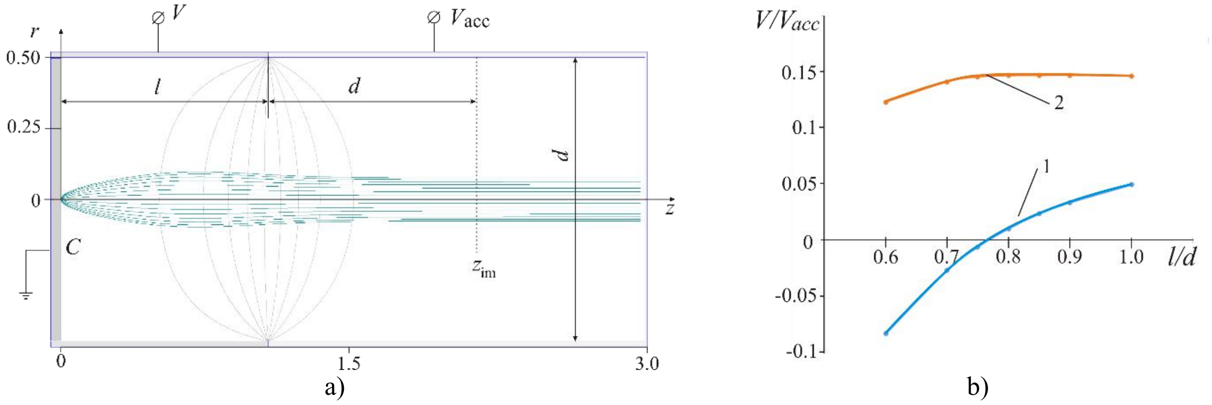

a) b)

Fig. 2. Results of modeling a paraxial three-electrode cathode lens: a – results of trajectory analysis in graphical form, b – graph of the relationship between the potential of the intermediate electrode V and its length l: 1 - in the collimator mode, 2 – in the telescopic mode.

Based on the calculation results, it was concluded that for each length l of the control electrode, varied in the range acceptable in practice, the potential V of this electrode is found, which ensures the collimator mode (7); moreover, it is noteworthy that the graph of the relative dependence $V/V_{acc}=f(l/d)$ (Fig. 2, b) crosses zero, i.e. the potential V can have both positive and negative values. Note that negative values of the potential are less preferable in practice, since in this case a bipolar source of electric power for the cathode lens would be required. The graphical dependence in Fig. 2, b is calculated for the case of a small value of the insulating interelectrode gaps δ=0.002d. In the work [15], as already noted, a lens with infinitely small insulating gaps was studied. A comparison of the results of both studies shows their practical coincidence, since the relative difference in the obtained values does not exceed $\Delta V/V_{acc}$ = 0.2%, which directly confirms the impeccability of the conclusions of works [14, 15] and the correctness of the numerical-analytical technique for studying paraxial cathode lenses presented here, implemented in the FOCUS CL application [16]. At the same time, the high accuracy of the calculation results of the proposed paraxial technique is demonstrated by comparison with the “reference” trajectory numerical analysis [21] of a cathode lens.

In this case, the electric field is numerically determined over the entire working region of the lens, not just on the axis, and the electron trajectories are the result of numerical integration over time of the classical Newtonian equations of motion. Such a comparison made it possible to identify a tendency for some natural growth of the calculation error in the paraxial approximation with an increase in the initial angle ϑ_c up to 70 ° and, most importantly, to fix the upper limit of this error $\Delta r/d$ = 0.1 %. Here $\Delta r=|r_{parax}(z_{im})-r_{num}(z_{im})|$ is the absolute deviation of the trajectories calculated using the paraxial $r_{parax}(z)$ and numerical $r_{num}(z)$ methods [21] in the $z=z_{im}$ plane. The error level, which is small beyond expectations and equal to 0.1% at large angles ϑ_c, emphasizes not only the high reliability of the results of the paraxial trajectories calculating in accordance with expression (5), but also the applicability of the paraxial method proposed in this paper for the trajectory analysis of wide-acceptance EOSs, and under low time-consuming conditions.

3.2 Telescopic mode of a three-electrode cathode lens

The graphs of particular solutions $p(z)$ and $g(z)$ for a three-electrode cathode lens with parameters l/d = 0.7 and V/V_{acc} = 0.141 (see Fig. 3, a) are shown in Fig. 3, b. On the $p(z)$ dependence, one can distinguish the section $p(z)$=const at $z \geq z_{im}$, where $z_{im} \approx l+d$, which is a specific feature of the telescopic mode. The proposed approach to analyzing particular solutions made it possible to establish a relationship between the length l and the potential V of the control electrode (Fig. 2, b) in the telescopic mode (8).

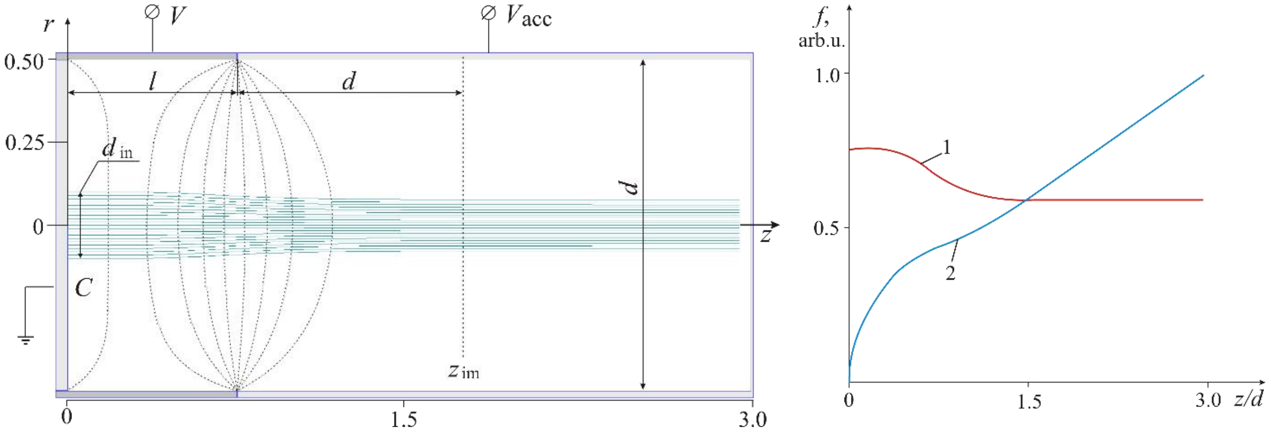

a) b)

Fig.3. Results of modeling of a paraxial three-electrode cathode lens:
a – electrons trajectories (5) with ϑ_c=0 and r_c = 0÷0.5d_{in} in the telescopic mode, d_{in} = 0.2d is an initial flow diameter,
b – particular solutions: 1 – $p(z)$, 2 – $g(z)$.

A detailed numerical study of the cathode lens of the design under consideration in the telescopic mode is presented in the author's work [20].

3.3 Cathode lenses of a real (non-idealized) design

The proposed numerical method for studying paraxial cathode lenses with numerical determination of the potential distribution on the axis of symmetry makes it possible to synthesize lenses those designs are not idealized, but are as close as possible to real ones, in particular leneses insulating interelectrode gaps are capable of maintaining electrical strength at voltages of 10 - 100 kV and higher.

4. Results and Discussion

The scheme of a lens with interelectrode gaps, the size of which does not allow electrical breakdowns to develop, is shown in Fig. 4, a. The synthesis of a lens to ensure the collimator mode (7) consisted in finding the potential V of the intermediate electrode for its predetermined length l. Calculations have shown that the lens scheme (Fig. 4) also has the property of changing the sign of the electrode potential in the process of successive change of its length, while the zero potential of the intermediate electrode $V/V_{\mathrm{acc}} = 0$ fixes the collimator mode for the electrode of length $l = 0.7041d$. Fig. 5 shows the axial distribution of the potential $\Phi(z)$ in this lens included in equations (1) and (3) and its two derivatives, as well as a graph of the particular solution $g(z)$ with the section $g(z)$=const characteristic of the collimator mode at $z \geq z_{\mathrm{im}}$.

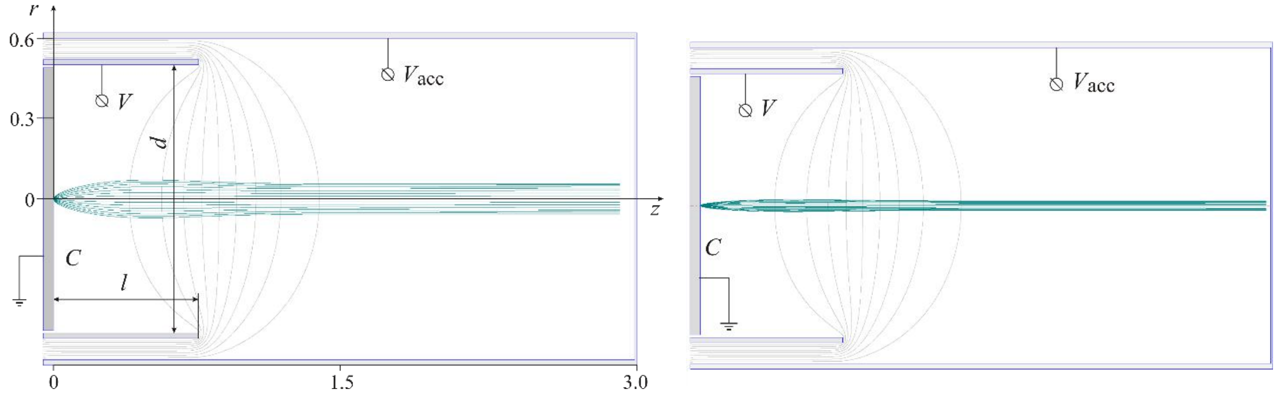

a) b)

Fig. 4. Results of numerical analysis of a real design cathode lens: a - $\varepsilon/V_{\mathrm{acc}}= 10^{-3}$, b - $\varepsilon/V_{\mathrm{acc}}= 10^{-4}$.

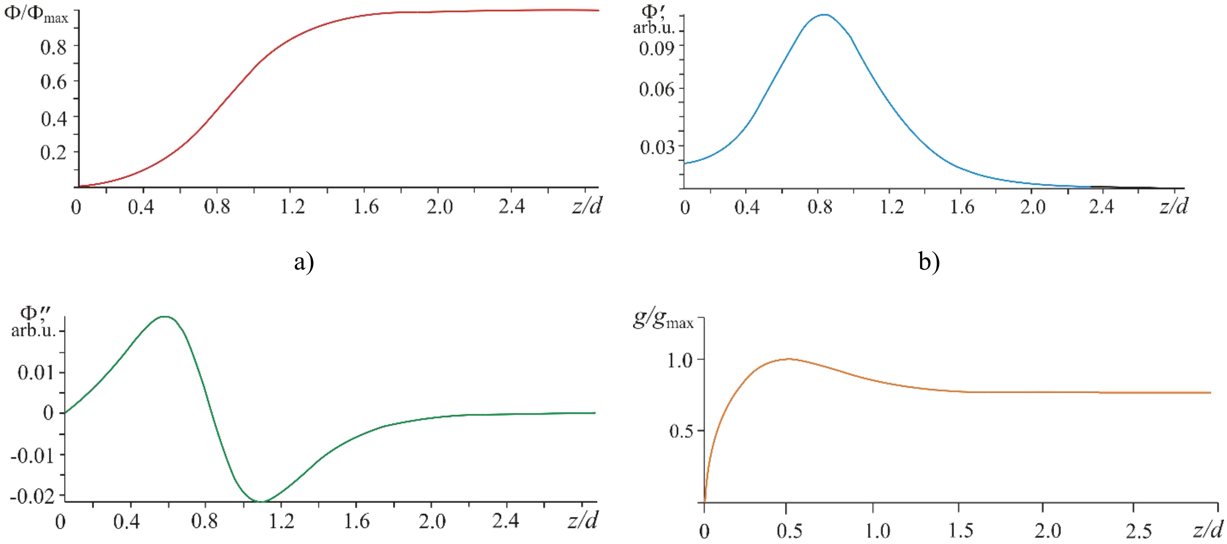

a) b)

c) d)

Fig. 5. Axial potential distribution (a) in a lens of the real design, the first (b) and second (c) derivatives of the distribution, and a graph of the particular solution g(z) (d). The subscript "max" indicates the maximum value of the function

Note that Fig. 4, a demonstrates the results of the numerical (not in the paraxial approximation) trajectory analysis of the lens in the range of angles ϑ_c=-70° - +70° with the initial relative energy of electrons $\varepsilon/V_{\mathrm{acc}}= 10^3$. The average absolute deviation of the trajectory inclination angle from 0° in the z=z_{im} plane is approximately equal to $\overline{|\vartheta_c(z_{\mathrm{im}})|} = 0.09°$, and the numerically determined position of the second-order focus [22] relative to the central angle ϑ_c=0 is $z_f \approx -100d$, which allows us to speak about a high degree of parallelism of the electron trajectories with the z axis in the field-free space $z \geq z_{\mathrm{im}}$. With increasing accelerating voltage (the ratio ε/V_{acc} decreases), a natural narrowing of the electron beam is observed (Fig. 4, b) with an improvement in the degree of parallelism: $\overline{|\vartheta_c(z_{im})|} = 0.007°$, $z_f \approx -400d$ for $\varepsilon/V_{acc} = 10^{-4}$.

The collimator mode can play a positive role in the development of emission systems with pointed cathodes - field emission and Schottky cathodes - since the parallel electron flow occupies a minimum volume of phase space in a series of converging and diverging flows and therefore can be focused into a spot of minimum diameter. To determine the telescopic mode conditions in a lens of a real design, we use the same algorithm. By varying the potential V of a control electrode of a specific length l, we check the fulfillment of the second condition of the system of expressions (8). The axial potential distribution $\Phi(z)$ for each value of V is calculated using the boundary element method. As a specific example of a lens of a real design in telescopic mode (Fig. 6), we present the following parameters: $l/d = 0.7$, $V = 0.137V_{acc}$.

After the telescopic mode conditions have been detected, a trajectory analysis is carried out with a real spread of initial angles in order to study the properties of the real lens design in more depth. Figure 6 shows the graphical results of a numerical trajectory analysis of a lens with a real design. The analysis used a range of initial angles of $\vartheta_c = -70°$ to $+70°$ at an electron emission energy of $\varepsilon = 10^{-6}\ V_{acc}$. The initial flow diameter was chosen to be $d_{in} = 0.2d$.

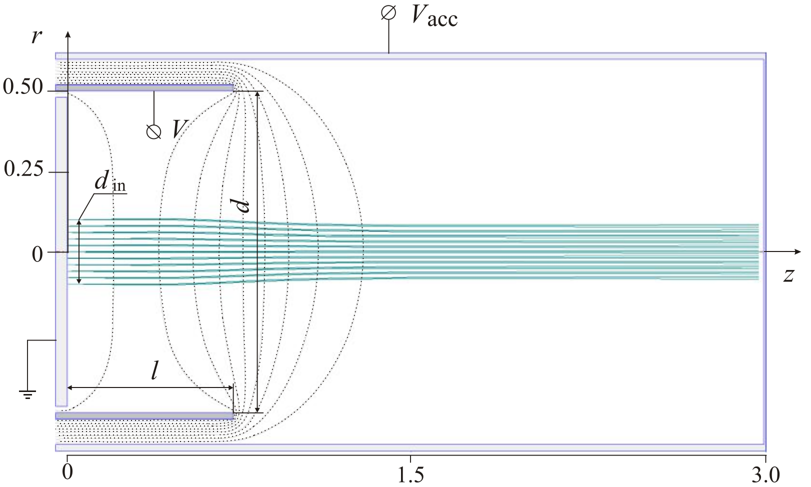

Fig. 6. Results of numerical analysis of a real design cathode lens in telescopic mode: $\varepsilon/V_{acc} = 10^{-6}$, $d_{in}/d = 0.2$, $r_c = -0.5d_{in} \div 0{,}5d_{in}$, $\vartheta_c = -70° \div +70°$.

The trajectory analysis results suggest that a high level of flow parallelism is maintained at the system exit. Quantitative estimates of the flow characteristics in the exit plane $z = l + 2d$ are as follows:

- the inclination angle of the central trajectories with $\vartheta_c = 0$ increases with increasing starting radius r_c, but does not exceed 0.02° at $r_c = d_{in}/2$;
- the spread of the angles of the two outer trajectories with $\vartheta_c = \pm 70°$ does not exceed ±0.08° for the entire initial range of r_c.

The telescopic mode will prove productive in the creation of emission systems with large-diameter flat cathodes, such as photocathodes.

5. Conclusion

This article develops an approach to theoretical analysis of a cathode lens in the paraxial approximation by calculating the potential distribution on the lens axis using the numerical boundary element method. BEM is the optimal method for solving this problem in terms of computation speed and accuracy, enabling both analysis and the synthesis of cathode lenses with specific properties in real time. The effectiveness of a two-stage development of cathode lens designs is demonstrated. After discovering new lens modes using theoretical paraxial optics, its electron-optical parameters are refined and studied using more accurate numerical methods.

This work includes the development of software for studying cathode lenses of a real (non-idealized) design in the paraxial approximation; criteria for the collimator and telescope modes of a three-electrode cathode lens with small and realistic interelectrode gaps are determined.

The development of methods for theoretical analysis of cathode lenses will enable targeted solutions to increase the brightness of accelerated electron sources.

Conflict of interest statement

The authors declare that they have no conflict of interest in relation to this research, whether financial, personal, authorship or otherwise, that could affect the research and its results presented in this paper.

CRediT author statement

Trubitsyn A.: Conceptualization, Methodology, Supervision; **Grachev E.**: Investigation, Formal Analysis, Writing-Reviewing and Editing; **Kochergin E.**: Software and Analysis, Validation; **Serezhin A.**: Writing - original draft, Review and Editing. The final manuscript was read and approved by all authors.

Funding

The research was funded by the Russian Science Foundation (grant no. 25-29-00124).

References

1 Guo X. (2024) *The Schottky emitter as a source for multi-electron-beam instruments*. Dissertation (TU Delft), Delft University of Technology. doi.org/10.4233/uuid:304cdd73-083a-4f89-ad47- f192e84a5313

2 Ohsawa S., Ikeda M., Sugimura T., Tawada M., Hozumi Y. and Kanno K. (2005) *High Brightness Electron Gun for X-Ray Source*. Proceedings of the 2005 Particle Accelerator Conference, Knoxville, TN, USA. 1488-1490. doi: 10.1109/PAC.2005.1590809.

3 Hideo Morishita, Takashi Ohshima, Kazuo Otsuga, Makoto Kuwahara, Toshihide Agemura, Yoichi Ose (2021) Brightness evaluation of pulsed electron gun using negative electron affinity photocathode developed for time-resolved measurement using scanning electron microscope. *Ultramicroscopy*, 230, 113386. doi.org/10.1016/j.ultramic.2021.113386.

4 Bronsgeest M. S., Barth J. E., Swanson L. W., Kruit P. (2008) Probe current, probe size, and the practical brightness for probe forming systems. *Journal of Vacuum Science & Technology B*. 26 (3), 949-955. doi: 10.1116/1.2907780

5 Han C, Sul I, Cho B. (2017) Edge shadow projection method for measuring the brightness of electron guns. *Rev Sci Instrum,* 88(2), 023302. doi: 10.1063/1.4974956.

6 Lauer R. (2020*) Characteristics of triode electron guns.* In P. W. Hawkes (Ed.), *Advances in imaging and electron physics*, 215. 195–266. Academic Press, London. doi.org/10.1016/bs.aiep.2020.06.007.

7 Kuriki M. (2022) *Theoretical limit of electron beam brightness generated from electron guns*. Proceedings of the 19th Annual Meeting of Particle Accelerator Society of Japan, October 18 – 21, Kyushu University, 1065-1069.

8 Fujita S, Shimoyama H. (2005) A new evaluation method of electron optical performance of high beam current probe forming systems. *J Electron Microsc (Tokyo)*. 54(5), 413-427. doi: 10.1093/jmicro/dfi063.

9 Cardona J. D., DietrichIsh k., Mukul M. et al. (2022) Simulations of a new electron gun for the TITAN EBIT. Journal of Physics: Conference Series 2244, 012075. doi:10.1088/1742-6596/2244/1/012075.

10 Wang RC., Jiao JQ., Zang K. et al. (2025) Development of pulsed electron gun based on PIC simulation. *Radiat Detect Technol Methods*. https://doi.org/10.1007/s41605-025-00591-z.

11 Sushkov A.D. (2022) *Vacuum Electronics. Physical and Technical Foundations*. Lan, St. Petersburg. 464. [in Russian]. Available at: https://lanbook.com/catalog/inzhenerno-tekhnicheskie-nauki/vakuumnaya-elektronika-fiziko-tehnicheskie-osnovy-3883606/?utm_source

12 Hawkes P.W. (1972) *Electron Optics and Electron Microscopy*. Taylor & Francis Ltd., London, 244. https://doi.org/10.1002/crat.19720071212

13 Smirnov V.I. (1974) *Course of Higher Mathematics, Vol. 3, Part 2*. Nauka, Moscow, 672. [in Russian] Available at: https://www.litres.ru/book/vladimir-smirnov-3/kurs-vysshey-matematiki-tom-iii-chast-2-6988781/?utm_source

14 Yakushev E.M. (2013) *Theory and Computation of Electron Mirrors: The Central Particle Method.* In P. W. Hawkes (Ed.), *Advances in imaging and electron physics*, 178. 147–247. Academic Press, London. https://doi.org/10.1016/B978-0-12-407701-0.00003-0

15 Yakushev E.M., Bimurzaev S.B., & Kholodov M.A. (2016) To Determine the Cardinal Elements and Angular Characteristics of Cathode Lenses with Rotational Symmetry. *Bulletin of the Aktobe Regional State University named after K. Zhubanov*, 44(2), 32 – 40. [in Russian] Available at: https://vestnik.arsu.kz/ index.php/hab/issue/view/12/18

16 Trubitsyn A.A., Grachev E.Yu., &Kochergin E.G. (2024) *Focus CL Program for Modeling Cathode Lenses. Certificate of State Registration of Computer Program No. 2024680471*. [in Russian]

17 Brebbia C.A., Telles J.C.F., Wroubel L.C. (2012) *Boundary Element Techniques: Theory and Applications in Engineering*. Springer Berlin Heidelberg, 464. https://doi.org/10.1007/978-3-642-48860-3

18 Korn G.A., Korn T.M. (2013) *Mathematical Handbook for Scientists and Engineers.* Dover Publications Inc, NY. 1152. Available at: https://www.scribd.com/document/530807645/Mathematics-Handbook-for-Scientists-and-Engineers?utm_source=chatgpt.com

19 Abramovits M., Stigan I.A. (1965) *Handbook of Special Functions with Formulas, Graphs, and Mathematical Tables*. Dover Publications Inc, NY. 1046. Available at: https://personal.math.ubc.ca/~cbm/aands/abramowitz_and_stegun.pdf

20 Trubitsyn A.A., Grachev E.Yu., & Kochergin E.G. (2025) Telescopic Mode of a Cathode Lens. *Pis'ma v zhurnal tekhnicheskoy fiziki, 51 (13), 32 – 36. [in Russian].* https://doi.org/10.61011/PJTF.2025.13.60701.20284 [in Russian]

21 Gurov V.S., Saulebekov A.O., & Trubitsyn A.A. (2015) *Analytical, Approximate-Analytical and Numerical Methods in the Design of Energy Analyzers.* In P. W. Hawkes (Ed.), Advances in Imaging and Electron Physics, 192. Academic Press, London, 212. https://doi.org/10.1016/S1076-5670(15)00103-2

22 Trubitsyn A.A. (2001) A Correlation Method of Search for Higher-Order Angular Focusing. *Technical Physics*, 46 (5), 630-631. https://doi.org/10.1134/1.1372960

AUTHORS' INFORMATION

Trubitsyn, Andrey Afanasievich – Doctor of Physical and Mathematical Sciences, Professor, Department of Industrial Electronics, Ryazan State Radio Engineering University, Russia; ORCID iD 0000-0002-9337-8947; assur@bk.ru

Grachev, Evgeny Yuryevich – Candidate of Engineering Sciences, Associated Professor, Department of Industrial Electronics, Ryazan State Radio Engineering University, Russia; ORCID iD 0000-0001-7813-7769; monopol_rus@mail.ru

Kochergin, Eduard Gennadievich – graduate student, Department of Industrial Electronics, Ryazan State Radio Engineering University, Russia; ORCID iD 0009-0007-7436-2708; a kochergin_aduard@mail.ru

Serezhin, Andrey Alexandrovich – Candidate of Engineering Sciences, Associated Professor, Department of Industrial Electronics, Ryazan State Radio Engineering University, Russia; ORCID iD 0000-0001-8134-8970; a andrei-serezhin@yandex.ru

.

EURASIAN PHYSICAL TECHNICAL JOURNAL

2025, Volume 22, No.4 (54)

https://doi.org/10.31489/2025N4/132-142

Received: 11/08/2025 Revised: 23/11/2025 Accepted: 22/12/2025

Original Research Article

UDC 53.05, 524.4

GAMMA-RAY BURST LIGHT CURVE RECONSTRUCTION WITH PREDICTIVE MODELS

Zhunuskanov A., Sakan A.*, Akhmetali A., Zaidyn M., Ussipov N.

Department of Electronics and Astrophysics, Al-Farabi Kazakh National University, Almaty, Kazakhstan
**Corresponding author*: aknursakan47@gmail.com

Abstract. *Gamma-ray bursts represent some of the most energetic and complex phenomena in the universe, characterized by highly variable light curves that often contain observational gaps. Reconstructing these light curves is essential for gaining deeper insight into the physical processes driving such events. This study proposes a machine learning-based framework for the reconstruction of gamma-ray burst light curves, focusing specifically on the plateau phase observed in X-ray data. The analysis compares the performance of three sequential modeling approaches: a bidirectional recurrent neural network, a gated recurrent architecture, and a convolutional model designed for temporal data. The findings of this study indicate that the Bidirectional Gated Recurrent Unit model showed the best predictive accuracy among the evaluated models across all gamma-ray burst types, as measured by Mean Absolute Error, Root Mean Square Error, and Coefficient of Determination. Notably, Bidirectional Gated Recurrent Unit exhibited enhanced capability in modeling both gradual plateau phases and abrupt transient features, including flares and breaks, particularly in complex light-curve scenarios.*

Keywords: Gamma-ray burst, deep learning, neural networks, light curve.

1. Introduction

Gamma-ray bursts (GRBs) are among the most energetic and transient phenomena in the Universe, characterized by brief flashes of high-energy photons, typically peaking above ~0.1 MeV [1]. These events exhibit a remarkable diversity in duration, ranging from milliseconds to several minutes, as well as highly variable temporal and spectral structures, which pose significant challenges for theoretical modeling. Over the past decade, the field of GRB research has undergone a rapid transformation, evolving from a specialized area of high-energy astrophysics into a major domain of observational cosmology and astrophysics. This progress has been driven by a succession of space missions that enabled both accurate localization and extensive multi-wavelength follow-up of GRBs.

The Burst and Transient Source Experiment (BATSE) onboard the Compton Gamma Ray Observatory provided strong evidence for the isotropic sky distribution of GRBs, implying an extragalactic origin [2]. The Swift Burst Alert Telescope (BAT) [3] detects prompt emission, and the follow-up afterglow is detected using the X-ray [4]. The subsequent BeppoSAX mission enabled the first detections of X-ray afterglows and accurate source localization, which led to the discovery of long-wavelength counterparts and host galaxies [5]. These breakthroughs were further advanced by the High Energy Transient Explorer (HETE-II) [6] and complemented by extensive ground-based observations in the optical, infrared, and radio bands.

The detection of long-lived afterglows has enabled in-depth studies of the circumburst environment and provided compelling evidence for collimated relativistic outflows. Given their extreme luminosities and detectability at high redshifts [8–10], GRBs serve as powerful probes of the distant Universe [11-13]. They offer a unique opportunity to investigate key aspects of cosmology, including the expansion history and the nature of dark energy, the cosmic star formation rate, the timing and processes of reionization, as well as the chemical enrichment of the interstellar and intergalactic media over cosmic time.

Consequently, GRBs are not only key astrophysical phenomena but also valuable tools for probing the Universe on cosmological scales. To fully utilize their potential, precise modeling of their light curves (LCs) is essential. In this context, machine learning (ML) has become an increasingly important tool in astrophysics [14-16], with successful applications in different areas of astronomy and other fields [17-22]. These advancements have led to a growing interest in using ML for GRB LCs reconstruction.

The t-Distributed Stochastic Neighbor Embedding (t-SNE) algorithm has demonstrated stable clustering of GRBs even with partial data removal, highlighting its robustness for dynamic or incomplete datasets [23]. ML has also proven effective in localizing previously unidentified GRBs, revealing uniform sky distributions and suggesting potential magnetar associations [24]. Clustering analyses of Fermi GRBs using spectral features have identified four consistent classes with distinct α and Epeak characteristics, enhancing our understanding of GRB subtypes [25]. Optimization-based modeling has successfully reproduced GRB-SN light curves, supporting magnetar-driven scenarios with physically plausible parameters [26]. Automatic Gaussian Mixture Model (AutoGMM) applied to t-SNE embeddings further revealed coherent density structures, validating the use of unsupervised clustering in GRB mapping [27]. Simulated GRB LCs generated with ML techniques have been shown to statistically match real data, confirming the reliability of data-driven models [28]. Large-scale classification using Uniform Manifold Approximation and Projection (UMAP), t-SNE, and K-means consistently separates Fermi GRBs into two main groups across different parameter spaces [29]. A similar two-cluster structure was observed in a study linking GRB groupings to physical origins, such as compact mergers and collapsars, rather than traditional duration-based classification [30]. These studies collectively demonstrate that ML not only enhances GRB classification but also offers a promising pathway for reconstructing their complex LC.

Recently, Dainotti M. G. et al. [31] applied stochastic reconstruction to GRB LC using Willingale (W07) and broken power-law (BPL) models, along with Gaussian processes. At 10% noise, uncertainties in key parameters-plateau end time, flux, and post-plateau decay index were reduced by up to 43.9%, enhancing the accuracy of GRB-based cosmological studies. Sourav S. et. al. [9] applied a novel approach using bidirectional LSTM proposed for GRB LC reconstruction to address gaps in observational data. Compared to traditional methods (W07, BPL, and their Gaussian Process variants), the Bidirectional Long Short-Term Memory (BiLSTM) model generally produced smoother reconstructions but showed a smaller decrease in flux uncertainty.

R. Falco et. al. [32] presents a quantitative analysis of GRB LCs performed using Principal Component Analysis (PCA) and t-SNE for dimensionality reduction and visualization. Synthetic LC were generated with properties closely matching real ones, showing good overlap in the embedded space. The similarity was further confirmed by statistical comparisons, with L2-norm and Wasserstein distances between histograms of real and synthetic LCs equal to 5.3 and 0.2, respectively. Building upon these recent advancements, the present work introduces a ML-based framework for the reconstruction of GRB LC, focusing on the plateau phase observed in X-ray data. Our approach explores and compares the performance of three distinct architectures: BiLSTM, Bidirectional Gated Recurrent Unit (BiGRU), and Temporal Convolutional Network (TCN). These models are well-suited for sequential data with missing values, enabling more robust reconstruction of LC and improved capture of temporal patterns.

The remainder of this paper is organized as follows: Section 2 describes the data preparation and preprocessing steps; Section 3 outlines the architecture and training process for each ML model; Section 4 presents the evaluation of metrics and experimental results; and Section 5 concludes with a summary.

2. Methodology

2.1 Data Collection and Preprocessing

The dataset used in this study consists of GRB LC obtained from the publicly available Swift XRT archive. Each LC was extracted from raw Flexible Image Transport System (FITS) files by extracting key observational parameters, including the observation time, flux, and flux uncertainties. To ensure consistency across the dataset, non-informative or incomplete entries were excluded during the initial data cleaning phase. To restore the temporal order of events, all LC were sorted in ascending order of observation time.

.

Subsequently, time values were normalized by dividing by 10^2, a transformation that standardizes temporal scales and facilitates stable training across models.

Given the wide dynamic range of GRB flux values, both the flux and its associated uncertainty were transformed into logarithmic space using the formula:

$$F(x) = ln\left(\frac{x}{a}\right) + 1, \tag{1}$$

where (x) - is the flux value and (a) - denotes the minimum non-zero flux in the given sequence. This transformation improves the numerical stability of the learning process by compressing large magnitudes and preserving fine variations in small-scale signals - a critical requirement for deep neural architectures sensitive to input distributions.

To address the inherent sparsity and temporal irregularity of GRB observations, a dense interpolation strategy was applied. Specifically, 19 equally spaced points were interpolated between each pair of consecutive observations. This approach significantly increases the temporal resolution of each sequence and provides more informative context for time-dependent models, such as RNNs and TCNs. The resulting sequences were segmented into fixed-size batches, ensuring uniform input dimensions for training. To prevent information loss due to short sequences, each batch was upsampled via repetition until the required length was met. This strategy enables the model to learn consistent temporal patterns across samples and mitigates overfitting, particularly in the case of limited observational windows. The interpolation strategy, normalization by dividing time by 10^2, and logarithmic transformation of flux values were adopted following the approach of Sourav S. et al. [9]. These preprocessing steps are essential for preparing the input data for sequential architectures, including Bidirectional Gated Recurrent Unit (GRU), Bidirectional LSTM, and TCN, all of which rely on structured temporal input for effective reconstruction of GRB LC.

2.2. Bidirectional Long Short-Term Memory Architecture

BiLSTM model was selected as a baseline due to its proven effectiveness in modeling complex temporal dependencies, particularly in irregular and noisy time series. BiLSTM architecture is well-suited for capturing both forward and backward temporal contexts, which is especially valuable when reconstructing GRB LC with observational gaps. The BiLSTM network extends the standard LSTM architecture by incorporating two parallel recurrent layers that process the input sequence in both forward and backward directions (Fig. 1). This bidirectional processing enables the model to capture context from both past and future time steps, improving its ability to learn temporal dependencies. The original BiLSTM architecture was introduced by Schuster and Paliwal [33]. Our implementation consists of five stacked BiLSTM layers, each incorporating internal memory mechanisms that allow the network to retain information across long sequences. The first four layers are configured with *return_sequences=True* to preserve the temporal structure throughout the network's depth. This design enables hierarchical feature extraction across multiple time scales. The final BiLSTM layer outputs a fixed-length representation, which is passed to a fully connected dense layer with a Rectified Linear Unit (ReLU) activation function. This layer maps the learned sequence representation to a single flux prediction value. Each BiLSTM layer comprises 100 hidden units, and the model is trained using the Adam optimizer with mean squared error (MSE) as the loss function. To prevent overfitting, early stopping is applied based on validation loss.

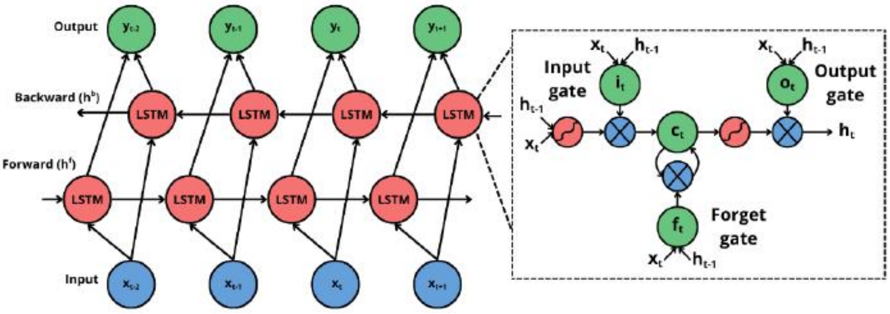

Fig. 1. Architecture of a BiLSTM network and the internal structure of an LSTM cell.

Unlike classical regression-based approaches such as the broken power-law (BPL) model - which imposes a predefined parametric form - the BiLSTM model provides greater flexibility in capturing the non-linear and non-stationary nature of GRB LC. It is capable of modeling rapid flux variations, plateau phases, and flaring behavior without requiring strict functional assumptions. The left part of the figure illustrates a BiLSTM model that processes the input sequence in both forward (h^f) and backward (h^b) directions to generate context-aware outputs at each time step. The right part shows the internal mechanism of an LSTM cell, which includes the input, forget, and output gates. These gates control the flow of information based on the current input x_t and the previous hidden state h_{t-1}, maintaining a memory cell state c_t that enables long-term dependency learning.

2.3. Temporal Convolutional Network Architecture

TCN architecture was selected as a non-recurrent alternative for sequence modeling, offering several advantages such as parallel computation, stable gradients, and effective long-range dependency capture through dilated convolutions. TCNs are particularly useful in time-series tasks where causal relationships must be preserved, and memory-efficient modeling is desirable. The TCN framework evaluated by Bai et al. [33] demonstrated strong performance in sequence modeling tasks compared to both LSTM and GRU architectures.

Our implementation includes three 1D convolutional layers with causal padding (Fig. 2) to ensure that predictions at time t do not depend on future inputs. Each layer uses 64 filters and a kernel size of 5, with ReLU activation applied after each convolution. To enable the model to capture longer temporal contexts without increasing kernel size, we employ increasing dilation rates of 1, 2, and 4 respectively across the three convolutional layers. This expands the receptive field, allowing the model to access information from broader time ranges. Following the convolutional layers, the output is flattened and passed to a fully connected dense layer, which outputs a single flux prediction per input. As with the BiLSTM model, the TCN is trained using the Adam optimizer and MSE as the loss function. Early stopping is employed to prevent overfitting, based on validation loss monitoring.

Unlike recurrent models, TCNs do not rely on internal memory states, which makes them less sensitive to vanishing gradients and more efficient for parallelization during training. Furthermore, their ability to handle sequences of varying lengths without explicit unrolling makes them attractive for modeling astrophysical signals with nonuniform sampling. In the context of GRB LC reconstruction, TCNs offer a unique perspective: they capture local and global temporal patterns via stacked convolutional filters while preserving causal dependencies. Their structural simplicity and training efficiency position them as a promising alternative to recurrent networks, particularly when reconstruction speed and computational cost are critical considerations.

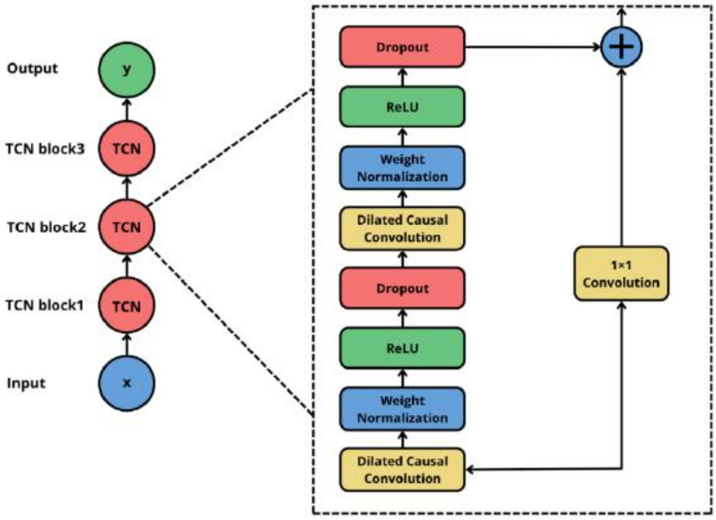

Fig. 2. Architecture of a TCN and internal structure of a residual block.

The left part of the figure illustrates a stacked TCN model composed of three residual blocks, which process the input sequence x to produce the output y. The right part shows the internal structure of a single residual block, featuring two layers of dilated causal convolutions, each followed by weight normalization, ReLU activation, and dropout. A 1×1 convolution is applied to the input to ensure dimensional compatibility before the residual connection is added. This design enables efficient modeling of long-range dependencies in sequential data.

2.4. Bidirectional Gated Recurrent Unit Architecture

GRU is a simplified recurrent neural architecture proposed by Cho et al. [34] as an alternative to the LSTM. GRUs simplify the memory gating mechanism of LSTMs while maintaining the ability to capture long-term dependencies in temporal data. When combined with a bidirectional architecture, GRUs become particularly effective at modeling sequences where contextual information from both past and future is relevant - a key characteristic of GRB LC with gaps and irregularities.

The BiGRU architecture used in this study consists of two stacked bidirectional GRU layers (Fig. 3). The first layer is configured with *return_sequences=True* to allow the second GRU layer to process temporal dynamics across the full sequence. Each GRU layer contains 64 hidden units, and both layers are wrapped in Keras's Bidirectional wrapper to process input sequences in forward and backward directions. The output of the second GRU layer is fed into a dense layer with a linear activation to produce the final flux prediction.

The model is trained using the Adam optimizer and MSE loss function. An early stopping mechanism is applied based on validation loss to ensure optimal convergence and to avoid overfitting. Due to its simplified gating and reduced computational cost, BiGRU offers faster training and lower memory consumption compared to BiLSTM. This makes it well-suited for applications where computational resources are constrained or where rapid prototyping is needed. Despite its lower complexity, the BiGRU model retains the ability to model complex temporal dependencies and non-linear relationships in the data.

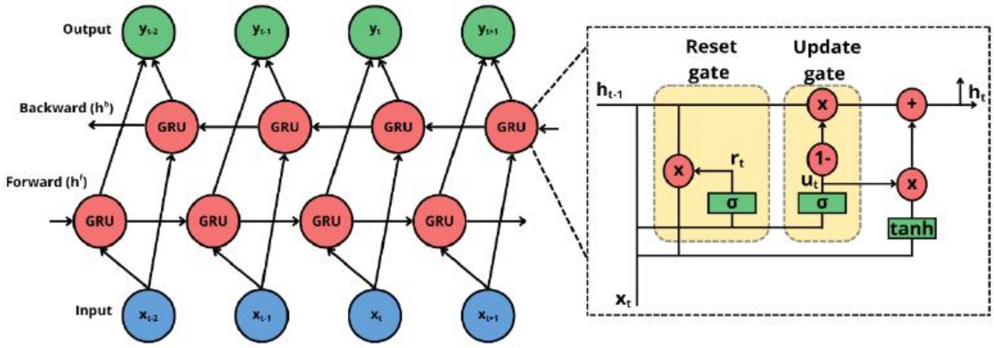

Fig. 3. Architecture of a BiGRU network and internal structure of a GRU cell.

The left part of the figure illustrates a BiGRU model that processes the input sequence x_t in both forward (h^f) and backward (h^b) directions to generate context-aware outputs y_t at each time step. The right part shows the internal mechanism of a GRU cell, consisting of the reset gate (r_t) and update gate (u^t), which regulate the flow of information. These gates control the balance between retaining previous memory and incorporating new input, with fewer parameters than LSTM while maintaining similar performance.

2.5. Training Procedure

All models in this study were trained individually on each GRB LC using the preprocessed, interpolated, and upsampled sequences described in Section 2.1. The training process was conducted using the TensorFlow/Keras framework, with GPU acceleration enabled where available. For each model (BiLSTM, BiGRU, and TCN), training was performed using the Adam optimizer and the MSE loss function. To prevent overfitting and improve generalization, we employed early stopping with a patience of five epochs, monitoring validation loss. The data was split into 70% for training and 30% for validation, ensuring that models were evaluated on unseen portions of the LC. During training, each GRB LC was divided into fixed-size batches. The batch size was user-defined and experimentally set to values such as 900 or greater, depending on the number of interpolated points. Each batch was treated as a separate training instance, and the model was trained iteratively across all batches. This approach allowed the models to focus on local temporal patterns while maintaining the ability to generalize across longer sequences.

Inputs were structured in the standard three-dimensional format [samples, timesteps, features], suitable for sequence models. For recurrent models (BiLSTM and BiGRU), the time dimension was explicitly preserved across layers with *return_sequences=True* in intermediate layers. For the TCN model, causal convolutions were used to respect temporal order and avoid leakage of future information into past predictions.

Each model was trained for up to 100 epochs with a batch size of 15, although early stopping typically resulted in faster convergence. After training, the model generated predicted flux values for each input time step. These predictions were then transformed back from logarithmic space into physical flux values for evaluation. The quality of reconstruction was assessed using three standard regression metrics:

Mean Absolute Error (MAE):

$$MAE = \frac{1}{n}\sum_{i=1}^{n} |y_i - \hat{y}_i| , \tag{2}$$

Root Mean Square Error (RMSE):

$$RMSE = \sqrt{\frac{1}{n}\sum_{i=1}^{n} (y_i - \hat{y}_i)^2} , \tag{3}$$

Coefficient of Determination (R^2):

$$R^2 = 1 - \frac{\sum_{i=1}^{n}(y_i - \hat{y}_i)^2}{\sum_{i=1}^{n}(y_i - \bar{y}_i)^2} , \tag{4}$$

where n is the total number of samples, i is the index of each sample, y_i is the true (observed) value, $\hat{y}_i$ is the predicted value, and $\bar{y}_i$ is the mean of the true values.

These metrics were calculated between the original and predicted flux values (after inverse transformation), allowing for quantitative comparison between the three model types. In addition, predicted LC were plotted alongside the original observations in log-log scale to visually assess the reconstruction quality. This training pipeline was applied identically to all models, ensuring a fair and controlled comparison across architectural types.

3. Results

This section presents the reconstruction outcomes of GRB LC using three deep learning architectures: BiLSTM, TCN, and BiGRU. The analysis focuses on two distinct categories of GRBs: Good GRBs and Break Bump/Bump Flare GRBs, evaluated using both quantitative metrics and visual inspection of the reconstructed LC.

3.1 Quantitative Evaluation

To quantify reconstruction accuracy, three standard regression metrics were employed: MAE, RMSE, and the R^2. Tables A1 and A2 summarize the comparative performance of each model across representative bursts from both categories. For Good GRBs, the BiGRU model consistently achieved the lowest MAE and RMSE, along with the highest R^2 values, indicating superior reconstruction fidelity. For instance, in GRB050318, BiGRU reduced the RMSE to 1.82×10^{-12}, compared to 2.49×10^{-12} for BiLSTM. Similarly, in GRB060421, all models exhibited strong performance ($R^2 > 0.999$), yet BiGRU maintained a slight edge in RMSE reduction.

In the case of Break Bump and Bump Flare GRBs, BiGRU again demonstrated the highest accuracy, particularly for bursts with complex temporal evolution, such as GRB141221A and GRB140304A. Here, BiGRU's RMSE was more than twofold lower than that of BiLSTM and TCN, while maintaining $R^2 > 0.99$ in most instances.

These results suggest that BiGRU excels in modeling both gradual and abrupt variations in GRB LC. While TCN demonstrated intermediate performance, generally outperforming BiLSTM but falling short of BiGRU, BiLSTM was the least effective, especially for bursts with non-monotonic features, resulting in higher errors and lower R^2 values.

.

3.2 Visual Evaluation

Complementing the quantitative analysis, visual inspection of the reconstructed LC (Figures 4-7) provides further insights into model performance. All reconstructions are plotted in logarithmic scale to emphasize dynamic range and temporal structure. Across all examples, BiGRU most accurately reproduces the observed light curves, including plateaus, flares, and decay phases, with minimal deviation. Notably, in GRB050607 and GRB140304A, BiGRU successfully captures complex features (e.g., sharp breaks, flaring activity) with high precision.

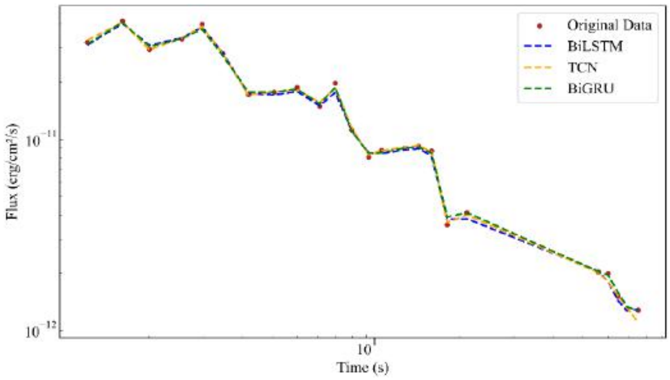

Fig. 4. Reconstructed LC of GRB090426 using BiLSTM, TCN, and BiGRU.

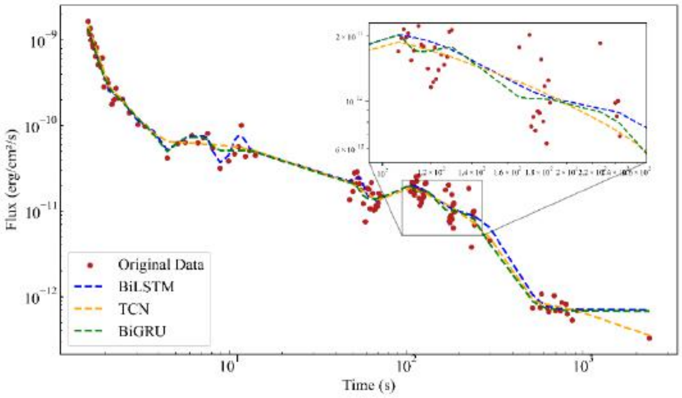

Fig. 5. Reconstructed LC of GRB050803 using BiLSTM, TCN, and BiGRU.

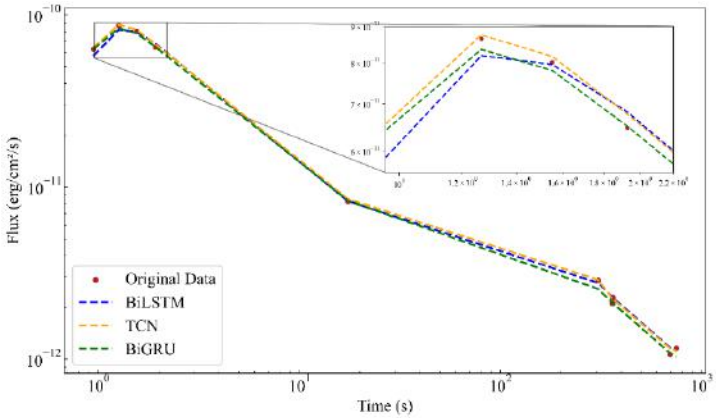

Fig. 6. Reconstructed LC of GRB060206 using BiLSTM, TCN, and BiGRU.

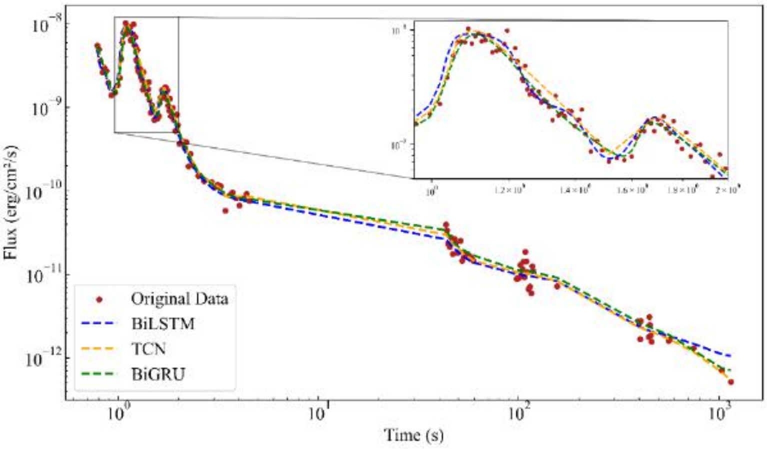

Fig. 7. Reconstructed LC of GRB050713A using BiLSTM, TCN, and BiGRU.

TCN generates smoother reconstructions, performing well for bursts with gradual variability but over-smoothing abrupt transitions, particularly in post-break or flaring regions. Conversely, BiLSTM tends to oversimplify variability, often missing localized structures. For example, in GRB141221A, BiLSTM fails to resolve the break feature entirely, whereas BiGRU reconstructs it accurately.

4. Conclusion

This study presents a comprehensive evaluation of three deep learning architectures - BiLSTM, BiGRU, and TCN - for reconstructing gamma-ray burst light curves from Swift-XRT X-ray afterglow data. Through systematic preprocessing, including logarithmic normalization, adaptive interpolation, and sequence batching, we established a robust framework for handling observational gaps and noise.

Quantitative analysis using MAE, RMSE, and R^2 metrics demonstrated BiGRU's superior performance, achieving up to 27% lower RMSE than BiLSTM and 15% improvement over TCN for complex Break Bump GRBs like GRB141221A, while maintaining MAE $< 2.1 \times 10^{-12}$ erg cm^{-2} s^{-1} and $R^2 > 0.99$ across all GRB types. The BiGRU architecture excelled particularly in capturing both gradual plateau phases and abrupt features such as flares and breaks, as evidenced in challenging cases like GRB140304A. While TCN performed adequately for monotonic decays, it showed systematic over-smoothing of rapid transitions (ΔRMSE $\approx$ 18% for flare-dominated segments), and BiLSTM struggled with fine-scale variability in high-noise regimes. These results position BiGRU as a powerful tool for advancing GRB studies, offering improved afterglow characterization, more accurate luminosity estimations for cosmological applications, and automated identification of physically significant features.

Future research directions should explore hybrid architectures combining BiGRU's temporal modeling with TCN's feature extraction, implement Bayesian uncertainty quantification, and investigate integration of physical constraints through differentiable hydrodynamic priors.

Conflict of interest statement

The authors declare that they have no conflict of interest in relation to this research, whether financial, personal, authorship or otherwise, that could affect the research and its results presented in this paper.

CRediT author statement

Zhunuskanov A., Akhmetali A.: Methodology, Data curation, Conceptualization; **Sakan A.:** Writing–original draft, Visualization; **Ussipov N., Zaidyn M.:** Writing – review & editing, Validation, Supervision; **Zhunuskanov A., Akhmetali A.:** Formal analysis; Investigation. The final manuscript was read and approved by all authors.

Funding

This research has been funded by the Science Committee of the Ministry of Science and Higher Education of the Republic of Kazakhstan (Grant AP19674715).

Acknowledgments

We would like to express our sincerest gratitude to the Department of Electronics and Astrophysics of the Al-Farabi Kazakh National University for supporting this work by providing computing resources (Faculty of Physics and Technology).

Reference

1 Kumar P., Zhang B. (2015) The physics of gamma-ray bursts & relativistic jets. *Physics Reports*, 561, 1-109. https://doi.org/10.1016/j.physrep.2014.09.008.

2 Meegan C.A., Fishman G.J., Wilson R.B., Paciesas W.S., Pendleton G.N., Horack J.M., Kouveliotou C. (1992) Spatial distribution of γ-ray bursts observed by BATSE. *Nature*, 355 (6356), 143-145. https://doi.org/10.1038/355143a0.

3 Barthelmy S.D., Chincarini G., Burrows D.N., Gehrels N., Covino S., Moretti A., Wijers R.A.M.J. (2005) An origin for short γ-ray bursts unassociated with current star formation. *Nature*, *438*(7070), 994–996, https://doi.org/10.1038/nature04392

4 Burrows D.N., Romano P., Falcone A., Kobayashi S., Zhang B., Moretti A., Gehrels N. (2005) Bright X-ray flares in gamma-ray burst afterglows. *Science*, *309*(5742), 1833-1835. https://doi.org/10.1126/science.1116168.

5 Boella G., Butler R. C., Perola G. C., Piro L., Scarsi L., Bleeker J. A. M. (1997) BeppoSAX, the wide band mission for X-ray astronomy. *Astronomy and Astrophysics Supplement Series*, *122*(2), 299-307. https://doi.org/10.1051/aas:1997136.

6 Ricker G.R., Vanderspek R.K. (2003) Gamma-ray burst and afterglow astronomy 2001: A workshop celebrating the first year of the hete mission. In *Gamma-Ray Burst and Afterglow Astronomy 2001: A Workshop Celebrating the First Year of the HETE Mission,* 662. https://doi.org/10.1051/0004-6361%3A200809709.

7 Willingale R., O'brien P.T., Osborne J. P., Godet O., Page K. L., Goad M.R., Chincarini G. (2007) Testing the standard fireball model of gamma-ray bursts using late X-ray afterglows measured by Swift. *The Astrophysical Journal*, *662*(2), 1093. https://doi.org/10.1086/517989.

8 Zhang Z. B., Choi C.S. (2008) An analysis of the durations of Swift gamma-ray bursts. *Astronomy & Astrophysics*, *484*(2), 293-297. https://doi.org/10.1051/0004-6361:20079210.

9 Sourav S., Shukla A., Dwivedi R., Singh K. (2023) Predicting Missing Light Curves of Gamma-Ray Bursts with Bidirectional-LSTM: An Approach for Enhanced Analysis. Available at: https://arxiv.org/abs/2310.02602.

10 Wang F., Zou Y. C., Liu F., Liao B., Liu Y., Chai Y., Xia L. (2020) A comprehensive statistical study of gamma-ray bursts. *The Astrophysical Journal*, *893*(1), 77. https://doi.org/10.48550/arXiv.1902.05489.

11 Abdikamalov E., Beniamini P. (2025) Reverse and forward shock afterglow emission from steep jets viewed off-axis. *Monthly Notices of the Royal Astronomical Society*, *539*(3), 2707-2717. https://doi.org/10.1093/mnras/staf649

12 Komesh T., Grossan B., Maksut Z., Abdikamalov E., Krugov M., Smoot G.F. (2023) Evolution of the afterglow optical spectral shape of GRB 201015A in the first hour: evidence for dust destruction. *Monthly Notices of the Royal Astronomical Society*, *520*(4), 6104-6110. https://doi.org/10.1093/mnras/stad538

13 Gritsevich M., Castro-Tirado A. J., Kubánek P., Pandey S.B., Hiriart D. (Eds.) (2025). *Early-time optical spectral shape measurements of GRB 200925B*. In *VII Workshop on Robotic Autonomous Observatories* (Revista Mexicana de Astronomía y Astrofísica, Serie de Conferencias, 59, 109–113. https://doi.org/10.22201/ia.14052059p.2025.59.20

14 Baron D. (2019) Machine learning in astronomy: A practical overview. arXiv preprint arXiv:1904.07248. https://doi.org/10.48550/arXiv.1904.07248

15 Fluke C. J., Jacobs C. (2020) Surveying the reach and maturity of machine learning and artificial intelligence in astronomy. Wiley Interdisciplinary Reviews: Data Mining and Knowledge Discovery, 10(2), e1349. https://doi.org/10.48550/arXiv.1912.02934.

16 Zhang H., Wang J., Zhang Y., Du X., Wu H., Zhang T. (2023) Review of artificial intelligence applications in astronomical data processing. *Astronomical Techniques and Instruments*, 1(1), 1-15. https://doi.org/10.61977/ati2024001.

17 Ussipov N., Zhanabaev Z., Almat A., Zaidyn M., Turlykozhayeva D., Akniyazova A., Namazbayev T. (2024) Classification of Gravitational Waves from Black Hole-Neutron Star Mergers with Machine Learning. *Journal of Astronomy and Space Sciences*, *41*(3), 149-158. https://doi.org/10.5140/JASS.2024.41.3.149.

18 Akhmetali A., Namazbayev T., Subebekova G., Zaidyn M., Akniyazova A., Ashimov Y., Ussipov N. (2024) Classification of Variable Star Light Curves with Convolutional Neural Network. *Galaxies*, *12*(6), 75. https://doi.org/10.3390/galaxies12060075.

19 Ussipov N., Akhtanov S., Zhanabaev Z., Turlykozhayeva D., Karibayev B., Namazbayev T., Tang X. (2024) Automatic modulation classification for MIMO system based on the mutual information feature extraction. *IEEE Access*, *12*, 68463-68470. https://doi.org/10.1109/ACCESS.2024.3400448.

20 Akhmetali A., Zhunuskanov A., Sakan A., Zaidyn M., Namazbayev T., Turlykozhayeva D., Ussipov N. (2025) *Luminis Stellarum et Machina: Applications of Machine Learning in Light Curve Analysis*. https://doi.org/10.48550/arXiv.2504.10038.

21 VanderPlas J., Connolly A. J., Ivezić Ž., Gray A. (2012) Introduction to astroML: Machine learning for astrophysics. *Proceeding of the 2012 conference on intelligent data understanding, IEEE*, 47-54. https://doi.org/10.1109/CIDU.2012.6382200.

22 Turmaganbet U., Zhexebay D., Turlykozhayeva D., Skabylov A., Akhtanov S., Temesheva S., Masalim P., Tao M. (2025). *Eurasian Physical Technical Journal*, *22*(2 (52), 121–132. https://doi.org/10.31489/2025N2/121-132.

23 Kruiswijk K., de Wasseige G. (2023). The classification and categorisation of gamma-ray bursts with machine learning techniques for neutrino detection. *arXiv preprint arXiv:2308*.12672. https://doi.org/10.48550/ arXiv.2308.12672

24 Zhang P., Li B., Gui R., Xiong S., Zou Z.C., Wang X., Zhao H. (2024) Application of Deep-learning Methods for Distinguishing Gamma-Ray Bursts from Fermi/GBM Time-tagged Event Data. *The Astrophysical Journal Supplement Series*, *272*(1), 4. https://doi.org/10.48550/arXiv.2303.00370.

25 Mehta N., Iyyani S. (2024) Exploring Gamma-Ray Burst Diversity: Clustering Analysis of the Emission Characteristics of Fermi-and BATSE-detected Gamma-Ray Bursts. *The Astrophysical Journal*, 969(2), 88. https://doi.org/10.3847/1538–4357/ad43e7.

26 Kumar A., Sharma K., Vinkó J., Steeghs D., Gompertz B., Lyman J., Pursiainen M. (2024) Magnetars as powering sources of gamma-ray burst associated supernovae, and unsupervised clustering of cosmic explosions. *Monthly Notices of the Royal Astronomical Society*, *531*(3), 3297-3309. https://doi.org/10.48550/arXiv.2403.18076.

27 Garcia-Cifuentes K., Becerra R.L., De Colle F. (2024) ClassiPyGRB: Machine Learning-Based Classification and Visualization of Gamma Ray Bursts using t-SNE. *arXiv preprint arXiv:2404.06439*, https://arxiv.org/abs/2404.06439

28 Misra K., Arun K.G. (2024) Diversity in Fermi/GBM Gamma-Ray Bursts: New Insights from Machine Learning. *The Astrophysical Journal*, *974*(1), 55. https://doi.org/10.3847/1538–4357/ad6d6a.

29 Chen J. M., Zhu K.R., Peng Z. Y., Zhang L. (2024) Unsupervised machine learning classification of Fermi gamma-ray bursts using spectral parameters. *Monthly Notices of the Royal Astronomical Society*, *527*(2), 4272-4284. https://doi.org/10.1093/mnras/stad3407.

30 Zhu S.Y., Sun W.P., Ma D.L., Zhang,F.W. (2024) Classification of Fermi gamma-ray bursts based on machine learning. *Monthly Notices of the Royal Astronomical Society*, *532*(2), 1434-1443. https://doi.org/10.48550/arXiv.2406.05357.

31 Dainotti M.G., Sharma R., Narendra A., Levine D., Rinaldi E., Pollo A., Bhatta G. (2023) A stochastic approach to reconstruct gamma-ray-burst light curves. *The Astrophysical Journal Supplement Series*, 267(2), 42. https://arxiv.org/abs/2304.00520.

32 Falco R., Parmiggiani N., Bulgarelli A., Panebianco G., Castaldini L., Di Piano A., Tavani M. (2025). A New Deep Learning Model for Gamma-Ray Bursts' Light Curves Simulation. In *Astronomical Society of the Pacific Conference Series* , 541, 230. https://doi.org/10.26624/BXNK3217

33 Bai S., Kolter J.Z., Koltun V. (2018) An empirical evaluation of generic convolutional and recurrent networks for sequence modeling. *arXiv preprint arXiv:1803.01271*. https://doi.org/10.48550/arXiv.1803.01271.

AUTHORS' INFORMATION

Zhunuskanov Alisher – Master (Sci.), Department of Physics and Technology, Al-Farabi Kazakh National University, Almaty, Kazakhstan; https://orcid.org/0009-0002-5435-9740; zhunuskanov_alisher1@live.kaznu.kz

Sakan Aknur – Master (Sci.), Department of Physics and Technology, Al-Farabi Kazakh National University, Almaty, Kazakhstan; Scopus Author ID: 59194448000; https://orcid.org/0009-0001-8784-4470; aknursakan47@gmail.com

Akhmetali Almat – Master (Sci.), Department of Physics and Technology, Al-Farabi Kazakh National University, Almaty, Kazakhstan, Scopus Author ID: 58759186800, https://orcid.org/0009-0005-7254-524X; akhmetalialmat@gmail.com

Zaidyn Marat – Bachelor (Sci.), Department of Physics and Technology, Al-Farabi Kazakh National University, Almaty, Kazakhstan; Scopus Author ID: 59194267200; https://orcid.org/0009-0006-8505-7277; zaidyn_marat@live.kaznu.kz

Ussipov Nurzhan – PhD, Acting Associate Professor, Department of Physics and Technology, Al-Farabi Kazakh National University, Almaty, Kazakhstan; Scopus Author ID:57226319348, https://orcid.org/0000-0002-2512-3280; ussipov.nurzhan@kaznu.kz

.

APPENDIX 1

Table A1. Quantitative performance comparison for Good GRBs using BiLSTM, TCN, and BiGRU.

GRB ID	**Model**	**MAE**	**RMSE**	**R^2**
GRB050318	BiLSTM	$1.46 \times 10^{-12} \pm 0.16 \times 10^{-12}$	$2.49 \times 10^{-12} \pm 0.28 \times 10^{-12}$	0.943 ± 0.012
	TCN	$1.35 \times 10^{-12} \pm 0.09 \times 10^{-12}$	$2.26 \times 10^{-12} \pm 0.08 \times 10^{-12}$	0.955 ± 0.003
	GRU	$1.10 \times 10^{-12} \pm 0.03 \times 10^{-12}$	$1.82 \times 10^{-12} \pm 0.02 \times 10^{-12}$	0.968 ± 0.0008
GRB050607	BiLSTM	$1.68 \times 10^{-11} \pm 5.52 \times 10^{-12}$	$3.92 \times 10^{-11} \pm 1.21 \times 10^{-11}$	0.9804 ± 0.0127
	TCN	$1.50 \times 10^{-11} \pm 3.59 \times 10^{-12}$	$3.07 \times 10^{-11} \pm 8.53 \times 10^{-12}$	0.9883 ± 0.0060
	GRU	$1.10 \times 10^{-11} \pm 3.66 \times 10^{-12}$	$2.64 \times 10^{-11} \pm 8.26 \times 10^{-12}$	0.9907 ± 0.0050
GRB050713A	BiLSTM	$2.80 \times 10^{-10} \pm 8.43 \times 10^{-11}$	$6.04 \times 10^{-10} \pm 1.65 \times 10^{-10}$	0.9383 ± 0.0319
	TCN	$2.54 \times 10^{-10} \pm 2.16 \times 10^{-11}$	$5.45 \times 10^{-10} \pm 5.83 \times 10^{-11}$	0.9522 ± 0.0117
	GRU	$1.60 \times 10^{-10} \pm 3.87 \times 10^{-11}$	$3.29 \times 10^{-10} \pm 5.84 \times 10^{-11}$	0.9818 ± 0.0060
GRB050915B	BiLSTM	$7.63 \times 10^{-11} \pm 2.39 \times 10^{-12}$	$1.58 \times 10^{-10} \pm 1.13 \times 10^{-11}$	0.9124 ± 0.0126
	TCN	$7.10 \times 10^{-11} \pm 6.63 \times 10^{-12}$	$1.48 \times 10^{-10} \pm 1.22 \times 10^{-11}$	0.9226 ± 0.0126
	GRU	$6.73 \times 10^{-11} \pm 4.22 \times 10^{-12}$	$1.34 \times 10^{-10} \pm 5.93 \times 10^{-12}$	0.9324 ± 0.0058
GRB060105	BiLSTM	$1.91 \times 10^{-10} \pm 1.79 \times 10^{-11}$	$3.09 \times 10^{-10} \pm 3.54 \times 10^{-11}$	0.9439 ± 0.0124
	TCN	$1.81 \times 10^{-10} \pm 2.50 \times 10^{-12}$	$2.93 \times 10^{-10} \pm 5.46 \times 10^{-12}$	0.9504 ± 0.0020
	GRU	$1.45 \times 10^{-10} \pm 5.55 \times 10^{-12}$	$2.36 \times 10^{-10} \pm 6.34 \times 10^{-12}$	0.9668 ± 0.0019
GRB060421	BiLSTM	$3.01 \times 10^{-13} \pm 3.41 \times 10^{-14}$	$4.97 \times 10^{-13} \pm 6.40 \times 10^{-14}$	0.9998 ± 0.0001
	TCN	$1.95 \times 10^{-13} \pm 1.04 \times 10^{-14}$	$2.72 \times 10^{-13} \pm 9.85 \times 10^{-15}$	0.9999 ± 0.0000
	GRU	$1.96 \times 10^{-13} \pm 2.77 \times 10^{-14}$	$3.71 \times 10^{-13} \pm 5.77 \times 10^{-14}$	0.9999 ± 0.0001

APPENDIX 2

Table A2. Quantitative performance comparison for Break Bump / Bump Flare GRBs.

GRB ID	Model	MAE	RMSE	R^2
GRB060206	BiLSTM	$1.31 \times 10^{-12} \pm 0.48 \times 10^{-12}$	$2.24 \times 10^{-12} \pm 0.81 \times 10^{-12}$	0.996 ± 0.003
	TCN	$1.47 \times 10^{-12} \pm 1.32 \times 10^{-12}$	$2.20 \times 10^{-12} \pm 2.12 \times 10^{-12}$	0.994 ± 0.010
	GRU	$4.16 \times 10^{-13} \pm 1.10 \times 10^{-13}$	$6.70 \times 10^{-13} \pm 1.55 \times 10^{-13}$	0.9996 ± 0.0002
GRB141005A	BiLSTM	$2.28 \times 10^{-12} \pm 9.25 \times 10^{-13}$	$3.80 \times 10^{-12} \pm 1.35 \times 10^{-12}$	0.9895 ± 0.0069
	TCN	$2.54 \times 10^{-12} \pm 6.80 \times 10^{-13}$	$4.19 \times 10^{-12} \pm 1.24 \times 10^{-12}$	0.9878 ± 0.0058
	GRU	$8.40 \times 10^{-13} \pm 1.75 \times 10^{-13}$	$1.44 \times 10^{-12} \pm 2.45 \times 10^{-13}$	0.9985 ± 0.0005
GRB141221A	BiLSTM	$9.04 \times 10^{-12} \pm 3.86 \times 10^{-12}$	$1.98 \times 10^{-11} \pm 8.08 \times 10^{-12}$	0.9896 ± 0.0066
	TCN	$1.52 \times 10^{-11} \pm 3.25 \times 10^{-12}$	$3.16 \times 10^{-11} \pm 5.80 \times 10^{-12}$	0.9767 ± 0.0085
	GRU	$3.15 \times 10^{-12} \pm 1.77 \times 10^{-13}$	$5.96 \times 10^{-12} \pm 8.47 \times 10^{-13}$	0.9992 ± 0.0002
GRB 140713A	BiLSTM	$2.93 \times 10^{-11} \pm 2.55 \times 10^{-12}$	$5.07 \times 10^{-11} \pm 5.14 \times 10^{-12}$	0.9564 ± 0.0088
	TCN	$3.26 \times 10^{-11} \pm 1.04 \times 10^{-12}$	$5.27 \times 10^{-11} \pm 2.31 \times 10^{-13}$	0.9541 ± 0.0015
	GRU	$2.055 \times 10^{-11} \pm 1.78 \times 10^{-12}$	$3.67 \times 10^{-11} \pm 3.84 \times 10^{-12}$	0.9680 ± 0.0123
GRB 050803	BiLSTM	$1.86 \times 10^{-11} \pm 0.27 \times 10^{-11}$	$5.33 \times 10^{-11} \pm 0.36 \times 10^{-11}$	0.971 ± 0.004
	TCN	$1.87 \times 10^{-11} \pm 0.07 \times 10^{-11}$	$4.53 \times 10^{-11} \pm 0.15 \times 10^{-11}$	0.979 ± 0.001
	GRU	$1.29 \times 10^{-11} \pm 0.14 \times 10^{-11}$	$3.21 \times 10^{-11} \pm 0.47 \times 10^{-11}$	0.988 ± 0.004
GRB 140304A	BiLSTM	$4.05 \times 10^{-11} \pm 9.26 \times 10^{-12}$	$9.61 \times 10^{-11} \pm 2.35 \times 10^{-11}$	0.9469 ± 0.0274
	TCN	$5.28 \times 10^{-11} \pm 4.63 \times 10^{-12}$	$1.01 \times 10^{-10} \pm 6.51 \times 10^{-12}$	0.9458 ± 0.0047
	GRU	$2.82 \times 10^{-11} \pm 4.59 \times 10^{-12}$	$6.36 \times 10^{-11} \pm 1.00 \times 10^{-11}$	0.9704 ± 0.0087
GRB 140713A	BiLSTM	$2.93 \times 10^{-11} \pm 2.55 \times 10^{-12}$	$5.07 \times 10^{-11} \pm 5.14 \times 10^{-12}$	0.9564 ± 0.0088
	TCN	$3.26 \times 10^{-11} \pm 1.04 \times 10^{-12}$	$5.27 \times 10^{-11} \pm 2.31 \times 10^{-13}$	0.9541 ± 0.0015
	GRU	$2.055 \times 10^{-11} \pm 1.78 \times 10^{-12}$	$3.67 \times 10^{-11} \pm 3.84 \times 10^{-12}$	0.9763 ± 0.0049
GRB 090426	BiLSTM	$5.077 \times 10^{-13} \pm 1.39 \times 10^{-13}$	$9.09 \times 10^{-13} \pm 3.33 \times 10^{-13}$	0.9935 ± 0.0039
	TCN	$4.073 \times 10^{-13} \pm 6.05 \times 10^{-14}$	$6.72 \times 10^{-13} \pm 7.45 \times 10^{-14}$	0.9971 ± 0.0007
	GRU	$2.67 \times 10^{-13} \pm 1.47 \times 10^{-13}$	$4.16 \times 10^{-13} \pm 2.00 \times 10^{-13}$	0.9986 ± 0.0016
GRB140709A	BiLSTM	$4.65 \times 10^{-10} \pm 9.20 \times 10^{-11}$	$7.83 \times 10^{-10} \pm 1.39 \times 10^{-10}$	0.9495 ± 0.0180
	TCN	$4.29 \times 10^{-10} \pm 9.28 \times 10^{-12}$	$7.33 \times 10^{-10} \pm 2.77 \times 10^{-11}$	0.9571 ± 0.0031
	GRU	$3.72 \times 10^{-10} \pm 7.42 \times 10^{-11}$	$6.14 \times 10^{-10} \pm 1.39 \times 10^{-10}$	0.9680 ± 0.0123
GRB050712	BiLSTM	$2.40 \times 10^{-11} \pm 6.27 \times 10^{-12}$	$4.22 \times 10^{-11} \pm 1.12 \times 10^{-11}$	0.9503 ± 0.0251
	TCN	$2.76 \times 10^{-11} \pm 2.06 \times 10^{-12}$	$4.95 \times 10^{-11} \pm 5.67 \times 10^{-12}$	0.9345 ± 0.0154
	GRU	$1.24 \times 10^{-11} \pm 3.34 \times 10^{-12}$	$2.24 \times 10^{-11} \pm 6.28 \times 10^{-12}$	0.9854 ± 0.0083

SUMMARIES ТҮСІНІКТЕМЕЛЕР АННОТАЦИИ

Кручинин Н.Ю., Кучеренко М.Г.

pH өзгерген жағдайда зарядталған алтын нанобөлшек бетінде орналасқан бинарлы полипептидтік кешендердің конформациялық құрылымы

Молекулалық-динамикалық модельдеу әдістерін қолдануы арқылы зарядталған сфералық алтын нанобөлшек бетінде орналасқан біртекті полипептидтерден құралған бинарлы кешендердің pH-қа сезгіш конформациялары зерттелді. Зарядталған сфералық нанообъект бетінде екі біртекті полимерден тұратын кешен ішіндегі өзара әрекеттесулерді ескере отырып, олардың конформациялық күйін сипаттайтын математикалық модель әзірленді. Нанобөлшек бетіне екі полипептид адсорбцияланған кезде макромолекулалық тәждің құрылымы бинарлы кешендегі полипептидтердің қандай комбинацияда орналасуына едәуір дәрежеде тәуелді болды. Бірдей екі біртекті полипептид үшін сутектік көрсеткіштің (pH) изоэлектрлік нүктеден ауытқуы олардың бейтарап бет бойымен бір-бірінен алыстауына әкелді, ал аттас зарядталған нанобөлшек бетінде макротізбекті тәждің айтарлықтай босаңсуы байқалды. Қарама-қарсы зарядталған екі полипептидтен тұратын кешен зарядталған нанобөлшек бетіне адсорбцияланған кезде полимерлік қабықшаның қабаттарға бөлінуі орын алып, оның айқын түрде ісінуі байқалды. Мұндай бинарлы кешенде полипептидтердің біреуінің изоэлектрлік нүктесіне жеткенде екінші зарядталған полипептид жазылып, алғашқы макротізбекпен байланысын үзіп, аттас зарядталған нанобөлшек бетінен алыстай бастайды.

Кілт сөздері: полипептидтік кешен, молекулалық-динамикалық модельдеу, конформациялық түрленулер, зарядталған нанообъект.

Кручинин Н.Ю., Кучеренко М.Г.

Конформационная структура бинарных полипептидных комплексов на поверхности заряженной золотой наночастицы при изменении pH

Используя молекулярно-динамическое моделирование исследованы pH-чувствительные конформации бинарных комплексов из однородных полипептидов, расположенных на поверхности заряженной сферической золотой наночастицы. Разработана математическая модель конформаций с учетом взаимодействий в комплексе двух однородных полимеров на поверхности заряженного сферического нанообъекта. При адсорбции на наночастице двух полипептидов структура макромолекулярной короны существенно зависела от того, в каких сочетаниях находились полипептиды в бинарном комплексе. Два одинаковых однородных полипептида при отклонении значения водородного показателя от изоэлектрической точки смещались друг от друга по нейтральной поверхности, а на поверхности одноименно заряженной наночастицы происходило сильное разрыхление макроцепной короны. На заряженной наночастице происходило расслоение полимерной оболочке из двух полипептидов разного знака, а сама она сильно разбухала. При достижении изоэлектрической точки одного из полипептидов в таком бинарном комплексе второй заряженный полипептид разворачивался и расцеплялся с первой макроцепью, смещаясь от поверхности одноименно заряженной наночастицы.

Ключевые слова: полипептидный комплекс, молекулярно-динамическое моделирование, конформационные преобразования, заряженный нанообъект.

Махабаева А.Т., Чиркова Л.В., Гученко С.А., Тулеуов С.Д., Маханов К.М., Шакирзянов Р.И, Афанасьев Д.А.

Титан оксинитридті қабықшалардың оптикалық және электрлік қасиеттерін зерттеу.

Бұл жұмыста аргон-оттегі-азот газдарының қоспасында магнетронды бүрку әдісімен шыны және кремний төсеніштерінің бетіндегі титан оксинитридінің қабыршақтары алынды. Алынған қабыршақтардың қалыңдығы, олардың тұндыру жылдамдығы және бетінің морфологиясы төсеніш түріне байланысты бағаланды. Шыны бетінде алынған қабыршақтардың оптикалық және электрлік қасиеттері зерттелді. Оптикалық мәліметтерді әдеби деректермен салыстыру аморфты қабыршақтардың $TiO_{1.27}N_{0.49}$ стехиометриялық құрамына жақын құраммен түзілуін көрсетті. Нәтижелер көрсеткендей, алынған қасиеттер әдеби мәліметтермен сәйкес келеді, бұл алынған титан оксинитридінің қабыршақтарын мемристорлардың белсенді элементі ретінде және заманауи материалтанудың басқа маңызды салаларында қолдану үшін жаңа мүмкіндіктер ашады.

Кілт сөздері: Титан оксинитриді, жұқа қабыршақтар, магнетронды бүрку, жұтылу спектрі, электр кедергісі.

Махабаева А.Т., Чиркова Л.В., Гученко С.А., Тулеуов С.Д., Маханов К.М., Шакирзянов Р.И, Афанасьев Д.А.

Исследование оптических и электрических свойств пленок оксинитрида титана.

В данной работе были получены пленки оксинитрида титана на поверхности стеклянных и кремниевых подложек методом магнетронного напыления в смеси газов аргон-кислород-азот. Толщина полученных пленок, скорость их осаждения и морфология поверхности были оценены в зависимости от типа подложки. Были изучены оптические и электрические свойства пленок, полученных на поверхности стекла. Сравнение

оптических данных с литературными показало образование аморфных пленок с составом, близким к стехиометрическому составу $TiO_{1.27}N_{0.49}$. Результаты показали, что полученные свойства соответствуют литературным данным, что открывает новые перспективы для использования полученных пленок оксинитрида титана в качестве активного элемента мемристоров, а также в других важных областях современного материаловедения.

Ключевые слова: оксинитрид титана, тонкие пленки, магнетронное напыление, спектр поглощения, электрическое сопротивление.

Середа Д.Б., Баскевич О.С., Середа Б.П., Кругляк И.В.

Кубтық құрылымды металл-металлоид қорытпаларындағы жақын реттіліктің фракталдық құрылымдарын модельдеу

Математикалық физика әдістерін қолдану арқылы электрқондыру әдісімен алынған $Fe_{88}P_{12}$ және $Cr_{88}C_{12}$ қорытпаларындағы қысқа қашықтықтағы реттіліктің кешенді модельдеуі жүргізілді. Модельдеу үшін бастапқы конфигурация ретінде негізгі металдың кристалдық құрылымы таңдалды. Рентгендік дифракция мен электрондық микроскопияны қоса алғанда, көптеген эксперименттік зерттеулер металл-металлоид қорытпаларындағы беткі микроқұрылымдардың басым түрде эллипсоидтық морфологияға ие екенін көрсетті. Осы эксперименттік бақылаулардың негізінде қорытпалар бетінде байқалатын макроскопиялық эллипсоидты түзілімдер геометриялық тұрғыдан салыстырмалы түрде қарапайым пішінге ие кластерлерден, атап айтқанда сфералардан немесе эллипсоидтардан тұрады деген болжам ұсынылды. Модельдеу нәтижелері бұл кластерлердің тән өлшемдері 30–50 ангстремнен аспайтынын және олардың векторлық өсуі негізінен жабынды бетіне қатысты бір радиал бағыт бойымен жүзеге асатынын көрсетті. Кластерлер өсуінің мұндай анизотроптық сипаты атомдық байланыстардың жергілікті энергиясындағы айырмашылықтармен және диффузия кинетикасымен түсіндіріледі, бұл кластерлер дамуының басым бағытта бағдарлануына әкеледі. Сонымен қатар, кластерлердің кеңістіктік таралуы мен өлшемдерінің біртектілігі жабындардың жалпы механикалық және физика-химиялық қасиеттеріне, соның ішінде қаттылыққа, тозуға төзімділікке және коррозияға қарсы тұрақтылыққа елеулі әсер ететіні анықталды. Модельдеу нәтижелерін эмпирикалық мәліметтермен үйлестіру электрқондырылған металл–металлоид жүйелеріндегі микроқұрылымдық эволюция механизмдерін тереңірек түсінуге мүмкіндік береді. Алынған нәтижелер бет құрылымын қалыптастыру және функционалдық жабындылардың пайдалану сипаттамаларын жақсарту мақсатында электрқондыру параметрлерін оңтайландыру үшін негіз бола алады.

Кілт сөздер: аморфты күй, электрқондыру, модельдеу, кластерлер.

Середа Д.Б., Баскевич О.С., Середа Б.П., Кругляк И.В.

Моделирование фрактальных структур ближнего порядка сплавов металл-металлоид с кубической структурой

С использованием методов математической физики проведено комплексное моделирование короткодействующего порядка в сплавах $Fe_{88}P_{12}$ и $Cr_{88}C_{12}$, полученных методом электроосаждения. В качестве исходной конфигурации для моделирования была выбрана кристаллическая структура основного металла. Многочисленные экспериментальные исследования, включая рентгеновскую дифракцию и электронную микроскопию, показали, что в сплавах металл-металлоид поверхностные микроструктуры имеют преимущественно эллипсоидную морфологию. На основании этих экспериментальных наблюдений была выдвинута гипотеза, что макроскопические эллипсоидные образования, наблюдаемые на поверхности сплавов, состоят из кластеров с относительно простой геометрической конфигурацией, например, сфер или эллипсоидов. Результаты моделирования показали, что эти кластеры имеют характерные размеры, не превышающие 30-50 ангстрем, а их векторный рост происходит преимущественно вдоль одного радиального направления относительно поверхности подложки. Такое анизотропное поведение роста объясняется различиями в локальной энергии атомной связи и кинетике диффузии, которые определяют преимущественное выравнивание развития кластеров. Кроме того, было установлено, что пространственное распределение и однородность размеров кластеров существенно влияют на общие механические и физико-химические свойства покрытий, включая твердость, износостойкость и коррозионную стойкость. Сочетание результатов моделирования с эмпирическими данными позволяет получить ценное представление о механизмах микроструктурной эволюции электроосажденных систем металл-металлоид. Эти результаты могут послужить основой для оптимизации параметров электроосаждения с целью формирования структуры поверхности и улучшения эксплуатационных характеристик функциональных покрытий.

Ключевые слова: аморфное состояние, электроосаждение, моделирование, кластеры.

Турдыбеков Д.М., Ибраев Н.Х., Копбалина К.Б., Кишкентаева А.С., Панкин Д.В., Смирнов М.Б.

N-(2-OXO-2H-CHROMEN-3-CARBONYL) цитизинінің электрондық және құрылымдық қасиеттерін теориялық зерттеу.

Цитизин мен кумарин негізіндегі жаңа қосылыстар фармацевтика өнеркәсібі үшін олардың болашағы зор биологиялық белсенділігіне байланысты үлкен қызығушылық тудырады. Бұл белсенділік молекуланың құрылымымен тығыз байланысты және ерекше электрондық қасиеттері арқылы байқалады. Осы жұмыста жаңадан синтезделген N-(2-oxo-2H-chromen-3-carbonyl)cytisine қосылысының электрондық және құрылымдық қасиеттерін теориялық тұрғыдан зерттеу нәтижелері келтірілген. Негізгі және бірінші қозған күйлердің молекулалық құрылымдары анықталып, олардың конформациялық әртүрлілігі ескерілген құрылымдық ерекшеліктері талданды. Жұтылу және сәуле шығару спектрлеріндегі жолақтардың қарқындылығын анықтайтын тік электрондық ауысулардың ықтималдықтары есептелді. Алынған теориялық нәтижелер этанол ерітінділерінің эксперименттік жұтылу және люминесценция спектрлерімен салыстырылды.

Кілт сөздер: цитизин, кумарин, кешен, тығыздық функционалы теориясы, УК-көрінетін спектроскопия, люминесценциялық спектроскопия.

Турдыбеков Д.М., Ибраев Н.Х., Копбалина К.Б., Кишкентаева А.С., Панкин Д.В., Смирнов М.Б.

Теоретическое исследование электронных и структурных свойств N-(2-OXO-2H-CHROMEN-3-CARBONYL) цитизина.

Новые соединения на основе цитизина и кумарина представляют интерес для фармацевтической промышленности в связи с их перспективной биологической активностью. Последняя, в свою очередь, тесно связана с структурой вещества, что проявляется в специфических электронных свойствах. В данной работе представлены результаты теоретических исследований электронных и структурных свойств недавно синтезированного N-(2-oxo-2H-chromen-3-carbonyl)cytisine. Установлена молекулярная структура основного и первого возбужденного состояния. Рассмотрены их структурные особенности с учетом конформационного разнообразия. Проведен расчет вероятностей вертикальных электронных переходов, определяющих интенсивности полос в спектрах поглощенич и эмиссии. Полученные теоретические результаты сопоставлены с измеренными спектрами поглощения и люминесценции этанольных растворов.

Ключевые слова: цитизин, кумарин, комплекс, теория функционала плотности, УФ-видимая спектроскопия, люминесцентная спектроскопия.

Бузяков Р.Р., Мехтиев А.Д., Нешина Е.Г., Алькина А.Д., Биличенко А.П.

Төмен қысымды бу электр жылытқышының жылу түтігінің әр түрлі жылыту элементтерімен қасиеттерін зерттеу

Бұл мақала автономды жылыту жүйелеріне арналған төмен қысымды бу электр жылыту құрылғысының жылу түтігін әзірлеу мен талдауға арналған. Зерттеу нысаны ретінде екі түрлі жылыту элементі алынған: нихромды спиральмен жабдықталған түтікше тәрізді электр жылытқыш және индукциялық жылытқыш. Жылыту сипаттамаларын, температуралық таралуды және энергия тиімділігін бағалау үшін эксперименттік талдау әдістері қолданылды. Индукциялық жылытқыштың жылуды жоғары жылдамдықпен және біркелкі тарата алатыны анықталды, ал түтікше тәрізді жылытқыш сенімділігімен және үнемділігімен ерекшеленеді. Алынған нәтижелер электр жылыту құрылғысының құрылымын оңтайландыру жолдарын ұсынуға мүмкіндік береді, бұл оның тиімділігі мен сенімділігін арттыруға бағытталған. Жасалған қорытындылар зерттелген құрылғыларды түрлі жылыту жүйелерінде практикалық қолдану әлеуетін растайды.

Кілт сөздері: бу электр жылытқышы, жылу түтігі, энергия тиімділігі, нихромды спираль, индукциялық жылытқыш, автономды жылыту, төмен қысым.

Бузяков Р.Р., Мехтиев А.Д., Нешина Е.Г., Алькина А.Д., Биличенко А.П.

Исследование характеристик тепловой трубки парового электро-обогревателя низкого давления с различными типами нагревателей

Статья посвящена разработке и анализу тепловой трубки парового электрообогревателя низкого давления, предназначенного для автономных систем отопления. Объектом исследования выступают два типа нагревательных элементов: трубчатый электрический нагреватель с нихромовой спиралью и индукционный нагреватель. Для оценки характеристик нагрева, температурного распределения и энергоэффективности использованы экспериментальные методы анализа. Установлено, что индукционный нагреватель обеспечивает более высокую скорость нагрева и равномерное распределение температуры, в то время как трубчатый нагреватель отличается стабильной работой и экономичностью. Полученные результаты позволяют предложить пути оптимизации конструкции электрообогревателя с целью повышения его эффективности и надежности. Выводы подтверждают практический потенциал применения исследуемых устройств в различных типах систем отопления.

Ключевые слова: паровой электрообогреватель, тепловая трубка, энергоэффективность, нихромовая спираль, индукционный нагреватель, автономное отопление, низкое давление.

Чепурный А., Якович А.

Нейрондық желілерді қолдану арқылы газтурбиналық қозғалтқышта метанолдың жануын сандық модельдеуді оңтайландыру.

Газ турбиналары жоғары энергиялы қуат өндіруде маңызды рөл атқарады, алайда NO_x және CO_2 шығарындыларын азайтуға қойылатын талаптардың артуы жану камераларының дәстүрлі конструкцияларын барған сайын күрделендіріп, қымбаттата түсуде. Бұл жұмыста шығарындыларды болжауды жеделдету мақсатында жоғары дәлдіктегі есептік гидродинамиканы нейрондық желілерге негізделген оқытумен үйлестіретін жаңа модельдеу парадигмасы ұсынылады. Есептік гидродинамика моделі Рейнольдс бойынша орташа алынған Навье-Стокс теңдеулерін, k-ε турбуленттік моделін және алдын ала араластырылмаған турбулентті жануды сипаттау үшін ықтималдық тығыздығы функциясы тәсілін пайдалану арқылы әзірленді. Метанның жану процесін модельдеуден кейін NO_x шығарындылары Зельдович механизмі негізінде есептелді. Модельді тексеру жанармай шығынын, артық ауа коэффициентін және қабырғадағы жылулық шығындарды өзгерту арқылы жүргізілді. Бағалауды жеделдету үшін есептік гидродинамика нәтижелері негізінде көпқабатты перцептрон типті нейрондық желі оқытылып, негізгі кіріс параметрлері (жанармай шығыны, артық ауа коэффициенті, температура, қысым және салқындату жағдайлары) бойынша NO_x және CO_2 шығарындыларын болжау жүзеге асырылды. Модель тәуелсіз тестілеу жиынында жоғары дәлдік көрсетіп, NO_x үшін детерминация коэффициенті (R^2) 0,998, ал CO_2 үшін 0,956 мәндерін көрсетті. Алынған нәтижелер эксперименттік мәліметтермен, сондай-ақ метан жануының егжей-тегжейлі кинетикалық сұлбасын Mech 3.0 қолданатын идеал реакторлар желісінің моделімен жақсы сәйкестік көрсетті. Ұсынылған нейрондық желі шығарындыларды бағалауға арналған жылдам суррогаттық модель ретінде қызмет етіп, төмен эмиссиялы жану камераларының конструкцияларын жедел оңтайландыруға мүмкіндік береді. Бұл тәсіл цифрлық егіздер мен жану процесін басқару жүйелеріне тиімді түрде енгізілуі мүмкін және сутек пен аммиак сияқты баламалы отын түрлеріне бейімделе алады.

Кілт сөздер: нейрондық желі; жану; газтурбиналық қозғалтқыш; сандық модельдеу.

Чепурный А., Якович А.

Оптимизация численного моделирования сгорания метанола в газотурбинном двигателе с помощью нейронных сетей.

Газовые турбины играют важнейшую роль в производстве высокоэнергетических мощностей, однако растущие требования к снижению выбросов NO_x и CO_2 делают традиционную конструкцию камеры сгорания все более сложной и дорогостоящей. В данной работе предлагается новая парадигма моделирования, которая сочетает высокоточную вычислительную гидродинамику с обучением на основе нейронных сетей для ускорения прогнозирования выбросов. Модель вычислительной гидродинамики была разработана с использованием уравнений Навье-Стокса, усредненных по Рейнольдсу, с k–ε моделью турбулентности и подходом к функции плотности вероятности для непредварительного смешивания для моделирования турбулентного сгорания метана. Выбросы NO_x рассчитывались после моделирования с использованием механизма Зельдовича. Проверка модели включала изменение расхода топлива, коэффициента избытка воздуха и тепловых потерь на стенках. Для ускорения оценок была обучена многослойная перцептронная нейронная сеть на результатах вычислительной гидродинамики для прогнозирования выбросов NO_x и CO_2 на основе ключевых входных данных (расход топлива, избыток воздуха, температура, давление, охлаждение). Модель показала высокую точность с коэффициентом детерминации (R^2) 0,998 для NO_x и 0,956 для CO_2 на независимом тестовом наборе. Результаты показали хорошее соответствие как экспериментальным данным, так и модели сети идеальных реакторов с использованием подробной кинетической схемы сгорания метана - Mech 3.0. Эта нейронная сеть служит быстрой суррогатной моделью для оценки выбросов, позволяя быстро оптимизировать конструкции камер сгорания с низким уровнем выбросов. Подход подходит для цифровых двойников и систем управления сгоранием и может быть адаптирован к альтернативным видам топлива, таким как водород и аммиак.

Ключевые слова: нейронная сеть, сгорание, газотурбинный двигатель, численное моделирование.

Аскарова А.С., Болегенова С.А., Нұғыманова А.О. Максимов В.Ю., Болегенова С.А., Оспанова Ш.С., Шортанбаева Ж.К., Аубакиров Н.П., Нурмуханова А.З.

Жану процестеріне оттықтар арқылы отынды енгізудің түрлі тәсілдерінің әсерін зерттеу.

Бұл жұмыста Шахтинская жылу электр станциясы БКЗ-75 қазандығының жану камерасының мысалын пайдалана отырып, оттық құрылғылары арқылы отынның түсуінің әртүрлі әдістерінің (тура ағынды және ұнтақ көмір ағынының бұралу бұрышы бар құйынды) әсерін зерттеу бойынша есептеу тәжірибелерінің жаңа нәтижелері берілген. Жану процестерін сандық модельдеу нәтижесінде келесілер алынды: толық жылдамдық векторының таралулары, температура өрістері, көміртегі оксидтері мен азот диоксиді NO_2 концентрация өрістері жану камерасының бүкіл көлемі бойынша және одан шығу кезінде. Ауа қоспасын берудің құйынды әдісі жоғары күлді көмірді жағу процесін оңтайландыруға мүмкіндік беретіні көрсетілді, өйткені бұл жағдайда алаудың өзегінде температураның жоғарылауы және жану камерасынан шығу кезінде оның төмендеуі

байқалады, бұл жану өнімдерінің пайда болуының химиялық процестеріне айтарлықтай әсер етеді. Құйынды оттық құрылғыларын пайдаланған кезде көміртегі тотығы СО үшін жану камерасының шығысындағы концентрация мәндері тікелей ағынды оттықтармен салыстырғанда шамамен 15%, ал азот диоксиді NO_2 үшін 20% төмендейді. Алынған нәтижелер ұнтақ көмір алауының жану процесін оңтайландыру, сол арқылы энергетикалық нысандардың тиімділігін арттыру және қоршаған ортаға зиянды заттардың шығарындыларын азайту бойынша ұсыныстар әзірлеуге мүмкіндік береді.

Кілт сөздер: жану, модельдеу, жылу электр станциясы, тікелей ағынды және құйынды оттықтар, температура, көміртегі тотығы, азот диоксиді.

Аскарова А.С., Болегенова С.А., Нұғыманова А.О. Максимов В.Ю., Болегенова С.А., Оспанова Ш.С., Шортанбаева Ж.К., Аубакиров Н.П., Нурмуханова А.З.

Исследование влияния различных способов подачи топлива через горелки на процессы горения.

В данной работе представлены новые результаты вычислительных экспериментов по исследованию влияния различных способов подачи топлива (прямоточного и вихревого с углом закрутки пылеугольного потока) через горелочные устройства на процессы горения на примере топочной камеры котла БКЗ-75 Шахтинской ТЭС (г. Шахтинск, Казахстан), сжигающего высокозольный карагандинский уголь. В результате численного моделирования процессов горения получены распределения вектора полной скорости, температурные поля, поля концентрации оксидов углерода и диоксида азота NO_2 по всему объему топочной камеры и на выходе из нее. Показано, что вихревой способ подачи воздушной смеси позволяет оптимизировать процесс сжигания высокозольного угля, так как в этом случае происходит повышение температуры в ядре факела и снижение ее на выходе из топочной камеры, что оказывает существенное влияние на химические процессы образования продуктов сгорания. При использовании вихревых горелочных устройств значения концентрации на выходе из топочной камеры по оксиду углерода СО снижаются примерно на 15%, а по диоксиду азота NO_2 на 20% по сравнению с прямоточными горелками. Полученные результаты позволяют разработать рекомендации по оптимизации процесса горения пылеугольного факела, что позволит повысить эффективность работы энергетических объектов и сократить выбросы вредных веществ в окружающую среду.

Ключевые слова: горение, моделирование, тепловая электростанция, прямоточные и вихревые горелки, температура, оксид углерода, диоксид азота.

Набиев Р.Н., Гараев Г.И., Рустамов Р.Р.

Дифференциалды-сыйымдылық датчигінің резонанстық жиіліктерінің уақытқа тәуелділігін зерттеу.

Мақалада әуежай периметрінің қауіпсіздігін қамтамасыз ету авиациялық қауіпсіздік саласындағы алдын алу шараларының бірі болып саналатыны атап өтіледі, ал инновациялық құрылғыларды ынталандыру қажеттілігі периметрлік күзет сигнализациясы жүйелерінде қолданылатын датчиктерді жетілдірудің өзектілігін арттырды. Периметрлік күзет сигнализациясы жүйелерінде ең кеңінен қолданылатын сенсор сыйымдылық датчигі екені көрсетіліп, оны қоршаған орта жағдайларының өзгерістеріне бейімдеудің маңыздылығы айқындалады. Зерттеудің мақсаты – дифференциалды-сыйымдылық датчиктер ретінде қолданылатын, цифрлық логикалық элементтер негізінде құрылған екі автогенератор жиілігінің қоршаған орта әсерінен уақыт бойынша өзгеру тәуелділігін зерттеу. Периметрлік күзет сигнализациясы жүйелерінде пайдаланылатын дифференциалды-сыйымдылық датчиктер рөлін атқаратын цифрлық логикалық элементтерден құралған екі автогенератор жиілігінің өзгеруін және олардың бір-біріне қатысты уақыт бойынша синхронды жұмыс істеуін сипаттайтын зерттеу нәтижелері келтірілген. Эксперименттер барысында әртүрлі ұзындықтағы сезгіш элементтерге қосылған автогенераторлардың резонанстық жиіліктері вариациясының математикалық күтілімі мен дисперсиясы есептелді және автогенератор жиіліктерінің өзара жоғары деңгейде синхронды өзгеретіні анықталды. Нәтижесінде, зертханалық жағдайларда ұзындығы екі метр болатын сезгіш элементтермен жабдықталған автогенераторлардың резонанстық жиіліктерінің уақыттық дрейфін ескере отырып, өлшенетін параметрлердің дискреттілігі жақындап келе жатқан объектінің салмағын анықтауға мүмкіндік беретіні эксперименттік түрде дәлелденді. Сонымен қатар, барлық жағдайларда екі автогенератордың резонанстық жиіліктері уақыт бойынша аздаған кідіріспен, бірақ екі бағытта да шамамен бірдей өзгеретіні анықталды.

Кілт сөздері: авиациялық қауіпсіздік, әуежай, периметр, күзет-ескерту жүйесі, дифференциалды-сыйымдылық датчик, резонанстық жиілік, сезгіш элемент, дисперсия.

Набиев Р.Н., Гараев Г.И., Рустамов Р.Р.

Исследование зависимостей резонансных частот дифференциально-емкостного датчика от времени.

В статье отмечается, что обеспечение безопасности периметра аэропорта считается одной из превентивных мер в области авиационной безопасности, и необходимость стимулирования инновационных устройств привела к необходимости совершенствования использования датчиков в системах охранной сигнализации периметра. Подчеркивается, что наиболее широко используемым датчиком в системах охранной сигнализации периметра является ёмкостный датчик, и показана важность адаптации к изменениям окружающей среды. Целью является исследование зависимости изменения частоты двух автогенераторов, построенных на цифровых логических

элементах, используемых в качестве дифференциально-ёмкостных датчиков, от окружающей среды. Приведено описание результатов исследований изменения частоты двух автогенераторов, построенных на цифровых логических элементах, используемых в качестве дифференциально-ёмкостных датчиков в системах охранной сигнализации периметра, а также их синхронной работы относительно зависимости друг от друга от времени. В ходе экспериментов рассчитаны математическое ожидание и дисперсия значений вариации резонансных частот автогенераторов, подключенных к чувствительным элементам разной длины, и установлено, что частоты автогенераторов изменялись более синхронно друг с другом. В результате экспериментально установлено, что с учетом временного дрейфа резонансной частоты автогенераторов с чувствительными элементами длиной два метра в лабораторных условиях дискретность измеряемых параметров позволяет определить вес приближающегося объекта, причем во всех случаях резонансные частоты обоих автогенераторов изменяются примерно одинаково в обоих направлениях с небольшой разницей во времени.

Ключевые слова*:* авиационная безопасность, аэропорт, периметр, охранно-предупредительная система, дифференциально-емкостный датчик, резонансная частота, чувствительный элемент, дисперсия.

Бақтыбеков К. С., Ашуров А. Е., Иванов А. В., Келгенбаев А. Ж., Жапанова А. С., Сайлаубайұлы С.

Бағдарламалы-анықталатын радиожүйелер негіздегі спутниктік станция антеннасының сипаттамаларын модельдеу және өлшеу.

Бұл зерттеу S диапазонындағы төмен жер орбитасындағы спутниктермен байланысуға арналған параболалық спутниктік антеннаның сипаттамаларын зерттейді. S диапазонын таңдау X диапазонымен салыстырғанда радиоарнаның айтарлықтай аз қуат тұтынуына байланысты. S диапазоны (2-4 ГГц) ауа-райының қолайсыздығына X диапазонына (8-12 ГГц) қарағанда аз сезімтал. Бұл факторлар Жерді қашықтықтан зондтау деректерін беру кезінде наноспутниктер үшін өте маңызды. S-диапазонындағы бу-боликалық антеннаның бағыттылық диаграммасын өлшеуге ерекше назар аударылады. Бұл өлшемдер антеннаның дизайны мен параметрлерін оңтайландыру үшін маңызды деректерді ұсынады, осылайша байланыс жүйесінің жалпы тиімділігін арттырады. Сынақтар күшейту бағытының имитацияланған және эксперименттік диаграммаларын, сондайақ эквивалентті изотроптық сәулелену қуаты, кіріс тогының тығыздығы және күшейтудің шу температурасына қатынасы сияқты негізгі антенна параметрлері өлшенді. Өлшенген және есептелген нәтижелерді, соның ішінде өлшеу дәлдігі мен қателіктерді салыстыру жақсы сәйкестікті көрсетті.

Кілт сөздері: бағыт диаграммасы, параболалық антенна, S диапазоны, жер станциясы, кірісті өлшеу, модельдеу.

Бактыбеков К.С., Ашуров А.Э., Иванов А.В., Кельгенбаев А.Ж., Жапанова А.С., Сайлаубайулы С.

Моделирование и измерение характеристик антенны спутниковой станции на основе программно - определяемой радиосистемы.

В данном исследовании изучаются характеристики параболической спутниковой антенны, предназначенной для связи со спутниками на низкой околоземной орбите в S-диапазоне. Выбор S-диапазона обусловлен значительно меньшим энергопотреблением радиоканала по сравнению с X-диапазоном. S-диапазон (2-4 ГГц) менее чувствителен к неблагоприятным погодным условиям, чем X-диапазон (8-12 ГГц). Эти факторы имеют решающее значение для наноспутников при передаче данных дистанционного зондирования Земли. Особое внимание уделяется измерениям диаграммы направленности параболической антенны в S-диапазоне. Эти измерения предоставляют важные данные для оптимизации конструкции и параметров антенны, тем самым повышая общую эффективность системы связи. В ходе испытаний были получены как смоделированные, так и экспериментальные диаграммы направленности усиления, а также ключевые параметры антенны, такие как эквивалентная изотопно излучаемая мощность, плотность входного потока мощности и отношение усиления к шумовой температуре. Сравнение измеренных и расчетных результатов, включая точность измерений и погрешности, показало хорошее соответствие.

Ключевые слова: диаграмма направленности, параболическая антенна, S-диапазон, наземная станция, измерение усиления, моделирование.

Сатыбалдин А.Ж., Шаймерденова К.М., Жандыбаев Б.Б, Бакибаев А.А., Алпысова Г.К., Сейтжан Р., Тянах С.

Жоғары вольтты қысқа импульсті электргидравликалық разряд жүйесінің және нанокомпозиттік катализатордың мұнай шламдарына деструкция әсерін зерттеу.

Бұл мақалада мұнай шламын жоғары вольтты қысқаимпульсті электргидравликалық разряд әдісімен өңдеу бойынша жүргізілген зерттеу нәтижелері ұсынылған. Разряд кернеуі, конденсаторлар батареясының сыйымдылығы, өңдеу уақыты, электродтар ара-қашықтығы және катализатор концентрациясы сияқты негізгі параметрлердің жеңіл және орта мұнай фракцияларының шығымына әсері талданды. Эксперименттік зерттеулер фракциялардың максималды шығымына (36,4 %-ға дейін) қол жеткізу үшін оңтайлы шарттар ретінде өңдеу ұзақтығының 6 минутты, электродтар ара-қашықтығының 10 мм-ді, конденсаторлар батареясының сыйымдылығының 0,125 мкФ-ты және нанокомпозитті катализатор концентрациясының 1 %

болуы қажет екенін көрсетті. Катализаторды қолдану жоғары молекулалық қосылыстардың деструкциясын күшейтетіні, ал электрфизикалық параметрлерді оңтайландыру процестің энергиялық тиімділігін арттыратыны анықталды. Алынған нәтижелер мұнай қалдықтарын кәдеге жаратуға арналған энергия үнемдейтін технологияларды әзірлеу барысында пайдаланылуы мүмкін.

Кілт сөздері: мұнай шламдары, нанокатализатор, жоғары вольтты қысқа импульсті электргидравликалық разряд, жеңіл және орта фракциялар.

Сатыбалдин А.Ж., Шаймерденова К.М., Жандыбаев Б.Б., Бакибаев А.А., Алпысова Г.К., Сейтжан Р., Тянах С.

Исследование влияния высоковольтной коротко-импульсной электрогидравлической разрядной системы и нанокомпозитного катализатора на деструкцию нефтешламов.

В данной статье представлены результаты исследования переработки нефтешлама методом высоковольтного коротко-импульсного электрогидравлического разряда. Проанализировано влияние таких ключевых параметров, как напряжение разряда, ёмкость батареи конденсаторов, время обработки, межэлектродное расстояние и концентрация катализатора, на выход лёгких и средних нефтяных фракций. Экспериментальные исследования показали, что оптимальными условиями для достижения максимального выхода фракций (до 36,4%) являются продолжительность обработки 6 минут, межэлектродное расстояние 10 мм, ёмкость батареи конденсаторов 0,125 мкФ и концентрация нанокомпозитного катализатора 1%. Установлено, что применение катализатора способствует интенсификации деструкции высокомолекулярных соединений, а оптимизация электрофизических параметров повышает энергетическую эффективность процесса. Полученные результаты могут быть использованы при разработке энергоэффективных технологий утилизации нефтяных отходов.

Ключевые слова: нефтешлам, нанокатализатор, высоковольтный короткоимпульсный электрогидравлический разряд, лёгкие и средние фракции.

Inyang E.P., Okoi P.O., Nwachukwu I.M.

Кванттық жүйелердегі Шеннон, Фишер және Реньи энтропияларын және осциллятор күштерін зерттеу.

Бұл зерттеуде радиалдық скалярлық дәрежелік потенциалды қолдану жағдайында бірөлшемді және үшөлшемді жүйелердегі Фишер мен Шеннон энтропиялары қарастырылады. Никифоров–Уваров әдісі Грин–Олдрич жуықтауымен үйлестіріле отырып, энергияның меншікті мәндері мен нормаланған толқындық функциялар алынды. Нәтижелер Шеннон және Фишер энтропиялары кванттық ақпараттың іргелі теңсіздіктерін, соның ішінде Бялыницкий-Бирулы-Мицельский және Стам-Крамер-Рао шектерін әртүрлі кеңістіктік өлшемдерде қанағаттандыратынын көрсетеді. Реньи энтропиясы да координаттар кеңістігінде де, импульстер кеңістігінде де талданып, оның экрандау параметріне тәуелділігі анықталды әрі өзара байланысқан аймақтар арасындағы өлшеу дәлдіктерінің өзара толықтырылуы айқындалды. Жекелеген жағдайларда радиалдық скалярлы дәрежелік потенциал Крацер потенциалына келтіріледі, бұл метилидин (CH) және азот (N_2) молекулалары үшін энергия спектрлерін есептеуге мүмкіндік береді. Энергияның бұрыштық моменттің артуымен өсуі молекулалық тұрақтылық пен спектроскопиялық ауысуларға әсер етеді, ал есептелген осциллятор күштері бұрынғы нәтижелермен жақсы сәйкестік көрсетеді. Бұл радиалдық скалярлық дәрежелік потенциал моделінің кванттық ақпарат теориясында да, молекулалық спектроскопияда да қолданылуға жарамдылығын растайды.

Кілт сөздері: Шрёдингер теңдеуі, осциллятор күші, Никифоров-Уваров әдісі, екіатомды молекулалар, энтропиялық анықталмағандық.

Inyang E.P., Okoi P.O., Nwachukwu I.M.

Исследование энтропий Шеннона, Фишера и Реньи и сил осцилляторов в квантовых системах.

В данном исследовании изучаются энтропии Фишера и Шеннона в одномерных и трехмерных системах при использовании радиального скалярного степенного потенциала. С помощью метода Никифорова-Уварова в сочетании с приближением Грина-Олдрича были получены собственные значения энергии и нормированные волновые функции. Результаты показывают, что энтропии Шеннона и Фишера удовлетворяют фундаментальным неравенствам квантовой информации, включая границы Бялыницкого-Бирулы-Мицельского и Стама-Крамер-Рао, в различных пространственных измерениях. Энтропия Реньи также была проанализирована как в пространстве положений, так и в пространстве импульсов, выявив ее зависимость от параметра экранирования и подчеркнув взаимодополняемость точности измерений между сопряженными областями. В частных случаях радиальный скалярный степенной потенциал сводится к потенциалу Крацера, что позволяет вычислять энергетические спектры для молекул метилидина (CH) и азота (N_2). Энергия возрастает с угловым моментом, влияя на молекулярную стабильность и спектроскопические переходы, в то время как рассчитанные силы осцилляторов согласуются с предыдущими результатами, что подтверждает применимость модели радиального скалярного потенциала мощности, как в квантовой теории информации, так и в молекулярной спектроскопии.

Ключевые слова: уравнение Шрёдингера, сила осциллятора, метод Никифорова-Уварова; двуатомные молекулы; энтропийная неопределенность.

Жанабаев З.Ж., Иманбаева А.К., Акниязова А.Ж., Ашимов Е.К.

FS CMa типті жұлдыздардың сигналындағы флуктуациялық-диссипациялық қатынасы

Қос жұлдыз физикасының маңыздылығына байланысты бұл объектілерді зерттеудің жаңа теориялары мен әдістері үнемі дамытылып отырады. Осы жұмыста флуктуациялық-диссипациялық теореманы қолдану арқылы алынған жаңа нәтижелер ұсынылған. Теоремаға сәйкес, жүйедегі флуктуациялар термиялық тепе-теңдік түрінде диссипацияны тудырады. Флуктуациялардың спектрлік корреляциялық функциясы фотондардың диссипация мөлшерімен байланысты. Бұл зерттеуде қос жұлдыздардың эволюциялық сатысы FS CMa типті күрделі жұлдыздық жүйелердегі диссипация мен флуктуация арасындағы байланысты талдау арқылы анықталады.

Кілт сөздер: флуктуациялық-диссипациялық талдау, FS CMa типті жұлдыздар, қос жұлдыздар, фотондардың диссипациясы.

Жанабаев З.Ж., Иманбаева А.К., Акниязова А.Ж., Ашимов Е.К.

Флуктуационно-диссипационное соотношения сигнала звёзд типа FS CMa.

В связи с важностью физики двойных звезд постоянно разрабатываются новые теории и подходы к исследованию этого объекта. В этой работе представлены новые результаты использованием флуктуационно-диссипационной теоремы. Согласно теореме флуктуации в системе создают диссипацию в виде теплового равновесия. Спектральная функция корреляций флуктуаций связано с количеством диссипации фотонов. В этой работе установлены степень эволюции двойных звезд путем анализа связи между диссипацией и флуктуацией в сложных звезд типа FS CMa.

Ключевые слова: Флуктуационно-диссипационный анализ, звёзды типа FS CMa, двойные звёзды, диссипация фотонов.

Трубицын А.А., Грачев Е.Ю., Кочергин Э.Г., Сережин А.А.

Катодтық линзаның коллиматорлық және телескопиялық режимдері

Эмиссиялық жүйелердің (электрондық микроскоптар, микротоғысты рентген түтіктері және т.б.) сипаттамаларын жақсартудың бір жолы - катодтық линзаның аберрацияларын азайту болып табылады. Мұндай төмендету тек олардың электронды-оптикалық сұлбаларын терең теориялық талдау негізінде ғана мүмкін. Бұл зерттеу аясында параксиалдық жуықтауда электродтарының конфигурациясы іс жүзінде еркін болатын катодтық линзаны модельдеу құралдарын әзірлеуге талпыныс жасалды және коллиматорлық әрі телескопиялық режимдерді іске асыру шарттары анықталды. Линзаның аталған жұмыс режимдерін қамтамасыз ететін параметрлердің өзара байланысы зерттелді. Нәтижесінде катодтық линзаның нақты (идеалдандырылмаған) конструкциясы үшін коллиматорлық және телескопиялық режимдерді сенімді түрде қамтамасыз ететін электронды-оптикалық сұлбалар әзірленді.

Кілт сөздер: электрондық оптика, электрстатикалық линза, параксиалдық оптика, потенциалдың таралуы.

Трубицын А.А., Грачев Е.Ю., Кочергин Э.Г., Сережин А.А.

Коллиматорный и телескопический режимы катодной линзы.

Один из способов улучшения характеристик эмиссионных систем (электронных микроскопов, микрофокусных рентгеновских трубок и др.) заключается в снижении аберраций катодной линзы. Такое снижение возможно лишь на основе глубокого теоретического анализа их электронно-оптических схем. В рамках настоящих исследований сделана попытка разработки средств моделирования катодной линзы с практически произвольной конфигурацией электродов в параксиальном приближении, определены условия реализации коллиматорного и телескопического режимов. Изучена взаимосвязь параметров, обеспечивающих указанные режимы работы линзы. Разработаны электронно-оптические схемы, гарантирующие коллиматорный и телескопический режимы катодной линзы реальной (неидеализированной) конструкции.

Ключевые слова: электронная оптика, электростатическая линза, параксиальная оптика, распределение потенциала.

Жунусканов А.А., Сақан А.Б., Ахметәлі А.Б., Зайдын М., Үсіпов Н.М.

Гамма-сәулелік жарқылдардың жарқырау қисығын болжамды модельдер арқылы қайта құру

Гамма-сәулелердің жарылыстары ғаламдағы ең жігерлі және күрделі құбылыстардың кейбірін білдіреді, олар жиі бақылауларды қамтитын жоғары айнымалы жарқырау қисықтарымен сипатталады. Бұл жарқырау қисықтарын қалпына келтіру осындай оқиғалардың қозғаушы күші болып табылатын физикалық процестер туралы тереңірек түсінік алу үшін өте маңызды. Бұл зерттеу рентгендік деректерде байқалатын үстірт фазасына арнайы назар аудара отырып, гамма-сәулелік жарылыстардың жарқырау қисықтарын қалпына келтіру үшін машиналық оқытуға негізделген құрылымды ұсынады. Талдау модельдеудің үш дәйекті тәсілінің өнімділігін салыстырады: екі бағытты қайталанатын нейрондық желі, қақпалы қайталанатын архитектура және уақытша деректерге арналған конволюциялық модель. Осы зерттеудің нәтижелері екі бағытты қақпалы қайталанатын

бірлік моделі гамма-сәулелердің жарылуының барлық түрлері бойынша бағаланған модельдер арасында орташа абсолютті қателікпен, орташа түбірлік квадрат қатілекпен және анықтау коэффициентімен өлшенетін ең жақсы болжамды дәлдікті көрсеткенін көрсетеді. Екі бағытты қақпалы қайталанатын қондырғы үстірттің біртіндеп фазаларын да, күрт өтпелі ерекшеліктерін де, соның ішінде алаулар мен үзілістерді, әсіресе жарық қисықтарының күрделі сценарийлерін модельдеуде кеңейтілген мүмкіндіктерді көрсетті.

Кілт сөздер: гамма-сәулелік жарылыс, терең оқыту, нейрондық желілер, жарқырау қисығы.

Жунусканов А.А., Сакан А.Б., Ахметали А.Б., Зайдын М., Усипов Н.М.

Реконструкция кривой блеска гамма-всплесков с помощью прогнозирующих моделей.

Гамма-всплески представляют собой одно из самых энергичных и сложных явлений во Вселенной, характеризующееся сильно изменяющимися кривыми блеска, которые часто содержат пробелы в наблюдениях. Реконструкция этих кривых блеска необходима для более глубокого понимания физических процессов, лежащих в основе таких событий. В этом исследовании предлагается основанная на машинном обучении система реконструкции кривых блеска гамма-всплесков, в которой особое внимание уделяется фазе плато, наблюдаемой в рентгеновских данных. В ходе анализа сравнивается эффективность трех последовательных подходов к моделированию: двунаправленной рекуррентной нейронной сети, закрытой рекуррентной архитектуры и сверточной модели, разработанной для временных данных. Результаты этого исследования показывают, что двунаправленная стробированная рекуррентная единичная модель продемонстрировала наилучшую точность прогнозирования среди оцененных моделей по всем типам гамма-всплесков, измеряемую по средней абсолютной ошибке, среднеквадратичной ошибке и коэффициенту детерминации. Примечательно, что двунаправленный стробируемый рекуррентный модуль продемонстрировал расширенные возможности в моделировании как постепенных фаз плато, так и резких переходных процессов, включая вспышки и разрывы, особенно в сложных сценариях кривой блеска.

Ключевые слова: гамма-всплеск, глубокое обучение, нейронные сети, кривая блеска.